The synergistic role of light and heat in liquid-based nanoparticle manipulation

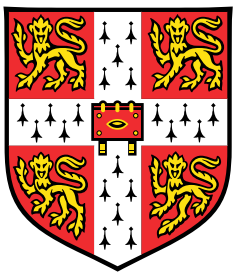

Omid Siddiqui

Department of Physics, Chemical Engineering and Biotechnology
University of Cambridge

This dissertation is submitted for the degree of
Doctor of Philosophy

Girton College December 2019

Declaration

This thesis is the result of my own work and includes nothing which is the outcome of work done in collaboration except as declared in the Preface and specified in the text. It is not substantially the same as any that I have submitted, or, is being concurrently submitted for a degree or diploma or other qualification at the University of Cambridge or any other University or similar institution except as declared in the Preface and specified in the text. I further state that no substantial part of my thesis has already been submitted, or, is being concurrently submitted for any such degree, diploma or other qualification at the University of Cambridge or any other University or similar institution except as declared in the Preface and specified in the text. It does not exceed the prescribed word limit for the relevant Degree Committee

Omid Siddiqui
December 2019

Abstract

The synergistic role of light and heat in liquid-based nanoparticle manipulation

Omid Siddiqui

Light and heat are synergistic tools used in the manipulation of nanoparticles and biomolecules. When optical effects dominate over thermal effects, the motion of nanoparticles can be controlled by optical forces. Here, we study the motion of 100 nm gold particles within a 1D optical potential, created by interfering counterpropagating beams. Tracking of particle trajectories revealed a large and asymmetric reduction in the nanoparticle diffusion constant in the presence of the traps, in agreement with theoretical predictions.

When thermal effects dominate, laser light can induce local temperature gradients. Here, this was achieved by absorption of near-infrared (NIR) laser light in a Chromium microdisc. This resulted in thermophoretic separation of sodium azide ions, causing a local electric field that was used to manipulate 26 nm polystyrene beads. The nanoparticles were observed to follow the NIR heating spot, enabling light-controlled nanoparticle swarming. The induced 3D temperature profiles were characterised by time-correlated single-photon counting microscopy, with a temperature-sensitive dye. Through analysis of the particle velocities, the thermoelectric field strength, as well as the previously unknown Soret coefficients of azide ions were quantified.

Transmission of laser beams through nanoparticle suspensions can lead to strong nonlinear lensing and soliton-like propagation effects. Literature has attributed these to redistribution of particles by optical gradient forces, and the effect is commonly described as an effective Kerr nonlinearity. To test this hypothesis, beam propagation experiments through a suspension of 40 nm plasmonic gold nanoparticles were carried out, and were found to be in agreement with previously reported results. To verify the nature of the effect, a new time-resolved z-scan technique was developed to measure the timescale and magnitude of the refractive index change. Surprisingly, the data demonstrates that the timescales can only be explained by thermal-absorption, -diffusion, and thermo-optic effects. As a result, the nonlinear effects are non-local and z-scan measurements will underestimate their magnitude.

To rhetoric and logic

"Nature composes some of her loveliest poems
for the microscope and the telescope."
— Theodore Roszak

Acknowledgements

I owe a debt of gratitude to my supervisors Tijmen Euser, and Clemens Kaminski for all their efforts and time spent in nurturing me to be a better researcher. Tijmen, you have been a fantastic mentor, and I have learnt so much from you in the past three years. I really cannot thank you enough for all the time you have spent with me discussing ideas and addressing challenges. I hope that you will continue to give the same level of dedication to your students as your group grows. Clemens, thank you for instilling me to always strive for the best and to have a clear premise. I will miss our ideas sessions in your office with Tijmen and Gabi. I have always admired your positivity and encouragement towards myself and others in the group, and I hope you continue to do so long into the future.

I would like to thank Jeremy Baumberg for providing such a nurturing environment, in his group, and the Cavendish as a whole. It's inspiring how you have such an enormous influence on people's work without being entirely aware of it.

My work would not have been possible without the support of the Engineering and Physical Sciences Research Council, Sensors CDT (Karen Scrivener, Oliver Hadeler, and Fernando da Cruz Vasconcellos), the Nano DTC (Kimberly Cole), the Winton Trust, Cavendish Laboratory (Barry Shores), and the Department of Chemical Engineering and Biotechnology (Jon Summerfield).

Thank you to the past and present members of Optofluidics group (Philipp Koehler, Ralf Mouthaan, Takashi Lawson, Jan Heck, Alex Gentleman, Jonathan Mortlock, Romain Tirole) for their support, their energy, and distractions they provided for the good and bad days in the lab. I would like to commend Ermanno Miele for his willingness to always share results, ideas, and insights into overcoming technical challenges.

The talented and supportive members of the Laser Analytics group has been hugely influential to my work. I'm very grateful to Amberley Stephens, Edward Ward, Katharina Scherer, Ioanna Mela, Maria Zacharopoulou, Eric Rees, Pedro Vallejo-Ramirez, Chetan Poudel, and Marcus Fantham for their training, time, support, and most importantly for being good fun to work with. Members of the Nanophotonics centre have aided and supported my work, which I am very grateful for, in particular, Dean Kos, Calvin Dumesnil, Andrew Salmon, Matthew Cheetham, Bart de Nijs, Marlous Kemp, and Rohit Chikkaraddy.

Thank you to my family for their ever-lasting supportive, and I hope you will forgive my lack of presence, especially in the last several months of this PhD.

I am very grateful to my partner, Ioana Olan, for being my sanity and giving me a push when I needed one. My life at Cambridge would have been infinitely harder without your support. Thank you to James Farmer for his continued encouragement and positive energy through my academic career. Thank you to my friends whom I met through the Sensors CDT: Oliver Vanderpoorten, Farah Alimagham, Miranda Robbins and Tristan Hughes, for lending an ear and sharing ideas to help me along with my work.

Thank you to Fabio Gardi, Konstantinos Pittas, Constantine Capsaskis, Sam Abujudeh, Maria Gomez, Eugene Seah, Sangjin Lee, Adelyne Chan, Mahnoush Bahjat for all the fun time and the copious amounts of food that we have shared.

Thank you to all the members of the Esposito lab for their warm welcome. I look forward to working with you all in the next chapter of my academic work.

Collaborations

All thin film deposition was conducted by Dean Kos at the Nanophotonics Centre.

The electronics for the custom made near-infrared laser was made by Barry shores at the Cavendish laboratory.

The heating stage for calibrating the lifetime-temperature dependence of Rhodamine-B was made by Jon Summerfield at the department of chemical engineering and biotechnology. The cartridge heaters for it was wired by the electrics suite at chemical engineering and biotechnology department.

The Time correlated single photon microscope was developed by the Laser Analytics group. The training was provided by Chetan Poudel.

The structured illumination microscope was built by Marcus Fantham and used as a fluorescence microscope in this work.

Table of contents

List of figures

List of tables

Chapter 1

Introduction

Every person who has peered through the eyepiece of a microscope and seen the scattered light from nanoparticles revealing their chaotic dance under Brownian motion, their collisions and clumping, knows that they are observing the consequences of many more unseen interactions. Yet replacing the nanoparticles with more complex structures, such as fluorescently tagged proteins or DNA, shows the same disorderly drifting and collisions, whilst most of the interactions remain elusive. Light and heat have been used to disturb and manipulate their motion, and consequently offer a glimpse of their hidden interactions.

The ambition behind the present study was to examine and explore the interaction of light and heat with proteins. Through these interactions, protein properties such as size, conformation, temporal binding kinetics, as well as how they interact with their chemical environment could be discerned by subjecting them to intensity- or thermal-gradients. Quantification of these metrics is hugely beneficial for researchers studying neurodegenerative diseases such as Alzheimer's Disease. Hence, this work aimed to develop microfluidic devices that combined light or heat in a geometry that effortlessly integrated with conventional or super-resolution microscopes. These devices would facilitate controllable trapping of proteins to judiciously induce aggregation sites, from which the rate of growth and binding kinetics could be determined. Furthermore, these devices would enable drug screening of potential aggregation inhibiting nano-bodies. However, proteins are inherently complex structures which are sensitive to a variety of environmental factors. Even in static environments, they have a broad size distribution, which changes with time. These factors make it challenging to isolate the fundamental

mechanisms by which light and heat interact with proteins.

As a first step, light and heat interactions were investigated using monodispersed nanoparticles in known fluidic environments. Intensity gradients were used to optically alter the motion of nanoparticles (Chapter 2). Thermally mediated nanoparticle manipulation is a more advantageous mechanism for studying nanoparticle properties, as it diminishes the probability of photodamage. Hence, strong thermal gradients were independently generated to control and trap nanoparticles (Chapter 3). The interplay of light with matter can cause heating through nanoparticle absorption, which gives rise to self-induced lensing effects. This phenomenon was also studied by determining how light is redistributed due to the self-induced refractive index changes (Chapter 4).

1.1 Optical trapping of nanoparticles

Of the trapping and manipulation mechanisms available for nanoparticles, optical forces are the most ubiquitous method. Ashkin was the first to experimentally observe the altered motion of micron-sized latex particles caused by the radiation pressure

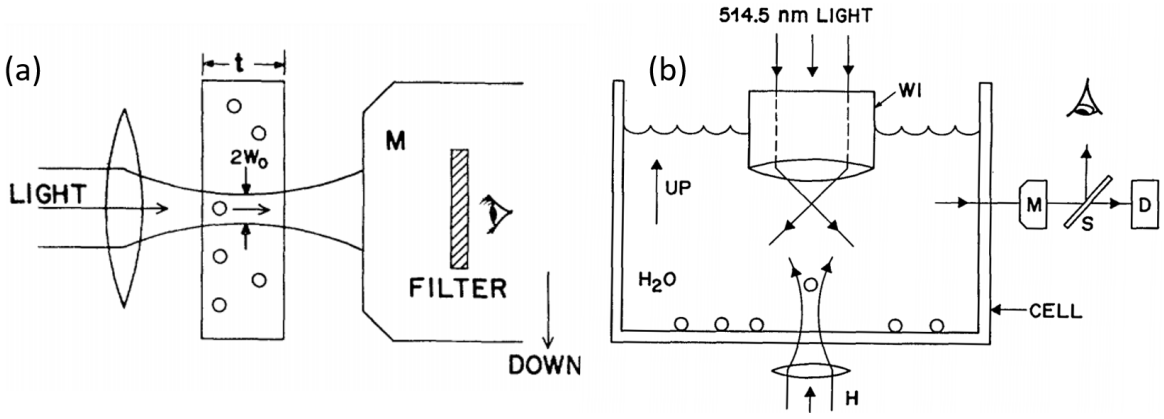

Fig. 1.1 Figure extracts from Noble prize winning work by Ashkin and his colleagues. **(a)** A 514 nm laser beam is focused into a fluidic chamber (with thickness $t = 120$ μm) where latex micro-beads are suspended. Ashkin observed that the beads were propelled into the direction of laser's propagation, as well as being drawn into the beam's central axis [1]. Glass beads of sizes 0.59 μm, 1.31 μm, and 2.68 μm were suspended in aqueous solution, and would ordinarily sink to the bottom due to their higher density. Ashkin used radiation pressure of one beam (emerging from the bottom of the cell) to deliver the glass micro-particles into a secondary tightly focused beam, where they were then optically trapped [2].

of a focused laser beam (Figure 1.1a) [1]. He found that the particles were attracted towards the beam centre, while simultaneously being pushed along the laser's propagation direction. Ashkin and his colleagues then demonstrated that by using a tightly focused laser beam, they could levitate 10 μm glass beads against gravity (Figure 1.1b) [2]. Ashkin's pioneering work led to a shared Nobel prize in 2018 and a myriad of contributions to science mediated by optical trapping and manipulation as a technology.

Ashkin and Dziedzic demonstrated that living biological samples such as motile-, and Escherichia coli-bacteria could be confined and manipulated in an optical trap without causing photodamage [37]. This inspired other biophysical researchers to use optical trapping. Svoboda *et al.* used optical trapping to show that kinesin motor protein movement occurred discrete 8 nm steps [38]. Wang *et al.* tethered DNA between an optically trapped bead and a coverslip to determine its stretchability, and found an intrinsic persistence length of 40 nm [39]. Selhuber-Unkel *et al.* observed variations in sub-cellular diffusion in the cytoplasm during cell-cycle by tracking the motion of trapped lipid granules [40]. Guck *et al.* used the optical force to determine viscoelastic deformation of red blood cells and murine fibroblasts [41].

Optical tweezers were also used as micro-scale force sensors and actuators. Ghislain and Webb used a trapped oblate bead as a force and scanning-probe sensor, analogous to atomic force microscopy, with 20 nm spatial resolution and pico-Newton forces generation [42]. Terray *et al.* created actuation valves mediated by an optical trap to steer particles [43]. In recent years, optical tweezers have become a popular technique to improve and aid the spectroscopic analysis of nanoscale material properties. Wang *et al.* mapped the photo-luminescence of individual high aspect ratio InP nanowires in hollow-graphic optical trap showing the wavelength variation of luminescence with size [44]. Rogers *et al.* incorporated a Raman spectroscopy with optical tweezing to selectively aggregate single-walled carbon nanotubes, demonstrating a clear increase in the Raman signal as the aggregate size grew with time [45].

Whilst there have been numerous and outstanding uses for optical trapping, it remains challenging task to confine and manipulate nano-sized particles, create multiple trapping sites, and reduce the effects of photodamage to the sample. An understanding of the fundamental mechanisms behind optical forces enables the experimenter to make judicious decisions in their experimental design.

1.1.1 Optical trapping theory

A single-photon being absorbed by particle will transfer a quantised amount of momentum ($p = h/\lambda$). A stream of N photons originating from a collimated light source with a power of P, will impart N amounts of quantised momenta on the particle per second. The force exerted on the particle, as a result of this photon bombardment rate is defined as:

$$F = \frac{dp}{dt} = \frac{P\lambda}{hc} \cdot \frac{h}{\lambda} = Q\frac{P}{c}$$

where λ is the photon wavelength, h is Planck's constant and c is the speed of light, and Q is the fraction of the trapping beam's momentum imparted on the particle [46]. If the photons are purely back-scattered by the particle, then the momentum transfer is doubled. For a 1 mW beam, a total optical force of 3.3 pN (in a vacuum) can act on the particle. However, only a small portion of the available photons interact with the particle due to its finite surface, meaning that a small portion of trapping beam's momentum is transferred to the particle. The bigger the optical cross-section of the particle, the higher the efficiency in the light-matter interactions. Just by considering this simple approximation, it becomes evident the optical forces on nanoparticles have small efficiencies, and therefore required a tightly focused laser beam and higher optical power to trap and manipulate them.

The relative size of a particle with respect to the trapping wavelength used is a crucial consideration in optical tweezing and manipulation. Visible and near-infrared wavelengths (400 - 1100 nm) are preferable to use due to their low absorption of the fluidic environments that the particles reside in [47]. For particles sizes much bigger than 1100 nm, a ray optics formalism is used to determine the optical forces exerted. However, for nano-sized particles, the light-matter interaction is modelled as a point dipole in an inhomogeneous electric field [48]. This leads to a dipole moment ($\vec{p} = \alpha_0 \vec{E}$) of the particle that is directly proportional to the electric field strength. The tendency of the particle to be polarised (with polarisability α_0, Equation 1.1 known as the Clausius-Mossotti relation) occurs from the difference in refractive index (real and imaginary) between the medium (n_m) and the particle (n_p), as well as the particle's

radius (r_p),

$$\alpha_0 = 4\pi r_p^3 \epsilon_0 n_m \frac{n_p^2 - n_m^2}{n_p^2 + 2n_m^2} \tag{1.1}$$

where ϵ_0 is the permittivity of free space [2, 49]. Hence, a larger size, and greater differences in the index of refraction, yield a greater magnitude in the polarisability of the nanoparticle. The particle's scattering (σ_{scat}) and absorption (σ_{abs}) cross-section (Equations 1.2 - 1.3), emerge from the real and imaginary component of the particle's refractive index,

$$\sigma_{scat} = \frac{|\alpha_0|^2}{6\pi} k^4 \tag{1.2}$$

$$\sigma_{abs} = \Im\{\alpha_0\} k \tag{1.3}$$

$$\sigma_{ext} = \sigma_{scat} + \sigma_{abs} \tag{1.4}$$

where k is the wave-number ($k = 2\pi n_m/\lambda$) and $\Im\{\alpha_0\}$ is the imaginary part of the polarisability [50].

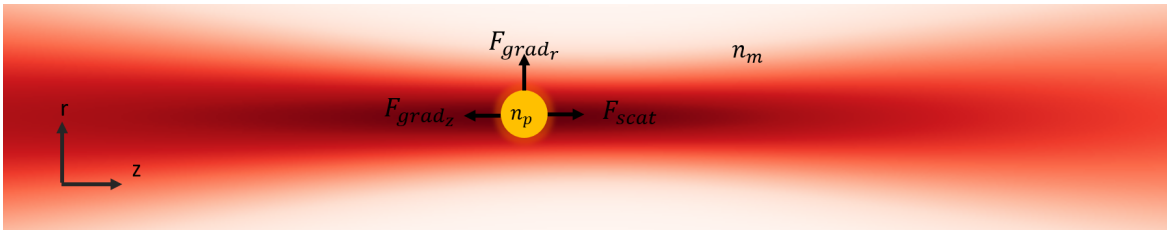

Fig. 1.2 A schematic of a single nanoparticle in a Gaussian beam. The scattering force (F_{scat}) propels the nanoparticle in the direction of laser propagation (more specifically, the direction of the time-average Poynting vector). There are two intensity gradients (in the vertical and horizontal direction) present. The nanoparticle (with a positive polarisability where the dipole is in phase with $\vec{E}$) moves to the region with the maximum intensity gradient in both directions (F_{grad}).

The total scattering and absorption (Equation 1.4), results in photo-phoretic movement of the particle, mediated by the scattering force (Equation 1.5, Figure 1.2)). The consequent movement of the particle is along the direction of the time-averaged Poynting vector ($\langle S \rangle_t$, equivalent to the time averaged intensity for a plane wave, Equation 1.5 [51]).

$$\begin{aligned} \vec{F}_{scat} &= \frac{n_m}{c}\sigma_{ext}\left\langle S\right\rangle_t \\ &= \frac{1}{2}\epsilon_0 n_m^2 \sigma_{ext}\left\langle |\vec{E}|^2\right\rangle_t \end{aligned} \tag{1.5}$$

In addition to the scattering force, the gradient force (F_{grad}, Equation 1.6) is also acting on the particle due to its polarisability,

$$\vec{F}_{grad} = \frac{1}{4}\epsilon_0 n_m^2 \Re\left\{\alpha_0\right\}\nabla|\vec{E}|^2 \tag{1.6}$$

where $\Re\{\alpha_0\}$ is the real part of the polarisability [49]. The magnitude of the gradient force scales with the gradient in intensity ($I = cn_m\epsilon_0|\vec{E}|^2/2$), hence a greater intensity change over a small unit of space, results in a large force experienced by the particle. The sign of the real polarisability component, dictates the particle's movement either towards a region of higher intensity (positive polarisability and in-phase with $\vec{E}$), where it polarises along the electric-field to minimise its energy, or vice versa (negative polarisability and anti-parallel alignment, and moving to low intensity gradients) [52].

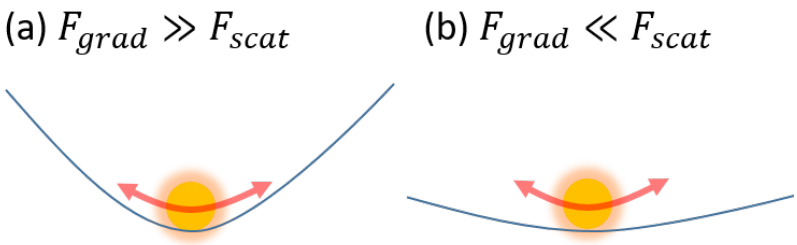

Fig. 1.3 Red arrow depicts Brownian motion in 1D. **(a)** The barrier of the potential well is high and the nanoparticle remains confined within the well. **(b)** The potential energy is reduced by photon bombardment, and the nanoparticle can be pushed out the well by Brownian motion. For stable trapping, the gradient force has to dominate, which can be achieved by using a trapping wavelength that minimises absorption of the particle, and the medium.

For stable nanoparticle confinement in each direction, the gradient force must be greater than the scattering force. An intuitive way to consider this is by determining the spatial derivative of the gradient and scattering force, which yield the potential energy associated with each force, often expressed in units of k_BT (Boltzmann constant and temperature of the median). The gradient force give rise to a potential well, with the

particle residing in the lowest part of the potential (Figure 1.3). Nano-sized particles experience greater thermal motion due to their inherently lower viscous drag, making them particularly difficult to trap. Furthermore, the magnitude of the scattering forces scales with r^6 ($F_{scat} \sim |\alpha_0|^2$), compared to the gradient forces which only scales with r^3 ($F_{grad} \sim \Re\{\alpha_0\}$). One of the main control parameters the experimentalist has in achieving stable optical confinement is through the wavelength of light used for trapping. The wavelength where the absorption cross-section is the least, is desirable (σ_{ext} is minimised), leading to a reduced scattering force (Equations 1.4, 1.6). Minimising absorption cross-section of the particle (to mitigate them acting as a heating source), and the absorption of the medium, lowers the contribution of Brownian motion. Furthermore, longer wavelengths are preferable as they intrinsically scatter less (Rayleigh scattering, k^4 term in Equation 1.2). It is not possible to trap every nano-sized particle as they may have little difference in their index of refraction relative to their medium. For these reasons, researchers in the past used optically trapped micro-sized particle tethered to a nanoscale object (such a kinesis [38] or DNA [39]) to study its properties.

A review of the technical methods used to trap nanoparticles in fluidic environments was conducted to evaluate experimental configurations that stably trap nanoparticles. More specifically, geometries that maximise intensity gradients, and innovatively minimise the destabilising scattering force.

1.1.2 Single beam optical traps

The simplest method of trapping nanoparticles is using a single, high numerical aperture (NA $>$ 1) oil or water immersion objective (usually 60x or 100x magnification). This creates a very tightly focused beam and thus a strong gradient in intensity. Considering that the beam waist (w_0) scales inversely with NA ($w_0 \sim 1/NA$), the resulting intensity can be several hundred milliwatts over an area of 0.5 μm^2. An important consideration for this type of geometry is to choose an objective lens that minimises aberrations in order to maximise intensity gradients [53].

Svoboda and Block were amongst the first to use high NA single objective to trap Au and polystyrene nanoparticles of approximately the same size (36 nm and 38 nm, respectively). By analysing the motion of the nanoparticles, they were able to estimate the trapping force and that it was approximately 7-times higher for Au nanoparticles compared to polystyrene, owning to the difference in their polarisability [54]. Au is a

plasmonic metal whereby the free electron cloud oscillates with the external electric field and thus enhancing its scattering and absorption characteristics [52]. For this reason, Au nanoparticles have become the prevalent sample of choice for optical trapping.

Hansen *et al.* investigated the size trapping range of Au spherical nanoparticles in a single beam optical trap, using a wavelength of 1064 *nm* (Figure 1.4a). In order

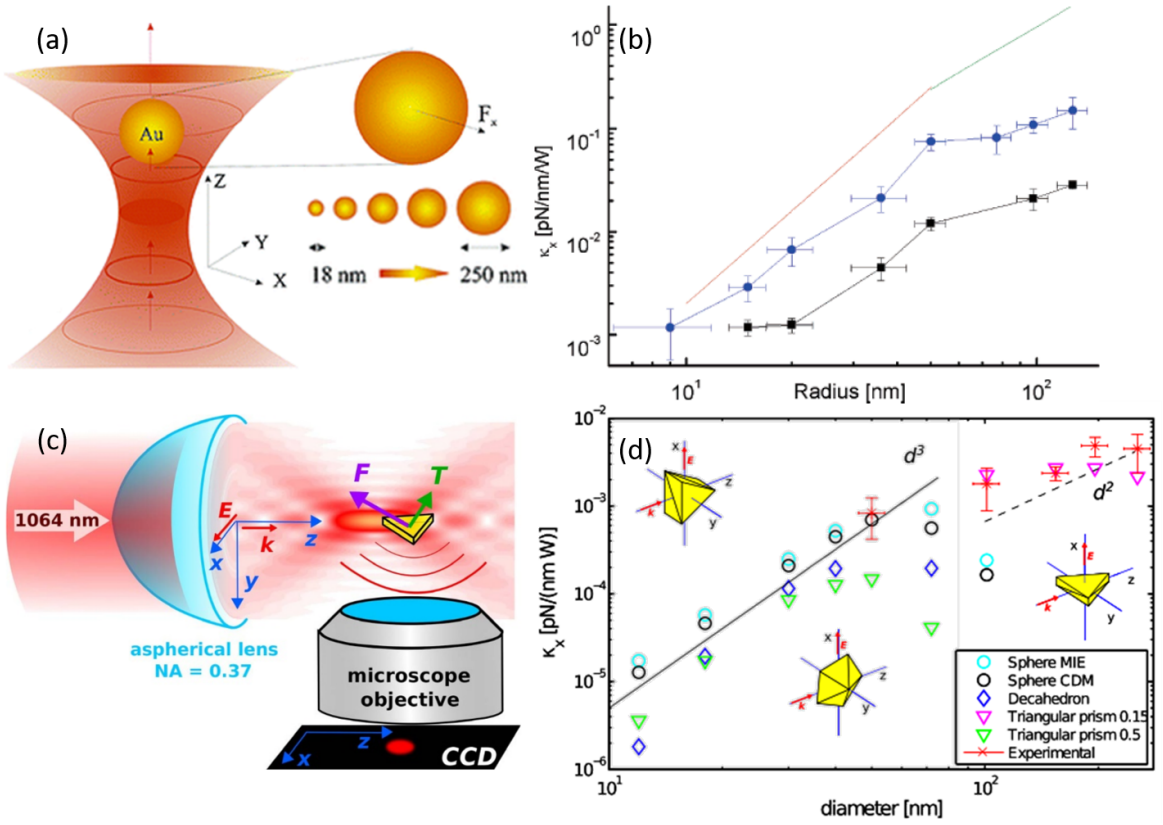

Fig. 1.4 **(a)** Illustration of a tightly focused beam to three-dimensionally trap Au nanoparticles of sizes 18-254 *nm*. A trapping wavelength of 1640 *nm* was used. **(b)** Comparison of the trapping stiffness of water immersion (1.2 NA, blue curve) objective compared to oil immersion (1.4 NA, black curve). The trapping stiffness is higher for the water immersion objective due to lower aberrations, despite being a lower NA than the oil objective. The red curve shows the r^3 scaling of trapping stiffness for nanoparticle sizes below 50 *nm*. For the larger sized nanoparticles, the slope of the trapping stiffness reduced to r^2 originating from the reduction of the field penetration relative to the nanoparticle size (green line). Modified from [3]. **(c)** Schematic of a low NA trap with minimised aberrations using a spatial light modulator for wave-front shaping, which enabled optical trapping of Au nanoparticles with different shapes and sizes. **(d)** A mixture of theoretical (Mie theory and coupled dipole method) and the measured trapping stiffness for different sizes, and shapes of Au nanoparticles. The size-trap stiffness scaling followed the result of Hansen *et al.*, modified from [4].

to utilise the full NA of the focusing lens, they slightly overfilled the back aperture of the objective. They were able to three-dimensionally trap nanoparticles from 18 - 254 *nm* using a size-dependent power range of 135-900 mW [3]. The scattered light from the trapped nanoparticle was collected onto a quadrant photodiode to discern its displacement, from which the Hookean trap-stiffness ($k_{x,y}$) was quantified ($F_x = -k_x x$, where F_x is the optical force in the x-direction). For comparison of trapping stiffness, they trapped the same set of nanoparticles using a water immersion objective (63x 1.2 NA) and an oil objective (100x 1.4 NA). They found higher trapping stiffness in water immersion objectives than oil immersion, attributing this to the greater degree of spherical aberrations presented in the oil objective, despite having a higher NA (Figure 1.4b). Furthermore, the measured trapping stiffness for both objectives scaled cubically with the radius of nanoparticles for sizes below 50 *nm* (green line in Figure 1.4b), quadratically thereafter (red line in Figure 1.4b). The cubic dependence is expected as the gradient force scales with volume. Hansen *et al.* associate the reduced trapping stiffness due to the decreased field penetration relative to the nanoparticle's size, and thus reducing the nanoparticle's polarisability [3].

Brzobohatỳ *et al.* extended the work of Hansen *et al.* by trapping non-spherical Au nanoparticles [4]. Moreover, they managed to trap them using an aspherical lens with a much lower NA of 0.37 (Figure 1.4c). A key element which enabled them to trap nanoparticles with a lower NA objective is the use of spatial light modulator (SLM) to correct for aberrations. Brzobohatỳ *et al.* too found an r^2 size dependence for the trapping stiffness of larger sized nanoparticles, (Figure 1.4d), and also associated it with the reduced ratio of the field penetration relative to the nanoparticle's radius. Their simulations (using Mie theory and coupled dipole method) also followed this trend [20, 55].

Aside from the NA of the trapping objective and minimising aberrations, the polarisation of the trapping laser is an important factor to consider, especially for nanoparticles with unequal dimensions. For particles with an aspect ratio greater than one, each dimension of the nanoparticle can be considered as an individual dipole which will favourably align with the polarisation of the trapping laser. Head *et al.* trapped CdSe–CdS core-shell nanorods with a high aspect ratio (33.5 *nm*, 2.5 *nm*) using a trapping wavelength of 1085 *nm* focused down by a 1.4 NA oil objective [5]. A half-wave place was used to control the laser polarisation, which preferentially

aligned the nanorods along its longer dimension. The emitted fluorescence from the trapped nanorods was collect by the trapping objective, split into each of its polarisation components, and detected by individual photodiodes (Figure 1.5a). Head *et al.* programmatically rotated the half-wave plate and observed an anti-correlated change in the detected polarisation of the emitted fluorescence (Figure 1.5b. The trapping wavelength can also change the preferred direction of nanorod alignment.

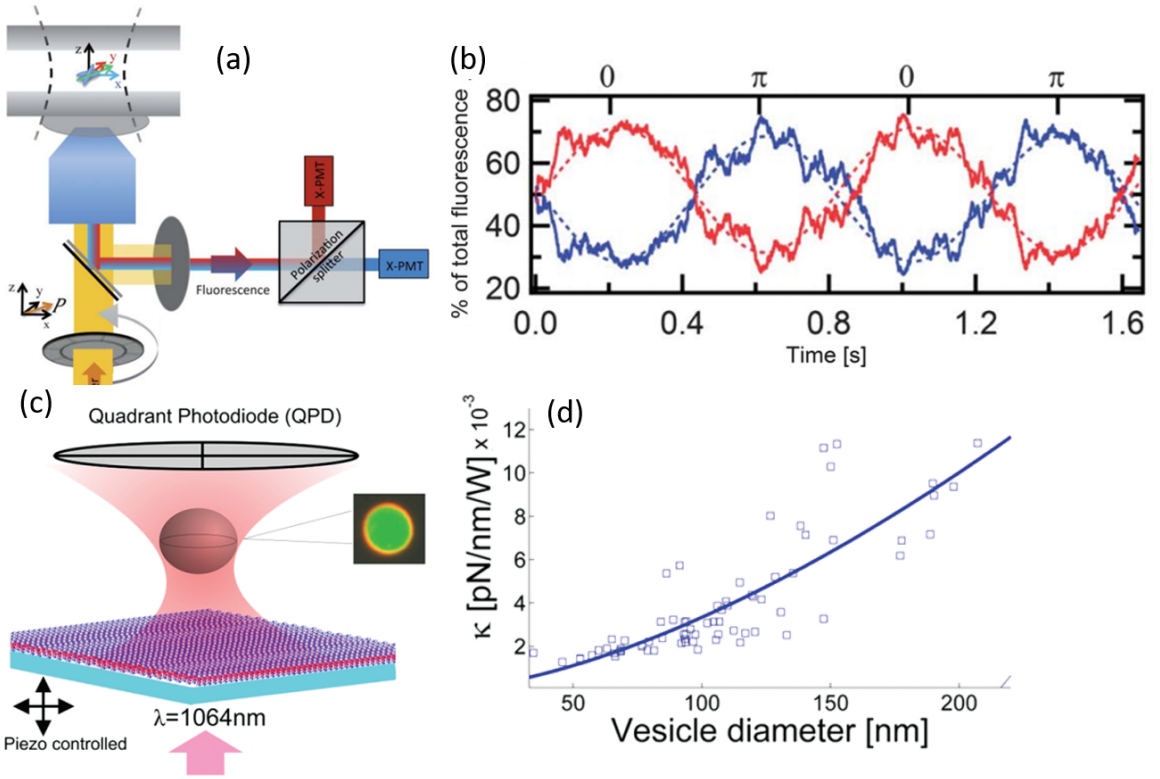

Fig. 1.5 **(a)** Optical set up showing a 1.4 NA oil objective used to trap CdSe–CdS core-shell nanorods. A half-wave plate is used to select the polarisation of the trapping beam. The emitted fluorescence from the nanorods are split into their polarisation components and individually detected by photo multiple tube.**(b)** The top axis describes the angle between polarisation and the horizontal axis. There is a pair-wise change in the detected polarisation as the nanorods rotate to align their long axis with the incident electric field. Modified from [5]. **(c)** Illustration of an optically trapped vesicle, with its motion monitored by a quadrant photodiode. Inset shows a confocal image of the fluorescently labelled membrane and lamin of the vesicle. The vesicle contains 1 *M* sucrose solution to increase its refractive index contrast with the medium, and thus increasing its trapping stability **(d)** The vesicle's radius against its trap stiffness has a slope of 1.6, which is lower than the r^3 theoretical scaling (Equation 1.6). Modified from [6].

There are instances when the refractive index can be engineered to optically trap nanoparticles, which are ordinarily not possible in their native state. Bendix *et al.* increased the refractive index contrast of their unilaminar vesicles by filling them with 1 M sucrose solution (index increase from n=*1.33* to n=*1.38*). An oil-immersion objective (1.4 NA) was used to trap the vesicles, which were fluorescently tagged in order to observer their motion using a quadrant photodiode (Figure 1.5c). A range of vesicle sizes were trapped (50- 200 nm) using laser powers between 170-1000 mW (Figure 1.5d). The membrane and lamin of the vesicles were tagged using different fluorescence dyes (inset of Figure 1.5c) to discern the deformation of the vesicles in the trap due to the optical force. A power dependant reduction of the fluorescent intensity of the membrane was observed, owing to its deformation [6].

A wide range of nanoparticle materials have been trapped using a single, high NA objective due to the simplicity of the optical geometry and its ease of integration with a microscope [56]. However, single beam trapping often yields only a single trapping site and require costly aberration minimising objectives or special optical elements such as an SLM. More importantly, single beam trapping often requires laser powers ranging in the hundreds of milli-Watts to create strong intensity gradients, which is detrimental to the sample, especially if it is a biomolecule. Rather than achieving strong intensity gradients by increasing the amplitude of the intensity, other optical trapping geometries reduce the spatial component of the intensity transition.

1.1.3 Standing wave optical traps

For a stable trap, the gradient force must be greater than the scattering force and Brownian motion, for each direction. By using counterpropagating beams, the opposing scattering forces cancel one another where they are equal in magnitude. Furthermore, if the counterpropagating beams are polarised along the same axis, they interfere, creating a standing wave with a periodicity of $\lambda/2n_m$ [7]. Given that the typical wavelength for optical trapping is 1064 nm, would result in a minimum to maximum intensity transition over 200 nm ($n_m \approx 1.33$). Both these effects add to increase the stability of the trap along the propagation direction of the interfered beams.

A single optical trap configuration can be converted into a counterpropagating trap by placing a mirror at the focal point of the trapping objective, as done by Demergis and Florin [8], and Wu *et al.* [7]. The mirror back-reflects the light while maintaining

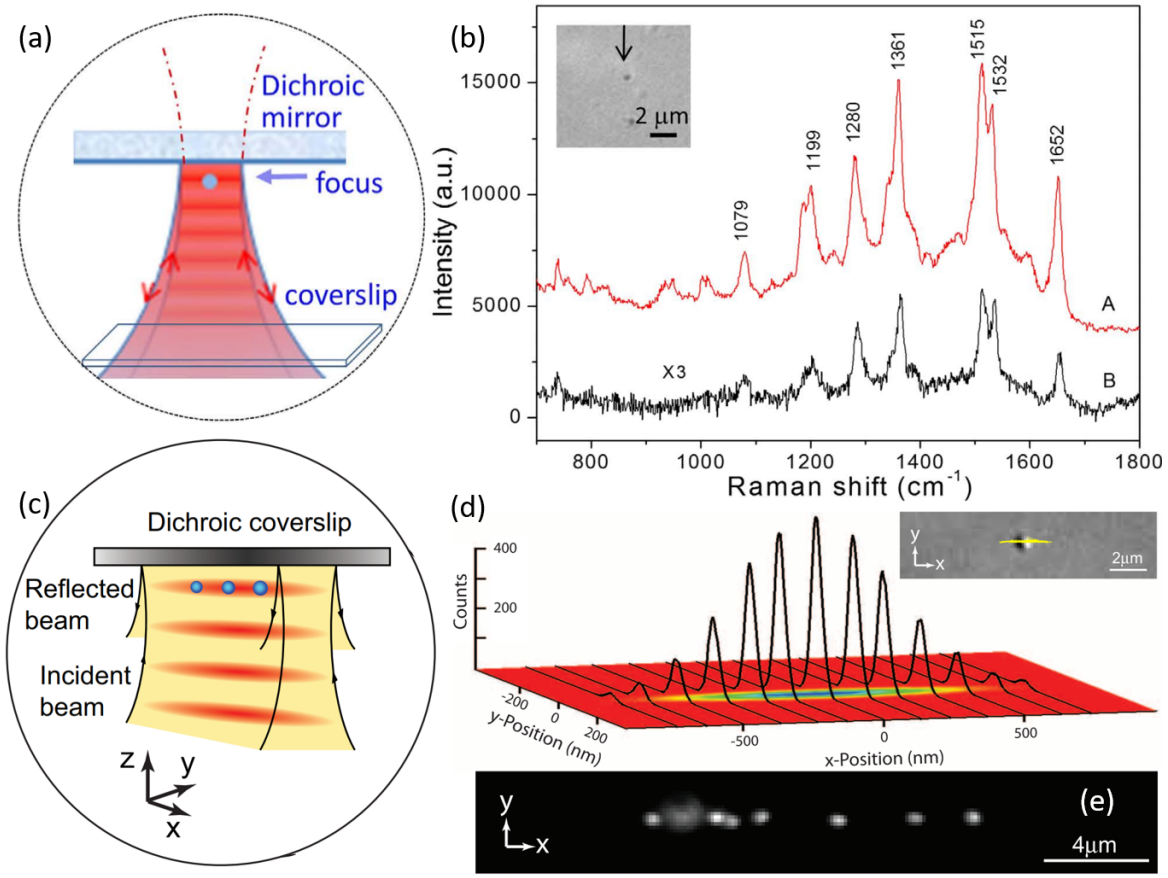

Fig. 1.6 Nanoparticle confinement in a standing wave optical trap. **(a)** A tightly focused beam is self-interfered by back-reflecting the incident light using a dichroic mirror ($\lambda = 780nm$). Due to the standing wave, the scattering force is reduced, and the gradient in intensity is increased. **(b)** a few 80 nm Au nanoparticles are trapped near the surface of the mirror (inset). The Raman signal of Rhodamine-B is significantly increased due to the increased scattering by the nanoparticle in the constructively interfering region (curve A, which is for 2.5 μM), relative to higher concentration bulk measurements (curve B, 100 mM). Modified from [7]. **(c)** Optical line trap creating by the interference of a tightly focused light-sheet beam with itself. This creates a periodic array of traps along the axial direction. **(d)** The positional distribution of a 500 nm polystyrene bead diffusing in the line trap near the surface of the coverslip. The nanoparticle is more confined in the y-direction than the x-direction due to the higher intensity gradient. Inset: differential interference contrast image of the polystyrene nanoparticle and its tracked diffusion. **(e)** Several 100 nm Au nanoparticles are being confined along the line trap. Modified from [8].

polarisation and interferes it with the incoming beam, creating a standing wave optical trap. Wu *et al.* trapped 80 *nm* Au nanoparticles in a solution containing 2.5 μM Rhodamine-B by using a trapping wavelength of 780 *nm* which was back-reflected by a dichroic mirror with >98% reflectivity (750–1100 *nm*) and >90% transmission for the visible region (Figure 1.6a). Due to the beam interference, several high-intensity gradients were formed along the axial direction of the beam where nanoparticles could be confined. Nanoparticles at the focus (near the surface of the mirror) were more stably confined aided by the tightly focused beam in the radial direction, and the array of strong intensity gradients in the axial direction (Figure 1.6b inset). The Raman spectra of Rhodamine-B was collected from the plane where the nanoparticles were trapped as they indicated regions were constructive interference of the intensity occurred, which consequently yielded much high Raman signal relative to bulk measurements (Figure 1.6b).

Demergis and Florin also used a dichroic mirror to create a standing wave optical trap. They also incorporated a cylindrical lens in the optical path, focusing the light only in direction, and thus creating an optical line trap (Figure 1.6c) [8]. By observing the diffusive motion of a 500 *nm* polystyrene bead over a period of 117 minutes, they mapped the probabilistic positional distribution of the particle relative to the intensity distribution (Figure 1.6d). The nanoparticle was found to spend the majority of its time where the intensity was the highest. The particle could diffuse more freely in the x-direction, relative to the y-direction, due to the lower intensity gradient. Demergis and Florin also observed the motion of several 100 *nm* Au nanoparticles in the line trap (Figure 1.6e). However, they were unable to quantitatively report the alternated motion of the nanoparticles in the line trap due to their diffraction limited imaging.

Čižmár *et al.* used two independent counterpropagating beams to create an optical conveyor belt for nanoparticles. The two beams were focused on the surface of a prism and overlapped using steering mirrors to create an interference pattern with an area of 40x10 μm^2 and a fringe separation of 200 *nm* (Figure 1.7a) [9]. Both beams are incident above the critical angle, and consequently, both a standing wave and surface standing wave are present, with the latter originating from the evanescent field. Čižmár *et al.* found that the smaller-sized nanoparticles were affected more by the surface standing wave, while larger particles by the conventional standing wave. Using this finding, they were able to separate and steer nanoparticles by changing the relative

phase and the power of each beam.

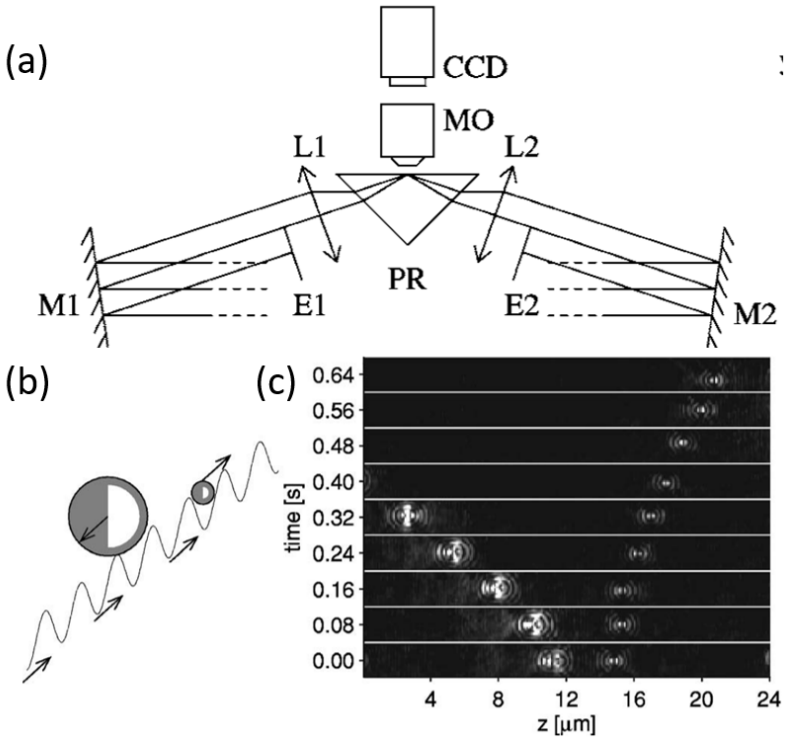

Fig. 1.7 **(a)** To beams are steered (using mirrors M1, M2) and focused (using lenses L1, L2) on the surface of a prism (PR). The incident angle of the beam was chosen to induce evanescent standing waves, as well as conventional standing waves. **(b)** Tilted potentials of the standing wave. The tilt originates from the total of the scattering force and gradient force at each point in space. Larger sized particles move left, while smaller sized particles are affected by the surface standing wave and move to the right. **(c)** Showing separation of 350 *nm* (to the right) and 750 *nm* polystyrene beads at the surface of the prism. Modified from [9].

The inference of the two beams created periodic potentials where the nanoparticles could be trapped within. Changing the power balance between the two arms of the beams, yielded tilted 'washboard' potentials, where it was more energetically favourable for the particle to escape in one direction, and hop into another neighbouring potential (Figure 1.7b). Polystyrene nanoparticles of sizes 350 *nm* (effected the by surface standing wave) moved towards the right, while the bigger sized nanoparticles (750 *nm* affected by the standing wave), move to the right to minimise their energy (Figure 1.7c).

Čižmár *et al.*'s work is substantial as it demonstrated trapping a range of nanoparticle sizes, as well as reconfigurability of their positions by adjusting the relative phase between the beams. Moreover, their experimental geometry separates the trapping optics from the imaging optics, facilitating a greater degree of flexibility.

1.1.4 Fibre based traps

The use of optical fibres for trapping nanoparticles also offers a means of disentangling the imaging and trapping optics, allowing for greater versatility. Additionally, optical fibres have been previously integrated with microfluidic, enabling the experimentalist to combine both optical and hydrodynamic effects. However, single mode optical fibres have an inherently low NA, and is limited by the amount of power that can be coupled at the input without causing photodamage, which makes optical trapping a challenge. Despite these limitations, researchers have innovatively trapped nanoparticles using optical fibres.

Li *et al.* created an optical trap for nanoparticles, using a micro-lens at the end of a tapered fibre (Figure 1.8a) [10]. A single mode optical fibre was tapered to a parabolic tip (diameter of 3 μm) to increase the chance of the titanium dioxide micro-lens attaching to the light-emitting core of the fibre (electrostatic attachment promoted through surface coatings). Without the micro-lens, Li *et al.* measured the full-width-half-maximum of the beam emerging from the tapered fibre to be 840 nm, which in the presence of the micro-lens, was reduced to 208 nm. Spatially confining the light to such an extent enabled them to trap fluorescently labelled 86 nm polystyrene beads (Figure 1.8b). Li *et al.* used the back-reflected light through the micro-lens and into the fibre as a means of monitoring when a particle was trapped. Before the nanoparticle was trapped, the reflected signal was low, which then increased by approximately 3-fold when the nanoparticle was confined. Once the trapping laser was turned off, the reflected signal returned back to its initial levels (Figure 1.8b) [10]. It is important to note that the nanoparticle remained trapped for the duration of the trapping beam being emitted.

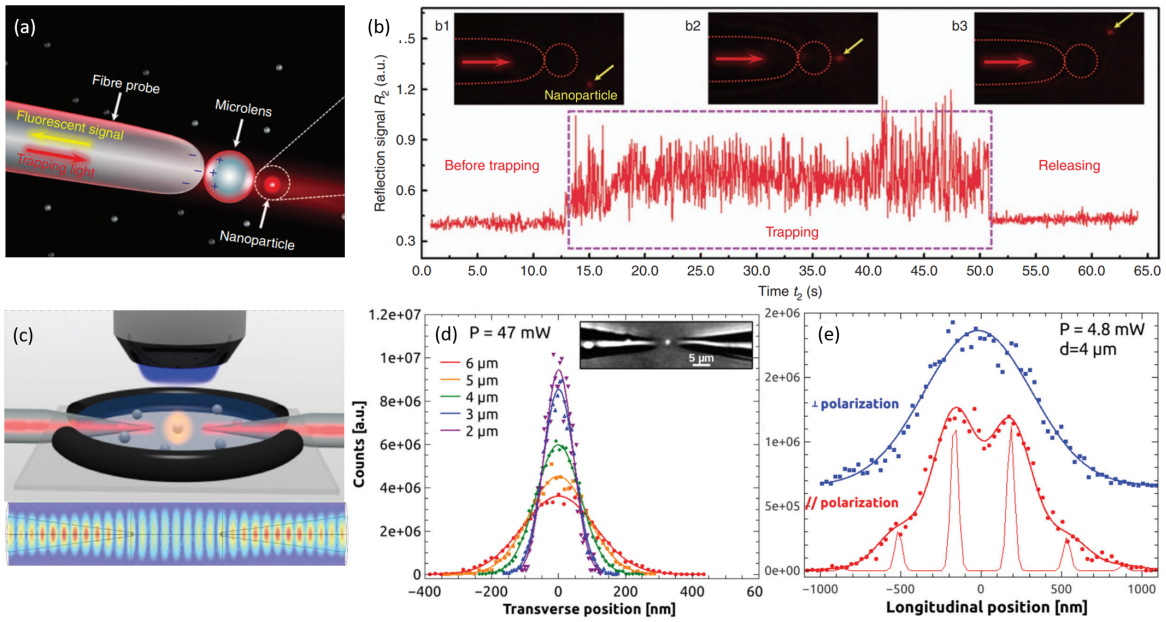

Fig. 1.8 **(a)** Illustration of the tapered fibre electrostatically bound to a micro-lens, which focused the light down to a size of 208 *nm* (FWHM), and thus creating a strong intensity gradient for trapping 86 *nm* polystyrene beads. Back-reflected light into the fibre was used to monitor the presence of the trapped nanoparticle. **(b)** A trace of the back-reflected signal with, and without the nanoparticle being trapped. A clear increase in the reflected light was observed owing to the presence of the fluorescent nanoparticle being trapped, remaining there until the trapping laser was turned off. Modified from [10]. **(c)** Schematic of the tapered fibre counterpropagating set up used by Decombe *et al.* to trap 300 *nm* YAG:Ce^3 nanoparticles. The bottom part shows the simulated electric field when both fibres are along the same polarisation. Trapped nanoparticles were imaged orthogonally using a separate objective. **(d)** Observed particle position with varying fibre separation distance, while keeping the trapping power constant. The detected positions obey a Gaussian distribution. The Gaussian width decreases with a reduction in fibre separation. **(e)** Observed particle positions with different relative polarisation between the fibres. When both polarisations are the same, nanoparticles were detected in segmented regions owing to the presence of interference fringes (separation of 350 *nm*). Modified from [11].

Decombe *et al.* used counterpropagating tapered fibres separated by a distance of 2-6 μm to trap 300 *nm* YAG:Ce^3 nanoparticles (Figure 1.8c) [11]. Nanoparticles were trapped at the middle distance between the two fibres were the counterpropagating scattering forces were annulled (Figure 1.8d inset). They monitored the position of a single trapped nanoparticle while varying the separation distance between the fibres (keeping a constant output power), and found that increasing the trap distance (widening the potential well) reduced the nanoparticle's axial spatial confinement (Fig-

ure 1.8d). Nanoparticles could still be trapped regardless of the relative polarisation between the fibres (Figure 1.8e). When the polarisation was the same across both fibres, nanoparticles were observed in distinct regions owing to the standing wave pattern formed (350 *nm* fringe spacing, 808 *nm* trapping wavelength) [11].

Shi *et al.* embedded a single mode fibre into a PDMS (poly-dimethyl siloxane) microfluidic chip, and concurrently trapped nanoparticles of different sizes [57]. The PDMS was used to create a quadrangular micro-lens (similar to two back-to-back prisms) shaping the Gaussian-like output from the fibre into a Bessel-like beam (Figure 1.9a,b) [58]. This yielded a tightly focused beam with a width of 250 *nm* and a low NA of 0.04, which is an inherent property of quasi-Bessel beam. Due to the diffractive nature of the beam formation, it can recover its shape if it was disrupted by a highly scattering particle (Figure 1.9b). While the authors do not explicitly mention, it is important to note that the light is focused only in one direction (much like a cylindrical lens) due to the flat wall of the PDMS channel. This means that a strong intensity gradient was present along the lateral direction of the beam propagation (perpendicular to the PDMS micro-channel's walls), and nanoparticles were able to diffuse parallel to the PDMS walls freely. Moreover, they experienced a strong scattering force and were pushed along in the direction of the beam propagation. Shi *et al.* countered the

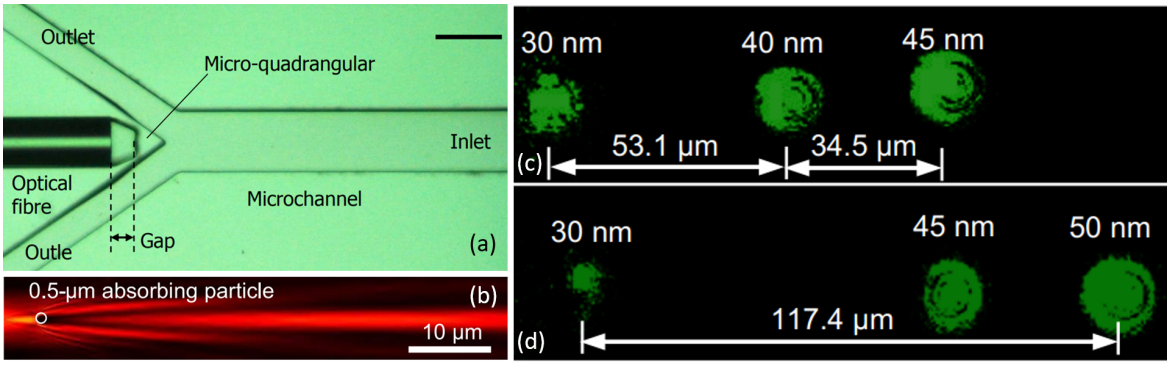

Fig. 1.9 Optical confinement of nanoparticles by balancing the scattering force using hydrodynamic effects. **(a)** An optical fibre embedded into microfluidics. A micro-quadrangular lens is used to generate a Bessel-like beam, from the emitted Gaussian beam emerging from the fibre. **(b)** Simulation of the self-recovering nature (beam is diffractively formed) of the Bessel-like beam after undergoing a highly scattering event induced by the presence of a nanoparticle. **(c,d)** Many nanoparticles are simultaneously trapped with a range of separation distances. It is not explained by Shi *et al.* how they achieve sizing of nanoparticle using diffraction limited optics.

scattering force by imposing fluidic flow in the opposite direction. In this way, they were able to trap nanoparticles with a range of sizes in two-dimensions (Figure 1.9) using an optical power of 400 mW and an opposing fluid flow of 300 $\mu m/s$ (Figure 1.9c,d) [57].

Due to the self-recovering nature of the beam shape, nanoparticles were able to be trapped downstream of other confined nanoparticles closer to the light source. As such, nanoparticles were trapped with a range of separation distances (Figure 1.9c,d). Hence, the low NA of the Bessel-like beam, which meant that the scattering forces were approximately constant across several tens of microns, combined with the laminar flow regime of the micro-channels ultimately aided Shi *et al.* to balance the optical-, and hydrodynamic-effects, enabling nanoparticle confinement.

1.1.5 Other methods of optical trapping

One of the main difficulties in three-dimensional optical trapping is overcoming the scattering force. In instances where the axial gradient force is not greater than the scattering force, the nanoparticles are propelled along the laser propagation direction. A frequent method of circumventing this limitation is to use a barrier, such as a counter-flowing fluid (as Shi *et al.* did) or a surface where the nanoparticles are pushed-up against. Fazio *et al.* used the scattering force to induce aggregation of Au nanorods against the domed surface of a coverslip in the presence of protein solutions (such as bovine serum albumin, Figure 1.10a) [12]. The aggregated clusters were used to enhance the Raman spectra of the biomolecules enabling low concentration detection of the proteins.

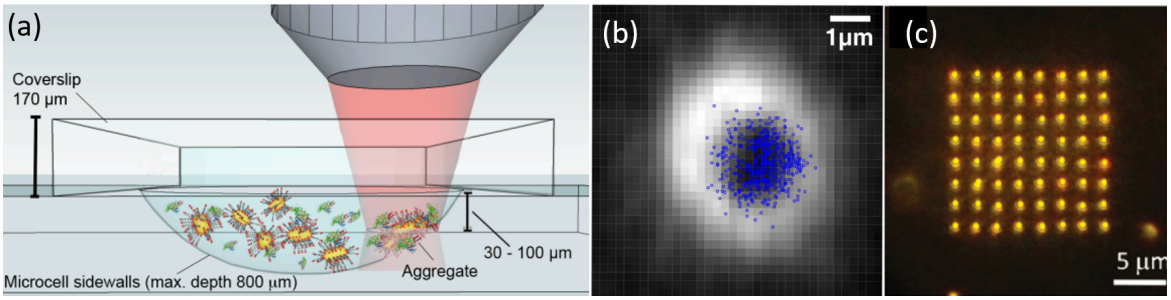

Fig. 1.10 Combating the scattering force by pushing nanoparticles up against a surface. **(a)** Au nanorods with proteins attached to their surface, is pushed against a coverslip by the radiation pressure. Clustered Au nanorods increase the Raman signal [12]. **(b)** 100 nm confined in the dark region of an AOM beam [13]. **(c)** A grid of nanoparticles made using individually addressable beams from a spatial light modulator [14].

Dienerowitz *et al.* used a doughnut-shaped Laguerre-Gaussian beam to pen 100 *nm* particles in the dark central region where the scattering force was minimal [13]. The nanoparticles were supported against a coverslip, and followed the orbital angular momentum of the beam's propagation axis, rotating around within the dark zone of the beam (Figure 1.10b). Nedev *et al.* also confined a grid of 64-nanoparticles (80 *nm* Au) against the surface of a substrate (Figure 1.10c). Nedev *et al.* used a spatial light modulator to create multiple trapping beams, each of which could individually be addressed. Initially, the substrate and the nanoparticles were electrostatically repulsive, and the presence of the strong scattering force from each beam was used to over the repulsion and promote van der Waals attraction to the substrate, and thus facilitate nanoparticle confinement and printing of any arbitrary pattern on a surface [14].

In recent years, the field enhancement by plasmonic nanostructures such as plasmonic nano-apertures, have also been used for trapping of single biomolecules and nanoparticles, as outlined in a review by Shoji *et al.* [59]. While these technologies are powerful, they require extensive nano-fabrication and are particularly susceptible to fouling. For these reasons, these methods of nanoparticle trapping were not considered in the scope of this work.

1.1.6 Optical trapping summary and intended work

Several optical trapping geometries using a continuous-wave laser source were considered for the confinement of nano-sized particles. From theoretical considerations, it was found that the gradient force has to be greater than the scattering for stable optical trapping [1]. Hence, researchers have used optical geometries that maximise intensity gradients by using tightly focused laser beam mediated by the use of a high numerical objective [54]. However, this method required high optical powers, which can induce unwanted local heating and photodamage to the nanoparticles [6]. Standing wave geometries were used to counteract the destabilising scattering force, enabled trapping with lower optical powers [8]. Despite the many geometries of optical trapping, it remains a challenge to three-dimensionally optical confine proteins without the use of chaperon particles (such as polystyrene microbeads or Au nanorods [12]), or the use of nano-fabricated devices.

Chapter 2 of this work demonstrates a novel optical trapping geometry that uses the interference between two counterpropagating optical fibres to generate an array of

strong intensity gradients. To validate the new trapping geometry, Au nanoparticles were used as the target particle owing to their higher polarisability, and the fact that it is the material of choice for proving the trapping concept in previously reported geometries [3, 4, 7, 8, 54, 57]. Strong nanoparticle confinement in one-direction was achieved by maximising gradient force in the axial direction using counterpropagating beams delivered by single-mode polarisation maintaining optical fibres embedded in a microfluidic chip. The fibres are commercially available and were not modified in any way to facilitate greater adaptability of the system by others. The use of optical fibres in microfluidics allowed the imaging optics to be separate from the trapping optics, enabling greater flexibility. The trajectories of several tens of nanoparticles were simultaneously tracked at different positions along the beam path to obtain the ensemble behaviour of the trap. Drawing inspiration from Demergis and Florin [8], and Wu *et al.* [7] work, a micro-mirror was embedded into the microfluidic chip, back-reflecting the light and creating an interface pattern with better phase-stability and stronger nanoparticle confinement in the axial direction. The interferometrically induced intensity gradient in this work are higher at lower optical powers relative to the work of others [3, 4], and therefore offer the possibility of trapping protein particles.

1.2 Thermophoretic characterisation & trapping of nanoparticles & biomolecules

The limiting factor with optical trapping is that nanoparticles or biomolecules have to be a different refractive index than its environment at a wavelength that minimises absorption, to maximise their polarisability, and be stably trapped. Moreover, the gradient force scales as r^3, hence a 10 nm particle requires 1000-times stronger intensity gradients for the same trapping stability needed for a 100 nm particle. One of the main uses for optical tweezers for biomolecules such as DNA, proteins or drug delivery platforms (metal-organic frameworks or DNA origami), all of which are in the nanometer size regime. It is for these reasons that in recent years, nanoparticle and biomolecule manipulation, has been transitioning to other method such acousto-fluidic tweezers [60], entropic traps in nano-fluidic channels [61], electro-kinetic traps [62], and thermophoretic traps [63]. The latter of these mechanisms has been particularly useful as it enables researchers to study biological processes in environments closely resembling physiological conditions, whereby salts and elevated temperatures are present

(as demonstrated in [64]). To this end, thermophoretic manipulation of nanoparticles was investigated, as it offers an attractive alternative to optical trapping, as well as, extending the size range of particles that can be trapped.

1.2.1 Principles of thermopheresis

In the absence of heating, nanoparticle suspensions at a constant temperature (T_{amb}) viewed through a microscope exhibit random movement mediated by Brownian motion, and fluctuations in concentration (Figure 1.11a). The motion of the particles can be characterised with a diffusion coefficient (D), which inversely scales with the hydration radius of the nanoparticle. In the presence of a temperature profile, the nanoparticles move with a velocity (v) proportional the temperature gradient, either away or towards the heating source (Figure 1.11b).

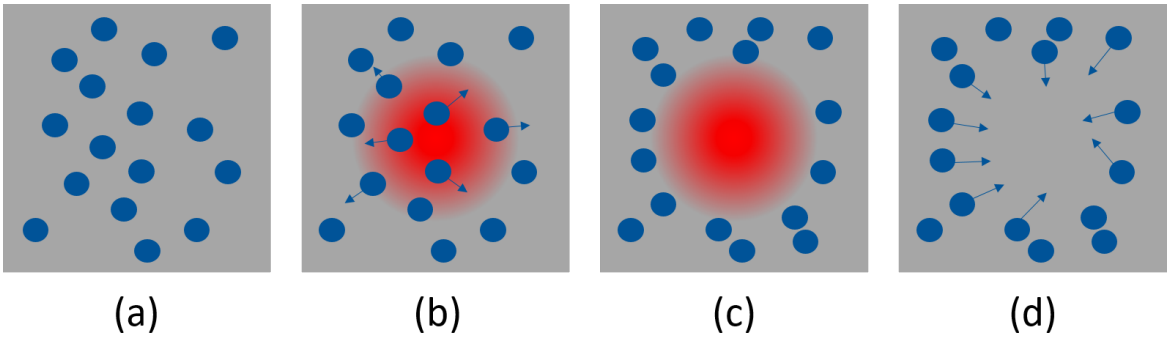

Fig. 1.11 Schematic of fluorescently nanoparticles diffusing freely **(a)**, in the presence of a thermal gradient and moving away from the heat source, assuming they have a positive Soret coefficient **(b)**. At steady state, the thermo-diffusion of nanoparticles mediated by the temperature gradient balances out concentration gradients **(c)**. With the heating source turned-off, the particles back-diffuse to homogenise concentration **(d)**.

Analogous to the diffusion coefficient, thermo-diffusion is the ratio of the particle velocities and the temperature gradient ($D_T = -v/\nabla T$) [64]. In steady state flow, the mass flux (j_c) due to concentration gradients balances the mass flux (j_T) induced by the temperature gradient, such that

$$\begin{aligned} j_c &= j_T \\ D\nabla c &= -cD_T\nabla T \\ \frac{c}{c_0} &= exp\left\{\frac{-D_T}{D}(T-T_{amb})\right\} \\ &= exp\left\{-S_T\Delta T\right\} \end{aligned} \tag{1.7}$$

where c is the particle concentration, which is normalised by the boundary condition of the initial concentration c_0 with temperature T_{amb} [64, 65]. The ratio of the thermo-diffusion and diffusion coefficient is known as the Soret coefficient (S_T), and its magnitude and direction are determined by the nanoparticle properties. A positive S_T value means it is energetically favourable to move away from the heated spot, and vice-versa. For a given biomolecule or nanoparticle, its Soret coefficient has empirically been determined from its hydration entropy, and its ionic shielding such that

$$S_T = \underbrace{-\frac{AS_{hyd}}{k_BT}}_{\text{Hydration entropy}} + \underbrace{\frac{A\beta\sigma_{eff}^2}{4k_BT^2\epsilon\epsilon_0}\lambda_D}_{\text{Ionic sheilding}} \tag{1.8}$$

where A is the surface area, S_{hyd} is the hydration entropy, σ_{eff} is the effective surface charge density, β is the temperature derivative of ϵ (permittivity of the nanoparticle), and λ_D is the Debye length [65]. The surface area and Debye length scale linearly, while the surface charge density scales quadratically, with the Soret coefficient. If the hydration entropy dominates (by minimising ionic shielding), the Soret coefficient is negative, and the nanoparticle moves towards the heated spot. The hydration entropy of the nanoparticle in a given medium can be determined by reducing the Debye length to zero, as conducted by Duhr *at al.* [65].

In more recent work, Peng *et al.* investigated the thermophoretic migration of polystyrene particles in non-ionic solutions [15]. They found that the surface interaction between the particle and the solvent dictates the thermophilic or thermophobic behaviour of the particle. A layered structure forms on the charged surface of the particle due to absorption solvent molecules, with dipoles aligning with the electric field generated by the charged particle [66]. In the presence of a temperature gradient, the hot side of the particle increases in entropy, due to the disordering of the interfacial

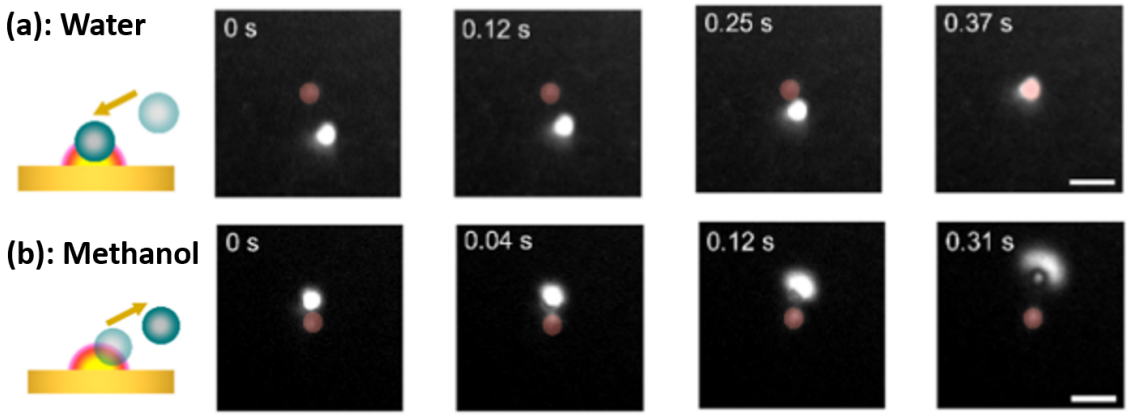

Fig. 1.12 The migration of a polystyrene particle towards a heated spot when entropy-induced forces dominate **(a)**, and away from the heated spot when the solvent's dispersion forces are higher **(b)**. Modified from [15].

molecular dipoles, leading to a charge density gradient across the particle, which subsequently induces a slip flow counteracting the gradient [15, 67]. This entropy-induced force is opposed by the inherent dispersion force of the solvent, and their interplay governs the motion of the particle in a temperature gradient. For a polystyrene particle suspended in water, the entropic forces are higher and caused thermophilic migration (Figure 1.12a). The dispersion forces dominate for methanol suspensions, and cause particles to drift away from a hot spot (Figure 1.12b).

For solutions comprising of nanoparticles, salt ions (such as sodium and chloride), and buffers to maintain pH, the thermophoretic motion of nanoparticles can become difficult to predict. The presence of the ions create additional effects both on the local nanoparticle scale, and globally since the ions themselves also migrate in a temperature gradient owning to their hydration entropy with the solvent [68].

In addition to the adsorbed ions that reduce the bare charge of the nanoparticle (right-hand side of Equation 1.8), the ion cloud itself is distorted by the temperature gradient, behaving as a capacitor, if the Debye length is greater than the hydrodynamic radius ($\lambda_D >> r_{hyd}$) [69]. This is prominent in short length single- and double-stranded DNA molecules which are negatively charged and get enveloped by positive ions, creating a localised spherical capacitor [70]. The stored energy of the capacitor reduces at lower temperatures, and hence the nanoparticle moves away from the heat source,

and consequently have positive Soret coefficient [69].

The free ions in the solution, which have different charges and sizes, and subsequent hydration entropies, experience dissimilar thermodiffusion. This manifests as a separation of ions, which consequently generate an electric field mediated by the presence of a temperature gradient [71]. This is analogous to the Seebeck effect used in Peltier devices for cooling and heating. The strength of the thermoelectric field (E_T) is defined such that,

$$E_T = \frac{\nabla T k_B T}{e} \left\{ \frac{\sum_{i=1}^{\infty} Z_i C_i S_{T_i}}{\sum_{i=1}^{\infty} Z_i^2 C_i} \right\} \tag{1.9}$$

where Z_i,C_i, and S_{T_i}, are the elemental charge, concentration, and Soret coefficient of it i^{th} ion species, and e is the electronic charge [69, 72]. The temperature and its corresponding gradient are directly proportional to the strength of the thermoelectric field. Vigolo *et al.* generated thermoelectric fields using sodium chloride, and sodium hydroxide (independently), to induce thermophoretic motion of sodium dodecyl sulfate micelles. They observed thermophilic movement of the micelles in thermoelectric fields, stemming from the differential migration of sodium-, and chloride-ions, and thermophobic migration for sodium-, hydroxide-ions [73].

The presence of temperature gradients have been shown to create salt concentration gradients (such as TMAOH and TBAOH), that induced diffusiophoretic migration of iron oxide nanoparticles [74]. Moreover, the seperation of hydroxide and hydronium ions in small isolated microfluidic chamber, creating stable pH gradients [75].

1.2.2 Nanoparticle binding and sizing in a temperature field

Several local and global effects can govern the migration of nanoparticles and biomolecules in a temperature gradient, which makes the use of thermopheresis to study particle properties a highly sensitive method. The framework to study the properties of fluorescently labelled biomolecules, such as size and binding kinetics using thermopheresis, has been developed by Stefan Duhr and Dieter Braun [76]. By monitoring the temporal changes in fluorescent intensity of the biomolecules, with-and-without heating, the

Soret coefficient can be determined, from which, inferences can be made about the biomolecule (Equation 1.8).

The microscale thermopheresis instrument conceived by Stefan Duhr and Dieter Braun, consists of a heating beam (IR), a temperature-controlled platform (TC), a micro-capillary containing the fluorescently labelled sample, and an objective and photodiode to collect the emitted fluorescence (Figure 1.13). The use of micro-capillaries, filled by capillary action, keeps the sample volumes of the analytes low as they can often be costly. The fluorescent intensity is used as a substitute for the concentration in determining the Soret coefficient (Equation 1.7). The initial fluorescence intensity (F_0) is determined at ambient temperature, kept at 300K by the temperature-controlled plate (Figure 1.13b, stage I). A 1480 nm beam is used to heat the solution, and induce a temperature jump of 2-5 K (Figure 1.13b, stage II) [76]. Before the molecules begin

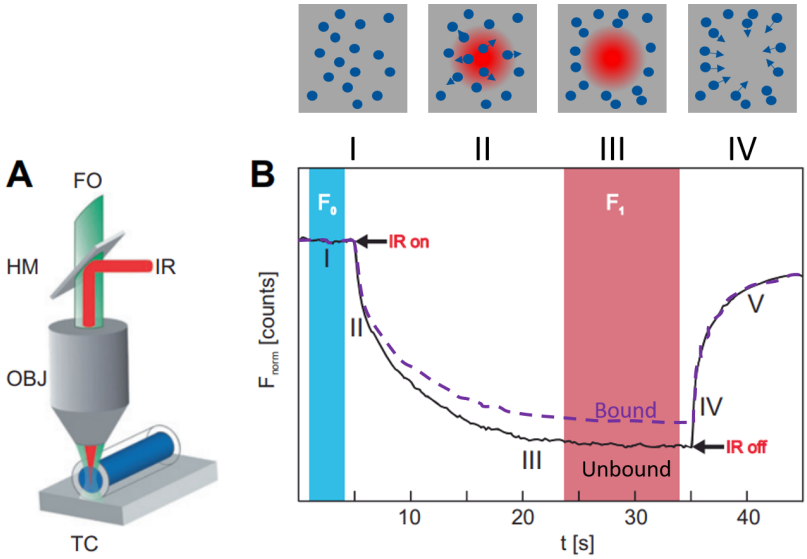

Fig. 1.13 **(a)** A schematic of the thermophoretic device built by Duhr and Braun. A temperature-control (TC) tray keeps the samples loaded in a micro-capillary at a constant temperature before heating. An objective focused an IR beam reflected from a hot mirror (HM) to the centre of the capillary to induced heating (2-5K). A photodiode collected the emitted fluorescence signal from the biomolecules. **(b)** Fluorescence trace over heated and non-heated regions. Stage I is the referenced normalised signal without heating. Stage II denotes the changes in fluorescent dye's behaviour due to the temperature and viscosity changes of the medium. Stage III shows little change of the fluorescence signal, meaning that an equilibrium has reached between the particle concentration gradient, and the temperature gradient. Stages IV,V are the recovery of the signal without heating. Modified from [16].

to move, a drop in the fluorescence is observed ($\delta F/\delta T$), originating from the reduction of the fluorescent dye's quantum yield, due to temperature and viscosity changes of the medium. This sudden reduction in intensity occurs in less than a second after the IR heating, and is important to consider in the fluorescence intensity normalisation [16]. For longer periods, the biomolecules move under thermophoretic flow away from the heating source, which causes further reduction of the fluorescence intensity, until it plateaus (F_1), indicating that steady-state flow has been reached (balance of concentration gradients and thermal gradients, Figure 1.13b, stage III). The heating laser is then turned off, and the molecules back-diffuse under the concentration gradient (Figure 1.13b, stage IV,V). The fluorescence signal does not return to its initial value (F_0) due to bleaching effects.

The normalised fluorescence (F_{norm}) is determined such that,

$$\begin{aligned} F_{norm} &= \frac{F_1}{F0} = \frac{c}{c_0} \\ &= 1 + \left(\frac{\delta F}{\delta T} - S_T\right)\Delta T \end{aligned}$$

where the exponential term ($e^{-S_T \Delta T} \approx 1 - S_T \Delta T$) is linearised since S_T is typically much less than one and ΔT is small [76]. When investigating the binding kinetics of two molecular species, the Soret coefficient increases in the bound state relative to the unbound state, which causes a decreased change in the fluorescence intensity at steady state (Figure 1.13b, stage III). By titration of the one species, while keeping the other fixed, the dissociation constant (K_D) can be determined through the quantitation of F_{norm} at each test concentration. Knowing the dissociation constant is useful for determining the concentration at which optimal binding occurs. Jerabek-Willemsen investigated the binding a single strand DNA tagged with 200 pM of a Cyanine5, with its complementary oligonucleotide strand (Figure 1.14a,b) [17]. They varied the concentration of the complementary strand (unlabelled) from 0.001 - 100 nM, and found the corresponding F_{norm}. The F_{norm} value decreased for as double strands were formed (Figure 1.14a). A sigmoid curve in the relative change of F_{norm} was obtained, from which a dissociation constant of 167 $\pm$ 8 pM was quantified through fitting (Figure 1.14b).

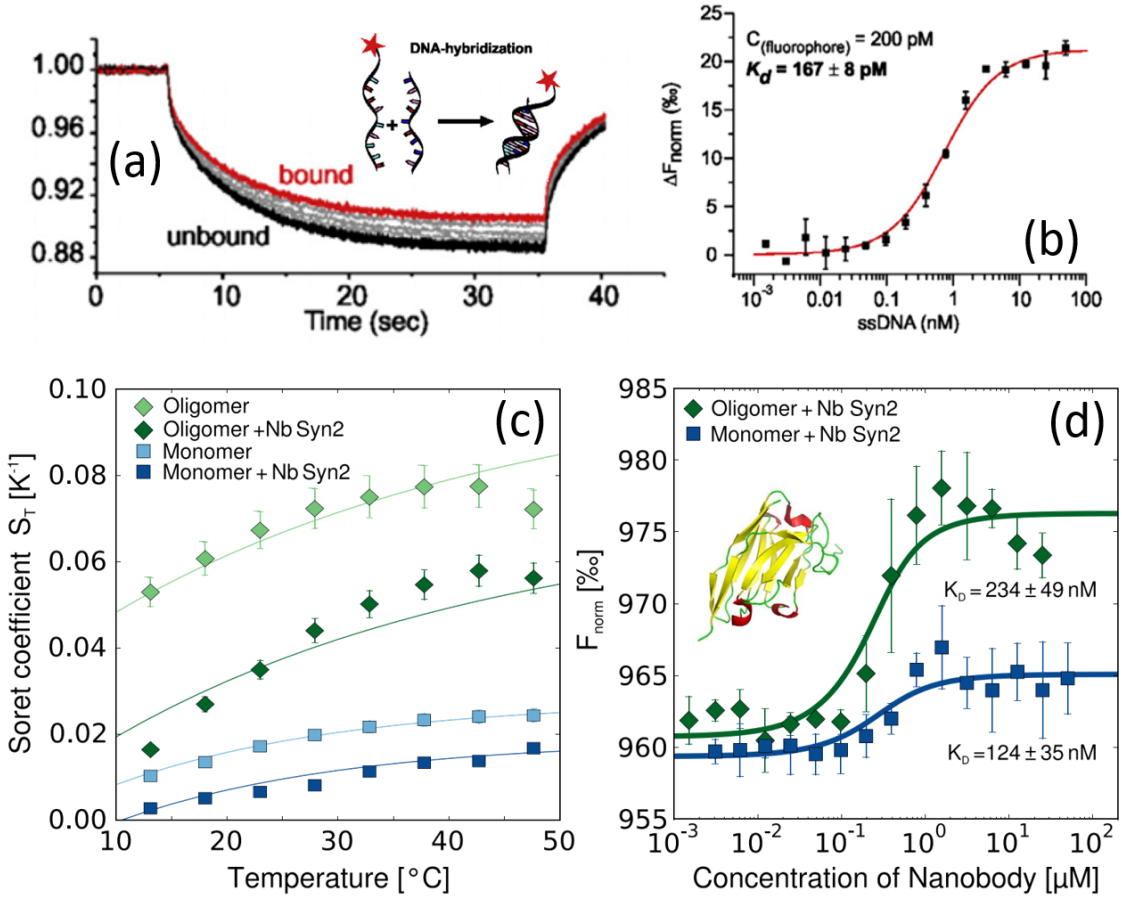

Fig. 1.14 **(a)** Normalised fluorescence of single-stranded DNA (ssDNA, unbound), and the formation of a double-stranded from two complementary single strands. The y-axis is F_{norm} **(b)** Binding kinetics of ssDNA as a function of the untagged strand. Fitting with a sigmoid curve of the relative change of F_{norm} yields K_D. Modified from [17]. **(c)** The measured Soret coefficient of monomeric and oligomeric $\alpha-$synuclein with *Nb Syn2* binding. Aggregated $\alpha-$synuclein, and nanobody bound proteins have a higher Soret coefficient. **(d)** Dissociation constant of the nanobody are different, depending on the aggregation state of $\alpha-$synuclein. From [18].

Wolff and co-authors used thermopheresis to investigate the aggregation state, and antibody binding kinetics of $\alpha-$synuclein [18]. By measuring the relative change in fluorescence intensity ($Fnorm$), and knowing the induced temperature difference, they were able to quantify the Soret coefficient of monomeric and oligomeric $\alpha-$synuclein, and the binding of each aggregated stage with the *Nb Syn2* nanobody. They found bigger aggregates $\alpha-$synuclein had higher Soret coefficient (Figure 1.14c). Moreover, they could differentiate when the nanobody had bound to protein, even in the monomeric

state. By varying the concentration of the nanobody and measuring F_{norm}, the quantified K_D for both oligomeric and monomeric $\alpha-$synuclein (Figure 1.14d).

1.2.3 Thermophobic nanoparticle accumulation

Proteins and DNA (Figure 1.14) have been shown to have a positive Soret coefficient in an pH buffered fluidic environment that preserves their shape. These molecules are thermophilic and move away from the heating source in all directions. Hence, trapping of such biomolecules requires experimental geometries that counteract the thermophoretic migration.

Duhr and Braun were able to concentrate 10k base-pair DNA by counterbalance the thermophobic displacement with confined fluid flow in a microchannel (Figure 1.15a) [19]. The fluorescently tagged DNA molecules moved away from the heated spot with

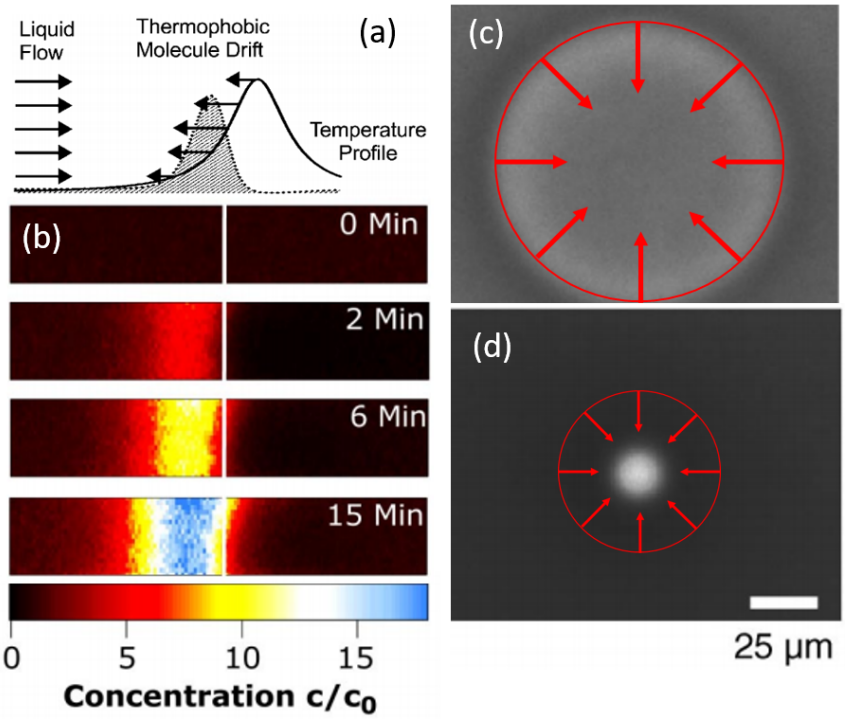

Fig. 1.15 **(a)** Trapping of DNA by balancing the fluid flow against the thermophoretic induced migration. **(b)** Accumulation of DNA molecules in a 10 μm channel. Fluorescence intensity (analogous to concentration) increases 16-fold over 15 minutes. **(c)** Radially scanned heating beam, gathering DNA molecules from a large area. **(d)** The beam is concentrically swept with smaller radii to pen the accumulated DNA molecules into a concentrated spot. Modified from [19].

an effective velocity of 0.55 $\mu m/s$, and were opposed by a similar fluid flow velocity in the opposite direction. Over 15 minutes, they were able to increase the concentration of accumulated DNA by 16 fold relative to the initial fluorescence intensity (Figure 1.15b).

By keeping the height of the fluidic chamber small (10 μm) and radially sweeping the heating beam, Duhr and Braun were able to accumulate the DNA molecules (Figure 1.15c,d). The sweeping area of the scanning beam reduced concentrically until the molecules were confined to a radius of to a 10 μm [19].

Similarly, Cichos' group swept a heating beam on the edge of a gold film to induce heating, and thus creating a cooler spot in the hollowed glass centre (Figure 1.16a, the

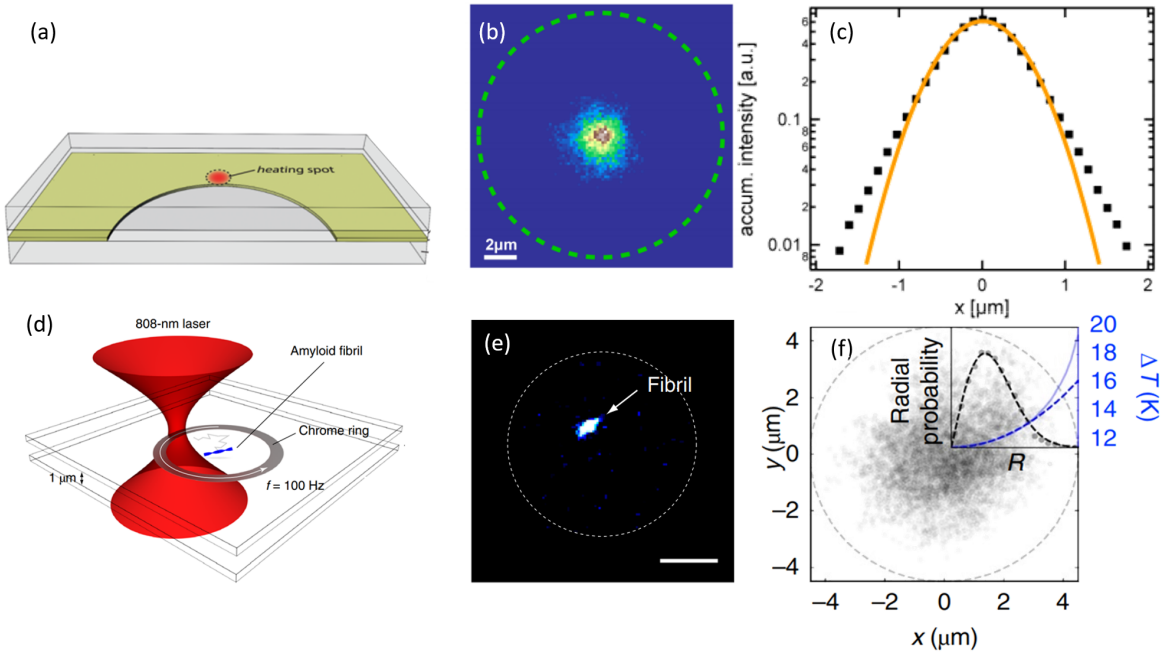

Fig. 1.16 **(a)** A thin film of gold with a hollow section is printed on a coverslip. A radially scanned laser generates heating, creating a temperature profile where the central hollow region has the lowest local temperature. **(b)** Probability density of the DNA's position. DNA molecules has the highest probability of being located at the centre. **(c)** Accumulate fluorescence intensity relative to the coldest local region. Gaussian fitting (orange curve) is used to determine the radius of gyration. Modified from [20].**(d)** Heating generated by radially scanning a beam over a chrome thin film. **e** Dash line shows the edge of the chrome ring. Single $\alpha\beta_x$-fibrils diffusing within the ring. Scale bar is 3 μm. **(f)** The detected centre of mass of the fibril. Inset shows the Rayleigh described distribution of fibril's detected positions, and the corresponding temperature profile. Modified from [21]

temperature profile is shown in the red curve in Figure 1.16c). Their simulations showed that a quasi-static beam generated stronger temperature gradients, and therefore a higher restoring force acting on the nanoparticle [77]. With this, they were able to confine 200 nm polystyrene beads and a single λ-DNA molecule (Figure 1.16b). Upon analysing the accumulated intensity of the DNA molecules in the confined region over time, they found that the centre DNA's centre of mass was where they expected the temperature to be lowest. Through Gaussian fitting of the accumulated intensity (orange curve of Figure 1.16c), the obtained a 0.66 μm radius of gyration. From this, they were able to conclude that the temperature profile across the molecule varies less than 0.1 K [20].

In more recent work, Cichos' group were able to confined single $\alpha\beta_{40}$-, and $\alpha\beta_{42}$-proteins in a heated chrome ring, and observe their rotational dynamics (Figure 1.16d,e) [21]. An 808 nm laser was radially scanned over a thin film of chrome to induce heating, and consequently, confined the proteins within a 10 μm region. It was found that the particle's radial position followed a Rayleigh distribution (Equation 12 of [21] supplementary information), mediated by the temperature gradient (Figure 1.16f) [21].

1.2.4 Thermoelectric nanoparticle confinement

The other branch of confining nanoparticles using thermopheresis is through the generation of thermoelectric fields mediated by the differential thermodiffusion of ions present in the solution (as outlined in Section 1.2.1). However, this requires that the nanoparticle of interest to have an electrostatic charge for the thermoelectric field to impart a force. In that instance, the thermos-diffusive velocity ($\vec{v} = -D_T \nabla T$) is analogous to electrophoresis ($\vec{v} = \mu_e \vec{E}$, where μ_e is the electrophoretic mobility of the charged nanoparticle) [72].

For three-dimensional stable confinement of the nanoparticles in a thermoelectric trap, the forces on the nanoparticle must balance in all direction. Zheng's group have successful confined a range of particle sizes, and materials, in a three-dimensional thermoelectric trap [72, 22, 78, 23, 24, 79]. In the subsequent technologies presented in this section, the governing thermoelectric field is created by the presence of CTAC (cetyltrimethylammonium chloride) cationic surfactant, the formation of positively charged CTAC micelles, and chloride anions.

In the instance where the nanoparticle to be trapped is a metallic (such as Au), the non-polar end of the CTAC molecules envelope the surface, and create a positively charged nanoparticle (Figure 1.17a). The remaining CTAC molecules form micelles (critical concentration of 0.13–0.16 mM), acting as macro-cations (Figure 1.17b). Some ions also attach on the surface of the thin Au film, creating a charge surface its own static field (E_r) Without any heating, the molecules freely diffuse randomly in all directions (Figure 1.17d). In the presence of a temperature gradient, the cations ($S_T \sim 10^{-2} K^{-1}$) and anions ($S_T = 7.18 \times 10^{-1} K^{-1}$) spatially separate owing to their different Soret coefficients. Both ions move away from the heating source (positive Soret coefficients), with greater thermally-driven diffusion the closer they are to the

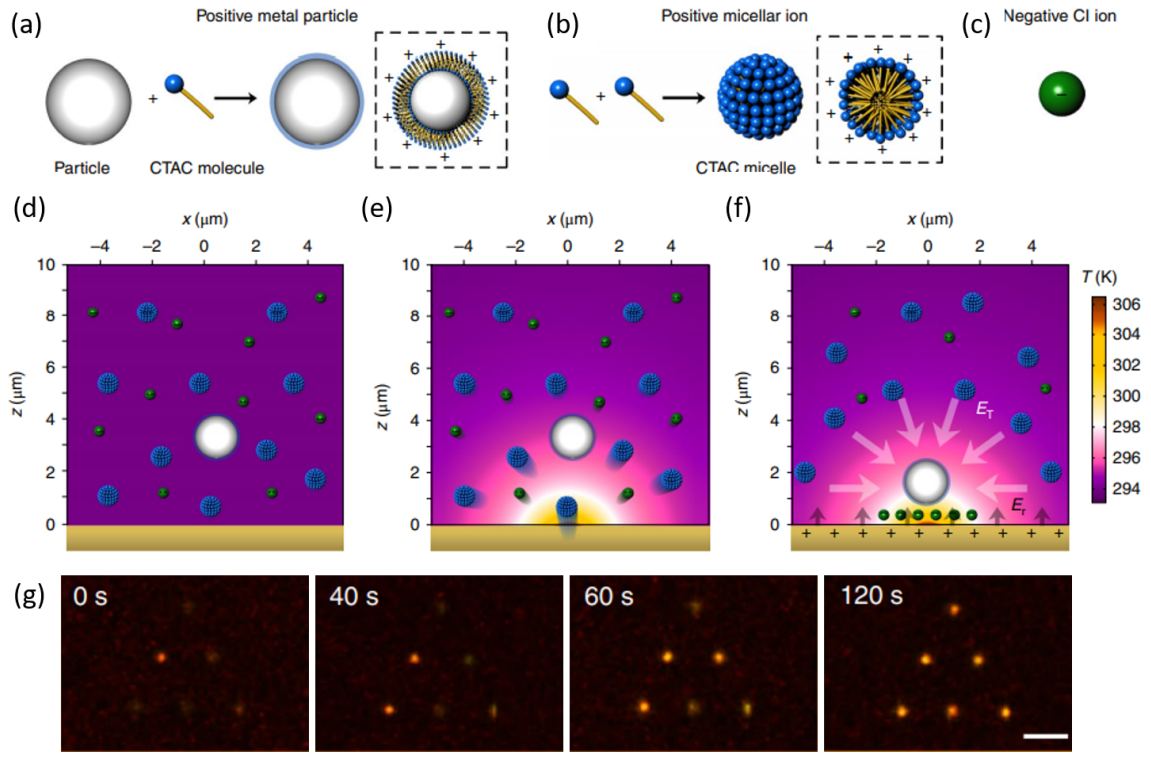

Fig. 1.17 **(a)** Coating of nanoparticle with CTAC molecules, forming a positively charged surface. **(b)** CTAC molecules forming positively charged macro-cations. **(c)** Schematic representation of a chloride anion. **(d)** Ions and nanoparticles are diffusing freely in solution without heating. **(e)** Ion thermo-diffusion in a temperature gradient, with greater displacement closer to the heating spot. Separation of ions occurs due to a large difference in their individual Soret coefficient. **(f)** Thermoelectric field formed, pointing towards the heated spot. The vertical component of E_T is balanced with the repulsive field (E_r) originating for the surface ions. **(g)** Simultaneous trapping of six-140 nm-size nanoparticles (triangular shape), in a triangular pattern. Scale bar is 10 μm. Modified from [22].

heat source (Figure 1.17e). In the steady state, the differentially separated ions accelerates the positively charged nanoparticle in the generated thermoelectric field (E_T), towards the heating source. The particles are pushed against the surface, and are confined due to the opposing repulsive field (E_r is balanced by the vertical component of the E_T) of the surface (Figure 1.17f). Hence, the nanoparticles reside above the surface at distance where the two fields are equal. The horizontal component of E_T point towards the heating source, and acts as a restoring force on a charged particle. When the heating source is removed, E_T is no longer sustained and the nanoparticles diffuse freely.

By combining the digital micro-mirror device in the optical path of the heating laser, Zheng's group were able to create multiple trapping sites for silica, polystyrene and Au nanoparticles (Figure 1.17g) [72, 22, 24].

Kotnala and Zheng were able to create a thermoelectric trap for 200 nm polystyrene beads at the end of a single-mode fibre (Figure 1.18) [23]. They were able to achieve this by coating the fibre facet with a thin Au film of 4.5 nm. The distal end of the fibre was pigtailed, coupling in laser light into the 9 μm-sized core to induce heating at the proximal, and trapping the positively charged nanoparticles (Figure 1.18a). The fibre was translated in the solution by a few hundred microns, and the nanoparticle remained trapped (Figure 1.18b-d). They were also able to trap individual nanoparticles using Au coated tapered fibres [23].

The use of an optical fibre in trapping nanoparticles is advantages as the same fibre can be used to spectroscopically scan and deliver a biomolecule or nanoparticle to specific locations.

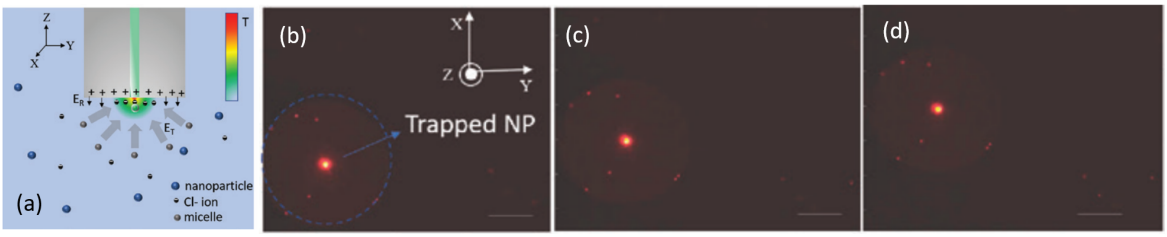

Fig. 1.18 **(a)** Thermoelectric trapping of 200 nm particles at the tip of a single mode fibre. **(b-d)** Translations of the fibre in the x-direction does not perturb the trapped particle. Scale bar is 50 μm. Modified from [23].

1.2.4.1 Applications of nanoparticle trapping with thermoelectric fields

Apart from the versatility to arrange nanoparticles using thermoelectric confinement, Zheng's group showed that it could also be used for spectroscopic experiments, and nanofabrication (Figure 1.19) [24, 78]. In conjunction with the CTAC cations and chloride anions, *Peng et al.* used a cross-linking molecule (PEGD) to form a polymer web over the nanoparticle and attach it to the substrate's surface (Figure reffig:etapplicationsa). Once the nanoparticle were trapped (Figure 1.19b,c), a UV lamp was used to promote cross-linking of the PEGD polymer, curing the nanoparticle in place. With the heating source turned-off, the nanoparticle remained in place (Figure 1.19e). This technique can be used to fabricate complex structures using nanoparticles as building blocks with a PEGD interstitial layer.

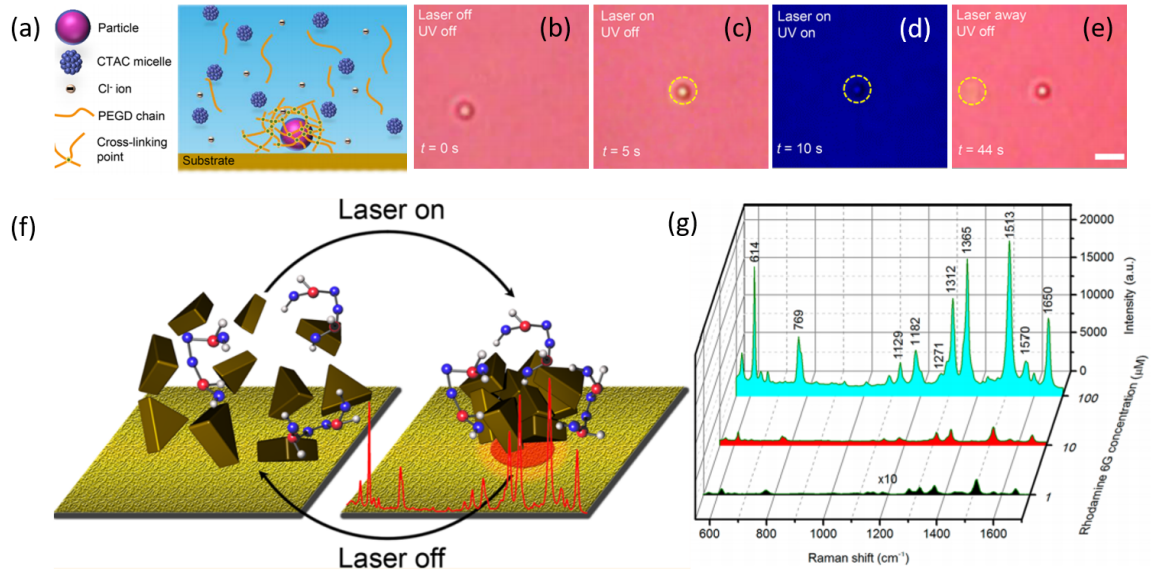

Fig. 1.19 **(a)** Trapping of polystyrene nanoparticles and PEGD (UV activated cross-linking polymer). **(b)** A single nanoparticle drifting freely. **(c)** Thermoelectrically confined nanoparticle. **(d)** UV is turned-on to cross-link PEGD, and holds the nanoparticle in place. **(e)** With the trapping field turned-off, the nanoparticle remains affixed to the surface. Modified from [23]. **(f)** Trapping of 150 *nm* triangular-shaped Au plasmonic particle in a thermoelectric field mediated by CTAC and chloride ion separation. *(g)* Surface-enhanced Raman signal of Rhodamine-6G at various concentrations. Modified from [24].

One of the main advantages of concentrating plasmonic nanoparticles is that they can be used for surface-enhanced Raman spectroscopy. Lin *et al.* used 150 *nm*-sided triangular Au particles in a thermoelectric trap to enhance the sensitivity of the

Raman signal for Rhodamine-6G [24]. The triangular shape nanoparticles increase the contacting surface area with each other, and the substrate (Figure 1.19f). As a result, the Raman spectra with varying concentrations of Rhodamine-6G became detectable (Figure 1.19g).

1.2.5 Summary and intended work

Nanoparticle properties such as its surface area, hydration entropy, and effective charge can be studies by subjecting them to a temperature gradient [65]. These properties are encapsulated in the nanoparticle's Soret coefficient (S_T), which is determined from the ratio thermo-diffusion, over diffusion in a static temperature environment ($S_T = D_T/D$). In addition to the thermally induced nanoparticles migration, ions and other dispersed molecules also undergo thermophoretic motion because of entropic forces at their surfaces [67]. Due to the size and charge of the ions, they experience dissimilar thermophoretic drift in a temperature gradient, leading to spatial separation of charged specifies that consequently generated a thermoelectric field [24]. This field has been used to confine nanoparticles of various sizes and materials, as demonstrated by Zheng's group [72, 22, 78, 23, 24, 79]. Hence thermopheresis is a method of both studying the nanoparticle properties, as well as manipulating and confining their motion.

The Soret coefficient of various protein sizes has been studied in the presence of aggregation inhibiting nanobodies [17, 18]. Proteins have also been confined using a heated chromium ring [21]. In these studies, the proteins reside in a complex solution of pH buffers, salts, and other solutes, making it difficult to discern the dominating thermophoretic effect that is responsive for the thermo-diffusive motion of the proteins. The work in Chapter 3 of this report simplifies this by using monodisperse polystyrene nanoparticles in a solution of Milli-Q water and sodium azide (inhibits bacteria growth in the solution). In this geometry, it was found that the thermoelectric field induced the migration of the nanoparticles in the presence of a temperature gradient. This was verified by mapping out the strength of the generated thermoelectric field by determining the velocities of the nanoparticles through particle tracking, and measuring microscale temperature gradients using the temperature-sensitive fluorescence lifetime of Rhodamine-B. Knowing the distribution of the temperature, and the thermoelectric field, enabled the quantification of the Soret coefficient for azide ions, which have previously not been reported.

1.3 Thermo-optic lensing of nanoparticle suspensions

In the first section of this chapter, the optical forces are the dominating effect, while in the second section, they are minimised, and thermal forces were used to confine, study and manipulate nanoparticle suspensions. A final consideration is the interplay between them. In particular, the manifestation of intensity dependant self-induced lensing effects, which are a direct consequence of the light-matter interaction of a focused beam in a nanosuspension (Figure 1.20). At low optical powers, lensing effects are not present, and the beam propagates with its inherent divergence through the medium (Figure 1.20a). Increasing the laser power such that the optical and thermal effects becoming significant, results in a reduced beam divergence through the cuvette (Figure 1.20c). At some critical power, the interplay between the opto-thermal force

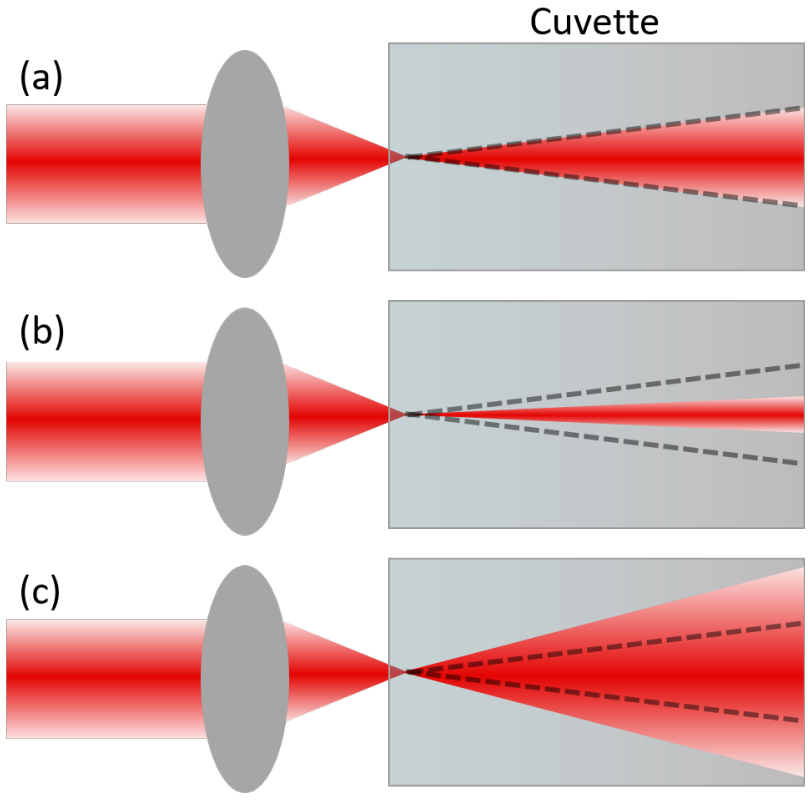

Fig. 1.20 Illustrations of the opto-thermal lensing effects at low **(a)**, medium **(b)** ,and high **(c)** optical powers. Dashed lines denote the beam shape at low power.

changes drastically, and consequently leads to a substantial increase in the beam's divergence, inducing lensing effects that defocus the light, relative to the low power case (Figure 1.20c).

The mechanism of the lensing effects has been attributed to optical forces [25], Kerr nonlinearities [80], thermo-optic effects [27], and thermophoretic effects [81]. All of those associated descriptions of the phenomena relate changes of the refractive index with the observed self-induced lensing.

An overview of the reported self-induced lensing by a focused Gaussian beam into nanoparticle suspensions is presented. Emphasise is given to how nanoparticle redistribution mediated by optical forces cause refractive index changes, as well as, nanoparticle absorption causing heating of the medium and its associated refractive index change. In addition, a method (z-scan) of quantifying the local nonlinear refractive index changes of a nanosuspension by a focused laser beam is reviewed, with particular focus on the reported intensity dependant refractive index changes for Au nanosuspensions. The magnitude and sign of the refractive index change can offer an explanation for the underlying mechanism behind the observed lensing effects.

1.3.1 Optical force mediated lensing

The optical forces acting on the nanoparticles can create local concentration differences. The optical gradient force, acting perpendicular to the beam's propagation direction can either attract and concentrate nanoparticles in the central beam axis (Figure 1.21a), or repel them away (Figure 1.21b). In both cases, the effective refractive index of the medium changes, which consequently affects the beam's propagating through the medium. The motion of the nanoparticle is contingent on its polarisability. The attractive of repulsive radial migration is a function of the refractive index difference ($\Delta n = n_p - n_m$) between the nanoparticle (n_p) and the medium (n_m). A positive Δn and the nanoparticle consequently has a positive polarisability, moving into the region of maximum intensity, and vice versa (Equation 1.1, Figure 1.21).

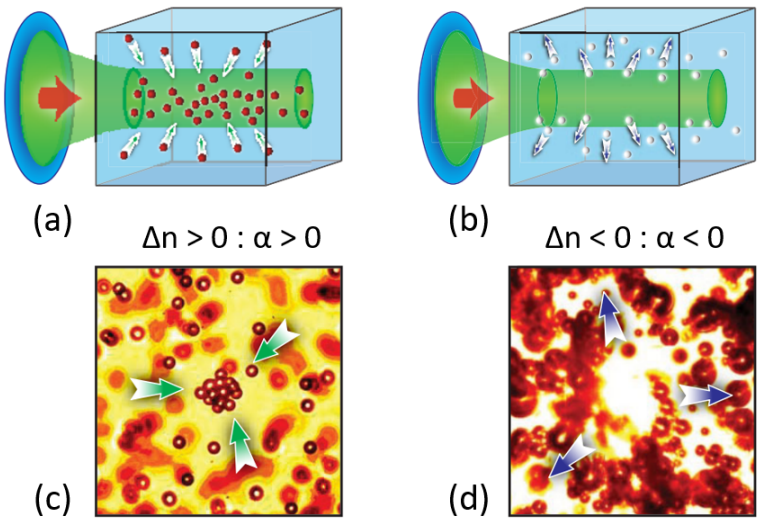

Fig. 1.21 Micron-sized particle in aqueous suspension with a laser beam (532 nm) focused into it. **(a, c)** 2 μ polystyrene beads ($np = 1.59$), have a higher refractive index than water, with a positive polarisability, and thus migrate to the region of highest intensity. **(b,d)** Hollow silica beads ($7\mu m$, $np = 1.2$) with a negative polarisability, moving away from the peak intensity region. Modified from [25].

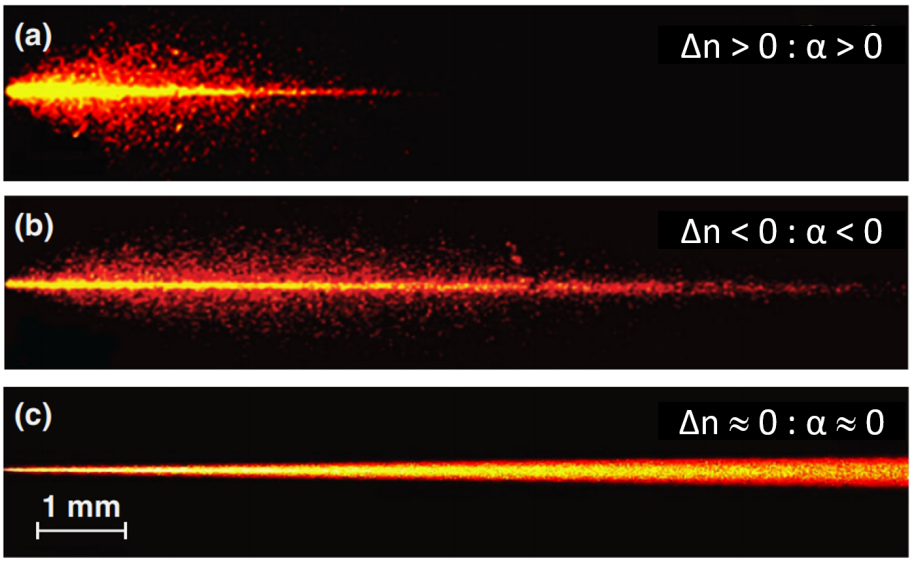

Fig. 1.22 The observed nonlinear lensing effects mediated by optical forces. **(a)** 200 nm polystyrene nanoparticles with positive polarisability migrating towards the region of highest intensity and causing scattering and increasing the local refractive index of the beam's central axis. **(b)** 200 nm PTFE nanoparticle with negative polarisability, moving away from the region of highest intensity, reducing scattering and mediated self-focusing of the beam. **(c)** Refractive index matched medium and PTFE nanoparticles. Scattering is minimised, and absorption is not affected. No lensing observed. Hence, self-induced lensing cannot be mediated by thermal effects. Modified from [25].

Man *et al.* demonstrated both self-focusing and -defocusing of a laser beam propagating in nanoparticle suspensions (Figure 1.22) [5]. A laser beam with a power of 3 W, was focused into a cuvette with a focal spot size of 11 μm (FWHM). The propagation of the beam through 200 nm polystyrene particles ($n = 1.59$) suspended in a Glycerin-water mixture (3:1 ratio,$n = 1.44$) only penetrated a few millimetres, and diverged very strongly (Figure 1.22a). The nanoparticles moved into the region of highest intensity ($\alpha > 0$) mediated by the radial gradient force, increasing the local refractive index and defocusing the light. Moreover, the nanoparticles concentrated in the beam's centre acted as scatterers, which is why the light only penetrated a few millilitres into the solution. For a suspension of PTFE (200 nm, $n = 1.35$) nanoparticles, which had a lower refractive index than Glycerin-water mixture, the beam penetrated much deeper into the suspension, and underwent self-focusing (Figure 1.22b). In this case, the local index of refraction reduced due to optical path clearing of the nanoparticles, which meant less scattering and beam diffraction.

As a control, Man *et al.* changed the Glycerin-water ratio (1:6) until it matched the refractive index of PTFE nanoparticles. In this instance, the beam's light-matter interactions were diminished, and the inherent beam divergence was observed (Figure 1.22c). Man *et al.* suggest that thermal effects do not induce self-lensing, as they would manifest themselves in the control experiment [25].

In contrast to Man *et al.*'s work, Fardad *et al.* report self-focusing behaviour of Ag-, and Au-nanoparticles suspensions, both of which have positive polarisability (Figure 1.23) [26]. At a wavelength of 532 nm, the Au nanoparticles are predominately absorbing, whilst the Ag nanoparticles are scattering (Figure 1.23a,b). With the focus (15 μm FWHM) set at the beginning of the cuvette, the beam divergence is significantly reduced (Figures 1.23d,g) relative to the low power (10 mW) beam divergence (Figures 1.23c,f). Fardad *et al.* also associate this behaviour to the migration of nanoparticles by the optical gradient force, for both Ag and Au, with higher optical powers needed for Ag to compensate for the increase scattering losses [26].

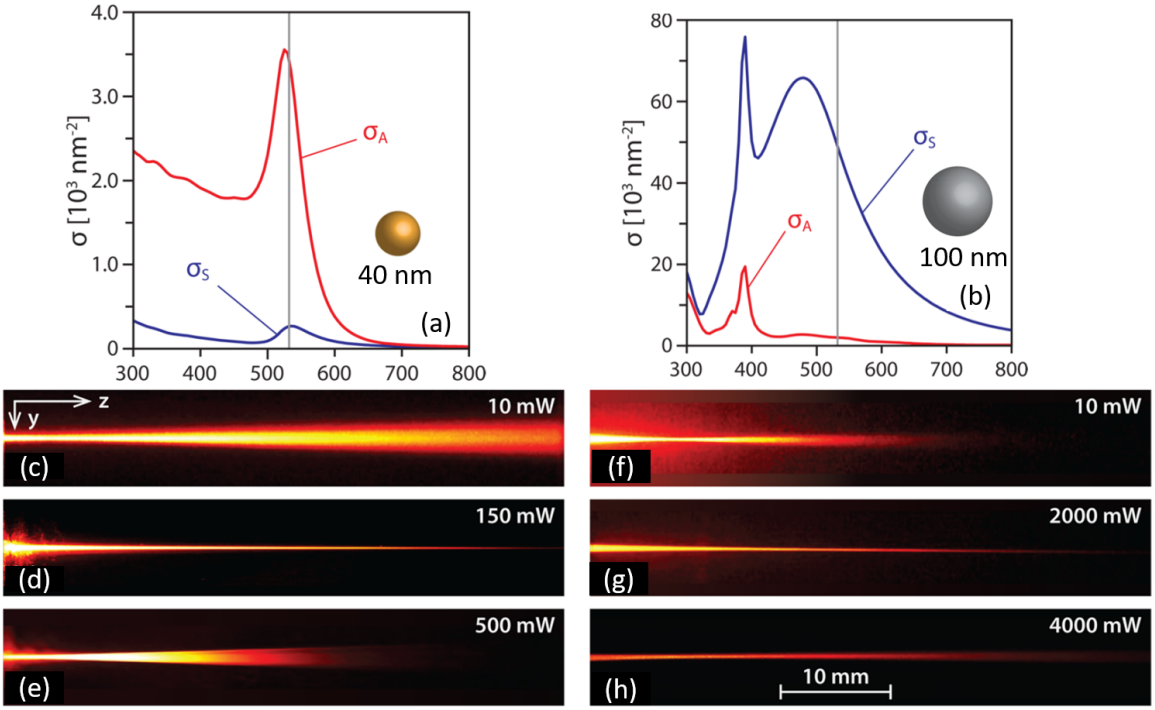

Fig. 1.23 Optically driven lensing effects for 40 *nm* Au nanoparticles, and 100 *nm* Ag nanoparticles in aqueous suspension.**(a,b)** Theoretical scattering and absorption cross-sections. Intensity dependant lensing of Au- **(c,d,e)**, and Ag- nanosuspension **(f,g,h)**. Self-focusing is mediated by optical effects, whilst defocusing by thermal effects [26]. Due to the higher absorption of Au nanoparticles, less power is required to obtain defocusing effects than Ag nanoparticles which predominately scatter light. Modified from [26]

Interestingly, Fardad *et al.* also report self-defocusing of the beam by increasing the laser power, whereby the divergence is significantly increased relative to the low power state (Figures 1.23e,h). They attribute this observation to thermal effects overcome the optical forces. Due to the increased laser power, the nanoparticles dissipate their heat into the medium, which given the negative thermo-optic coefficient of water, acts to reduce the refractive index of the environment and defocuses the beam [26]. The works of Fardad *et al.* have been corroborated Kelly *et al.* who also observed self-focusing effects for 40 *nm* Au nanoparticle suspension in a pump-probe beam optical set up [82].

The alternate mechanism for self-focusing and -defocusing behaviour have also been associated with thermal effects.

1.3.2 Opto-thermal lensing in nanoparticle suspensions

The works of Liberman *et al.* and Ortega *et al.* ascribe their observed nonlinear lensing effects to a thermally driven decrease of the medium's refractive index [27, 28]. They both used ∼5 *nm* Au nanoparticles in aqueous suspension due to their dominant absorption cross-sections relative to their scattering. Liberman *et al.* calculated the scattering-to absorption-cross section ratios, and found that for Au nanoparticles, absorption dominates for sizes below 60 *nm*. This essentially means that the lensing behaviour is likely to be thermally driven, rather than optically for such nanoparticle sizes.

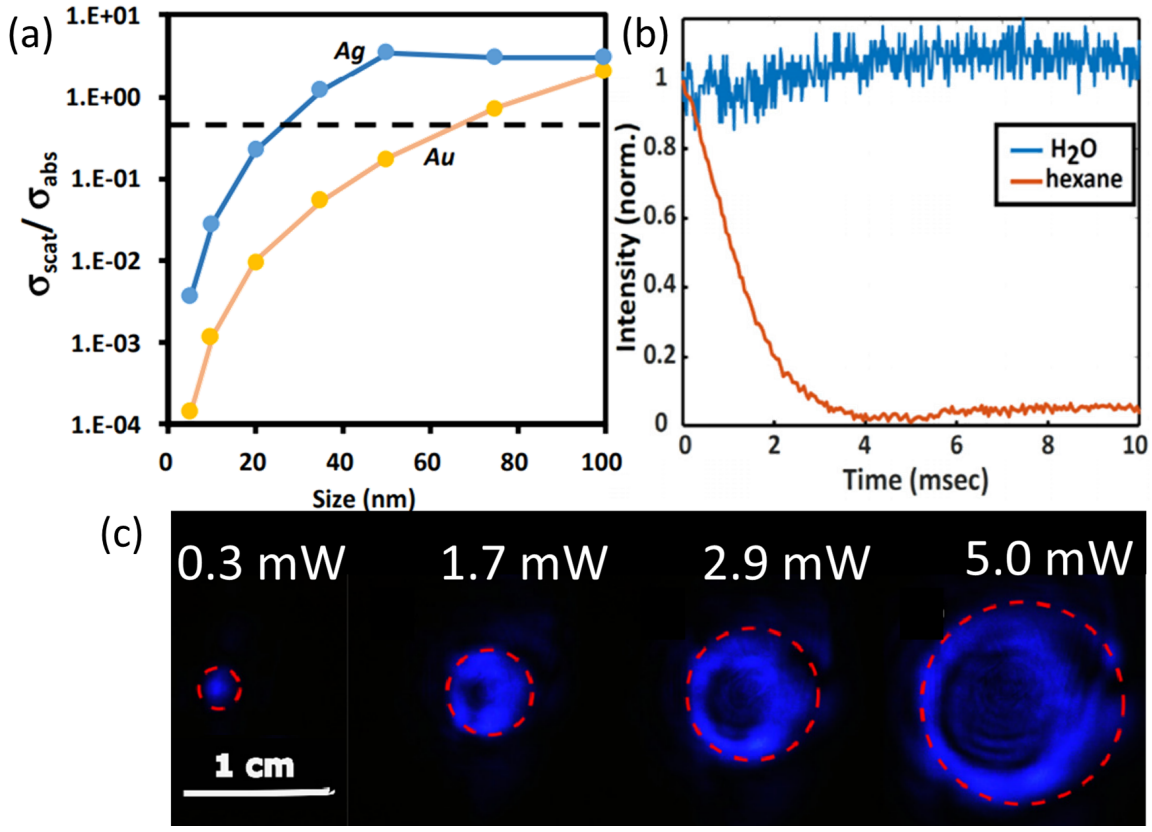

Fig. 1.24 **(a)** Theoretical ratio of scattering and absorption cross-sections. For Au-nanoparticles below 60 *nm*, absorption is the dominating effects leading to heating of the solution. **(b)** Lensing effects as a function of time normalised to the power measured through an aperture. Hexane has higher thermal-optic coefficient than water, and yeilded increased lensing effects. The temporal dynamic of the self-induced lensing occurred over ca. 2-3 *ms*. **(c)** Increasing far-field defocusing as a function of laser power. The dashed red circles represent beam size. Modified from [27].

Liberman *et al.* investigated the nonlinear lensing effects of Au nanoparticles suspended in water and hexane to verify that lensing effects were thermally mediated. Hexane has a lower thermal- conductivity and diffusivity than water, and therefore lensing effects are expected to be amplified [27]. Using a wavelength of 405 nm, focused into the beginning of a cuvette (w_0= 60 μm), nonlinear lensing was observed for both water and hexane Au nanoparticle suspensions by imaging the far-field beam propagation as a function of laser power (Figure 1.24c). As the laser power was increased from 0.3 mW to 5.0 mW, the far-field beam size increased drastically, owing to the negative thermo-optic coefficient (dn/dt) of water ($0.91\times10^{-4}/k$) and hexane ($5.2\times10^{-4}/k$).

Liberman *et al.* studied the temporal dynamics of the defocusing behaviour by measuring the trace of the light transmitted through an aperture and onto a photodiode, for both water and hexane suspended Au nanoparticles (Figure 1.24b). In a 10 ms acquisition window, the normalised intensity transmission through the aperture for the hexane suspended nanoparticles decayed to near 0 within 4 ms, while the signal intensity for water suspended nanoparticles remained constant. This observation is a direct consequence of the different thermo-optic coefficients of the two fluids [27].

Ortega *et al.* show that the focusing or defocusing behaviour could selectively be chosen by moving the cuvette such that the focal position was incident at different

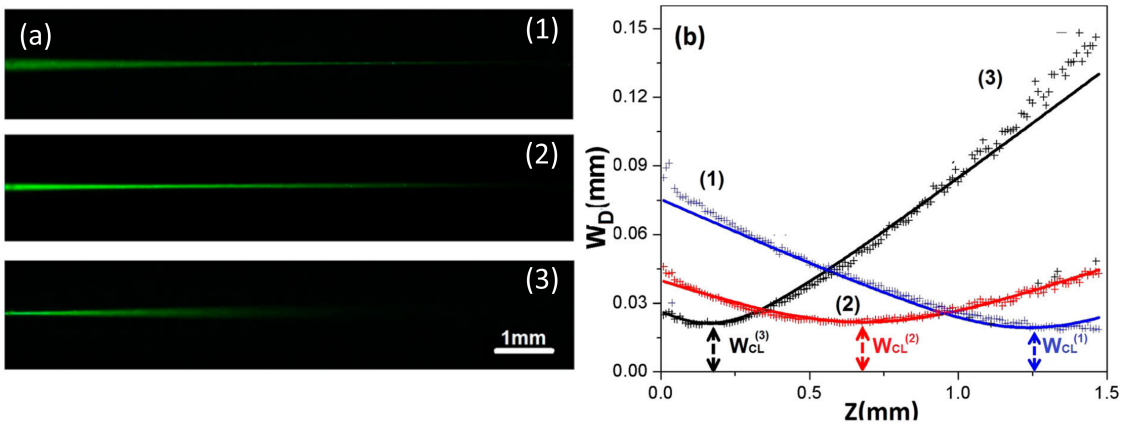

Fig. 1.25 Self-focusing and defocusing is dependant on the focal position of the focused beam inside the nanosuspension. **(a)** Side cuvette images of the beam at various focal positions. **(b)** Measured beam profiles and its correspond lesing effect with respect to the focal position inside the cuvette. Laser power is kept constant (70 mW). Modified from [28].

locations inside the cuvette, whilst keeping the laser power constant ($P = 70\ mW$) [28]. They imaged the beam propagation inside the cuvette and obtained the beam size (through a Lorentzian fitting function) as it propagated through the nanosuspension (Figure 1.25). With the focal position set near the cuvette's end (Figure 1.25a1, blue curve in Figure 1.25b), the beam penetrated deep into the solution, with a 'needle-like' beam profile. When the focal position was set near the middle of the cuvette (Figure 1.25a2, red curve in Figure 1.25b), a slightly higher divergence was observed relative to the initial position due to lensing by the solution. A clear increase in the beam divergence was observed when the focal position was set near the cuvette's entrance facet (Figure 1.25a3, black curve in Figure 1.25b). The focus set at this position meant that the highest intensity was available for absorption by the nanoparticle, which consequently heated the surrounding fluid, lowering its index of refraction and increase the beam divergence [28].

The work of Ortega *et al.* can help elucidate some of the conflicting literature reported around the lensing effects for Au-nanosuspensions of sizes 60 nm and below (the works of Fardad *et al.* and Liberman *et al.* having different focal positions inside the cuvette but not precisely reporting on the exact location). A more quantitative way of pinpointing the exact mechanism behind the intensity dependant lensing effects is by enumerating the sign and magnitude of the local nonlinear refractive index changes, which is possible through the z-scan technique.

1.3.3 Quantification of the refractive index change

The reported nonlinear lensing behaviour in the previous section is intensity dependent. A strong intensity gradient is required for optical forces and thermal effects to become significant. The self-focusing and-defocusing observed in long optical path length cuvettes, where the beam propagates several Rayleigh lengths (Z_R) further complicates matters as the first part of the nanosuspension redistributes the intensity seen by latter segments, analogous to an array of back-to-back lenses. This is evident in the fact that the lensing behaviour changes depending on the focal position inside the cuvettes (Figure 1.25). Hence, by using a much smaller optical path length cuvette, the individual contributions of the lensing effects can be determined as a function of laser intensity.

The z-scan technique, which is a ubiquitous method of quantifying the nonlinear index of refraction for semiconductor materials, was considered as a way of quantifying

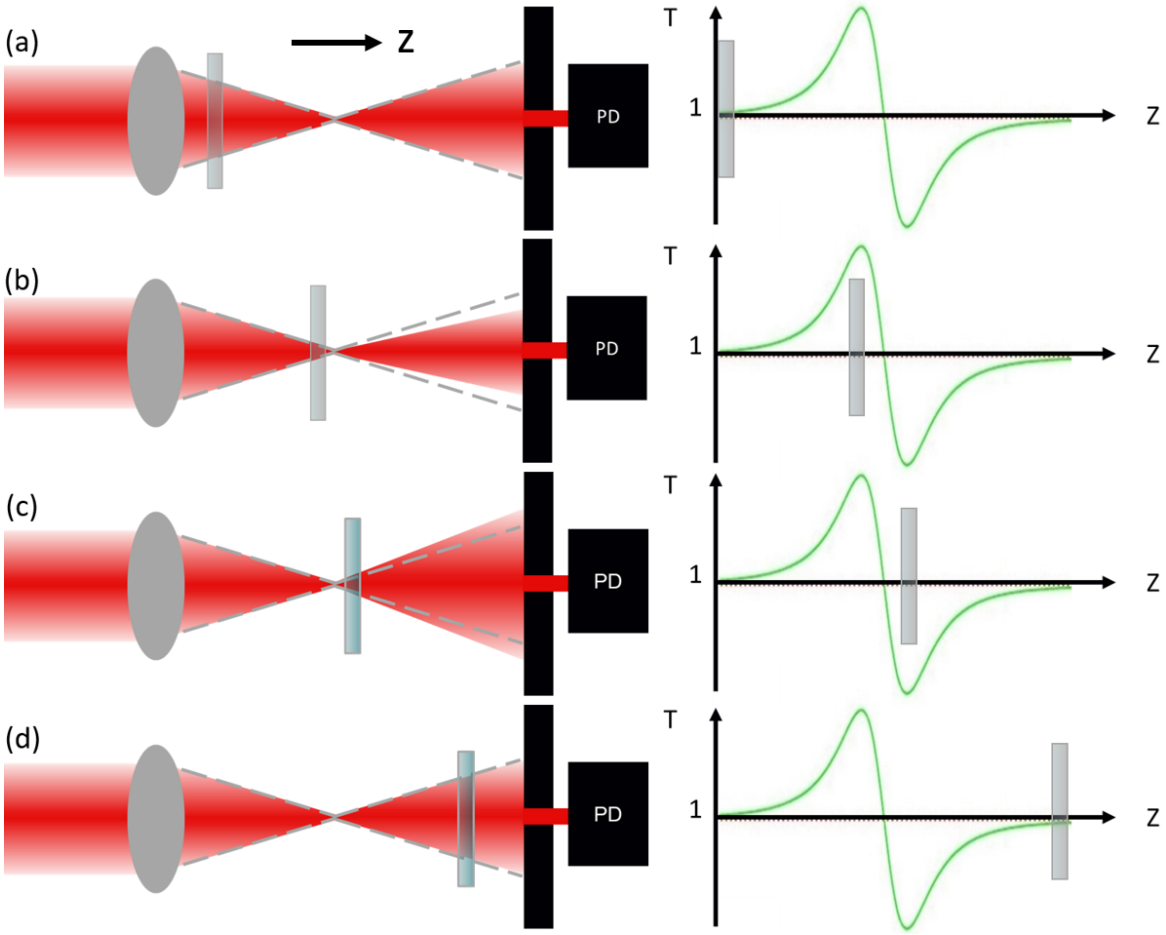

Fig. 1.26 Illustration of the closed-aperture setup and corresponding signal for z-scan method. This illustration is for a negative n_2 value (reduction of the refractive index from its linear value). A lens is used to focus a Gaussian laser beam. A thin sample with nonlinear lensing behaviour is scanned across the beam and the transmission of the light though an aperture and onto a photodiode is used to determine nonlinear refraction of the sample. **(a)** With low irradiance on the sample, the transmission of the light is unaffected and remains constant. As incident intensity on the sample increases, nonlinear opto-thermal effects change the local index of refraction and alters the propagation of the light. When the thin cuvette is before the focal point, the radius of curvature of the focused light is negative. A negative Δn, resists the radius of curvature from tending to zero at the focus, and hence the focal point shifts forward, yielding a less diverging beam, which consequently increases the amount of light transmitted through the aperture. **(c)** When the cuvette is position post-focal point, a negative Δn increases the radius of curvature of the beam, increasing beam divergence, and consequently less light is transmitted through the aperture. **(d)** Far away from the focus, the opto-thermal effects diminish, returning the number of photons transmitted through the aperture to its baseline value. Figure inspired from [29].

the refractive index change by the nanosuspension [83]. The technique simply involves scanning a thin cuvette containing the nanosuspension, in the propagation direction of the focused laser beam, and monitoring the transmission of light through an aperture placed in the far-field (Figure 1.26). This method considers the nanosuspension as an effective optical Kerr medium, whereby its refractive index is a function of the incident intensity [84]. At low intensities (and small E-fields, $I \sim |E|^2$) the polarisation ($\vec{P}$) per unit volume of the nanosuspension scales linearly with the electric field ($\vec{P} = \epsilon_0 \chi \vec{E}$, where χ is the electric susceptibility ($\chi = 1 - n_m^2$)) [29, 84]. With high incident intensities, the opto-thermal effects nonlinearly change the refractive index of nanosuspension, hence $\vec{P}$ no longer scales linearly with $\vec{E}$. As a result, a coefficient (n_2) is introduced to compensate for the nonlinearly refractive index scaling of the nanosuspension, such that:

$$n = n_0 + n_2 I_0 \tag{1.10}$$

$$= n_0 + \Delta n \tag{1.11}$$

where I_0, n_0, and Δn denote the intensity at the focus, the linear refractive index, and the change in the refractive index, respectively [84, 85]. In conjunction to the nonlinear refractive index response of a material, there is also a nonlinear absorption ($\alpha = \alpha_0 + \beta I$, where α_0 is the linear absorption, and β is the nonlinear absorption coefficient) [85]. The z-scan technique is used to quantify both n_2 (closed-aperture scan) and β (open-aperture scan). The methodology developed by Sheik-Bahae *et al.*, calculates the transmission (T) through an aperture due to an on-axis phase shift ($\Delta\Phi$) at the focus induced by the thin cuvette containing the nanosuspension, such that,

$$T = 1 - \frac{4\Delta\Phi x}{(x^2 + 9)(x^2 + 1)} \tag{1.12}$$

where x is a dimensionless parameter (Z/Z_R, normalised to the Rayleigh length) that represents the cuvette's position with respect to the focal point [86]. The corresponding phase shift (or change) at the focusing in the presence of nonlinear lensing by the nanosuspension is:

$$\Delta\Phi = k\Delta n L_{eff} \tag{1.13}$$

where k is the wave-number and L_{eff} is the effective propagation length inside the nanosuspension ($L_{eff} = 1 - e^{\alpha_0 L}/\alpha_0$, where L is the optical path length of the cuvette) [86]. The following criteria or assumptions need to be met in order for the z-scan method to evaluate the value of nonlinear refraction (n_2)and absorption (β) [86]:

1. Beam is Gaussian in shape
2. Aperture is placed in the far-field: d » Z_R
3. Aperture and focusing lens is kept constant and only the cuvette is translated
4. Aperture size is kept constant
5. L < Z_R: to ensure constant beam diameter within the cuvette. Lens has the same shape as the beam (slowly varying envelope approximation)
6. $|\Delta\phi| \leq \pi$: Ensures constant peak-to-trough separation distance in Z-scan trace, aiding curve fitting and comparison between datasets

The z-scan literature for Au-nanosuspension all have a negative $n2$ value for various sizes and optical powers (Figure 1.27, and tabulated results in Table 1.1). Hence, the refractive index change is negative for the reported nanoparticle range (5 - 50 nm). All authors used a CW laser and observed no nonlinear absorption, or they did not report a value.

Jia *et al.* was the first to report nonlinear refractive values of Au nanosuspension of 50 nm nanoparticles using the z-scan method (Figure 1.27a) [30]. Ortega *et al.* showed that the peak-to-trough value of normalise transmission through the aperture increases with optical power, whilst the value of n_2 stays constant (Figure 1.27b) [28]. They consequently observed an increasing Δn ($\sim \times 10^{-3}$ for powers between 60-120 mW, inset of Figure 1.27b). Lenart *et al.* demonstrated the presence of Au nanoparticle significantly increased the nonlinear refraction behaviour of liquid crystals (Figure 1.27c) [31]. Ortega *et al.* found that the Sheik-Bahae formalisation best fitted the data for Au nanosuspensions than other proposed models (Figure 1.27d) [32].

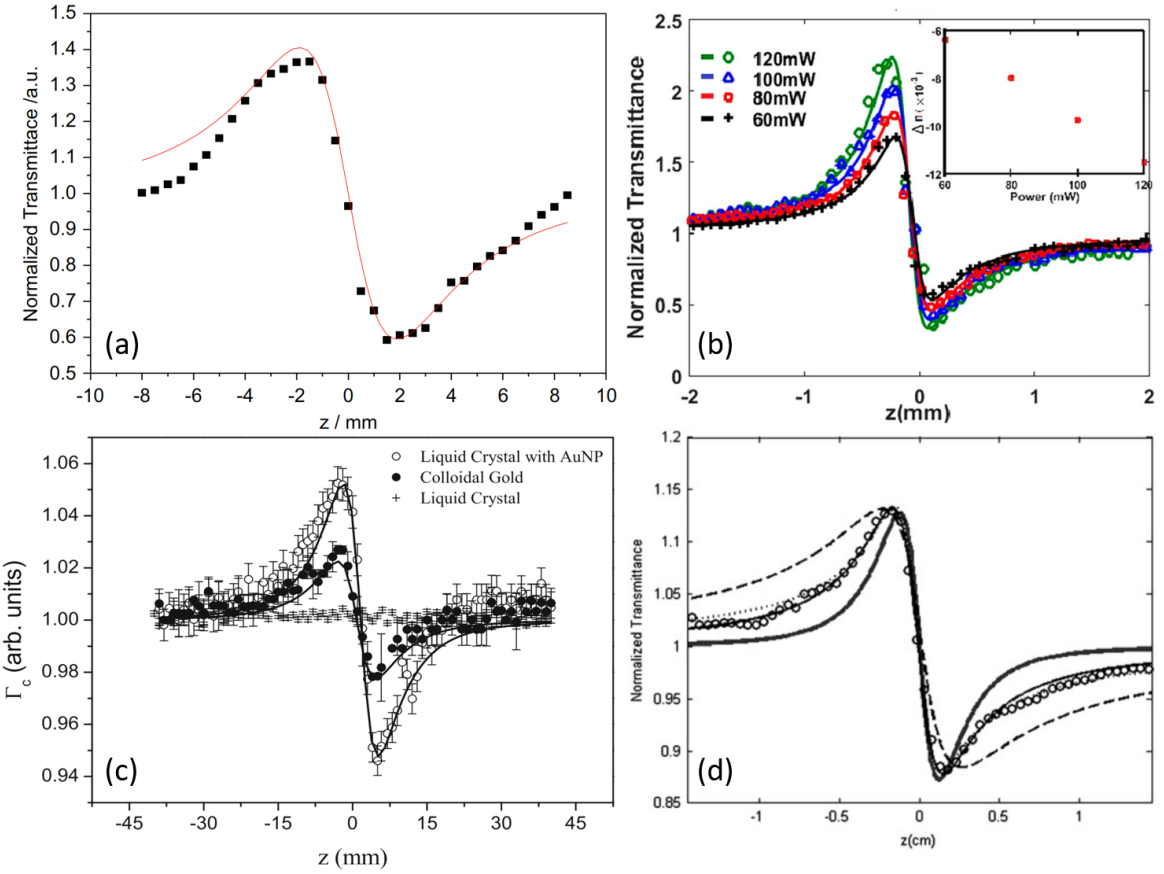

Fig. 1.27 The main results for the reported z-scan literature for Au-nanosuspensions using CW illumination. All figures are for close-aperture scans to determine $n2$, as nonlinear absorption was not observed or reported in the tested intensity range. **(a)** For 50 *nm* sized Au nanoparticles under 532 *nm* illumination [30]. **(b)** Increase in the peak-to-trough values for 5 *nm* nanosuspension as a function of laser power [28]. Inset shows the corresponding refractive index change. **(c)** The presence of Au nanoparticles (12 *nm* forming clusters) greatly enhances the nonlinear fractive index properties of liquid crystals [31]. **(d)** Various theortical models fitted to a z-scan data for Au nanosuspensions (25 *nm*) with heik-Bahae formalisation (thin black line) yielding the best fit. [32]. Summary of results presented in Table 1.1.

It should be noted that in the reported size range (5-50 *nm*), the nanoparticles are predominately absorbing rather than scattering the light (as shown in Figure 1.24a), consequently increase the temperature of the medium, and thus the refractive index change is due to the negative thermo-optic coefficient of water.

Size [nm]	Wavelength [nm]	P [mW]	n_2 [m^2/W]
5 [28]	532	60-120	-10^{-12}
12* [31]	532	18	-10^{-11}
25 [32]	514	2.5	-
50 [30]	633	110	-2.23×10^{-12}

Table 1.1 Summary of results for reported $n2$ values for Au nanosuspensions. *denote clusters of 12 nm Au nanoparticles.

1.3.4 Summary and intended work

For optical trapping, a high intensity region is created by a focusing lens to confine nanoparticles. As a consequence, optically trapped nanoparticle change the local refractive index, which in turn redistributes the intensity, leading to self-lensing effects. The local refractive index can either increase or decrease depending on the polarisability of the nanoparticle, as demonstrated by Man using PTFE and polystyrene nanoparticles *et al.* (Figure 1.22). Interestingly, for Au nanoparticle suspensions, this self-lensing behaviour has been attributed to either optical (by Fardad *et al.* and Kelly *et al.*) or thermal effects (Ortega *et al.* and Liberman *et al.*), whereby the nanoparticle's absorption increases the local temperature of the medium. In this work, self-focusing and -defocusing behaviour is extensively studied (by replicating the experimental geometry of Fardad *et al.* and Kelly *et al.*), and varying laser power, focal position inside the cuvette, nanoparticle concentration, and the medium of the nanoparticles, to discern the fundamental mechanism behind the self-lensing effects.

An insight into pinpoint the governing forces for self-lensing effects is to quantify the refractive index change, which is made possible by the z-scan technique. Currently, quantification of nonlinear refraction for Au nanosuspension is sparsely reported. All currently reported n_2 values (Table 1.1) are negative for Au nanoparticles in the size range of 5 - 50 nm. These nanoparticles are predominantly absorbing the incident light, and are likely increasing the temperature of their medium through heat dissipation. A full sweep of parameters (mention above) are taken for 40 nm nanosuspensions by replacing the long optical path cuvette used to determining self-lensing effects with a much short optical path length cuvette. In addition, z-scans measurements is performed as a function of time to determine the characteristic transients of the

self-lensing behaviour. As mentioned in the thermophoretic section of this chapter, heat dissipation is like to occur in less than 1 s, while particle migration (onset by optical or thermophoretic forces) is on longer time scales. Hence knowing associated temporal dynamics of the lensing behaviour, can elucidate the governing mechanism of the self-induced lensing phenomena.

Chapter 2

Microfluidic fibre based interferometric optical trap for nanoparticles

2.1 Introduction

The ability to manipulate and trap nano-sized particles using laser is desirable in many fields such as biology [37, 38], chemistry [45], material science [44], and engineering [42, 43], to name a few. In this chapter, the nanoparticle manipulation in a fluidic environment was achieved by maximising the optical effects and keeping thermal ones to a minimum.

Nanoparticle confinement is challengingas smaller nanoparticles sizes have reduced light-matter interactions. Moreover, light-matter momentum transfer is likely to lead to photophoretic migration of the nanoparticle, rather than its confinement. Typically, the wavelength of the light used to manipulate nanoparticles, is much larger than the nanoparticle's size, meaning that they effectively act as dipoles in an electric field, which preferentially align with the external field to minimise their energy [2]. Hence, maximising the gradient in the electric field, enhances the light-matter interactions and facilitates nanoparticle manipulation. For this reason, researchers have routinely used a tightly focused laser beam to create strong intensity gradients, overcoming the photophoretic effects, and confining nanoparticles [54, 3, 55, 6].

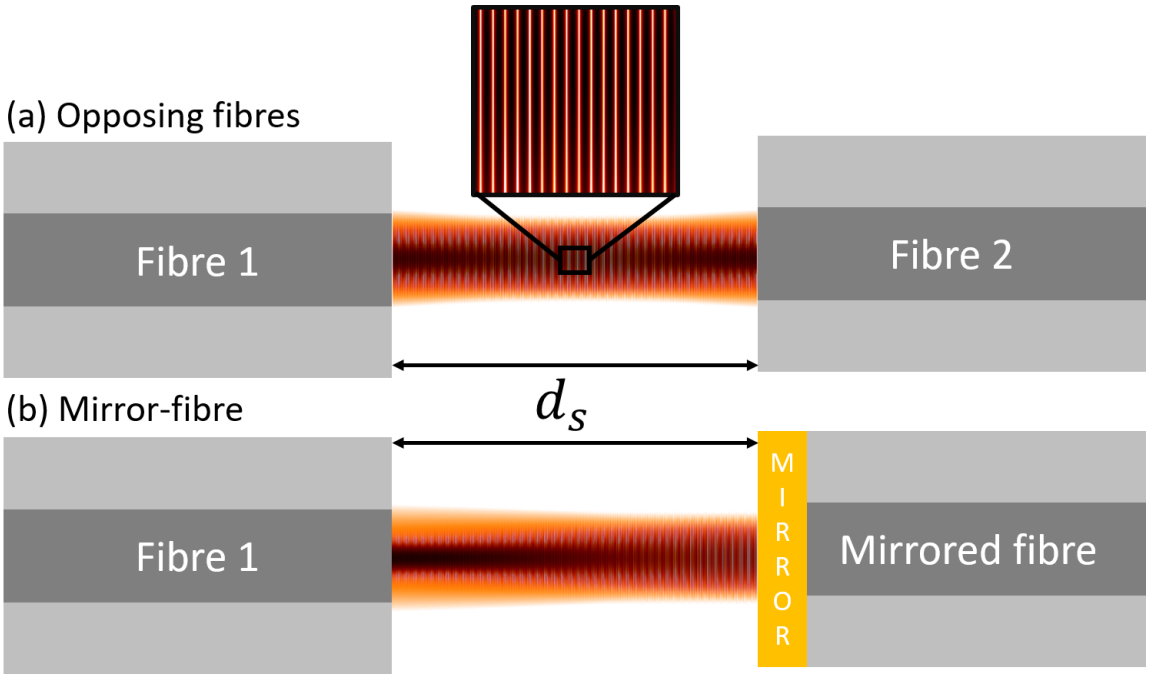

Fig. 2.1 Optical trapping geometries for nanoparticles. **(a)** Interference of laser light emerging from opposing polarisation maintaining fibres aligned along the same axis. An array of strong intensity gradients are generated, which maximise the gradient force over the scattering force. **(b)** Self-interfering pattern created from the retro-reflected light by a micro-mirror (Au coated fibre). d_s is the separation distance between the optical fibre facets ($\sim$ 66 μm used in this work).

Trapping of a variety of nanoparticles and biomolecules have been reported using a single beam. However, this is limited as a method as typically a single nanoparticle is confined, and the same optics are used for imaging and trapping, which is limiting (Section 1.1.2). These constraints are circumvented by using standing wave traps which inherently generate an array of intensity gradients with high spatial periodicity due to interference ($\lambda/2 * n_m$) [7]. In this work, inspiration was taken from Decombe *et al.*'s experimental architecture, as they used a counterpropagating tapered fibre geometry to trap 300 nm YAG:Ce^3 nanoparticles (Figure 1.8c) [11]. Instead of the tapered fibres, commercially available polarisation maintaining fibres were used in this work to optically confine nanoparticles, making the geometry more adoptable by other researchers. A significantly larger fibre separation distance was used (compared to Decombe *et al.*) such that a multitude of trapping sites were created, allowing for multiplexed analysis of nanoparticle confinement (Figure 2.1a). Phase instability can arise from light coupled into a single mode fibre, which causes trapping instabilities. To overcome this, a second geometry was also conceived whereby a micro-mirror to

back-reflect the light emitted from the opposing fibre (Figure 2.1b).

The trapping geometries of Figure 2.1 were simulated by modelling the interference of Gaussian beams to discern trapping potentials for 100 *nm* Au-nanoparticles at various laser powers (Section 2.2). A microfluidic chip was build to house the optical fibres and provide a controlled fluidic environment with zero net flow where the anomalous diffusion of the confined nanoparticles was determined from video-rate particle tracking (Section 2.3).

2.2 Optical interferometric trapping simulations

To simulate the scattering and gradient forces for the optical geometries of Figure 2.1, each beam was considered to a Gaussian beam propagating in a water medium. The interference of the beams were then simulated, from which the corresponding intensity gradients and Poynting vectors were numerically calculated. The polarizability for 100 *nm* diameter Au nanoparticles were enumerated using the Clausius–Mossotti relation, and Mie theory, from which the scattering and gradient forces were discerned.

2.2.1 Calculating nanoparticle polarisability

The Clausius–Mossotti (CM) relation (Equation 1.1) was used to calculate the polarisability for 100 *nm* Au-nanoparticles for the visible and near-infrared wavelengths. The tabulated refractive index of Au (Johnson and Christy [87]), and water (Hale and Querry [88]) were obtained from literature. A cubic interpolation function was used to selectively determine the index of refraction for Au and water, at any given wavelength in the 400 - 1000 *nm* range. As a verification, the polarisability of 36.2 *nm* Au-nanoparticles were calculated and found to be in agreement with the reported values by Svoboda *et al.* (Table 1 in ref [38]).

For 100 *nm* Au-nano-spheres, the real and imaginary parts of the polarisability (Figure 2.2a) were calculated from CM relation shows a pairwise increase-and-decrease around the 530 *nm* wavelength, respectively. The imaginary component tends to zero around 620 *nm*, while the real part plateaus to a value of $\sim 0.4x10^{-32}Cm^2/V$.

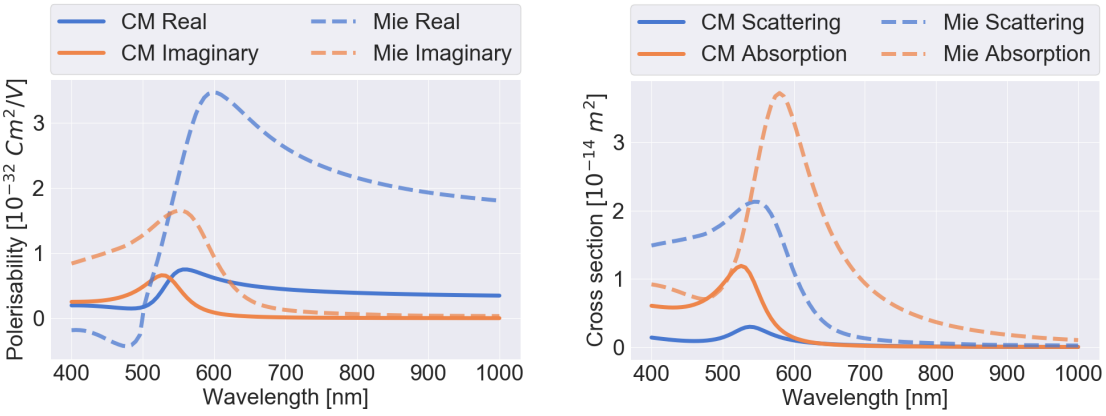

(a) (b)

Fig. 2.2 Comparison of the polarisability and cross-sections for 100 *nm* Au nanoparticles using Clausius–Mossotti (CM) relation, and Mie theory. **(a)** The Mie theory polarisability values are higher as it takes into account the enhanced light-matter interactions due to plasmonics. The peak values for both the real and imaginary components are red-shifted from the Mie-theory obtained values relative to the CM relation values. The real part of the polarisability dominates for wavelengths longer than 600 *nm*. For this wavelength region, the gradient force is expected to be higher than the scattering force. **(b)** Scattering-, and absorption-cross-section also vary between the different methods. For wavelengths shorter than 600 *nm*, the absorption cross-section is higher than the scattering. CM relation underestimates the cross sections for 100 *nm*-sized particles as it does not take into account the plasmon-enhanced behaviour [33].

As Au nanoparticles are plasmonic, they exhibit enhanced scattering and absorption [13]. Additionally, the relative contribution of scattering and absorption differs with size, which manifests as a shift in the peak wavelength value of the extinction cross-section [33]. This intensification of light-matter interaction is not taken into account by the CM relation. The relative refractive index between the nanoparticle and water remains constant in the CM relation, and is only scaled by the radius of the particle. To verify this limitation, Equations 1.3 and 1.2 were used to compare the scattering and absorption cross-sections quantified by the CM relation, against Mie theory values (obtained from NanoComposix website [36], and varied against Dienerowitz *et al.* work [13], Figure 2.2b). As a result of the plasmon enhancement, both scattering and absorption cross-sections are much high in magnitude relative to calculated values by the CM relation. Furthermore, the peak values do not coincide and are red-shifted in the Mie theory results. Scattering processes are also much more

favoured.

Equations 1.2 and 1.3 were used to back-calculate the polarisability from Mie-theory cross-sections. However, the sign is lost in the real part of the polarisability because of the modulus. This manifests as an inflexion point where the curve should be smooth. This was corrected by computing the gradient of the curve, and flipping the values around the point of zero-gradient (at the inflexion point). The resulting polarisability values are consequently greater in magnitude and a better representation of reality. The negative polarisability region is not present in Clausius–Mossotti values for the real part (Figure 2.2a). This is not an artefact of the back-calculation and represents the anti-parallel alignment of the nanoparticle with respect to the polarisation of the external field.

A trapping wavelength of 850 *nm* was selected because the real part of the polarisability dominates the imaginary component (which has tended to zero, Figure 2.2aa Mie curve). As a result, the magnitude of the gradient force increased, while minimising the effects of the destabilising scattering force.

2.2.2 Gaussian beam electric fields

Single mode fibres only guide the fundamental Gaussian mode within a given wavelength range. Due to this property, the emerging field from the fibre has a Gaussian-like profile with a given beam waist that is defined by the mode-field diameter of the fibre (equivalent to the physical size of fibre core). As the field propagates away from the fibre facet, it inherently undergoes diffraction that increases the Gaussian-like envelope size and induces a change in radius of curvature of the wave-fronts. The field evolution (in cylindrical coordinates, and approximated as a Gaussian) as a function of propagation distance (z) is described by Gaussian propagation theory (Equation 2.1),

$$\begin{aligned} \vec{E}(r,z,w_0,\lambda_0) &= E_0 \frac{w_0}{w(z)} e^{\frac{-r^2}{w^2(z)}} e^{-i\phi} \\ \text{with } \phi &= \underbrace{e^{\left\{-i(kz-tan^{-1}(z/z_R))\right\}}}_{\text{Longitudinal Phase}} \underbrace{e^{\frac{ikr^2}{2R(z)}}}_{\text{Radial Phase}} \end{aligned} \tag{2.1}$$

which has an amplitude term E_0, a Gaussian envelope function that scales with the initial beam radius (w_0), and an oscillatory phase term ϕ [89]. The Rayleigh length (Z_R) is the distance over which the beam can be considered as non-diffractive, and is a key parameter that determines both the beam envelope size ($w(z)$, Equation 2.3), and the extent of wave-front curvature ($w(z)$, Equation 2.4), as a function of propagation distance [90]. The phase advances longitudinally (in z-direction) and radially, with r being the distance from the z-axis (Equation 2.1). The wave-fronts are initially planar and evolve spherically in shape as the beam propagates.

$$
\begin{aligned}
Z_R &= \frac{\pi w_0^2 n_m}{\lambda} && (2.2)\\
w(z) &= w_0\sqrt{1+\left(\frac{z}{Z_R}\right)^2} && (2.3)\\
R(z) &= z\left[1+(Z_R^2/z)^2\right] && (2.4)\\
& && (2.5)
\end{aligned}
$$

The intensity ($I \sim |E|^2$) decreases as the beam propagates because the beam envelope increases, spreading the beam over a larger area. The total intensity distribution of the beam across all space is proportional to the power (P), such that:

$$
\begin{aligned}
P &= \int_0^{2\pi} d\theta \int_0^{\infty} rI(r)dr\\
&= \int_0^{2\pi} d\theta \int_0^{\infty} r\frac{\epsilon_0 n_m c}{2}|E|^2 dr\\
&= 2\pi E_0^2 \frac{\epsilon_0 n_m c}{2}\int_0^{\infty} r\frac{w_0^2}{w(z)^2}e^{\frac{-2r^2}{w^2(z)}}dr\\
&= \frac{1}{4}\pi\epsilon_0 n_m c E_0^2 w_0^2 && (2.6)
\end{aligned}
$$

where $I(r))$ is the radial intensity profile. Equation 2.6 relates the beam power to the electric field amplitude E_0^2. Hence, the beam propagation for any given wavelength, with an initial beam waist (or beam waist at the focus), and power were modelled using Equation 2.7.

$$\vec{E}(r, z, w_0, \lambda, P) = \sqrt{\frac{4P}{\pi\epsilon_0 n_m c w_0^2}} \quad \frac{w_0}{w(z)} e^{-\frac{r^2}{w^2(z)}} e^{-i\phi(r,z)} \tag{2.7}$$

The interference of two beams separated by a distance d_s, is simply the superposition of the electric field at each point in space. The interference of two electric fields ($E_1(k)$ and $E_2(-k)$), emerging from two opposing fibres, and emitting 850 nm laser light with a power 100 mW each, was computed using Equation 2.7. The initial beam waist from each fibre was set to 2.65 μm, based on the 780HP polarisation maintaining fibre. As a first step, the contribution of each field was determined independently for the central radial position ($r = 0$) and propagated 4 units of λ/n_m (Figure 2.3). This step was used to ensure the correct interference behaviour of both phase and amplitude for a simplistic model.

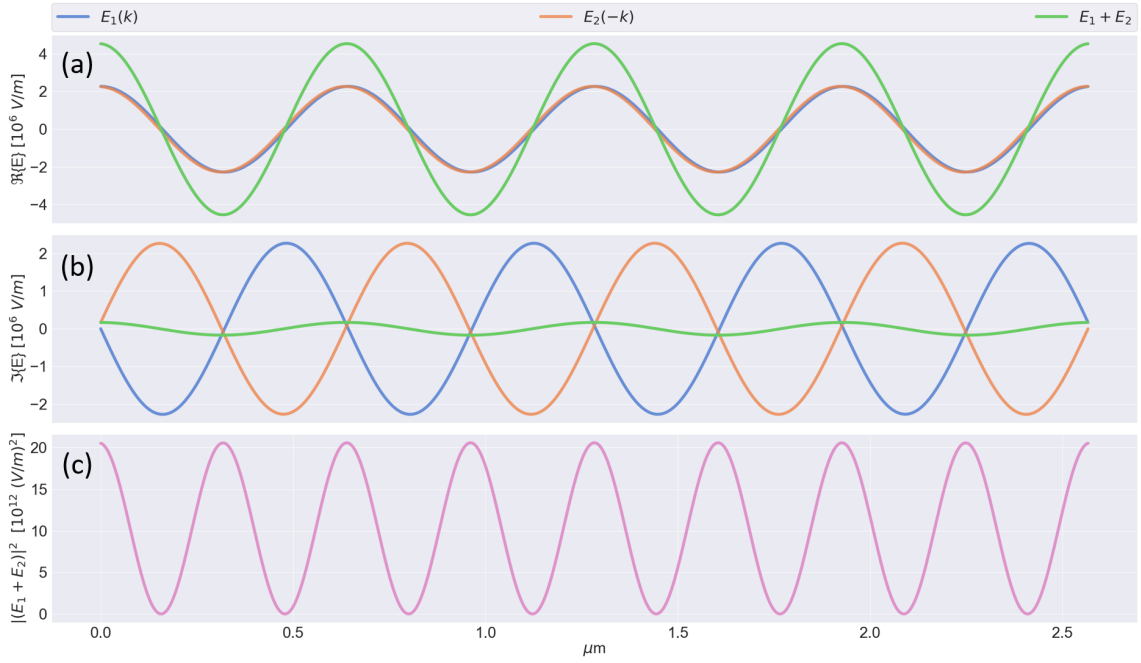

Fig. 2.3 A snapshot of a Gaussian-shaped electric field propagating along the central axis ($r = 0$). **(a)** Real component of two electric fields propagating in opposite directions and their superposition. **(b)** Imaginary part of the two counterpropagating electric fields. The phase delay occurs due to the Gouy phase. **(c)** The absolute-squared of the superposition of the two electric fields (equivalent to the intensity). The fringes are separated by $\sim$ 320 nm, and the maximum intensity variation occurs over half the cycle ($\sim$ 160 nm).

The amplitude varies as a cosine (periodicity of 641 nm (850 nm /n_m), Figure 2.3a). The phase of the imaginary part for each field does not complete a full cycle (Figure 2.3b). This emerges from the second part of the longitudinal phase term (Equation 2.1), known as the Gouy phase. Due to the arc-tan nature of this term, the phase change rapidly accumulates over a few Rayleigh lengths, after which it tends to $\pi/2$. The emerging interference fringes have a separation of 319.54 nm ($\lambda/2n_m$, Figure 2.3c). The minimum-to-maximum intensity variation occurs over 160 nm, yielding strong intensity gradients.

The model was extended to two dimensions by performing the same computation over a multitude of radial position, spanning $\pm w(d_s)$ (Equation 2.3) and increasing the separation distance (d_s) to 70 μm (117 units of λ/n_m), similar to the experimental separation distance. To reduce computational expense, $E_2(-k)$ is calculated by flipping the values determined for $E_1(k)$ along the z-direction (Figure 2.4a,b).

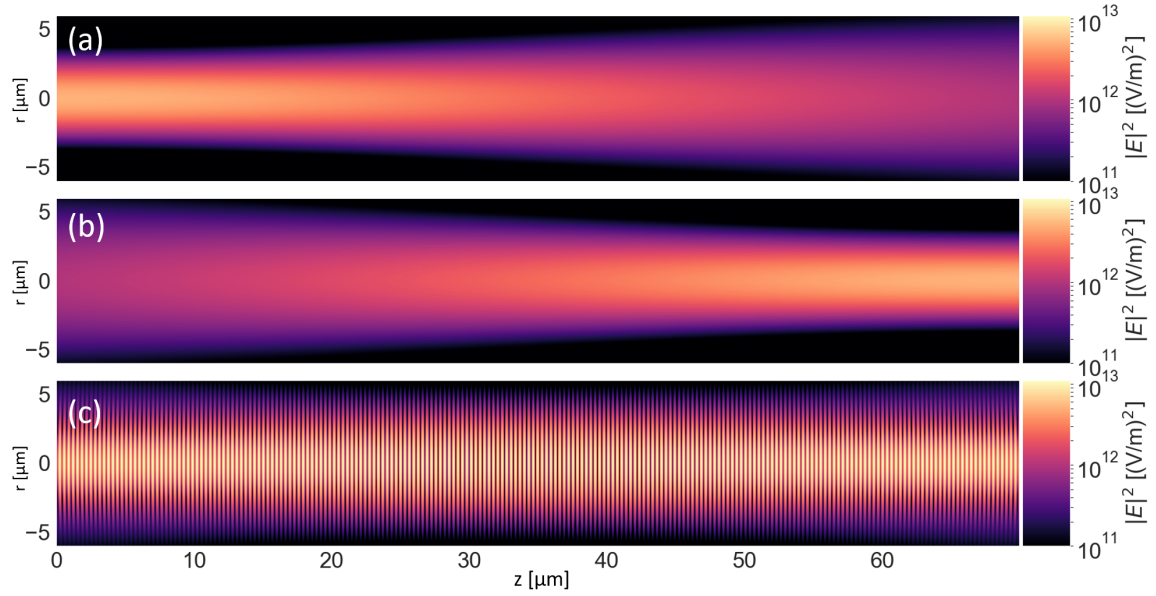

Fig. 2.4 **(a)** Gaussian beam ($w_0 = 2.65\ \mu m$) emerging from left and propagating over a distance of 70 μm, to the right. Propagation is in an aqueous medium ($n_m \sim 1.33$). The $|E|^2$ is calculated for a laser power of 100 mW. **(b)** Gaussian beam traversing in the opposite direction to the top figure, in the same spatial domain. **(c)** Superposition of the beam's counterpropagating electric fields creating an interference pattern. The two opposing beams are perfectly radially aligned. A power of 100 mW is emerging from each fibre. Logarithmic colour scaling used for clarity.

Laser light emerges from the left of Figure 2.4a, with a Gaussian radial profile. The intensity ($I \sim |E|^2$) distribution decreases as the beam propagates in the z-direction, but the total power of the beam remains constant (conservation of energy). The interference of the counter-propagating beams yields finely spaced fringes (Figure 2.4c). As a result, a periodic array of strong intensity gradients are created. Numerical differentiation was used to quantify the intensity gradients in both the r- and z-directions (Figure 2.5).

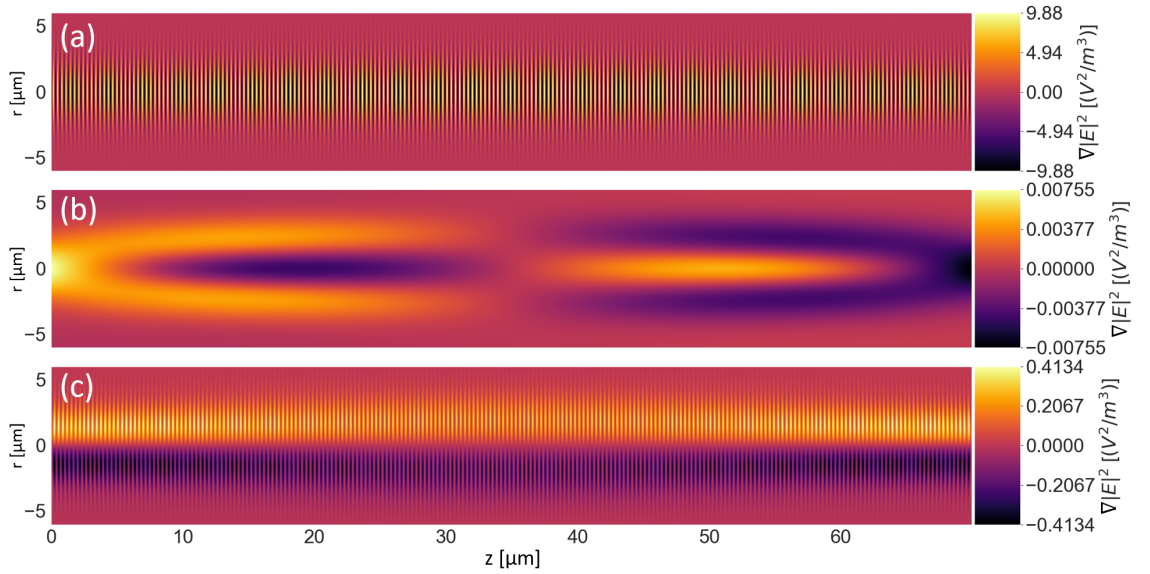

Fig. 2.5 All colour bars scales as 10^{19} (V^2/m^3). **(a)** Gradient force in the z-direction when the two beams are interfering. The central radial region has the highest intensity gradients, stemming from the Gaussian profile. **(b)** The gradient in intensity in the z-direction if the opposing beams are cross-polarised and there is no interference. The values are approximately four orders of magnitude smaller in this configuration compared to when interference is present. **(c)** The r-direction gradient in intensity when the counterpropagating beams are interfering. The gradients are stronger near the entrance of the beams (at 0 μm and 70 μm). The gradient force is much stronger in the axial direction (z) than the lateral.

The high spatial frequency fringes yield $\pm 10^{20}$ $V^2 m^{-3}$ intensity gradients (in the z-direction, Figure 2.5a) which are an order of magnitude greater than that used by Brzobohatỳ *et al.*, and Hansen *et al.* who successfully trapped nanoparticles of various sizes (18-254 nm) using a single beam trap [3, 4]. This is a direct consequence of that fact the intensity change from minimum to maximum is over 160 nm. Due to the Gaussian beam profile, the maximum gradient is at the central radial position. When the two beams do not interfere (cross-polarised, Figure 2.5b), the gradients in intensity are 3000 times smaller in comparison. In this case, the gradients are from

beam spreading due to diffraction ($1/w(z)$ scaling in Equation 2.1). There is a small radial intensity gradient, stemming from the Gaussian beam profile (Figure 2.5c). The radial gradient in intensity is lowest at the halfway point between the fibres, were the Gaussian beam has spread out more due to its inherent diffraction.

2.2.2.1 Self-interfering Gaussian beam electric fields

The same formalism as described in the previous section was used to determine the interference of an electric-field emerging from a single fibre, propagating a distance d_s, back-reflecting from a micro-mirror, and interfering with itself. The initial and back-reflected beams were modelled by propagating the electric field a distance of $2d_s$, and then splitting resulting electric field into two equal segments of d_s, in the z-direction. The first half represents the field contribution that emerges from the fibre (Figure 2.6a). The latter section was flipped (equivalent to propagation in $-k$-direction) with a 3% reduction in magnitude (as calculated in Section 2.3.3) to replicate the loss of light due to absorption by the gold mirror surface at 850 nm (Figure 2.6b). The total power emitted from the single fibre was set to 200 mW, equivalent to the total power used in the previous configuration.

The back-reflected beam is larger than the initial, which is caused by increased diffraction, consequently lower its intensity. The differences between beam-sizes create regions where interference does not occur (Figure 2.6c). Accordingly, interference only occurs in regions outlined by the smaller sized initial beam. The corresponding intensity gradients were numerical computed in the r- and z-direction (Figure 2.7).

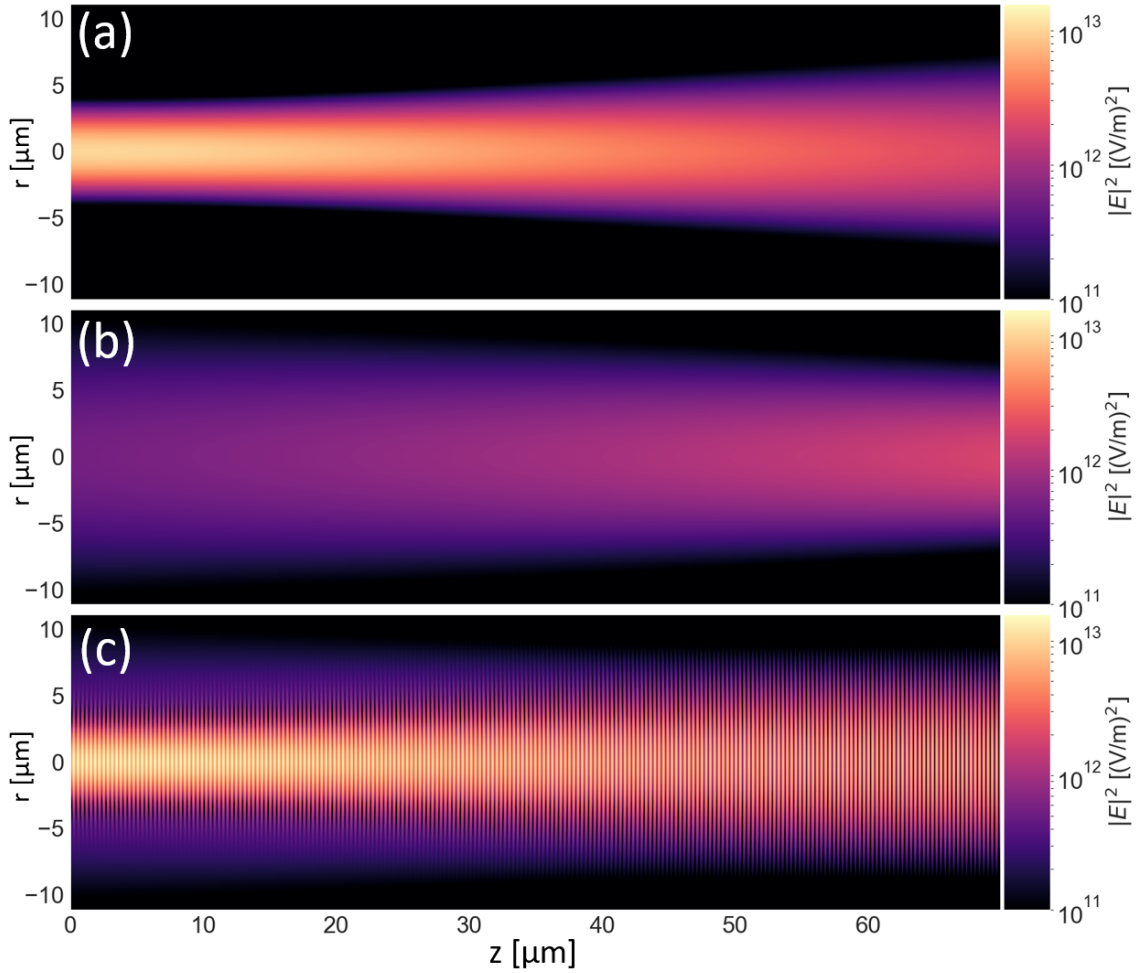

Fig. 2.6 **(a)** Single Gaussian beam ($w0 = 2.65\ \mu m$, P=200 mW) emerging from the left and propagating in a water medium towards a micro-mirror placed at 70 μm. **(b)** Showing just the back-reflected portion of the light. The beam continues to diverge, spreading out more in the radial direction. **(c)** Interference of the forward propagating and back-reflected beams shown in the figures above. There are regions where no interface was observed due to the difference in beam size between the forward and back-reflected components.

Despite the fact the beam intensity is more spread out, the generated gradients are still in the order of $\pm 10^{20}\ V^2 m^{-3}$. The maximum gradient is only about 5% less than the two-opposing fibre geometry (Figure 2.7a). The radial gradient is most substantial near the fibre facet and diminishes in magnitude with increasing z-position (Figure 2.7b).

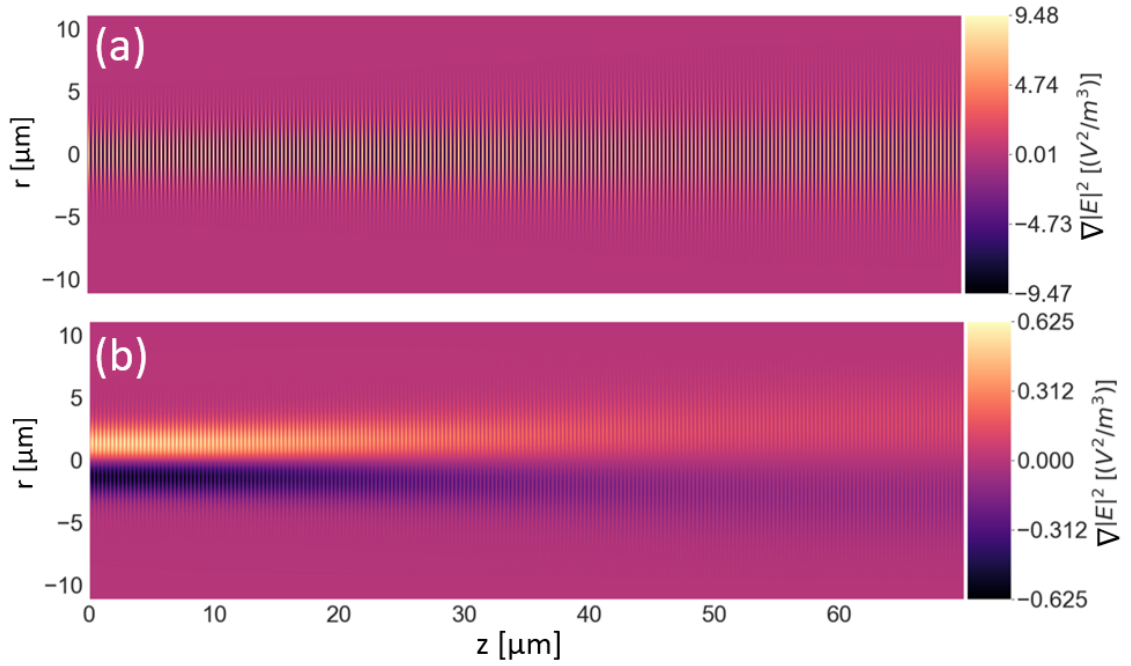

Fig. 2.7 **(a)** Gradient in intensity in the z-direction. The central radial region has the highest values. Despite some regions of the beam not interfering (Figure 2.6a), the magnitude of the gradient in this direction is ca. 5% smaller compared to the opposing fibre geometry. **(b)** Intensity gradient in the radial direction, with strongest region being near the entrance of the light. As the beam spreads out due to diffraction, the radial gradient in intensity reduces.

With the intensities and their corresponding gradients known in both geometries, the optical gradient and scattering forces were calculated.

2.2.3 Optical gradient and scattering forces

The polarisability for 100 nm Au-nanoparticles at 850 nm, and their complementary cross-sections were determined in Section 2.2.1, using data from Mie theory. From these values, the gradient force and the scattering force, was enumerated using Equations 1.5 and 1.6. For the scattering force, the time-averaged Poynting vector ($\langle S \rangle_t = \langle I_1(z) + I_2(-z) \rangle$) was determined individually for each component of the beam, and then summed together. Both forces were evaluated by assuming that there exists a nanoparticle at each enumerated location of the electric field, and that they are non-interacting.

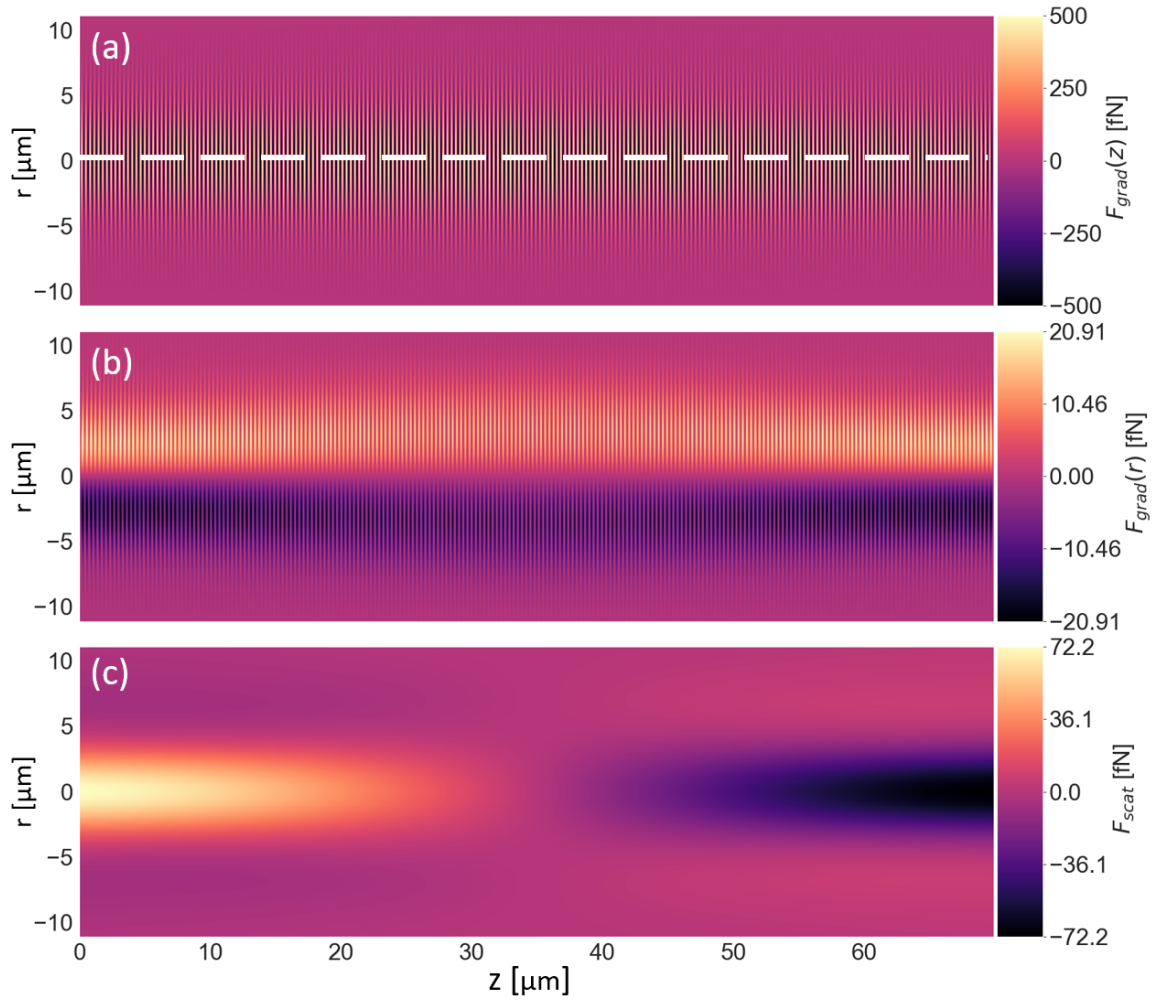

Fig. 2.8 Gradient and scattering force on 100 *nm* Au nanoparticles. **(a)** Gradient force in the z-direction varies between ± 500 *fN*. The dashed white line indicates the region where numerical integration was conducted to evaluate a corresponding trapping potential (Figure 2.11). **(b)** Radial gradient force is about 25-times lower than the axial direction. **(c)** The scattering force due to the two opposing beams. At the middle distance between the fibres, they are equal in magnitude and cancel out. The closer the nanoparticles are to the light source, the stronger the scattering force they feel. The maximal scattering force is approximately $1/5^{th}$ of the maximum axial gradient force.

The gradient and scattering forces for the two-opposing fibre geometry was calculated (Figure 2.8). The axial gradient force ($F_{grad}(z)$) varies $\pm$ 500 *fN* (for a total power of 200 *mW*), being strongest at the central radial position (Figure 2.8a). The radial gradient force ($F_{grad}(r)$) is much weaker (± 20 *fN*) since the intensity varies over several microns (Figure 2.8b). The scattering force is maximal near the facet of both

fibres, where the intensity is the highest. As the beam propagates, the magnitude of the force reduces and competes with the counter-propagating radiation pressure from the opposing fibre (Figure 2.8c). At half the distance between the two fibres, the opposing scattering forces cancel out. The position at which this occurs is determined by the relative intensity between the two fibres.

2.2.3.1 Effects of fibre radial-misalignment

In reality, the fibres are not likely to be perfectly radially aligned. Hence, a radial misalignment was simulated to discern how it would affect the magnitude of the gradient and scattering forces. A misalignment of 3 μm between the central axis of the fibres were introduced. The corresponding interference was determined, from which the gradient and scattering forces were enumerated (Figure 2.9).

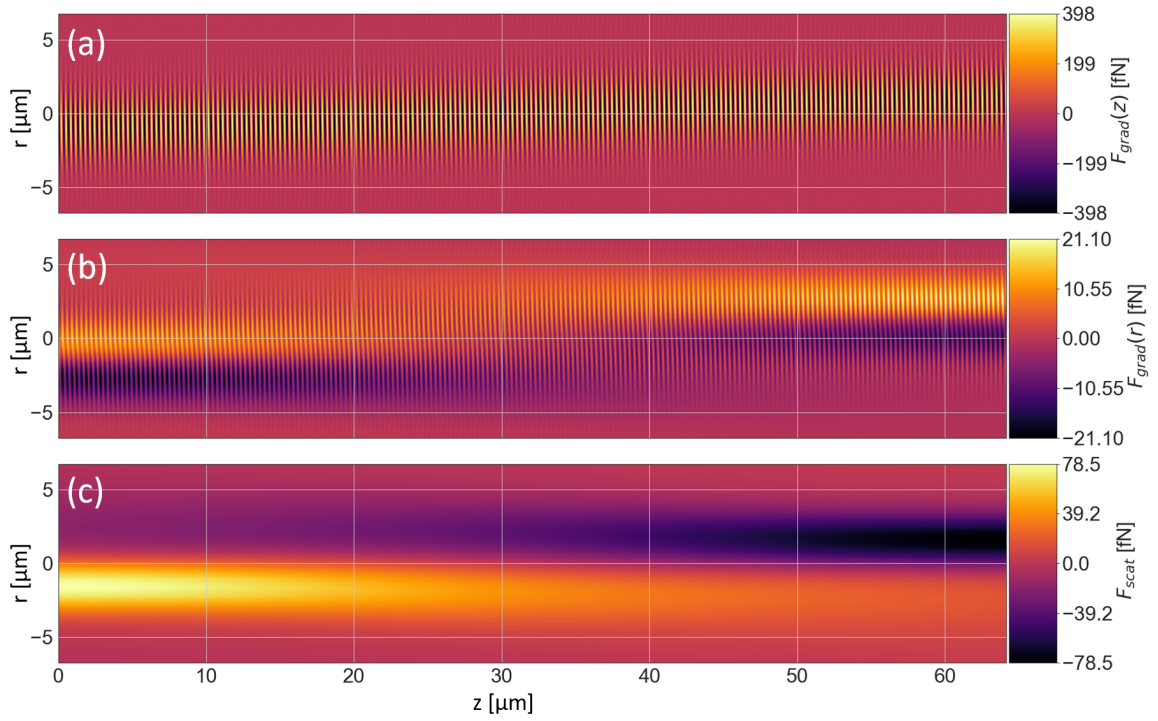

Fig. 2.9 Simulated optical forces with the opposing fibres radially misaligned by 3 μm. **(a)** The axial gradient force is reduced by ~ 100 fN, and the fringes are now tilted due to the regions of the beam interacting with a higher radius of curvature than previously. **(b)** The maximal values are slightly decreased in the presence of the misaligned fibres. **(c)** The maximal scattering force increases by ca. 10%, and there are fewer regions were the forces are equal in magnitude and cancel out.

The maximal axial gradient force is approximately reduced by a fifth in the presence of the radial fibre misalignment (Figure 2.9a). The resulting inference fringes are no longer parallel with the vertical axis as parts of the beam that are now interfering have an increased radius of curvature. In the radial direction, the maximal gradient force is remarkably almost the same as when no misalignment (Figure 2.9b). This is because the region that the maximal gradient force occurs (near the fibre facets) receives slight less light from the opposing fibre. The maximal scattering force increases in magnitude, and there are fewer points where they are equal in magnitude than previously (Figure 2.9c).

2.2.3.2 Self-interfering optical forces

The gradient and scattering forces for a self-interacting beam was determined in order to draw comparisons between the two experimental geometries (Figure 2.10). The maximal axial gradient force is at the central radial position and close to the fibre facet. Here, the force fluctuates between 480 *fN*, and is only 20 *fN* smaller than the maximal force generated in the counter-propagating beam geometry (Figure 2.5a). The modulation depth of the axial gradient force (at r=0) reduces with increasing z-position down to 380 *fN* near the mirror surface.

The radial gradient force (Figure 2.10b) is higher than the previous configuration because all the power is emerging from a single fibre rather than being split. The scattering force is predominately in the forward ($+z$-direction) as the majority of the beam energy resides in the non-reflecting component. The force generated is more than double the maximum of the scattering force in the two opposing fibres. This is because the returning radiation pressure has a much lower in magnitude and does not nullify the initial beam to the same extent. There is also a small negative scattering force that originates from the size difference between the initial and reflected beam.

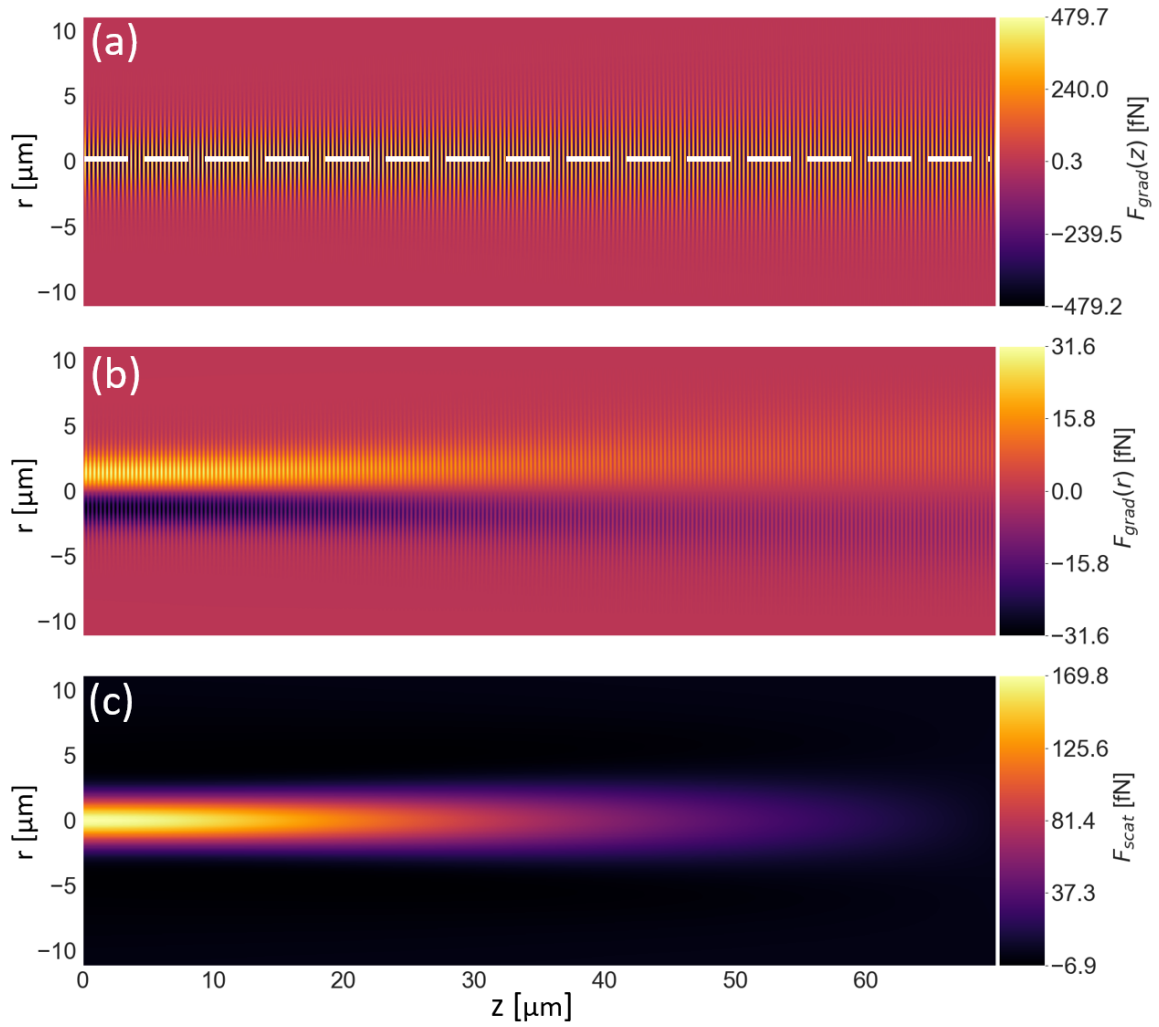

Fig. 2.10 Optical gradient and scattering forces for a retro-reflected Gaussian beam. **(a)** Gradient force along the z-direction. The maximal force is about 20 fN lower for the same total power in the counterpropagating geometry. The dashed white line indicates the region where numerical integration was conducted to evaluate a corresponding trapping potential (Figure 2.14). **(b)** The radial gradient force decreases as the beam propagates due to diffraction. It has higher in this geometry since all the light is emerging from one fibre, rather than being split between two fibres. **(c)** The maximal scattering force is also much higher in magnitude for the same reason. At around 10 μm from the mirror surface, the scattering force begins to diminish and is annual by the back-reflected light.

2.2.4 Optical trapping potentials

For stable nanoparticle trapping along the desired dimensions, the gradient force has to be greater than both the scattering and Brownian motion. The axial gradient force

is maximal along the central radial position, hence is the region where nanoparticles have the highest likelihood of being trapped (along z-direction). The potential for the gradient and scattering force was considered for this region to discern the motion of the nanoparticles along the axial direction. It is important to note that the gradient force is conservative, while the scattering force is not. Hence, the potential arising from the scattering force, is a pseudo-potential.

The potential energy corresponding to the axial gradient and scattering force relative to the thermal energy of the system was evaluated numerical using the cumulative trapezoidal integration method. The thermal energy of the system was defined as k_BT, with k_B being Boltzmann constant, and T the temperature of the medium. Conventionally, the thermal energy is evaluated at $20°C$. However, the nanoparticles are likely to have finite absorption that raises the temperature of their water medium by approximately $1°C$ (4.06×10^{-21} J at 294.15 K, P=100 mW), as an approximation since the theoretical cross-section for the trapping wavelength of 850 nm is very small (Figure 2.2b).

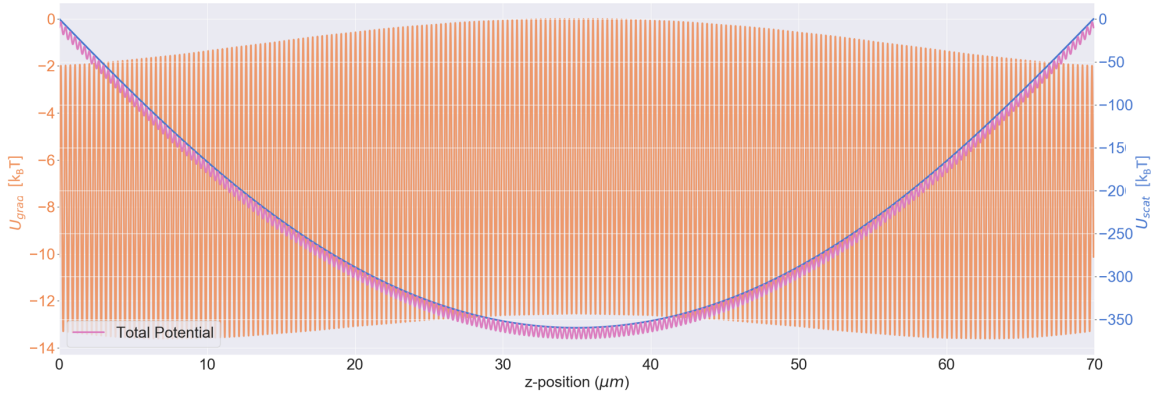

Fig. 2.11 The gradient potential (orange curve, left axis) and the scattering pseudo-potential (blue curve, right axis) for the central radial position, where nanoparticle's have the maximum likelihood of being confined. The gradient potential wells have approximately the same modulation depth (ca. 10 k_BT). The scattering pseudo-potential is much lower. The summation of the potentials give rise to an array of tilted and asymmetric potentials, with the scattering pseudo-potential dominating the landscape (pink-curve).

Due to the symmetry of the two opposing fibre system, the calculated potentials are symmetrical (Figure 2.11). The determined scattering pseudo-potential was greater

than the axial gradient potential. The oscillatory gradient potential varies ± 6 k_BT across the entire z-positions. The scattering pseudo-potential is parabolic in shape, with a minimum at the midpoint between two the fibres. The summation of the gradient potential and scattering pseudo-potential yielded an array of smaller skewed potentials. The scattering pseudo-potential distorts the landscape of the potential wells that confined that nanoparticles. Hence, the trapping potentials were defined as the energy needed for a particle to be 'kicked-out' from one valley, into the next (Figure 2.12). The trapping potential was determined by finding the difference between peak and trough energies (orange and green dots, respectively).

Near the fibres, the gradient potential is the most distorted by the strong asymmetric scattering that is present (Figure 2.12a,c). Consequently, the effective trapping potential is the weakest at these locations. The trapping energies are symmetric around the half separation point, where the trapping is potential was the greatest (Figure 2.12b,d). This is because the scattering potential is flat at the location, meaning that the gradient potential landscape is the least affected.

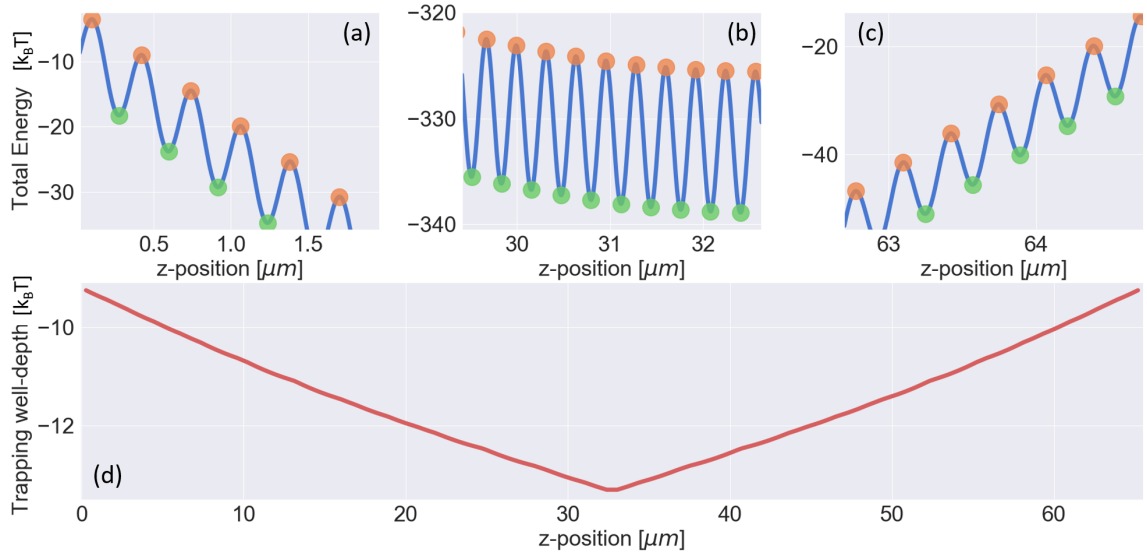

Fig. 2.12 **(a-c)** The tilted potentials at different positions along the z-direction. The asymmetry of the potentials, shifts from the left side to the right side. At the centre, the potentials are quadratic-like and symmetric. **(d)** The effective trapping potential determined numerically by subtracting the peak (orange dots) from the troughs (green dots) in the top . The ensemble potential across the entire region is approximately -11.5 k_BT.

In this geometry, the opposing scattering forces compensate and cancel each other to reduce the overall scattering force. In turn, the gradient potential becomes less slanted by the curve of the scattering pseudo-potential. In the mirror-fibre geometry, there is a substantial imbalance between scattering forces, causing significant distortion of the gradient potential.

2.2.4.1 Self-interfering trapping potentials

The reflected intensity in the mirror-fibre arrangement is lower in magnitude than the initial beam, which gives rise to an overall asymmetric intensity distribution. As a result, the scattering pseudo-potential and gradient potential were also inherently asymmetric (Figure 2.13).

The modulation depth of the axial gradient potential is constant, varying between ± 4.5 k_BT. This is 1.5 k_BT lower than the previous symmetric geometry. The scattering potential dominates the gradient potential, being much higher in magnitude. Thus the overall, energy is strongly determined by the landscape of the scattering potential (Figure 2.13).

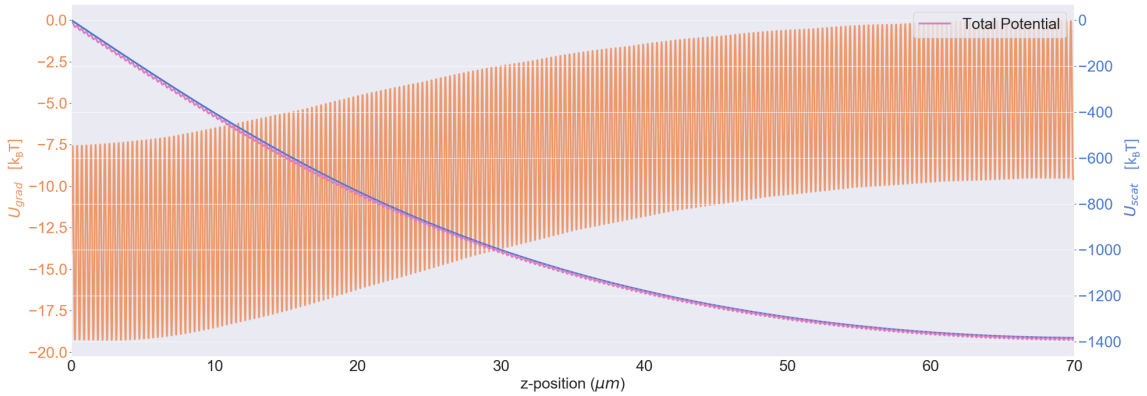

Fig. 2.13 The gradient potential (orange curve), and the scattering pseudo-potential for the mirror geometry, both of which are asymmetric. The gradient potential has a constant modulation depth ($\sim 10\ k_BT$). The scattering pseudo-potential dominates the total effective potential (pink curve)

The region closest to the fibre surface is most skewed, leading to shallower potentials consisting of a few k_BT (Figure 2.14a). The total potential remain slanted at the midway point between the mirror and fibre, but the well-depths are less shallow. At

distances a few-microns away from the mirror surface, the potential begins to plateau, increasing the peak-to-trough energy difference Figure 2.14b,c).

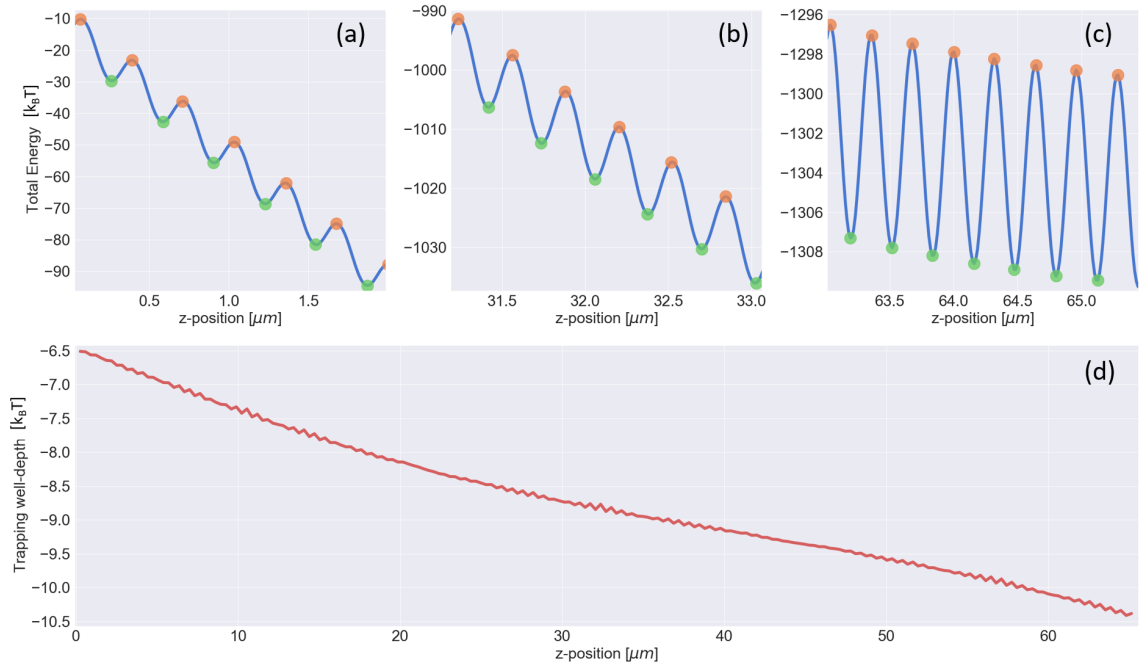

Fig. 2.14 **(a-c)** Zoomed-in regions of the total potential (pink curve in Figure 2.13. The potential is higher for a nanoparticle to move to the left than the right (positive z-direction). This asymmetry reduces the closer the nanoparticle is to the mirrored surface (at 70 μm). **(d)** Effective trapping potential of the nanoparticle across the entire fibre separation distance. Nanoparticles near the mirror have a higher tendency to be confined. Ripples in the red curve come from computation error in detecting peaks and troughs in the top figures.

The nanoparticle trapping well depth increases from - 6.5 k_BT near the fibre facet, to -10.5 k_BT near the mirror surface, where scattering effects are less dominant. Even though the scattering processes on the nanoparticle are much more significant in the mirror-fibre geometry, the trapping energies are enough to confine the nanoparticles.

The evaluated trapping potentials for both geometries concluded that 100 nm Au-nanoparticle could be trapped using a total power of 100 mW with a separation distance of 70 μm. Reducing the distance would result in even deeper trapping potential wells.

2.3 Materials and experimental methods

2.3.1 Interferometric optical setup

The trapping laser light was generated by a Titanium Sapphire (TiSa) laser system (MSquared SolsTiS). Laser light in the 72 - 945 *nm* range was generated by the Titanium doped Sapphire crystal pumped by an 18 W, 532 *nm* laser (Lighthouse Photonics Sprout). The emitted beam had a narrow line-width (ca 50 *kHz*) and thus a long coherence lengths (a few kilometres), making it ideal for interference experiments. The TiSa had a closed-loop feedback via a wave-meter that could lock and tune the cavity onto a single wavelength with four-decimal accuracy. Hence, any desired wavelength within its emission range was maintained for long periods at a single wavelength. A Faraday isolator was used to ensure that back-reflected laser light was not back-coupled into the cavity, which would be detrimental to the laser's stability. With the pump laser set to 18 W, the TiSa produced approximately 3.5 W at 850 *nm*. A half-waveplate and a polarising beam splitter (PBS) was used attenuate the power as a function of the half-waveplate's angle.

The laser was then split into a diagnostic- and measurement-paths via a beam splitter (Figure 2.15). In the diagnostic path, the beam power, mode shape, and the position was monitored using the beam transmission through an aperture, and on to a power meter. The pump laser had a tendency to change pointing direction caused by thermal instabilities, which consequently affected the mode and emitted power of the near-infrared beam. Hence, any power drop measured through the aperture throughout an experiment meant that the measurement path had to be re-referenced ($>\pm 5\%$). This was achieved by tweaking the pump laser's steering mirrors into the TiSa cavity until the same power was measured through the diagnostic aperture.

A second beam splitter was used to divide the beam into two the arms used to create an interferometric trap (Figure 2.15). Each arm was coupled into polarisation maintaining fibres (PMF (PM-780HP)) via a plano-convex lens and two dielectric steering mirrors. The fibres were stably held in place at the in coupling end by angled physical contact connectors (Thorlabs). Light was coupled onto the slow-axis of the PMF fibre, matching the laser polarisation. Coupling efficiencies of 55-60% were achieved for each arm. The power emitted at the distal end of each arm was balanced by adjusting the in-coupling mirrors. The outlet of the PM fibre was stripped bare

from its plastic jacket and polymer coating, and cleaved using a fibre cleaver. The bare fibres were held securely into a fibre rotators which allowed selectivity in the polarisation of the emitted light. The fibres were rotated until maximum transmission was achieved through a horizontal polarisation analyser. This orientation resulted in an increased dipole emission scattering pattern from the nanoparticle, onto the detector, which was positioned orthogonally (out of the page in Figure 2.15).

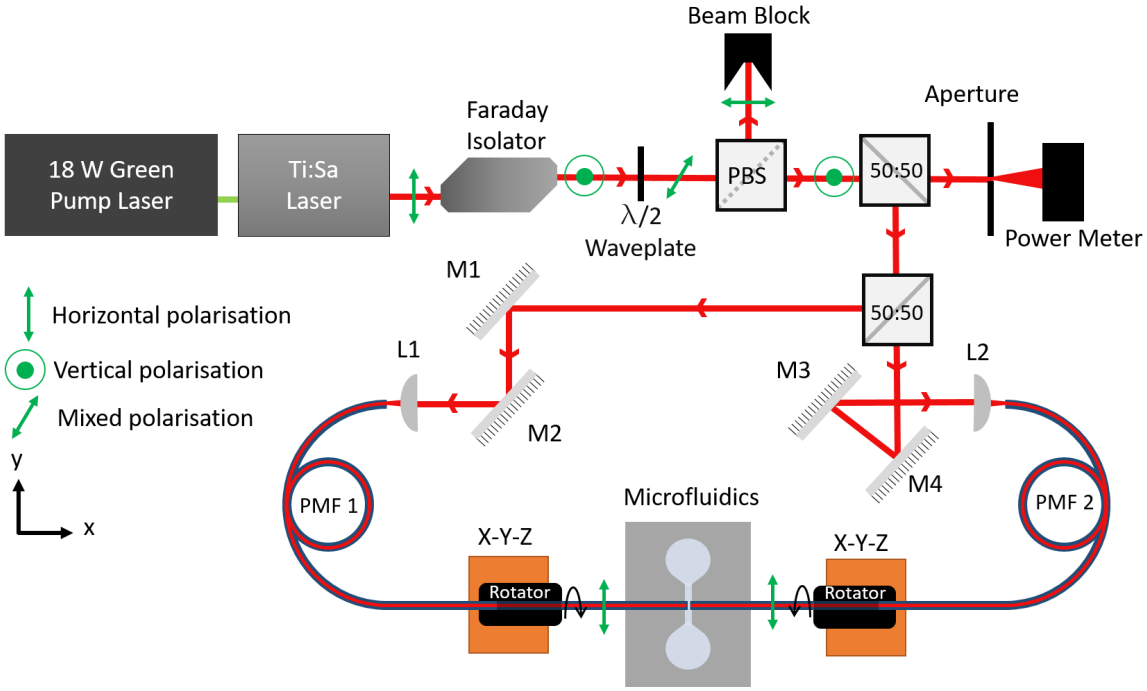

Fig. 2.15 Top-down view of the optical diagram used for creating interferometric trapping of nanoparticles. Laser light from a TiSa (850 nm) was coupled with equal transmission into two polarisation maintaining fibres (PMF), which were embedded into a microfluidic block. Fibre rotators were used to align the output polarisation between the fibres to the same axis (horizontal to maximise dipole emission into the camera).

Three-axis translational stages were used in conjunction with the fibre rotators to position the PM fibres into the microfluidic chip. The chip was used to hold and align the fibres, and contained the sample solution. A glass slide was used to hold the microfluidic device on a flat surface (van der Waals non-permanent adhesion). With the fibres positioned into place and the sample solution pipetted on the chip, a coverslip was then placed on top to provide flat imaging plane and restrict the evaporation of the solution (Figure 2.16).

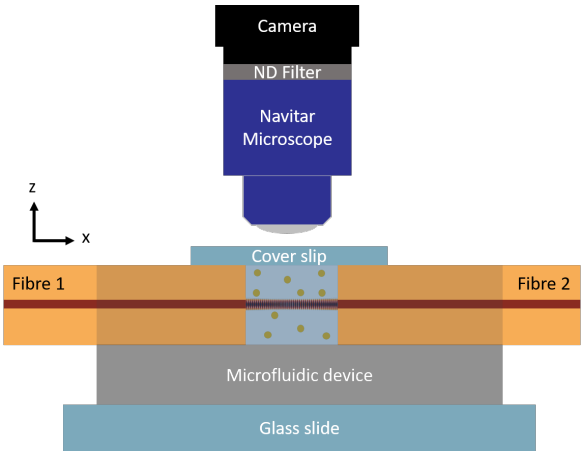

Fig. 2.16 Side view of the microfluidics device and the fibres embedded into it. Imaging optics are independent of the trapping optics. A solution of Au nanoparticles was pipetted into the microfluidics chamber and then a coverslip was placed on top to prove a flat imaging surface to image the motion of the nanoparticles in the interferometric trap. The Navitar microscope had an effective magnification of 100x, and absorbing neutral density filters were used to ensure the camera was not saturated by the scattered light from the nanoparticles.

The light interaction with the nanoparticles was imaged using a Navitar upright microscope. A long working distance objective (Mitutoyo 20x, 0.42 NA) was used to collect the scattered light from the nanoparticles. The Navitar microscope also had a zoom lens which provided an additional 5x magnification, yielding an effective magnification of 100x for the whole system.

A CMOS 8-bit resolution monochrome camera with a quantum efficiency of 40% at 850 nm, was used to capture the scattered light from the nanoparticle. A neutral density filter (absorbing ND 4) was used to attenuate the milli-Watt nanoparticle scattering down to a few micro-Watt, reducing it into the unsaturated range of the camera. The gamma correction factor was set to 1 to ensure linear pixel intensity response. The dynamic range of the pixels was maximised by manually setting the black count level as low as possible without cutting the noise floor. The camera acquired each frame row-by-row, hence reducing the number of pixel rows from the full 1280, to just under 300, facilitated higher frame rates (>frames per second).

The light interaction with the nanoparticles was imaged using a Navitar upright microscope. A long working distance objective (Mitutoyo 20x, 0.42 NA) was used to collect the scattered light from the nanoparticles. The Navitar microscope also

had a zoom lens which provided an additional 5x magnification, yielding an effective magnification of 100x for the whole system.

A CMOS 8-bit resolution monochrome camera with a quantum efficiency of 40% at 850 nm, was used to capture the scattered light from the nanoparticle. A neutral density filter (absorbing ND 4) was used to attenuate the milli-Watt nanoparticle scattering down to a few micro-Watt, reducing it into the unsaturated range of the camera. The gamma correction factor was set to 1 to ensure linear pixel intensity response. The dynamic range of the pixels was maximised by manually setting the black count level as low as possible without cutting the noise floor. The camera acquired each frame row-by-row, hence reducing the number of pixel rows from the full 1280, to just under 300, facilitated higher frame rates (>frames per second).

2.3.2 Microfluidic devices

A key element in achieving interference was the relative alignment of the fibres, which have 5 μm sized cores, and consequently required micron level positioning. The better the alignment of the fibres, the stronger the trapping potentials, as demonstrated in Section 2.2.3.1. Furthermore, the fibres needed to interface with the sample solution in a controlled manner. Inspiration was taken from Gouk *et al.*'s and Kolb *et al.*'s experimental geometry as it incorporated optical fibres with a fluidic chamber [41, 91]. The microfluidic chip allowed easy integration of optics and fluidic with any conventional microscope as it provided a stable platform for imaging.

Polydimethylsiloxane (PDMS) is often used for microfluidics due to its ease of reproducible fabrication. PDMS starts in liquid form, meaning that it can take the shape of a mould, and hardens to a flexible, non-brittle gel that is easy to handle and cut. The fibre diameters have a tolerance of ± 2 μm, hence the flexibility of PDMS means that it can morph around the fibre to hold them securely in place. This meant that an exact fit of the channel sizes for holding the fibre was not needed. PDMS is inherently hydrophobic and therefore interacts very little with water-soluble samples.

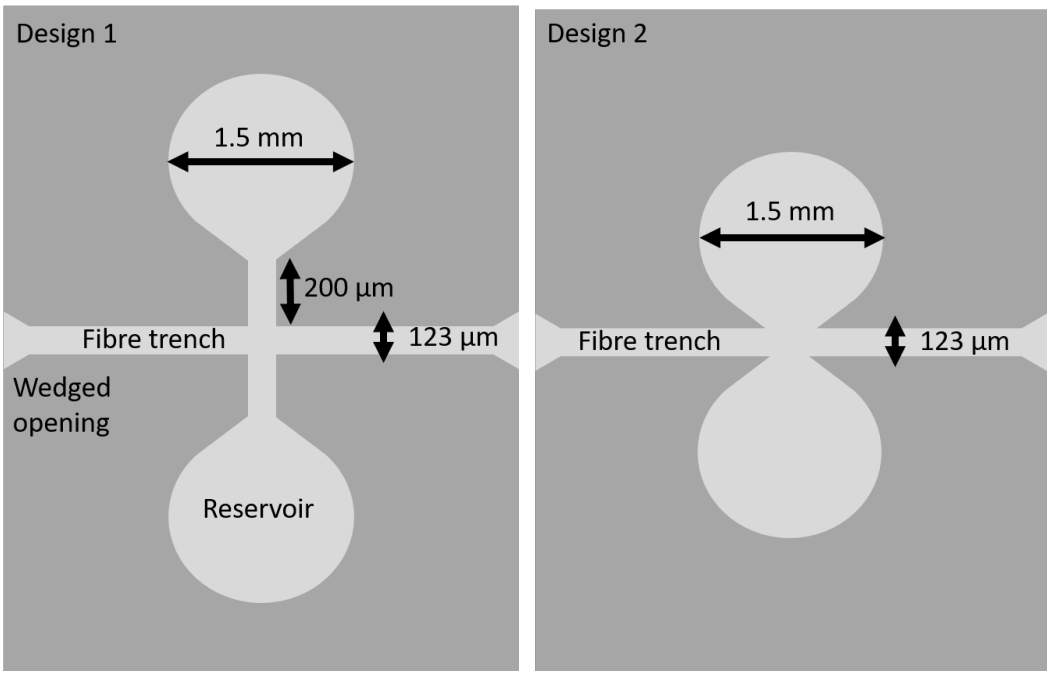

(a) (b)

Fig. 2.17 Microfluidic design for integrating optics and fluidic. Both designs aid fibre alignment and have no inlets or outlets as the trapping of nanoparticles are studied under zero net flow. **(a)** More PDMS material between the fluidic channels and the fibre grove allowed for a stable aligned of the fibres but suffered from wetting issues. **(b)** Wettable surface, but fibres were more misaligned about their central axis. This configuration was more suited for the mirror-fibre interferometric trap as alignment was less critical.

Two versions of fibre holding microfluidic devices were made, each with its advantages and disadvantages (Figure 2.17). The devices were made using the protocol outline in Appendix 5. Both designs have fluidic reservoirs and fibre holding trenches. Each reservoir was designed to contain 0.5 μl of the sample solution. Inlet and outlet ports were not needed as flow control was not required, and particle trapping was only studied under Brownian motion (zero net flow). The fibre aligning grooves were made to be 123 μm (2 μm smaller than the nominal fibre diameters) to ensure a tight fit (water-sealed). Wedged openings were positioned at the entrance of each fibre holding trench to make the initial fibre alignment, which is done by eye, more comfortable.

The first geometry (Figure 2.17a) had more supporting material around the fibres and thus offered better fibre alignment. The extra supporting material meant that the reservoirs had a to be positioned away from the fibre grooves and connected by

an additional 200 μm channel. The channel did not consistently fill with fluid, due to its narrow size and the hydrophobic property of PDMS. For the latter geometry (Figure 2.17b, the reservoirs are directly connected to the fibre holder grooves, and thus provided less supporting PDMS for fibre-alignment. The wider connecting area of the reservoirs to the fibre holding channels resulted in reliable wetting of the central region.

2.3.2.1 Embedding fibres in microfluidic channels

Translational stages were used to course align the fibres over the wedged opening of the PDMS by eye. Then the fibres were lowered closer to the surface of the PDMS, and the Navitar microscope was used to further check the alignment of the fibres with respect to the groove. The fibres were pushed into the trenches with a set of tweezers.

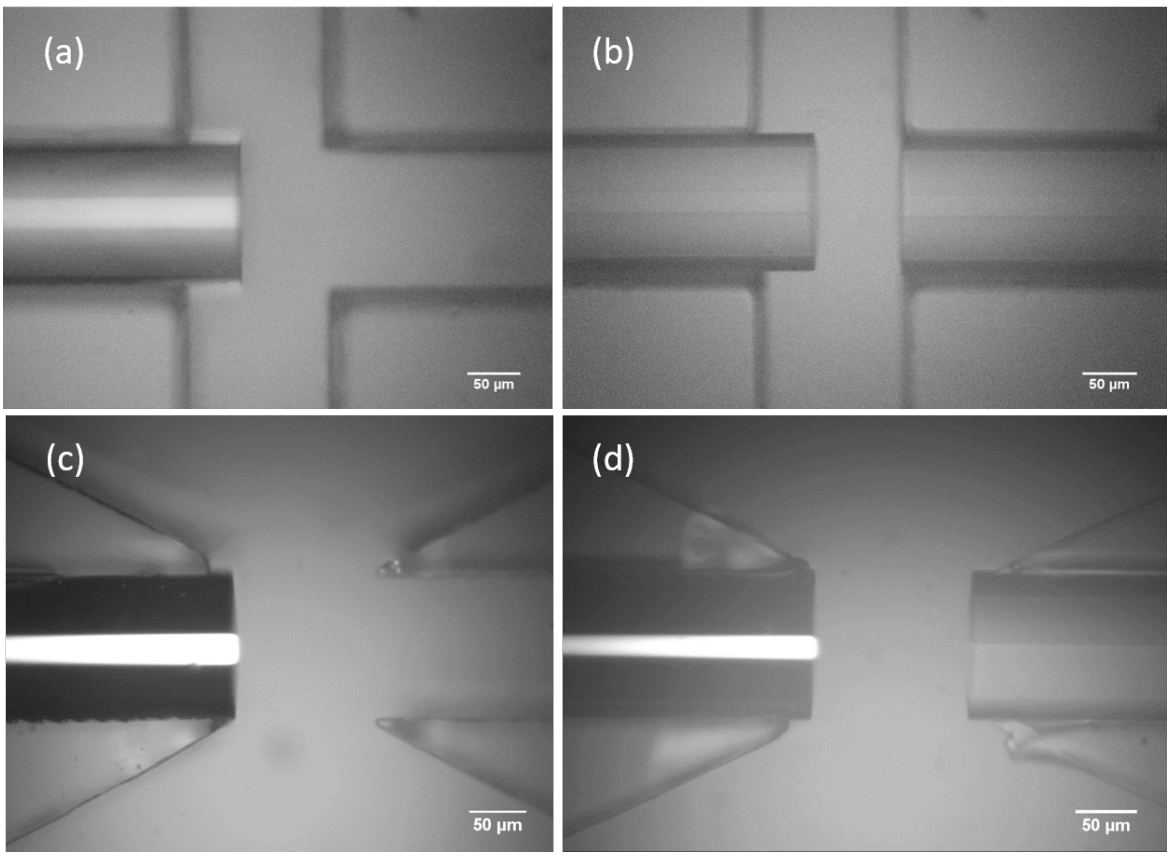

Fig. 2.18 **(a)** PMF fibre embedded into design 1 of Figure 2.17a. **(b)** Opposing fibre aligned using the translation stages and fibre rotator to overcome the friction between the fibre and the PDMS walls. **(c)** Au coated fibres inserted into the PDMS fibre trench of design 2 (Figure 2.17b). **(d)** The light delivering fibre aligned into the groove. The large surface area of the Au mirror meant that alignment was less critical.

Once the fibres were in place, the friction between the fibre and the PDMS wall restricted the fibres from moving back and forth within the fibre grooves. This is ordinary beneficial as it holds the fibre firmly in place. This friction was overcome by using the fibre rotators to release the stress and thus allow the fibres to be moved forwards and backwards until positioned at the desired location. This occasionally buckled the PDMS but rotating the fibre in the opposite direction released the stress on the PDMS. The fibres were then set back to their initial rotation orientation such that the emitted light would be horizontally polarised.

Each fibre was positioned at a time (Figure 2.18). The correct position was determined when the top edge of both fibres are brought into focus (within the ca. 4 μm depth of the focus).

The same fibre insertion procedure was used for both microfluidic designs, including the mirrored fibres (Figure 2.18). Once aligned within the PDMS, the sample solution was pipetted into fluidic chambers and a coverslip placed on top, which spread out the fluid into the microchannels.

2.3.3 Creating and characterising micro-mirrors

Microfluidics integrated with fibre optics provides an essential platform to trap nanoparticle. However, the alignment of the fibres such that the beam interfere is not possible once the fibres are embedded. The use of a mirror much larger than the fibre core meant that alignment was far less critical.

Currently, mirrors for microfluidic use are not easily sourced. The smallest commercial mirrors are bigger than 5 mm^2, which are far to large to incorporate with microfluidics. Hence a custom-made mirror was created by a thin film coating of Au on the fibre tips. Mirrored surface require surface flatness for specular reflection. When a fibre was cleaved, a crack in the silica propagated along the fibre facet, separating it into two parts. This created a flat surface suitable for thin film deposition to create a mirrored surface.

Microfluidics integrated with fibre optics provides an easy to use platform for nanoparticle trapping. However, the alignment of two opposing fibres can be cumbersome. The use of a larger micro-mirror than the fibre core size meant that alignment

was far less critical. Currently, mirrors for microfluidic use are not easily sourced. The smallest commercial mirrors are bigger than 5 mm^2, which are far too large to incorporate with microfluidics. Hence, a custom-made mirror was created by thin-film coating on the fibre facet. Mirrored surfaces require surface flatness for specular reflection. When optical fibres are cleaved, a crack in the silica propagated along the fibre facet, separating it into two parts. This created a flat surface suitable for thin film deposition.

Au is highly reflective in the near-infrared and is a metal that does not oxidise in the presence of air and water. Fresnel equation for reflectance (R_{Au}) used to determine reflectivity of a Au thin-film deposited on fibre facet (Equation 2.8) [92].

$$R_{Au} = \left| \frac{n_m - n_{Au}}{n_m + n_{Au}} \right|^2 \tag{2.8}$$

The reflectivity depends on the index of refraction between the water medium and Au film. The incident angle was approximated to be normal to the Au-film's surface. For conservation of energy, the sum of reflected and transmitted contributions must be equal to 1 ($T_{Au} = 1 - R_{Au}$). The transmitted wave either passes through the thin Au layer or gets absorbed. This ratio depends on the film thickness. The penetration depth relation (δ_p) determines the characteristic thickness whereby the amplitude of any transmitted portion of the intensity is attenuated by 86% ($1 - 1/e^2$ of the initial intensity). The penetration depth is directly proportional to the imaginary part of the Au refractive index ($\Im\{n_{Au}\}$ in Equation 2.9) [92].

$$\delta_p = \frac{\lambda}{4\pi} \Im\{n_{Au}\} \tag{2.9}$$

Reflectance and penetration depth values were evaluated using Equations 2.8 - 2.9 for Au thin-films in the TiSa wavelength range (Figure 2.19).

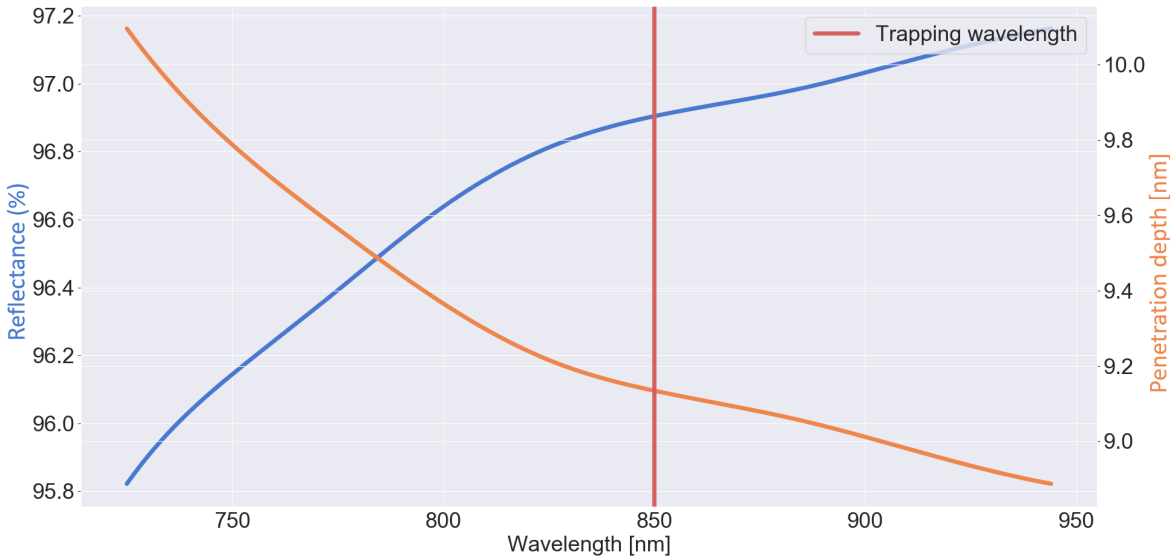

Fig. 2.19 Reflectance and penetration depth (calculated using Equations 2.8 - 2.9) for a water-Au interface in the TiSa wavelength range. At the trapping wavelength the reflectance was 96.9%, and intensity decayed to 86% of I_0 (transmitted 3.1%) after a distance of 9 *nm*. The high reflectance value meant that the large majority of the incident light is back-reflected.

Reflectivity increased with longer wavelengths, while skin depth decreased. At the trapping wavelength of 850 *nm*, 96.9% of incident light was back-reflected. Consequently, 3.1% is transmitted, of which, 86% was absorbed in the first 9 *nm*. Hence, for a beam with a power 100 mW incident perpendicularly to the film surface of thickness 100 *nm*, 3 mW is absorbed and 97 mW is back reflected.

2.3.3.1 Protocol for fabricating mirrored-fibres

A PDMS fibre holder was made to keep fibres upright for deposition. The holder had an array of 125 μm groves to hold fibres securely in place. The polymer coating of the fibres was shaved off using a razor blade, and the deposition end of the fibre cleaved. Each cleave was inspected using a microscope before being inserted into the fibre holder. The holder was sandwiched between two glass slides, which were taped together (Figure 2.20). This clamped the fibres in place and provided a flat base for placement inside the deposition chamber.

A 10 *nm* layer of Cr was first deposited as an adhesion layer to bind the Au (100 *nm*) and the silica fibre facet (Deposition conducted by Dean Kos, Nanophotonics

Centre, Cambridge). After the deposition, the fibres were kept in the PDMS holder encase in a cover to keep away from dust.

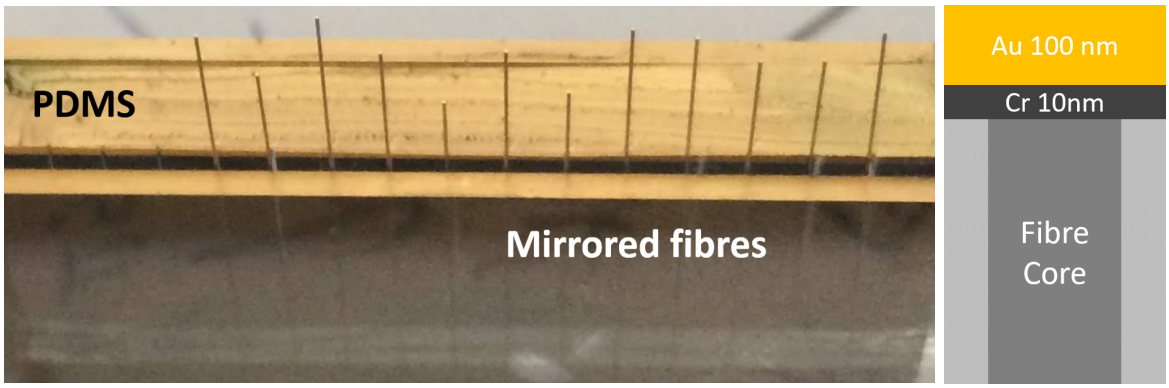

(a) (b)

Fig. 2.20 **(a)** Image of several Au coated fibres in a PDMS holder used for thin-film deposition. The top glass slide was removed, and individual mirrored-fibres were then embedded into the microfluidic chip for interferometric trapping. **(b)** A schematic of the Au mirrored fibres (multi-mode fibre with a large core). The Cr layer acts as an adhesion layer between the silica and the Au. The mirrored fibre and the light-emitting PM fibre were chosen to have the same diameter (125 μm) to ease alignment in the microfluidic chip.

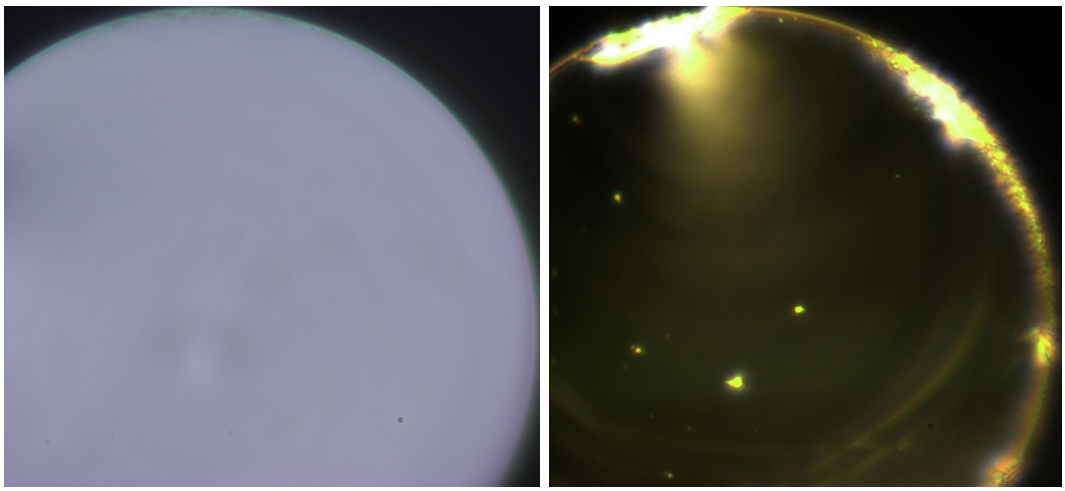

(a) (b)

Fig. 2.21 **(a)** Pre-deposition darkfield image of the multimode fibre with a flat surface and no debris present as there was no scattering observed. **(b)** Post-deposition darkfield image showing a few scattering particles either from dust or the deposition process. The majority of the surface areais without scattering and offers a good reflecting surface. The edges are more scattering, but these regions are not used to back-reflect light.

The mirrored fibres were inspected using a dark field illumination to highlight defects before use. There are scattering sites at the edges with a few speckled regions randomly deposited on the face of the fibre (Figure 2.21b). However, the majority of the Au deposited surface was unable as a micro-mirror to back-reflect the incident light and induced interference.

2.3.4 Quantifying reflectance, interference and phase drift

A Michelson-interferometer was built to verify the presence of interference, determine wavefront flatness, and to quantify the reflectance of the mirrored fibres.

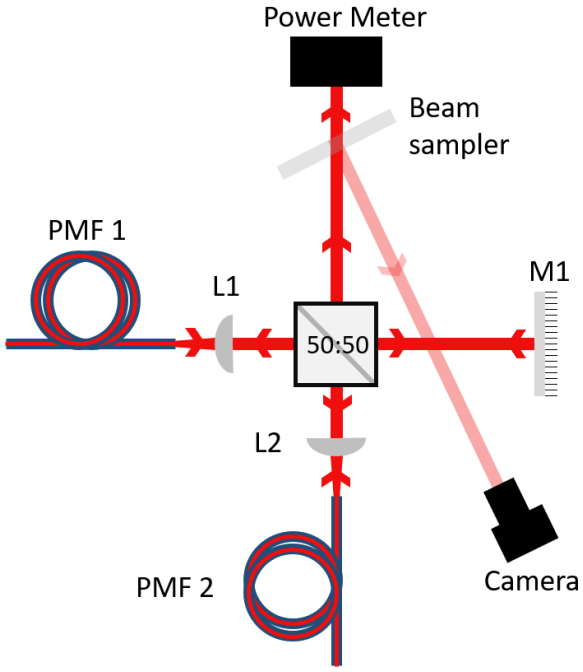

Fig. 2.22 Michelson-interferometer optical setup to discern the wavefronts flatness and their phase stability of the induced interference pattern. The emitted light from the fibres are collimated, and interfered, before being incident on a camera. This configuration was also used to test the reflectance (reusing a power meter) of the Au mirrored fibres by substituting them in for PMF 2.

Light was coupled into the PM fibre as described in section 2.3.1. The light emerging from the fibres were collimated using 10x objective, and the fibres were orientated to output vertically polarised light. This light was then divided by a beam splitter, with half of it being transmitted and the other half orthogonally reflected. The transmitted light was back-reflected by a dielectric mirror, onto the beam splitter, and split again.

The transmitted light emerging from the second fibre was then combined and interfered with the reflected light of the first fibre. A beam sampler was used to attenuate 96% of the emitted light from the fibres, onto a camera's detector, allowing direct observation of the interference pattern.

The same setup in Figure 2.22 was used to measure the reflectance of mirrored fibre by substituting it in place of the second PM fibre and measuring the power of the reflected beam from this path. The mirrored fibres had a nominal reflectance of 90%, which is lower than the expected theoretical value of 97%. The measured reflectance value takes into account the respective losses of the other optical components.

2.3.5 Nanoparticle characterisation and preparation

In order to observe optical trapping and make comparisons between measurements and theory, it is imperative that the nanoparticle samples were similar to their theoretical behaviour as outline in Section 2.2.1. Optical spectroscopy was performed to ascertain the quality of the nanoparticles, its concentration, and size distribution.

The 100 *nm* diameter colloidal Au nanoparticle (BBI Solutions) was suspended in water and had an 8% size distribution. They were specified to have an optical density (OD) 1 per *cm* at the resonant wavelength, which corresponded to a concentration of 5.6×10^9 particle per *ml*. Nanoparticle aggregation was inhibited through charge stabilisation mediated by citrate molecules on the Au-surface. The nanoparticles tended to sediment (over several hours) due to their larger size. Hence, the solution was vortexed for 30 *s* before use to re-disperse them.

A spectrometer (Ocean Optics USB2000) and a halogen lamp was used to characterise the OD (in a 1 *cm* optical path length cuvette) of the sample such that,

$$OD = \frac{A}{l} = -\frac{1}{l} log\left(\frac{I_{sig} - I_{bkg}}{I_{ref} - I_{bkg}}\right) = \sigma_{ext} N_{1/ml} \tag{2.10}$$

here A is the absorbance of the sample, l is the optical path length, and $N_{1/ml}$ is the number of particles per *ml*. The signal measured from the sample (I_{sig}) was referenced to the transmitted intensity per wavelength of the light source (I_{ref}). The background noise level of the spectrometer in the presence of no light (I_{bkg}) was subtracted from

both the sample- and the reference signal, to obtain the OD of the sample. It is evident from Equation 2.10 that the measured OD is proportional to the extinction cross-section of the particle and its concentration.

An OD of 0.73 (at 571 nm) was measured for the 100 *nm* particles referenced to water a using Quartz cuvette with an optical path length of 1 *cm* (Figure 2.23 left). This was 0.3 OD lower than specified by the manufacturer, which maybe due to pipetting errors and loss of some nanoparticles adhering to bottom of its native storage bottle.

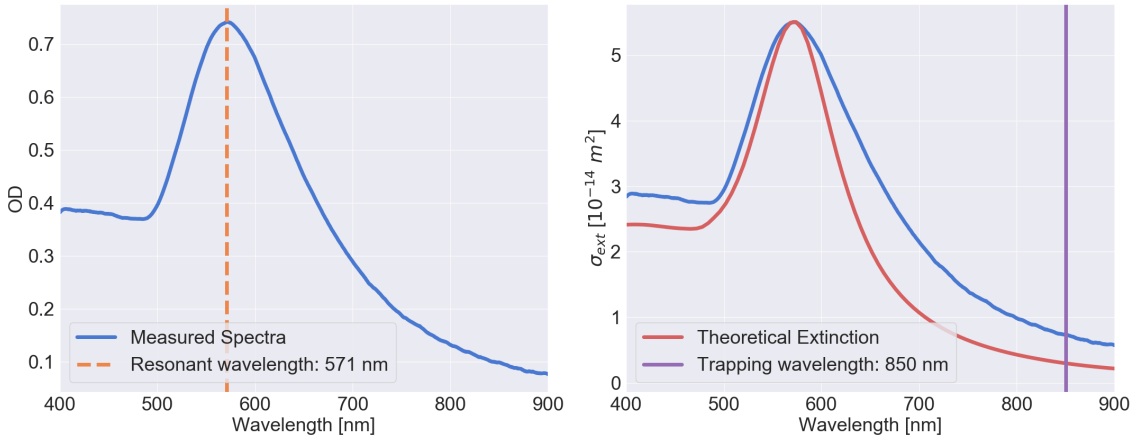

Fig. 2.23 **(a)** Optical spectrum of the 100 *nm* diameter nanoparticles referenced with the light source and background subtracted. This was taken using a Quartz cuvette with an optical path length of 1 *cm*. The measured OD per *cm* was 0.3 OD lower than the manufacturer's specification. **(b)** Measured spectrum normalised to the theoretical extinction cross-section for comparison. The measured spectrum has a wider distribution around the peak, originating from the ±8% size distribution specified by the manufacturer. As a consequence, there is likely to be higher scattering present at the trapping wavelength than theoretically expected.

The measured spectra were normalised to the theoretical extinction cross-section for comparison. The resonant wavelength for both theory and measurement were an exact match. However, the measured spectra were more broad, owing to the more extensive actual nanoparticles size distribution (Figure 2.23 right). At the trapping wavelength of 850 *nm*, the shape of the measured curve begins to flatten out, similar the theoretical curve, but at a higher value. This resulted in an increased scattering (due to the scattering processes being dominate for this wavelength region) of the light

into the detector from the larger-sized particles present in the sample.

2.3.5.1 Nanoparticle hydrodynamic radius

The nanoparticles have a physical size, but due to its citrate charge stabilisation, its effective size will is bigger in the presence of a fluidic environment where ions are present. The citrate molecules attached to the Au-surface are negatively charged and attract positive ions. This double layer gathers more ions until the electrostatic potential away from the particle's surface reaches the potential of the medium. At a distance away from the particle's centre where ions can be freely gathered and lost into the medium, known as the slipping plane, is defined as the hydrodynamic radius (r_h) [93]. This is the effective radius of the particle in the sample solution and was measured using dynamic light scattering. Assuming that the particle is spherical, the ensemble diffusion coefficient (D) of the nanoparticle is determined from the hydrodynamic radius such that:

$$D = \frac{k_B T}{6\pi\eta_w r_h} \tag{2.11}$$

where η_w and T is the temperature dependent viscosity of water and temperature, respectively [94]. The hydrodynamic radius of the 100 nm Au-particles were measured using the back-scattered light at 21 $°C$ (approximate temperature of the medium during the trapping experiments). A series of measurement sets were taken to accumulate the size distribution statistics. A single peak was detected and fitted to a Gaussian to determine size variance and mean hydrodynamic radius (Figure 2.24).

A mean hydrodynamic radius of 82 $\pm$ 20 nm was calculated from Gaussian fitting. The presence of the single peak and small standard deviation indicates that the particles have not aggregated due to its charge stabilisation. The corresponding ensemble diffusion coefficient was quantified to 2.6 $\pm$ 0.6 $\mu m/s^2$ using Equation 2.11.

2.3.6 Determining diffusion metrics from particle tracking

As seen in Section 2.2.4, a multitude of possible trapping sites generated by the interferometric trap. Conventional back focal plane interferometry techniques of determining optical trapping force are unsuitable as it only probes the motion of one

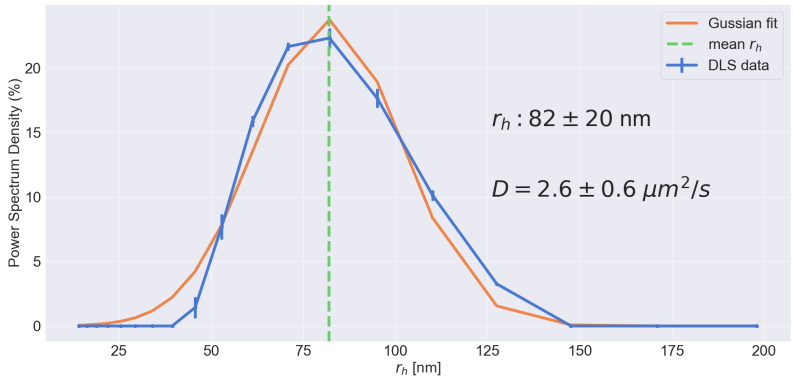

Fig. 2.24 The hydrodynamic radius of 100 *nm* (diameter) nanoparticles were measured using a Malvern Zetasizer, with the cuvette temperature set to 21°*C*. A Gaussian was fitted to the measured values to discern the mean and deviation.

nanoparticle. In this work, particle movement between the fibres was recorded using a near-infrared camera. Hence, the trajectory and its corresponding diffusion metrics for each particle in the recorded videos were obtained using particle tracking. The measured diffusion data was used to quantify the trapping effects on the particles under different trapping conditions.

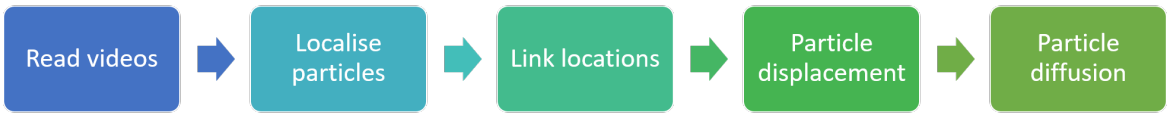

Fig. 2.25 Particle tracking protocol.

The overarching protocol of measuring particle motion from video frames regardless of the particle localisation method or the programming language used, is outlined in Figure 2.25. In this case, *Python* was used to convert the video files into arrays using the *PyAv* package. For each frame of the video, particle locations were determined, after which, trajectories were formed by linking particles across successive frames. The displacement for each particle was then calculated, from which the ensemble diffusion was obtained.

The critical aspect of obtaining accurate diffusion metrics relies on the image analysis method used. There are a variety of techniques for obtaining particle locations per frame and linking the particles, as outline in Chenouard *et al.*'s work [95]. Two

widely-used approaches to pinpoint bright spots against a dark background in *Python* are the Crocker and Grier (CG) and the Laplacian of Gaussian (LoG) methods [96, 97].

2.3.6.1 Particle localisation methods

The *Trackpy* package implemented the CG method in Python [98]. Firstly, images were preprocessed by convolution with a Gaussian kernel of 1 σ (set as a constant) to remove high-frequency intensity variations, followed by a rolling average window to inhibit low-frequency noise. The processed images were then detected for peaks given a separation distance of $2R + 1$, where R is the user-defined particle radius in pixels. The peaks are detected using a grey-scale dilation operation where all pixels within a given window are replaced by the brightest pixel. The resulting image is then compared to the original and peaks are located where pixel values are equal between the images. Peaks were also detected in the noisy regions of the image. These spurious points were negated by integrating the brightness up to a distance R for each peak, and then eliminating peaks below the 64-th percentile. Finally, the identified position was refined by calculating the intensity weighting centroids. The refinement step can localise spots with sub-pixel accuracy.

The LoG is a size-invariant method of spot detection and was implemented by the *scikit-image* package of *Python*. Particle locations and sizes were obtained through the convolution of a Laplacian of Gaussian kernel ($g(x, y\sigma)$) with the original image (I(x,y)), as described in Equation 2.12 [97, 99].

$$\begin{aligned} LoG(x, y, \sigma) &= -\nabla^2 g(x, y, \sigma) * I(x, y) \\ &= \left\{ -\frac{1}{\pi\sigma^4} \left[1 - \frac{x^2 + y^2}{2\sigma^2} \right] e^{-\frac{x^2 + y^2}{2\sigma^2}} \right\} * I(x, y) \qquad (2.12) \\ S_{norm} &= -\nabla^2 g(x, y, \sigma_i)\sigma_i^2 * I(x, y) \qquad (2.13) \end{aligned}$$

The convolution step was repeated for a series of Gaussian widths (σ_i) (Equation 2.13 to ensure adequate selectively in particle size-distribution (illustrated in Figure 2.26). The LoG kernel was then multiplied by the square of the i-th σ to normalise the response of the convolution step. The series of convolved images were stacked in a 3D array (S_{norm}) with each level representing the i^{th} sigma LoG convolution. Peaks

were detected from the stack, returning particle positions and its corresponding size. Taking inspiration from the CG method, particle positions were refined by determining the intensity weighted centroid for each particle and thus facilitated scale-invariant sub-pixel nanoparticle localisation.

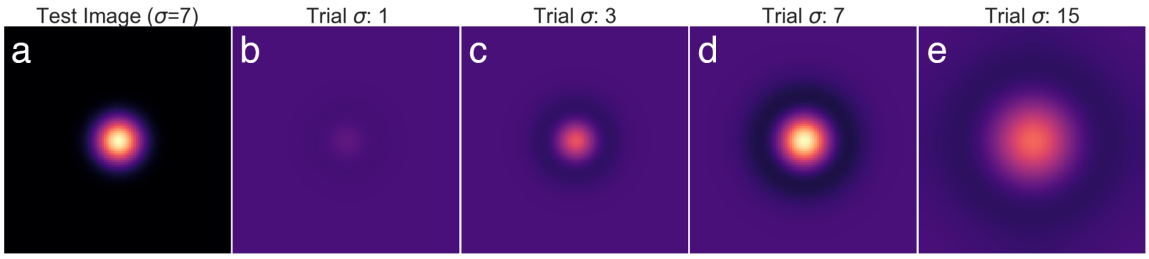

Fig. 2.26 **(a)** A test blob with a Gaussian intensity profile (in 2D), and a width of 7 pixels was created. **(b-e)** The test image was the convolved with a LoG kernel of varying width. When the tested LoG kernel matched with the size of the test blob, the yielded imaged **(d)** had the highest intensity relative to other kernel size trials *(*b,c,e). Peak detection was then performed on images to localise the blob's position.

The LoG localisation process was tested using a two-dimensional Gaussian spot at the centre of a black background and with a width of 7 pixels (Figure 2.26a constructed by 2D Gaussians using Equations 5-8 in reference [100]). This phantom image was then convolved with a series of LoGs with varying σ (as described in Equation 2.13). For σ values below 7 pixels, the LoG convolved image had identified a blob at the centre with a low brightness(Figures 2.26b and 2.26c). When the trial σ was 7 pixels, the resultant image is the brightest amongst the tested σ-range due to the response of the convolution being maximal. For σ values higher than 7 pixels, the blob is smeared out and had a lower intensity. Hence, convolution with a LoG kernel inherently filters by size. This property of LoG localisation allowed spots with intensities near the noise floor to be detected, as shown in Figure 2.27).

An array of Gaussian blobs with a width of 7 pixels were generated and added to a dark-counts image of the camera. The dark counts represented the inhomogeneous noise floor present in the data (Figure 2.27a and b). The amplitude of the Gaussian peaks were set to be a few grey pixel values above the noise floor to test the limit of detection capabilities of the LoG localisation method. The resulting LoG convolution with a σ value of 7 pixels recovered spot locations from the low signal-to-noise ratio image (Figure 2.27c). However, the symmetry of the original spots were lost as the resulting blob shapes are skewed relative to the noise present around it.

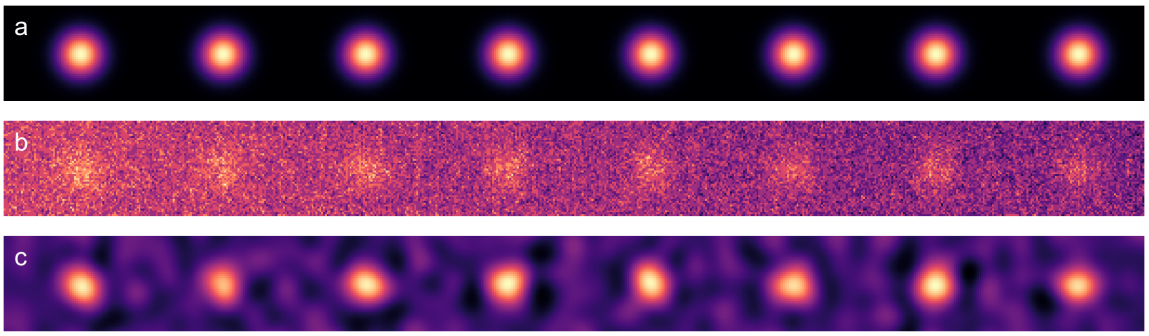

Fig. 2.27 Showing the detection capability of the LoG method, which was sensitive enough to detect particles with peak brightness comparable to the noise floor. **(a)** Generated array of Gaussian particles with the same size, evenly spaced along the horizontal axis. Their amplitudes were set to be a few pixel values higher than the noise floor (dark counts) of the imaging camera. **(b)** The Inhomogenous dark counts from the imaging camera (no laser beam but room lights on) was used to represent the noise floor, on top of which an array of blobs were digitally synthesised. The generated blobs are dominated by noise and lose most of their Gaussian shape. This imaged acted as the test image, from which the LoG localisation method was used to find the particle's location. **(c)** Result of the LoG convolution with the same kernel size as the blobs (7 pixels). The LoG process increased the contrast between the blobs and the background, albeit they are no longer symmetrical. Peak detection was then conducted on this imaged to localise the blobs positions.

Both the CG, and LoG method with the additional localisation refinement step, were capable of sub-pixel spot detection against a dark background. The CG method was computationally less expensive than the LoG but required active thresholding for each frame to minimise spurious peak detection. A series random Gaussian spots were generated with random widths (between 5 pixels and 15 pixels), to assess the performance of each localisation technique. The central position of each blob was randomly off set by ± 0.1 - 0.9 pixels (sub-pixel displacement) to discern if the methods were capable of localising particles with sub-pixel accuracy. Smaller sized spots were scaled to be brighter, and therefore more intense, to emulate them being in focus (Figure 2.28). The intensity distribution of the spots were scaled to match the range of the acquired datasets. The CG and LoG localisation methods were then used to find the centres of the generated spots.

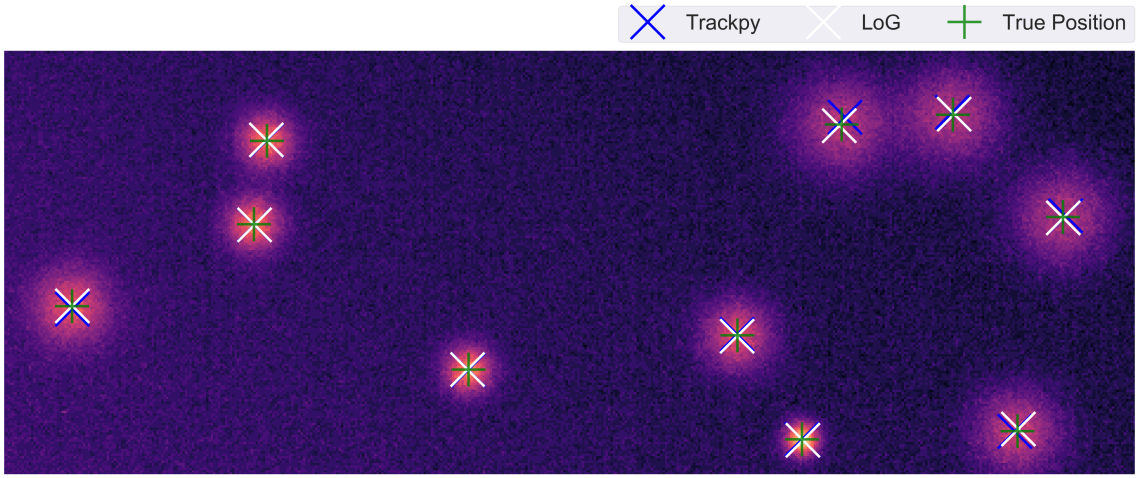

Fig. 2.28 Comparison of the particle tracking methods for a phantom dataset. Randomly generated blobs with sub-pixel positions and various sizes were created. The signal-to-noise ratio approximately reflected the measured data (Figure 2.29). The LoG method was better at finding the nanoparticles as it had a lower localisation error (the difference between the known and detected location).

The identified spot positions from both methods were then compared against the known generated positions. The LoG approach had a root-means-squared (RMS) error of 0.3 pixels (16 *nm*, 1 pixel is 52 *nm*), which was much lower than CG RMS error of 0.4 - 1.2 pixels (20 - 42 *nm*), which was dependent on the value of R. The majority of the error originated from the larger sized spots, as can be seen in Figure 2.28. Due to its superior accuracy over the CG approach, the LoG method was used to locate the particles for each video frame of the acquired dataset with a search size range between 5 and 20 pixels.

2.3.6.2 Particle locations to trajectories

With the particle locations determined for each frame of the datasets, they then had to be linked between consecutive frames to form trajectories. Conceptually, a particle in the first frame can be linked to every particle in the next frame. However, the system under investigation does not have any net flow and particles are randomly diffusing in a fluidic environment meaning that they undergo limited displacement in the time taken to capture two video frames. This prior information about the system reduces

the number of permutations of particle affiliation across several successive frames. This approach was outlined by Crocker and Grier and implemented in *Trackpy* [96, 98].

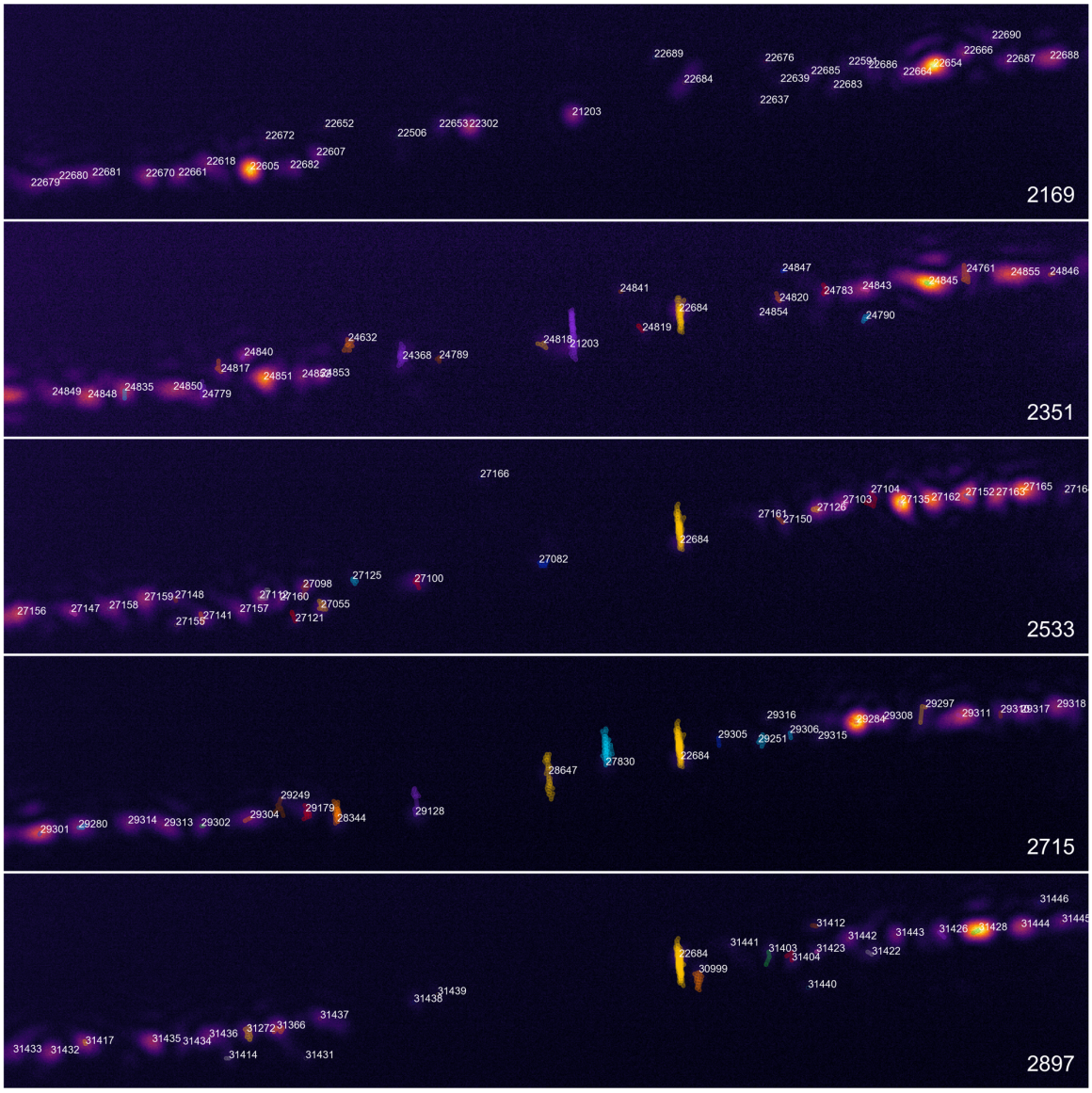

Fig. 2.29 LoG detected particle trajectories for the two opposing fibre geometry using a total power of 150 mW. The frame number is written in the bottom right corner, and the detected particle number is written to the right of its location for a given frame. It can be seen from the particle number count that several thousand individual trajectories have been identified with longer lasting tracks towards the middle of the image. Each frame shown spans approximately 11 μm vertically, and 70 μm horizontally.

Particles locations between sequential frames were connected to form trajectories if its incremental displacement was less than or equal to a user-defined maximal dis-

placement (d_{max}). It was essential to select a reasonable d_{max} value to merge particle locations. Small values led to broken tracks, with particles lasting only a few frames, while a large d_{max} values resulted in the trajectory of several particles intermixing when the original particle had left the depth of focus. Given that the time difference between two frames are in the order of a few milliseconds, particles were unlike to diffuse more than their apparent point-spread size within this time frame. Hence, the mean detected size from the LoG localisation step for all frames and particles was set to d_{max}. Inspection of the trajectories overlaid on top of the original video frames did indeed confirm that this was a justifiable approximation (Figure 2.29).

Only the scattered light from the nanoparticles was detected by the camera. Hence, only particles outside the 'cone of light' emerging from the opposing fibres were detected. The majority of the particles lasted only a few frames before they left the depth of focus or the area of illumination. The central region between the fibres had the most extended trajectories because of the larger illumination area. The trajectory of the longest existing particle (trajectory number 22684) is shown in Figure 2.29. This particular particle remained in few for 728 frames. In that time, many other particles entered and left the illumination area and depth of focus.

Upon comparison of Figure 2.29 and Figure 2.9, the interference bands are tilted, which yielded tilted particle trajectories relative to the vertical. To disentangle the motion of the particles in the x- and y-direction independently, a coordinate transformation was performed to rotate the trajectories such that they were parallel with the y-axis, using Equation 2.14.

$$\begin{bmatrix} x \\ y \end{bmatrix} = \begin{bmatrix} cos(\theta) & -sin(\theta) \\ sin(\theta) & cos(\theta) \end{bmatrix} \begin{bmatrix} x' \\ y' \end{bmatrix} \tag{2.14}$$

Here θ is the anti-clockwise rotation angle in radians, and x' and y' are the original unrotated coordinates for a particle in a given frame. Alternatively, an image rotation can be performed, but this can alter the shape of the particle due to the pixel interpolation used in this process. A 4° anti-clockwise rotation was performed on every detected particle location, after which, their positions were linked to form trajectories.

2.3.6.3 Particle diffusion and displacement from trajectories

The evolution of particle trajectories with time is an indicator of its motion in confined or non-confined environments. The position of a freely diffusing particle in an unbound one-dimensional space is described by a Gaussian probability density function (P(x,t), Equation 2.15), with a width scaled by the diffusion coefficient (D_x) of the particle which increases with time (t) [101]. By integrating the probably density function across all space, the particle's mean square displacement ($\langle x^2 \rangle$) is determined, and scales linearly with time (Equation 2.16).

$$P(x,t) = \frac{1}{\sqrt{4\pi D_x t}} exp\left(\frac{-x^2}{4D_x t}\right) \tag{2.15}$$

$$\begin{aligned} \left\langle x^2(t) \right\rangle &= \int_{-\infty}^{\infty} x^2 P(x,t) dx \\ &= 2D_x t \end{aligned} \tag{2.16}$$

When particles diffuse in a confined environment, such as the potentials created by an interferometric trap, the Gaussian probability density function is no longer an accurate description of the particle's position at a given time [102]. Consequently, the linear scaling of time with MSD is no longer upheld due to the limited motion of the particles. Instead, MSD scales as a power-law of time, known as the anomalous factor (γ_x), which describes the confined motion or the presence of an external force that transports the particle beyond its inherent velocity (Equation 2.17) [102]. For $0 < \gamma < 1$, the motion is sub-diffusive, and for $1 > \gamma > 2$ particles are super-diffusive. In this way, nanoparticle confinement was quantified by determining the diffusion coefficient and its associated anomalous factor.

$$\left\langle x^2(\Delta t) \right\rangle = 2D_x \Delta t^{\gamma_x} \tag{2.17}$$

For every particle trajectory, the displacement was calculated in the x- and y-directions relative to the initial position (Equation 2.18). This yielded a list of displacements for each particle as a function of time, with an epoch (Δt_i), set by the videos frame rate. From this list, the MSD was calculated for the N-number of particles that existed for a given epoch (Equation 2.19). The MSD error at each epoch

was determined by the standard deviation of the displacement-squared, divided by the square-root of the number of particle in that epoch.

$$x^2(\Delta t_i) = (x(\Delta t_i) - x(0))^2 \tag{2.18}$$

$$\left\langle x^2(\Delta t_i) \right\rangle = \frac{1}{N} \sum_{n=1}^{N} (x_n(\Delta t_i) - x_n(0))^2 \tag{2.19}$$

With the MSDs known as a function of time, Equation 2.17 was used to obtain the values of D and γ for both directions using the least-squares fitting method. The fit is forced to start at the origin to ensure that the returned parameters were physical.

2.4 Interferometric optical trapping results

2.4.1 Interference phase stability and wavefront distortion measurements

The interference of light generated potential wells that confined the nanoparticle's motion. In order to examine how nanoparticle diffusion was affected, the generated potentials were static over the observation period (before the particle left the trap), which was typically in the order of a few hundred milliseconds. If the potentials were non-static, the observed particle movement was affected by the shifting potential positions. The phase shift of the interfered light was quantified to determined the drift of the periodic potentials over a 10 seconds period.

Interference of the laser light was obtained by splitting a single source into two, coupling them into PM-fibres, and imaging the emitted light onto a camera (Figure 2.22). The images of the two paths on the camera were then overlapped, aligning the paths of each arm and interfering the two beams (Figure 2.30a). A small subset of camera pixels were selected to boost the frame rate to 1,370 frame per second and thus increase the time resolution of the phase drift (Figure 2.30b). For each frame of the acquired high-frame-rate video, the columns were summed and normalised to the brightest value within that frame (Figure 2.30c). The phase of the normalised column values was then tracked over time (Figure 2.31).

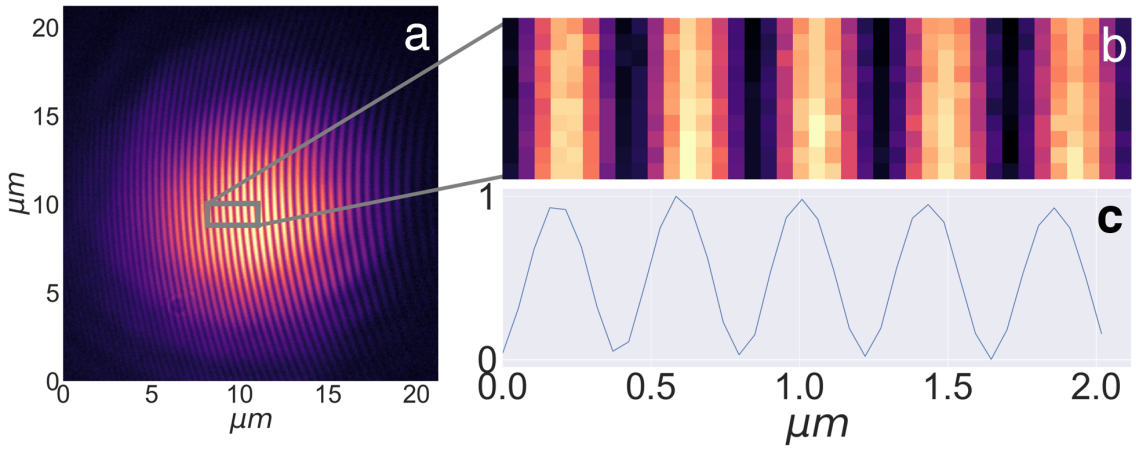

Fig. 2.30 **(a)** Interference pattern of the overlapped light emitted from the polarisation maintaining fibres (see Figure 2.22). The fringes have a small curvature, which suggests that wavefront distortion was negligible. **(b)** A small pixel region was scanned to increase the frame rate of the camera and better temporally resolve phase drift. **(c)** The image in b is vertically summed to increase the signal-to-noise-ratio. The emerging interference pattern appeared, albeit it was somewhat quantised.

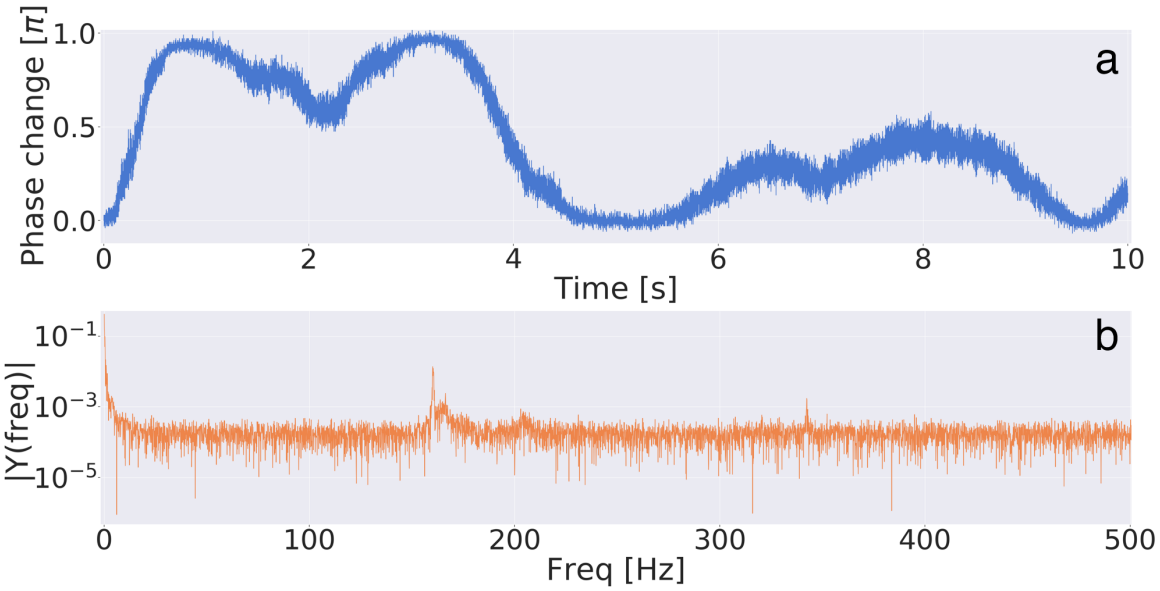

Fig. 2.31 **(a)** Relative phase change of the interference pattern as a function of time. There were slow and fast phase change components. Maximal phase change of $\pm\pi$ can occur over 250 *ms*. **(b)** Fourier analysis of the phase change in a. Some of the identified frequencies were likely to be harmonics. The higher frequency components were possible due to the video encoding.

The largest and most probable phase instability could arise from any stress or movement of the PM-fibres. Hence, the fibres were taped down on the optical table and the room itself was temperature- and humidity-controlled. Over a duration of 10 seconds, a maximal phase shift of $\pm\pi$ was observed (Figure 2.31a). The phase variation over time has slow and fast components, which were quantified by a Fourier transform (Figure 2.31b). Three key frequency components of 4 Hz, 168 Hz, and 340 Hz were identified from the Fourier analysis. Hence, a maximal phase change of $\pm\pi$ could occur in 250 ms (4 Hz), which corresponded to the minimum or maximum of the potential wells shifting by 159 nm ($\Delta\phi\lambda/4\pi n_m$). The higher frequency phase fluctuations were small in magnitude, and likely originated from video encoding or camera noise.

2.4.1.1 Wavefront distortion from mirrored-fibre

Phase fluctuations for the mirrored-fibre geometry could not be present in the interference pattern. However, the back-reflected light from the mirrored surface could have been distorted due to its small physical curvature. To observe that the mirrored fibres did indeed self interfere, the second PM-fibre in Figure 2.22 was replaced by a Au-mirrored fibre. An image of both the light emitted from the PM fibre core and the light reflected by mirrored-fibre's surface formed on the camera. The beam from the PM-fibre was scanned across the mirrored-fibre's facet to determine wavefront distortion at various positions (Figure 2.32).

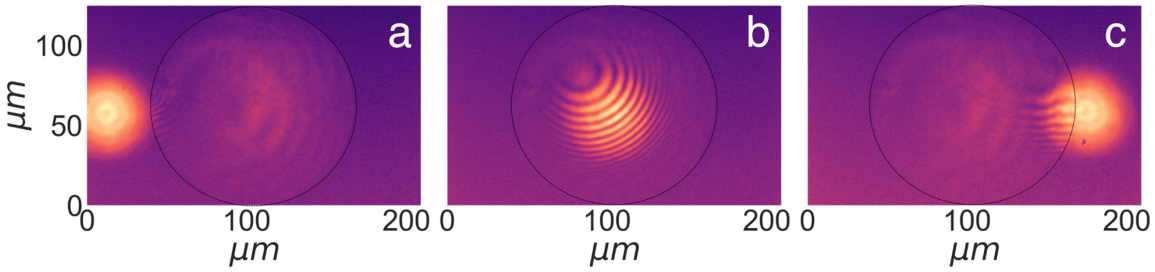

Fig. 2.32 Dashed-black line mark the edge of the mirrored-fibre. **(a)** The left spot was the light emitted from the fibre, and the right spot light reflected from the mirrored-fibre. They did not overlap and no interference pattern was observed. **(b)** Circular interference fringes with little wavefront distortion when the beams overlapped. **(c)** Wavefront distortion at the edge of mirrored fibre due to edged effects in the Au deposition process.

As expected, no interference was observed when the beams did not overlap (Figure 2.32a). With the PM fibre positioned at the centre of the mirrored-fibre, approximately

uniform circular interference fringes were present, meaning that the back reflected light had little wavefront distortion (Figure 2.32b). When PM-fibre beam was positioned at the boundary, interference was still observed (Figure 2.32c), but the wavefronts were visibly distorted. Darkfield images of the mirrored fibre showed defects at the edges, which were responsible for the distortion.

Au-coated fibre facets did indeed act as a mirror, the central region back reflected approximately 90% of the incident light and did not significantly distort the wavefronts. Critically, the use of mirror to create a stand wave eliminated phase instabilities.

2.4.2 Radiation pressure from single Gaussian beams

With the fibres embedded into the PDMS holder (separated by a distance $\sim 66\ \mu m$) and the sample solution of 100 nm Au-nanoparticles pipetted into the PDMS reservoirs, the scattering force exerted on the particles from a single beam was investigated in the first instance. This was done by blocking the in-coupling light of one PM-fibre, and then tracking the motion of nanoparticles as they were pushed along in the direction of laser propagation of the remaining PM-fibre. Each fibre independently emitted 115 mW (P_{tot}), meaning that the nanoparticles felt a strong scattering force in the axial direction and a weak gradient force in the radial direction near the fibre facet (superimposed particle trajectories shown in Figure 2.33).

By inspection of Figure 2.33, the length of the trajectories were longer in the x-direction compared to the y-direction, meaning that the displacement was larger in x-direction. There was a net forward motion relative to the laser propagation, as expected from the strong scattering force in that direction.

The scattered light from the nanoparticles onto the camera meant that the particle trajectories traced the beam waist and position of the light emitted from each fibre. Over a distance of 66 μm, the beam expanded from a size of 5.3 μm (diameter) to 13 μm. The fibre misalignment was determined by drawing a horizontal line at the centre position of each beam's trajectory and measuring the separation distance between each line. An approximate misalignment of 3 μm was present between the PM-fibre cores. This was expected given the tolerance of the fibre sizes by the manufacturer (ca. 2 μm), and the tolerance of the fabrication process for the microfluidic chips. It should be

noted that fibre was from the same spool and would therfore have comparable tolerances.

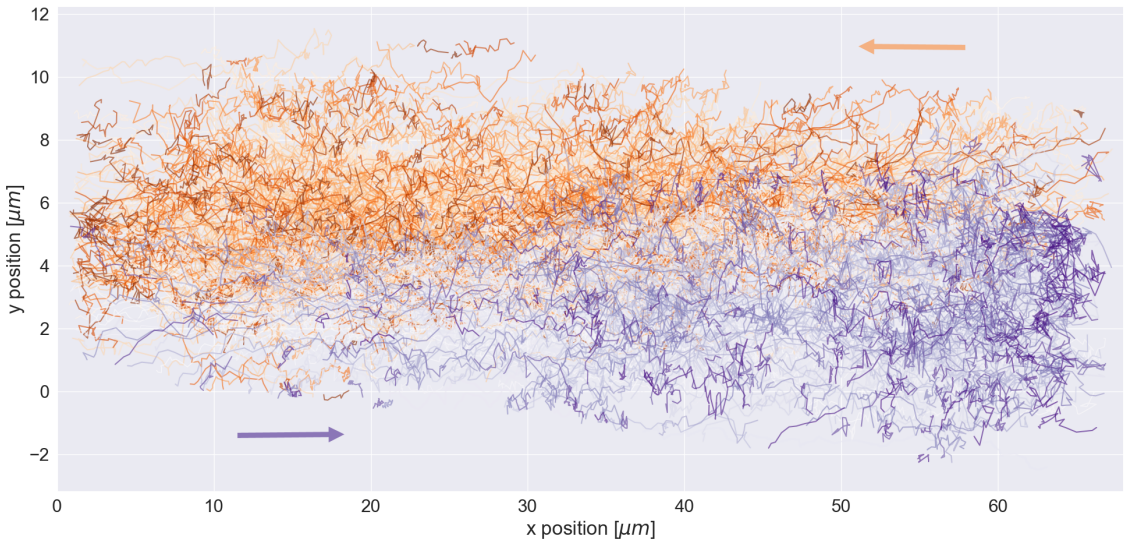

Fig. 2.33 Tracked nanoparticle trajectories due to the scattering force from each independently emitting fibre with a power of 115 mW. The displacements were larger in the x-direction relative to y-direction due to the photopheresis. The trajectories essentially mapped out the intensity of the light emitted from each fibre. Nanoparticles near the central axis of each fibre would therefore have a higher velocity. The misalignment between the central axis of the two fibres was evident as the majority of the orange and blue trajectories do not overlap. This was expected since the simulated scattering force for this geometry (Figure 2.9) showed the same behaviour.

The motion of particles being propelled along by the radiation pressure was quantified by MSD analysis. The displacement-squared of each particle for each beam was determined and merged together, from which, the MSD was determined.

Particle trajectories did not last more than 700 ms due to the strong scattering force present (Figure 2.34). The majority of tracks in the x-direction had MSD_x in excess of 1000 $\mu m^2/s^{\gamma_x}$. The fitted MSD_x curve had small residuals and represented well the measured MSD_x values. In the y-direction, there was a greater distribution of individual particle displacement values. There were several trajectories in which the particle returned to its starting point on its random walk. The fitted curves for the MSD values in both directions were reported in Table 2.1.

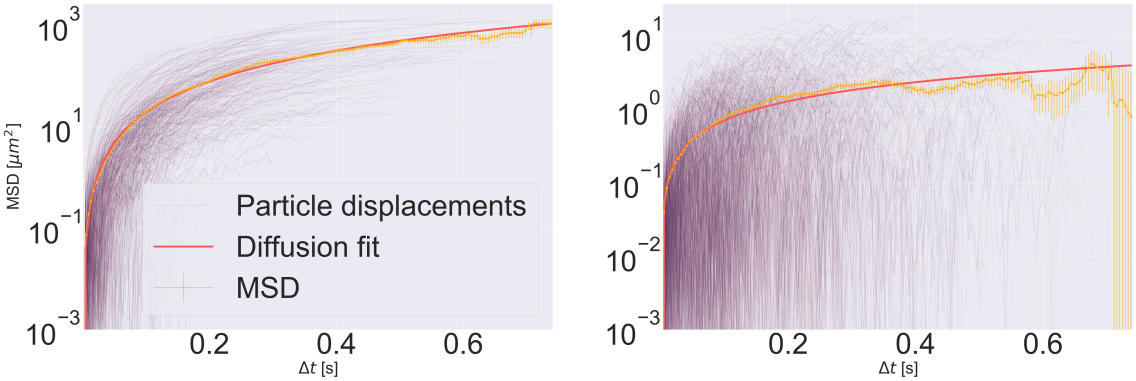

(a) MSD_x (b) MSD_y

Fig. 2.34 Mean squared displacements for trajectories in Figure 2.33. The purple lines show the individual particle displacements as a function of increasing epochs. **(a)** The mean square displacement in the x-direction scaled quadratically with time as the nanoparticles were undergoing photophoretic migration, obtained from fitting to the anomalous diffusion (Equation 2.17). **(b)** The individual particle displacements were widely varying due to the presence of Brownian motion. The obtained diffusion coefficient from fitting (Table 2.1) matched the DLS value. Note that the y-axis is in log scale.

The MSD_y was Brownian-like as the epoch (Δt) exponent was 1 within the reported error. However, the mean exponent value suggests small confinement is present, which was expected in the radial direction of the gradient force. The diffusion coefficient value of 2.1 $\pm$0.1 $\mu m/s^{\gamma_y}$ was similar to the measured ensemble value using DLS (2.6 $\pm$0.6 $\mu m^2/s$).

P_{tot} (mW)	D_x ($\mu m^2/s^{\gamma_x}$)	γ_x	D_y ($\mu m^2/s^{\gamma_y}$)	γ_y	R_D
115	1198 $\pm$ 10	2.0 $\pm$ 0.1	2.1 $\pm$ 0.1	0.9 $\pm$ 0.1	599

Table 2.1 MSD least-squares fit (to Equation 2.17) values for single beam trajectories where interference was not present and particles experience a strong scattering force. An R_D value less than 1 constituted nanoparticle confinement, whilst $R_D > 1$ means nanoparticles were diffusing faster than Brownian motion.

The x-direction motion of nanoparticle was super-diffusive due its high γ_x value of 2 $\pm$ 0.1 and its corresponding D_x value. This essentially meant that the temporal displacement of the nanoparticles, which were usually linear in the presence of Brownian motion, scaled quadratically since the scattering force acted as a transportation

mechanism for the nanoparticles. The nanoparticle still experienced Brownian motion in all directions.

A comparison of the diffusion coefficient values was made between the x- and y-directions in the form of a ratio ($R_D = D_x/D_y$). In the presence of a single laser beam, the nanoparticles had an increased diffusion by 599 times in the x-direction, compared to the y-direction. R_D was only a relative indication of the diffusion between different axis, and it should be noted that units did not match due to the different Δt scaling.

2.4.3 Diffusion characteristics of optically confined nanoparticles in tilted potential

In contrast to the previous section, light from both PM-fibres was simultaneously allowed to emit along the same polarisation (horizontal) to create an interference pattern where the motion of nanoparticles became confined. Three video sets were taken for low (70 mW), medium (150 mW) and high (230 mW) powers (total) to investigate nanoparticle trapping within varying potentials depths in both directions. The localised nanoparticle positions and trajectories were then combined for each power set to statically improve MSD analysis.

For a total power of 70 mW, the trajectorieswere similar to the single beam case discussed in the previous section, which were longer in the x-direction (Figure 2.35a). This was especially the case for regions $\pm$ 4 μm radially away from fibre cores, where the well-depths were expected to be less than 1 k_BT. Around the mid-separation distance between the fibres, there appeared to be a few longer trajectories in the y-direction relative to the x-direction, indicating possible nanoparticle confinement. The presence of the two opposing beams yielded a reduced net scattering force experienced by the nanoparticle. Overall, this was likely to be a net forward motion in the direction of the dominating Poynting vector relative to the nanoparticle's position between the beams. Particle trajectories were interweaved with each other and there was no clear particle confinement at this power.

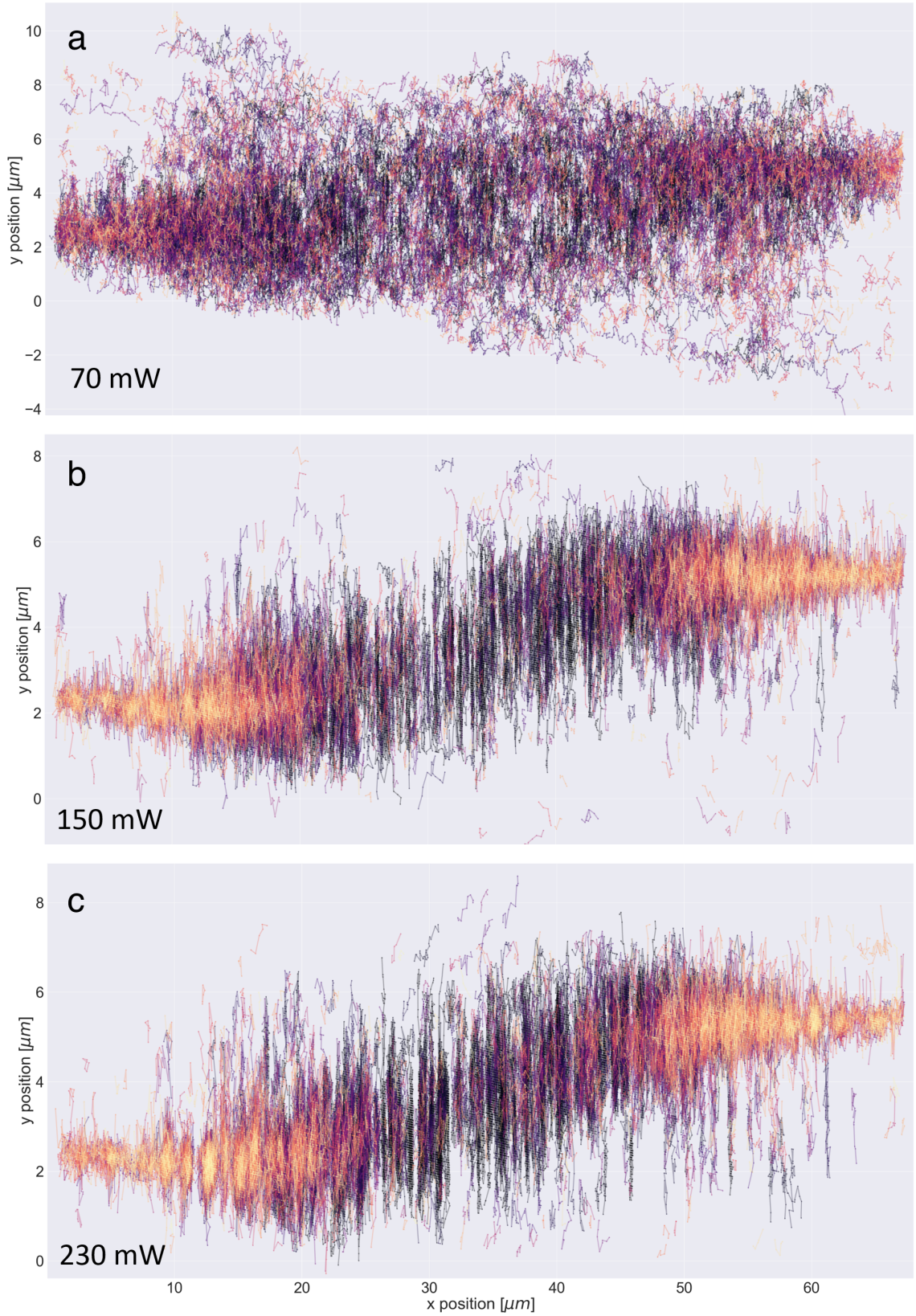

Fig. 2.35 Detected nanoparticle trajectories and their altered motion due to the presence of the optical interferometric trap. Each trajectory is plotted in a different colour. All the trajectories from three-independent datasets for each laser power are shown. **(a)** Some nanoparticles weakly confined. Scattering force dominated and nanoparticles did not stay trapped. **(b-c)** Trajectories were longer in the y-direction owing to the confined motion of the nanoparticles in the x-direction.

Increasing the total power to 150 mW resulted in banded and narrow nanoparticle trajectories in the y-direction, as a result of confinement. This was especially evident for the mid-separation distance between the fibres (Figure 2.35b). Trajectories away from the central radial axis were slightly longer in the x-direction, owing to the shallower potential wells in these regions. Further increasing the total power to 230 mW consequently produced clear segmented regions where nanoparticle trajectories existed across the entire fibre-separation gap (Figure 2.35c). Trajectories were more striated in the y-direction at the halfway point between the fibres compared to the edges. Overall, the trajectories were significantly longer in the y-direction relative to the x-direction. Nanoparticle tracks detected at the extremities of the cone of light exhibited hopping between different potential wells.

MSD analysis was performed on the detected trajectories of Figure 2.35 to quantify the altered motion of the nanoparticles due to the optical confinement at different powers (Figure 2.36). The fitted parameters for all the powers in both direction were tabulated in Table 2.2.

The scattering force was still dominating for a total power of 70 mW since the value of γ_x was greater than 1, and the diffusion coefficient (D_x) was bigger than D_y (for the same power) and the values measured by DLS (Figure 2.36a, Table 2.2). Whilst Figure 2.35a shows some trajectories being longer in the y-direction (indication confinement in the x-direction), the MSD analysis in the x-direction suggests that even on short time scales, there was little to no confinement, since the MSD_x smoothly increased with time (Figure 2.36a). The MSD_y values (Figure 2.36a) yielded diffusion coefficient similar to measured DLS values, suggesting no (or very little) altered motion of the nanoparticle by the radial gradient force.

A large reduction in the value of γ_x and D_y was obtained through fitting the MSD_x curve for a power of 150 mW (Table 2.2), confirming the confined motion of the nanoparticles in the x-direction (Figure 2.36c). Inspection of the measured MSD_x (orange curve in Figure 2.36c) showed a kink at 0.7 s, with an increased slop thereafter. This suggests that nanoparticles were trapped for approximately 0.7 s on average before escaping. Confinement was also present in the y-direction since the value of γ_y was now below 1 (Figure 2.36d, Table 2.2). Further reduction of γ_x and γ_y was measured

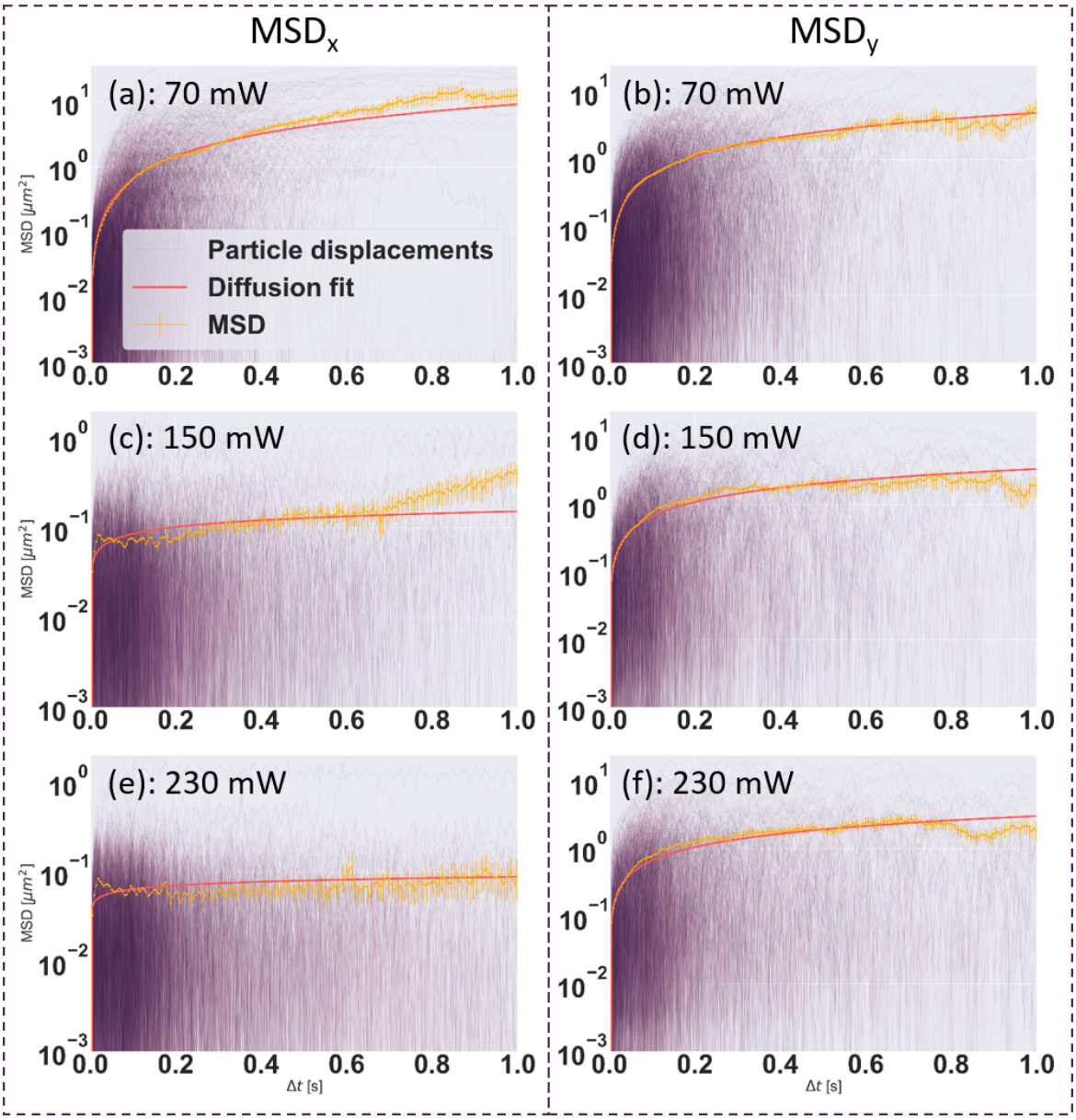

Fig. 2.36 MSD analysis of the particle trajectories in Figure 2.35. MSD values were obtained for a window size 1 s. The purple line shows squared displacement for individual trajectories. The MSD values were determined from the mean of squared displacement across every epoch (Δt). Error for each epoch as the ratio of the MSD and square-root of the number of observation for each epoch ($MSD(\Delta t_i)/\sqrt{N(\Delta t_i)}$). Left column: all MSD_x values, right: MSD_y **(a)** Scattering force accelerating particle, little to no confinement of nanoparticles. **(b)** Radial gradient force was weak and the motion of nanoparticles was Brownian. **(c)** Nanoparticles confined in the x-direction for an average of ca. 0.7 s. **(d)** Radial gradient force was significant, and drawing nanoparticles towards the central region (confinement factor (γ_y) was less than 1. **(e)** Nanoparticles remained confined for the entire analysis window. **(f)** Radial confinement of nanoparticle further increased due to an even greater reduction in the confinement factor compared a total power of 150 mW. Fitted values were reported in Table 2.2.

for powers of 230 mW (Figure 2.36e-f, Table 2.2). The measured MSD_x values stayed constant, meaning that the nanoparticles remained in the trap for at least 1 s.

P_{tot} (mW)	D_x $(\mu m^2/s^{\gamma_x})$	γ_x	D_y $(\mu m^2/s^{\gamma_y})$	γ_y	R_D
70	4.3 ± 0.2	1.12 ± 0.01	2.5 ± 0.1	0.92 ± 0.1	1.72
150	0.076 ± 0.002	0.25 ± 0.01	1.7 ± 0.1	0.70 ± 0.1	0.04
230	0.044 ± 0.001	0.13 ± 0.01	1.5 ± 0.1	0.65 ± 0.1	0.01

Table 2.2 Fitted MSD values from Figure 2.36.

The simulated trapping potentials were symmetric about the mid-separation distance between the fibres (Figure 2.12). The trapping potentials were about -9 k_BT at the edges of the fibre, and increased to -13 k_BT at the central separation distance (for a total beam power of 200 mW). Hence the trapping potential increased by about 45% from the edge to the mid-way point. To discern if the acquired dataset followed the same trend, nanoparticle trajectories for the 230 mW power set were binned in sizes of 13.2 μm (5 bins) along the x-direction. MSD analysis along the x-direction was performed to determine how the confinement factor and the diffusion coefficient changed as a function of axial distance (Figure 2.37).

Both γ_x and D_x reduced at the mid-separation distance between the fibres, meaning that nanoparticles were more centrally confined than near the fibre facets, which was

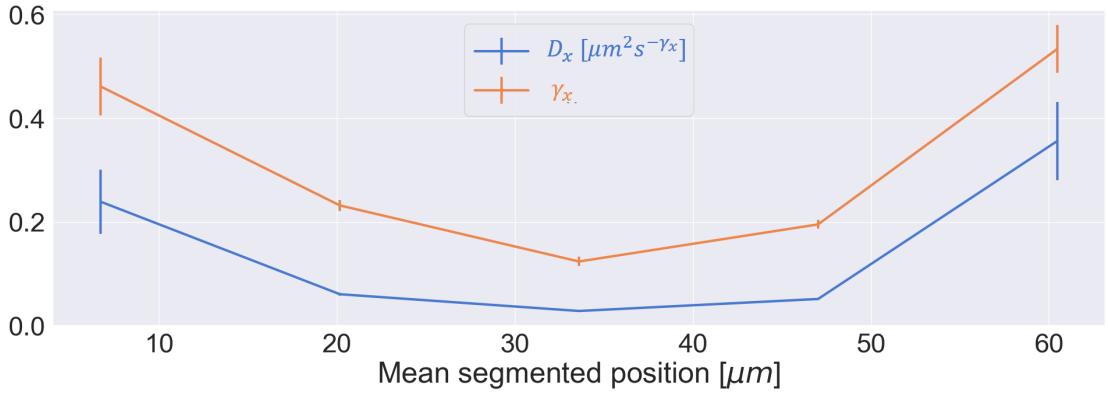

Fig. 2.37 The trajectories of the 230 mW dataset were axially binned. For each bin, MSD analysis was performed. Nanoparticles were more confined at the central separation distance between the fibre and than the edges, which was in agreement with the simulated symmetric potential of the nanoparticles (Figure 2.12). Diffusion and confinement factor were higher on the right side relative to the left, which may be a result of the slight power imbalance between the two fibres.

in agreement with the simulated results (Figure 2.12). The confinement factor reduced by approximately 0.5 (near the fibre facets) to 0.18 at the central separation distance, and D_y decreased by a factor of 3. There was also a slight asymmetry between the left and right side of the γ_x, D_x values, which may have been a result of a power imbalance between the two fibres.

2.4.4 Self-interfering optical trap

The Au micro-mirror with an opposing single fibre geometry (Figure 2.18d) was used to back reflect the incident light and create an interference pattern for nanoparticle trapping. The laser emitting fibre was positioned approximately at the same separation distance as the two opposing fibre geometries (ca. 65-70 μm). A total laser power of 115 mW was then used to confine nanoparticles in the stand wave trap (Figure 2.38).

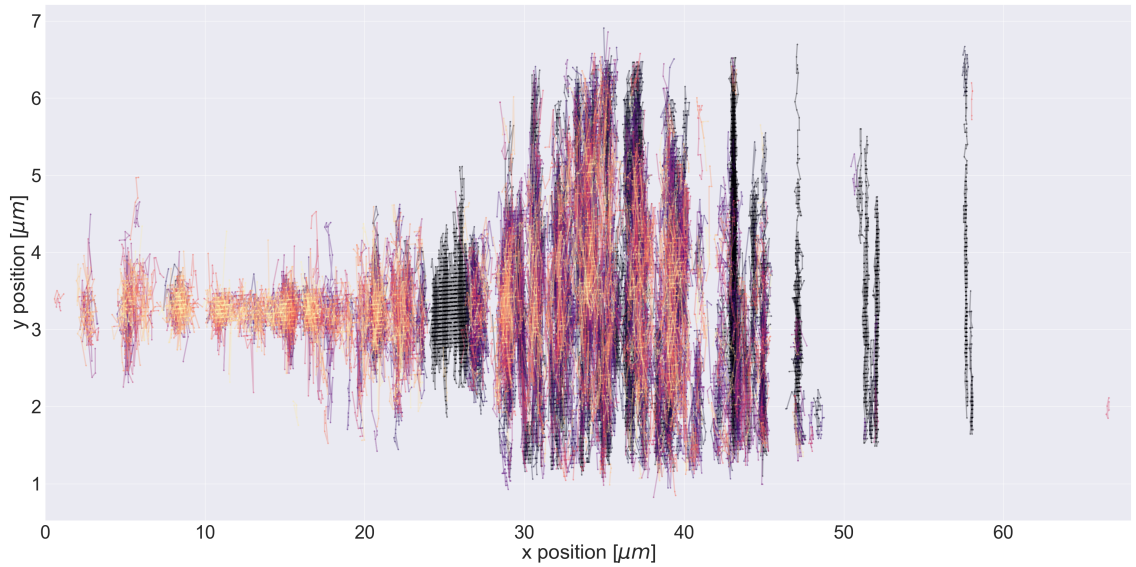

Fig. 2.38 Detected nanoparticle trajectories in the fibre-and micro-mirror geometry where the beam underwent self interference, creating an array of optical potential wells. The laser light from a single PM fibre emerged from the left, and the micro-mirror (Au coated fibre) was placed on the right. Only one dataset (5000 frames with several hundred trajectories) was taken for this configuration. Fewer trajectories were detected near the mirrored surface. The width of the striated tracks decreased in the x-direction towards the mirror surface. This was due to the increase potential well depth mediated by the reduction of the scattering force.

Long trajectories were detected in the y-direction owing to the confined mobility of the nanoparticles in the x-directions. The width of the tracks in the x-direction became narrower towards the mirrored surface, due to deeper effective potentials arising from the diminishing scattering force in the forward propagating component of the beam. This behaviour was in accordance with the simulated potentials for this geometry (Figure 2.14). MSD analysis was conducted on the detected nanoparticle trajectories of Figure 2.38 to quantify the confinement factor and its corresponding diffusion coefficient for both directions (Figure 2.39).

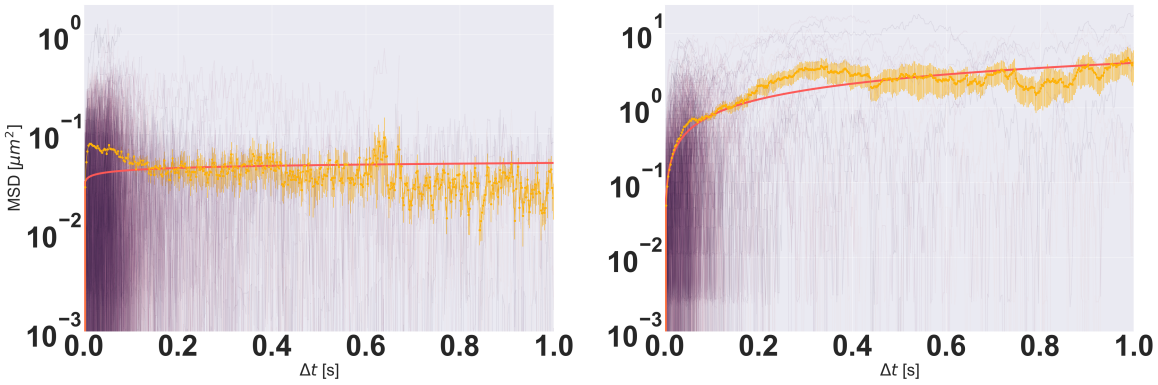

(a) (b)

Fig. 2.39 MSD analysis of the nanoparticle trajectories in Figure 2.38. **(a)** MSD_x measured values and fitting. The measured values had a slightly negative slope suggesting more stable confinement with increasing time spent in the trap. This may have been a result of the nanoparticles being pushed into deeper potential wells by the forward scattering force. **(b)** MSD_y measured values and its correspondence fit. All fitting values were reported in Table 2.3.

The majority of the detected particle trajectories lasted less than 0.2 s before they left the depth of focus of the illumination area. The measured value for the MSD_x had a negative slope suggesting that the nanoparticles became more confined with increasing time spent in the trap (Figure 2.39a). Despite the lower power used in this geometry, the confinement and diffusion coefficient was lower than the opposing fibre geometry for a power of 230 mW (Table 2.2). This was a direct consequence of the phase stability of the self interfering beam. Nanoparticle confinement was also present in the y-direction as the γ_y fitting value obtained from the measured MSD_y had a values of 0.7 (Figure 2.39b, Table 2.3).

P_{tot} (mW)	D_x $(\mu m^2/s^{\gamma_x})$	γ_x	D_y $(\mu m^2/s^{\gamma_y})$	γ_y	R_D
115	0.025 ± 0.001	0.07 ± 0.01	2.0 ± 0.1	0.7 ± 0.1	0.04

Table 2.3 Fitted MSD values from Figure 2.39 .

2.5 Summary

In the present study, an array of trapping locations is created (ca. 200 potentials in axial direction) using interference of light facilitating multiplexed nanoparticle confinement analysis without micro- or, nano-fabrication (plasmonic structures, micro-lenses, tapered fibres), or the use of specialised optical elements such as spatial light modulator and digital micro-mirror devices. The optical set-up is judiciously kept simple whilst using readily available components to increase the flexibility of the experimental architecture.

Au nano-spheres with a diameter of 100 nm are used to demonstrate the concept of the interferometric trap owing to their higher polarisability, and because they are commonly used for surface enhanced Raman spectroscopy [12], nano-patterning [14], and cancer therapeutics [103]. To better represent the polarisability for 100 nm nanoparticles for optical trapping simulations, the enhanced absorption and scattering cross-sections using Mie theory are used to quantify the polarisability (Figure 2.2b). In addition, the absorption and scattering cross-sectional data are used to select a trapping wavelength (850 nm) which maximise the gradient force over the scattering force (maximise the ratio of nanoparticle scattering over absorption). The interference of two Gaussian beams is simulated (Figures 2.4 and 2.6), from which the effective trapping energy from the tilted potential wells is quantified for both of the two opposing fibres (Figure 2.12) and the mirror-fibre geometry (Figure 2.14). For a total optical power of 200 mW and a fibre separation distance of 70 μm, a mean trapping energy of -11.5 k_BT, and -8.5 k_BT is determined for the former and latter geometries, respectively. In reality, the opposing fibres are not going to be perfectly centrally aligned and hence the trapping potential is likely to be comparable to the mirror-fibre potential, which is insensitive to misalignment. For both geometries, the effective trapping potentials could be increased by reducing the fibre separation distance.

The light emitting fibres and micro-mirror are passively aligned by embedding them into a microfluidic device (Figure 2.18). Only the relative orientation of the polarisation between the fibres and the separation distance can be tuned. The microfluidics also provide a controlled fluidic environment with no net flow and in laminar regime, both of which minimise any fluidic driven migration of the nanoparticles. Surface effects are also minimised as the nanoparticles are confined in the central region of the microfluidic channel (62.5 μm above the bottom surface of the PDMS).

A Michelson interferometry set-up is created to measure phase instability in the opposing fibre geometries, and wavefront distortion of the custom-built micro-mirror. A maximal phase drift of $\pm\pi$ ($\pm$156 nm shift of the potentials) over 250 ms (Figure 2.31). Using the same optical setup, the reflectance of the micro-mirror is measured to be $\sim$90% ($\sim$97% expected), and no significant wavefront distortion is observed (Figure 2.32).

Video rate particle tracking using the a modified Laplacian-of-Gaussian method is used to localise the nanoparticles, and track their altered motion in the presence of the optical interferometric trap. The anomalous diffusion of the nanoparticles is obtained from the detected nanoparticle trajectories (several hundred particle trajectories detected for each power set). In the instance when a single fibre is emitting light and no interference present, the nanoparticles are pushed along the direction of laser propagation with significantly increased diffusion (Figure 2.33, Table 2.1). When both opposing fibres are emitting light, optical trapping is strongly observed in the axial direction, with weak confinement in the radial direction for 150 mW and 230 mW (Figure 2.39, Table 2.2). Remarkably, a lower confinement factor is measured for the mirror-fibre geometry than for the opposing fibre geometry at double the optical power (Figure 2.39, Table 2.3). This is a direct consequence of the radial misalignment and phase instabilities present in the two opposing fibre geometry.

Chapter 3

Thermo-electro-phoretic confinement of nanoparticles

3.1 Introduction

While the previous chapter focused on maximising intensity gradients, the work presented in this chapter employed temperature gradients to induce nanoparticle swarming towards a heat source, whilst diminishing optical effects. The study of nanoparticle properties in a temperature gradient is a powerful tool as it can be used to obtain information about the particle surface charge, hydration entropy and surface area (Equation 1.8). The technique has high sensitivity and has been used in many biological applications involving proteins [18], DNA [76] and antibody binding [104]. In addition to obtaining nanoparticle properties, thermopheresis can also be used to manipulate and trap the nanoparticle [63, 77, 72].

Zheng's group achived trapping of nanoparticles by chemically engineering the environment, which induces a thermoelectric field in the presence of the temperature gradient [72, 22, 78, 23, 24, 79]. In their work, they use the dissimilar thermo-migration of CTAC micelle anions, and chloride cations to create a thermoelectric field. As a reminder, the strength of the thermoelectric field E_T (Equation 3.1) is directly proportional to the temperature and its corresponding gradient. The sum of the ionic species and their elemental charge, Soret coefficients, and concentration, also contribute to the trapping field. However, these parameters can be considered as constants, and are not necessary under the experimenter's control.

$$E_T = \frac{\nabla T k_B T}{e} \left\{ \frac{\sum_{i=1}^{\infty} Z_i C_i S_{T_i}}{\sum_{i=1}^{\infty} Z_i^2 C_i} \right\} \tag{3.1}$$

This chapter built on the work conducted by Zheng's group, using thermoelectric fields to confine smaller nanoparticles (26 nm) than previously reported, and in an environmentwhich is native to the nanoparticle's medium (sodium azide to stop bacterial growth), rather than chemically engineering the solution using CTAC micelles. More importantly, the strength of the thermoelectric field was quantified and mapped, which up until now, has only been estimated. One of the main challenges for the quantification of the thermoelectric field strength is the ability to measure temperatures on the microscale. Herein, three-dimensional microscale thermometry has been achieved through the temperature sensitive fluorescence lifetime of Rhodamine-B molecules. Finally, the Soret coefficient of azide ions was quantified from knowing the strength of the thermoelectric field.

It is important to note that the thermoelectric effect is the dominant mechanism for the observed thermophoretic migration of the nanoparticles. Proton gradients did not exist due to the pH neutrality of the solution. Capacitor effects were negligible since the Debye length was expected to be smaller than hydration radius of the particle. Hence, the nanoparticles were considered as point changes [69].

3.2 Simulations of heat diffusion, convective flow, and thermoelectric fields, in a microfluidic chamber

In this work, the near-infrared (780 nm) absorption of a Chromium micro-disc deposited on glass was used to induce temperature gradients in a fluidic environment. A small microfluidic sample chamber was created using a 90 μm spacer sandwiched between a glass slide and a coverslip (Figure 3.1). For this given geometry, the laser absorption and transmission of the glass-Cr-Au layers was quantified (Section 3.2.1), and used in the heat generation term to simulate the ensuing temperature profiles within the fluidic chamber (Section 3.2.2).

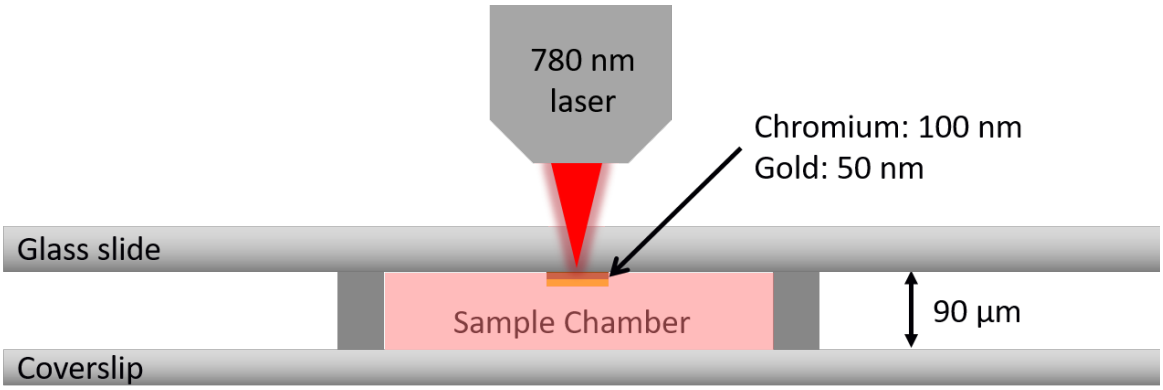

Fig. 3.1 A drawing of the device used to generate temperature gradients, and thermoelectric fields. Heating was induced by a Chromium (Cr) absorption of 780 *nm* laser light. A simple and sealed microfluidic chamber was made using a 90 μm spacer sandwiched (a sticker with a hole) between a glass slide and coverslip. This geometry was used in the subsequent heat-diffusion and fluid flow simulations.

The simulated heating profile was then coupled into the Navier-Stokes equation to discern the magnitude and flow direction of the fluid due to temperature mediated density variations (Section 3.2.3). In addition, the gradients of the simulated temperature profile were used to quantify the thermoelectric field strength for a solution containing sodium chloride (Section 3.2.4).

3.2.1 Thin film absorption

The three main methods of heat generation on the microscale are electrical (resistive or pelter) [105–107], optical absorption of the media (1064 *nm* or 1480 *nm*) [19], and optical absorption of a thin film (metallic-structures or -nanoparticles) [22, 108–110]. Electrical methods are spatially non-specific, and the flow of current in the electrodes generates fields which alter the path of changed particles. Optically heating the media can also affect the motion of the particles through optical forces, as well as induce photobleaching and damage. Hence, absorption of laser light of thin metal film was chosen as the method to generate temperature gradients on the micron-scale. The laser light did not interact with the sample or its medium, and only the region where the beam was incident was heated.

Fluorescence excitation and emission of dyes and molecules were predominately in the visible region. Hence, a near-infrared laser was chosen to induce heating in Cr thin films printed on glass, similar to the experimental geometry of Yu *et al.* [111]. In

addition, a layer of Au on top of Cr was also considered to prevent oxidation. This layer also back reflected any transmitted light from the Cr. The absorption and transmission of a 780 *nm* laser through the glass slide-Au-Cr layers were determined using Equations 2.8 and 2.9 (Figure 3.2).

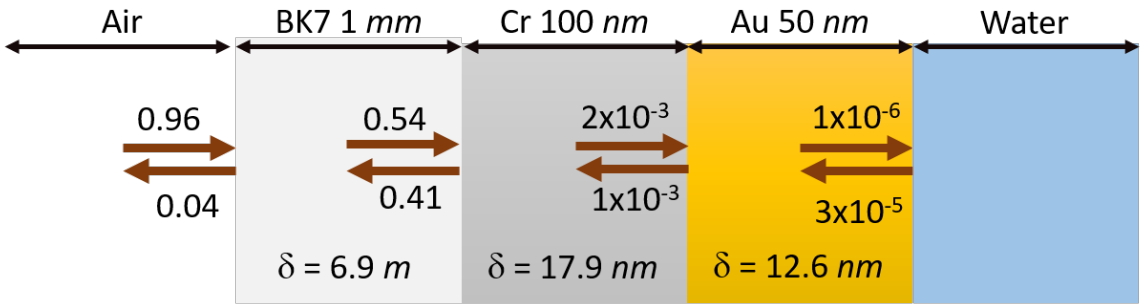

Fig. 3.2 Transmission and absorption at each interface calculated using Fresnel coefficient and the refractive index of each material. I assumed that all photons are perpendicularly incident at each interface. δ denote the penetration depth of each layer at 780 *nm*. From the initial intensity, 54% was available for absorption the Cr layer. A very small portion of the light reached into the water layer.

The air-glass slide interface transmission was quantified using the refractive index of BK7 [112]. At this interface, 96% of the light was transmitted and very little was absorbed due to the long skin depth of BK7 relative to the glass slide thickness. At the glass slide-Cr boundary, 41% of the initial power was reflected back and 54 % was available for absorption (calculated using the refractive index of Cr [113]). For a Cr thickness of 100 *nm*, 99.6% of the light transmitted into the layer was absorbed. The remaining reflected light was transmitted into the Au layer, which had a shorter penetration depth than Cr, and hence only one-millionth of the initial light reached into the water layer where the sample resided.

3.2.2 Thin film heat transfer simulation in an aqueous environment

An important aspect in the strength of the generated thermoelectric fields was the induced temperature and its associated gradient. The heating profile created by Cr absorption of near-infrared light was modelled using the heat diffusion equation (Equation 3.2),

$$\rho C_p \frac{\partial T}{\partial t} + \rho C_p \vec{u} \cdot \nabla T - \kappa \nabla^2 T = \vec{Q} \tag{3.2}$$

where ρ, C_p, and κ corresponded to the volume density, specific heat capacity at constant pressure, and the thermal conductivity of material where the heat was diffusing within, respectively [114–116]. The heating source was defined as $\vec{Q}$. The temperature profile could be affected by a fluid flow (denoted by $\vec{u}$), which could carry heat away. Hence, for a more comprehensive model of the temperature distribution, any induced flow caused by density changes in the fluid (due to temperature differences) was also taken into account by solving the Navier-Stokes equation (Equation 3.3)

$$\rho \frac{\partial \vec{u}}{\partial t} + \rho \vec{u} \cdot \nabla \vec{u} = -\nabla p + \nabla \cdot \left(-\mu (\nabla \vec{u} + (\nabla \vec{u})^T) - \frac{2}{3} \mu (\nabla \cdot \vec{u} \vec{I}) \right) + \vec{F}_{bouy} \tag{3.3}$$

where p was the pressure field of the fluid, $\vec{I}$ was the identity matrix, and $\vec{F}_{bouy}$ was the buoyancy force due to gravity [115, 117]. This form of the Navier-Stokes equation is for incompressible flow of a single phase fluid, whereby the maximum velocity of fluid is less than 0.3 *Mach*, which was expected in this work [114]. The momentum equation (Equation 3.3) and the continuity equation (Equation 3.4) were used to quantify the fluid flow.

$$\frac{\partial \rho}{\partial t} + \nabla \cdot (\rho \vec{u}) = 0 \tag{3.4}$$

The Navier-Stokes equation and the heat diffusion equation are inextricably linked. A change in the temperature or velocity field in one equation, directly changes the pressure, density, heat capacity and thermal conductivity values in the other. It should be noted that the time-dependent form of the equations were presented. For steady state solutions, the time derivative part was set to zero.

Comsol multi-physics software was used to solve the heat diffusion equation and the Navier-Stokes equation, as well as, coupling the physical parameters between the two, given a set of initial and boundary conditions (Figure 3.3). The glass-slide, fluidic chamber, and the coverslip were modelled as the geometry for which the heat diffusion and its consequential fluid flow were simulated. The entire geometry was modelled as a

2D-axis symmetric system (represented by the dashed lines in Figure 3.3a-b) to reduce the computation time. Each domain was assigned to a specific material, using the built-in physical material properties (C_p, ρ,etc.) within Comsol. The glass-slide and coverslip were considered to be silica glass, whilst the fluidic chamber was modelled to have the properties of water. The Heat transfer at the boundary between domains was also taken into account by the model and depended on the material properties and temperature differences across the boundary.

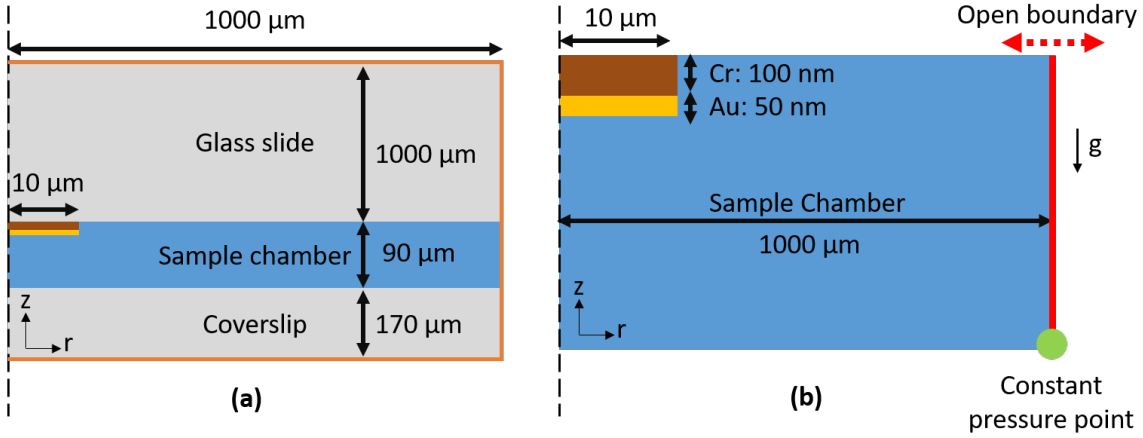

Fig. 3.3 **(a)** Geometry used to quantify the temperatures induced by Cr absorption of near-infrared light. The glass was modelled using Silica glass material properties. The brown and yellow boxes represent the Cr and Au. The Cr domain was defined as the heating source. The orange boundary around the geometry was set to the ambient temperature. **(b)** The direction of gravity (g) is in the -z-direction. The left side of the system was considered as an open boundary, which allowed free fluid flow in and out of the simulated region. The bottom edge of the sample chamber was considered as a constant pressure point, which was needed for an analytical solution for the Navier-Stokes equation.

For heat diffusion, all domains and boundaries initially started at ambient temperature (20 $°C$, T_{amb}). The outer boundaries of the system (orange lines in Figure 3.3) were set to T_{amb}, as the temperature was approximated to decay to ambient due to being a sufficiently large distance away from the heating origin. The Cr micro-disc's domain was designated to the heat source, with a heat density $\vec{Q}$:

$$\begin{aligned} \vec{Q} &= T_I \alpha_{Cr} I(r,z) \\ &= 0.54 \alpha_{Cr} \frac{2P}{\pi w_0^2} exp\left[-\frac{2r^2}{w_0^2}\right] exp\left[-z\alpha_{Cr}\right] \end{aligned} \tag{3.5}$$

where T_I (0.54), α_{Cr} (5.45×10^7 m^-1), $I(r,z)$, P, and w_0^2 (3 μm) were the transmission at the Cr interface, the linear absorption of Cr ($1/\delta_p$), the intensity of the near-infrared beam, the laser power, and the beam size, respectively. The exponential was the Beer-Lambert intensity decay with the Cr in the z-direction. The heat density was defined in the same manner as in Zhao *et al.*, who also modelled Cr absorption of laser light [109].

In conjunction with the heat diffusion, the initial and boundary conditions for the Navier-Stokes equation were also defined but only for water domain (Figure 3.3b). The contacting boundaries with the water domain was defined as a wall with a no-slip boundary condition (velocity of the fluid was zero at the wall since the wall was stationary). An open boundary was appointed at the right most margin of the system, which allowed fluid to freely flow in-and-out of the region, and thus effectively represented the actual size of the fluidic chamber, which was approximately an order of magnitude bigger in the r-direction than the modelled system. The initial pressure of the fluid, without the presence of heating was set to be 1 *atm*. Furthermore, a constant pressure point (1 *atm*) was designated at the lower-left edge of the sample chamber, which acted as the reference pressure. This position was sufficiently away from the heating source, and thus the pressure remained approximately constant. As the fluid flow was modelled as compressible ($\vec{u} < 0.3$ *Mach*), a constant pressure point was needed in order to restrict pressure variations within 5% from the reference pressure value [118].

The resulting temperature and flow field for a series of laser intensities (3-67 $\mu W/\mu m^2$, 100 -2000 μW) were simulated using an extremely fine mesh size (free-triangular meshing automatically generated by Comsol). The temperature was evaluated at 180 s (in steps of 10 s) after the laser was switched-on, matching the data acquisition duration for temperature measurements using fluorescence lifetime. The solutions were then imported into Python for plotting and analysis. Only the temperatures of the Cr, Au and water domain were of interest and shown in Figure 3.4b. The temperature of the glass slide and coverslip were also modelled to ensure that the heat dissipation was representative of the real system but were not considered for subsequent analysis.

For the highest intensity simulated (67 $\mu W/\mu m^2$), a peak temperature of $41°C$ was reached by water at the Au interface (Figure 3.4b). In the x/y-direction, the

temperature returned to ambient within 100 μm from the heating source (Figure 3.4b). There was a kink in the temperature profile which corresponded to the edge of the Au-, Cr-layer, and the temperature of the water layer on top of the glass-slide. This occured because of the higher thermal conductivity of Au and Cr, than water. In the z-direction, the temperature rapidly decayed, but did not reach ambient at the surface of the coverslip, which was 90 μm away from the heating source (Figure 3.4c).

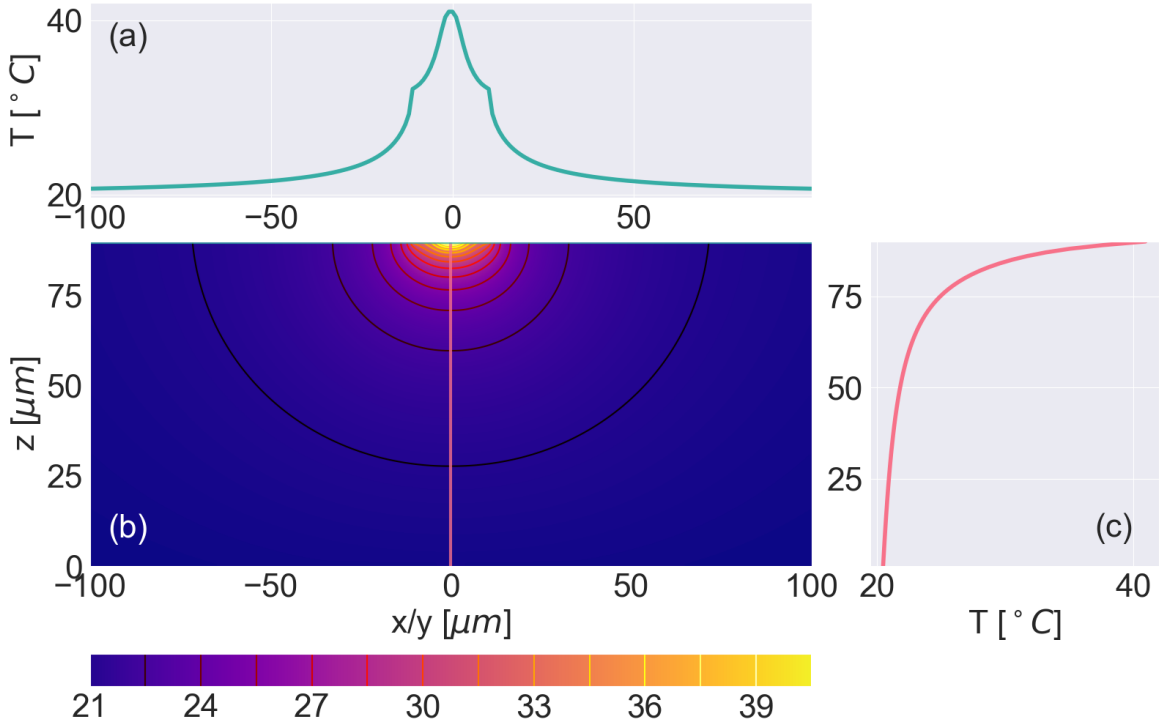

Fig. 3.4 Temperature profiles of Cr absorption of near-infrared laser light with an intensity of 67 $\mu W/\mu m^2$. For clarity, the temperature of the Cr, Au and water domains were only shown for a region of ± 100 μm in the r-direction (x/y-direction), rather than the entire ± 1000 μm. **(a)** Temperature profile in x/y-direction. The kink was due to the thermal conductivity difference between the Au-Cr-layer and water. **(b)** 2D temperature profile with isotherms of the heating generated. **(c)** Heating profile in the z-direction. The temperature did not fully return to ambient at the bottom of the fluidic chamber.

.

For lower laser intensities, the kink was still present for the surface temperature profile in the x/y-direction (Figure 3.5). The peak temperature rose linearly with increasing intensity (Figure 3.5 inset). Upon linear fitting, a slope of 0.314 $°C/\mu W/\mu m^2$ was obtained, with an intercept value of T_{amb}. Hence, a laser intensity of 254 $\mu W/\mu m^2$ (7.2 mW given a beam size of 3 μm), would cause the water to boil.

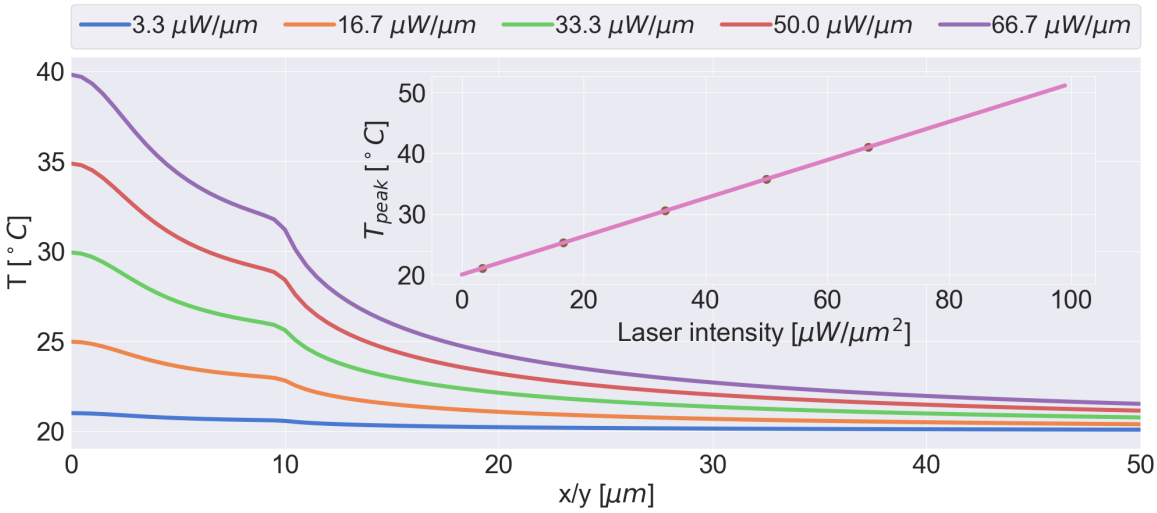

Fig. 3.5 The radial (x/y-direction) temperature profiles at the surface of the glass slide for a variety of laser intensities. Only half the temperature profile was shown, and was symmetric around the vertical axis. The kink in the profile originated from the differences in the thermal conductivity of the Au-Cr layer and water. Inset: The peak temperature increased linearly with intensity.

The extent of the heat dissipation was defined by quantifying the full-width-half-maximum (FWHM) in both the x/y- and z-direction. This was found to be 20.8 μm and 9.7 μm, respectively, for all intensities. Whilst the peak temperature rose with intensity, the FWHM did not since it was determined by the geometry and thermal diffusivity of the materials within which the heat is dissipating. Normalising the temperature profiles for each intensity and direction, would yield the same temperature profiles which would be perfectly overlayed on top of one another. The temperature dissipation was more extensive in the x/y-direction, as the heat was spread by the Au-Cr thin-film which had higher thermal diffusivity than water. In the z-direction, the heat was carried away by the silica glass, which had a larger heat diffusivity than water (3.4×10^5 $\mu m^2/s$ and 1.43 $\times10^5$ $\mu m^2/s$) [119].

3.2.3 Temperature induced convective fluid flow

The temperature profiles in both direction decayed to approximately T_{amb} in $\pm$ 100 μm from the heating source, for the highest laser intensity modelled (Figure 3.4). The variations in temperature resulted in density differences within the fluid. This induced convective fluid flow which served to equilibrate the differences. This mechanism cooled the system, as the heat was carried away by the flowing fluid, and thus affected

the steady-state ($t = 180\ s$) temperature profile. It was for this reason that the solution of heat diffusion equation was coupled into the Navier-Stokes equations, and vice-versa. The steady-state fluid flow, given the temperature profile of Figure 3.4 with an initial velocity of 0 $\mu m/s$, was determined for both directions using the temperature-coupled Navier-Stokes equation. The flow field was then calculated by determining the magnitude and direction for every evaluated positional velocity in the two directions (Figure 3.6). For increased resolution, only the positive half of x/y-direction was shown, and the heat source was at the top left corner of Figure 3.6.

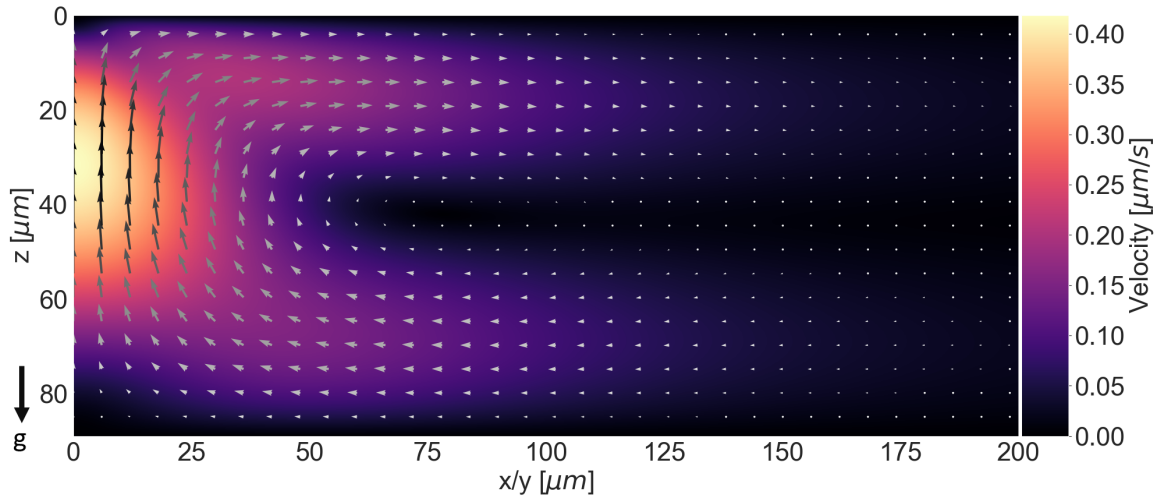

Fig. 3.6 Induce convective flow of the fluid due to the temperature profile of Figure 3.4. The length of the arrow was proportional the magnitude of the velocity. The flow field was symmetric about the vertical axis, and the heat source was at the top left corner. The direction of gravity was denoted by the black arrow (used in F_{bouy} in Equation 3.3). The convective flow was clockwise with a maximum velocity of 0.42 $\mu m/s$, which occurred at 30 μm directly above the heating surface.

Note that the buoyancy force due to gravity was also taken into the account when determining the flow velocity in the z-direction (direction of gravity shown in Figure 3.6). The flow velocity was higher in the z-direction, compared to the x/y-direction, due to the more confined heating profile. A maximum velocity of 0.42 $\mu m/s$ occured at the central axis, at ca. 30 μm above the surface of the heating source. The magnitude of the velocity was very similar to the values reported by Roxworthy *et al.*, for a similar geometry and heating profile [120]. The flow direction was clock-wise, and extended to approximately 200 μm, after which, the velocity was diminished everywhere. The flow direction was the same as in the simulations conducted by Wang *et al.* in a very similar experimental geometry [121]. The fluid was circulated as a result of the density

and pressure gradients mediated by heat dissipation profile. The central position of the circulating flow was approximately 75 μm, and 42 μm away from the heating source in the x/y-, and z-direction, respectively. Note that the fluid flow was solved for a 2D-axis symmetric system and therefore the 3D flow profile was toroidal-like in shape.

If the temperature induced convective flow is the dominating force acting on a tracer particle used to map out the flow profile of the fluid, then the drag force experienced by the particle would be directly proportional to the velocity of the fluid at any given point. Any tracer particles near the heated spot would be carried away from the heat source. However, if the velocity or direction differ from the profile of Figure 3.6, then it is likely that the dominating force on the tracer particle is not the temperature induced convective fluid flow.

3.2.4 Thermoelectric field generation mediated by temperature gradients

In the presence of a temperature gradient in a fluid containing charged particles, the separation of ions can occur, which subsequently generates the aforementioned thermoelectric field (E_T). The field strength is directly proportional to the temperature and its corresponding gradient. Hence, the spatial derivative of the temperature profile in Figure 3.4 was numerically calculated for both directions (Figure 3.7).

The gradients were concentrated near the heating source in both axis, being higher in magnitude in the x/y-direction. There were two main strong gradient regions in the x/y-span corresponding to the edges of the Au-Cr micro-disc, and around $\pm 3\mu m$ from the heating source (Figure 3.7a). In the z-direction, the temperature gradient was almost entirely located over the Au-Cr micro-disc, being highest in magnitude approximately 1 μm above the surface of Au.

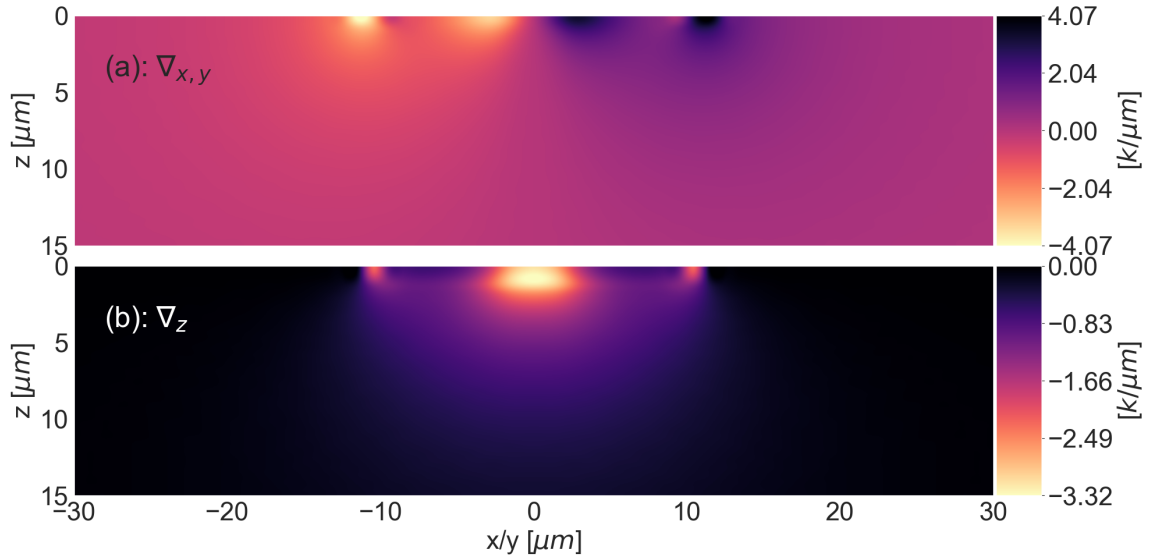

Fig. 3.7 Temperature gradients determined numerically in the x/y- **(a)**, z-direction **(b)**, using data from Figure 3.4. The magnitude of the gradients in the x/y-direction are higher than the z-direction. A noticeable temperature gradient is present at the edge of the Au-Cr disc in both directions.

In this work, the separation of sodium-, and azide-ions was used to generate thermoelectric fields. Hence, the theoretically obtained thermal gradients of Figure 3.7, could have been used to estimate the strength of the field (using Equation 3.1). However, the Soret coefficient of azide is not reported in literature, and therefore a theoretical field strength for the generated field measured in this work could not be evaluated. Instead, the typical field strength for a common salt was considered, which has been ubiquitously used for biological work. The Soret coefficient for sodium (4.69 $\times 10^{-3}$ $1/K$) and chloride (7.18 $\times 10^{-4}$ $1/K$) have been previously reported [69]. The concentration of physiological saline solution is 154 mM of sodium chloride [122], and the fluidic chamber of thermo-electric devices used herein was approximately 3 μl, which meant that 46 μ-moles of each ion were present in the sample chamber. Using this, the temperature profile of Figure 3.4 and the gradients in Figure 3.7a-b, the thermo-electric field in each direction was calculated (Equation 3.1). The maximum resulting thermo-electric field was -40.2 V/m, and -179.1 V/m in the x/y-, and z-direction, respectively. If a tracer particle with an electrophoretic mobility of -5 is used $\mu mcm/Vs$ (corresponding to the tracer particles used herein), then its velocity would be proportional to the strength of the electric field in each direction ($\vec{v} = \mu_e \vec{E}$), and would therefore, map the thermo-electric field (Figure 3.8).

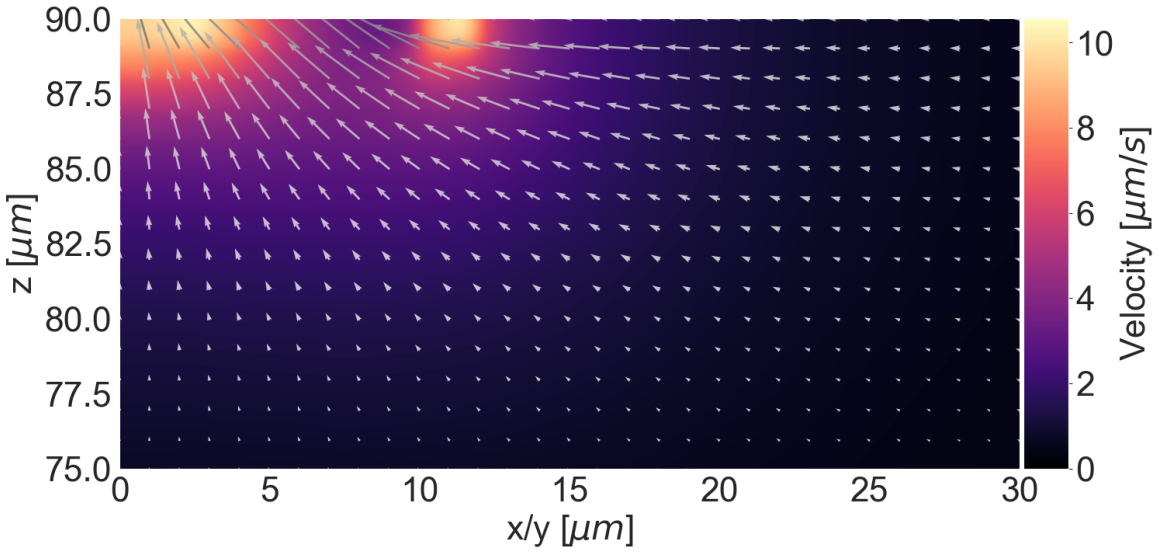

Fig. 3.8 The velocity of a negatively charged tracer particle experiencing the thermo-electric field generated by sodium-, and chloride ions at physiological concentrations. The heated region was in the top left corner, and only half the fluidic chamber was shown for clarity. There were two regions of high velocity corresponding to the edge of the Au-Cr, and the centre of heated spot.

The tracer particle would be drawn towards the heating spot, with ever increasing velocity since the strength of the field is increasing. Hence, moving the laser spot, would also relocate the centre of the thermo-electric field. The velocity profile in Figure 3.8 was higher by an order of magnitude compared to the convective flow induced by the presence of temperature variations Figure 3.6. Furthermore, the direction of flow between the two effects were opposite in direction: towards the heating spot, rather than away in the x/y-direction.

For the tracer particle to be trapped, an opposing electric field must be present with an equal magnitude. The equilibrating field can originate from the build-up of charge on the Au-surface, as is the case in the work presented herein.

The strength of thermoelectric field generated by sodium chloride was small because the Soret coefficient of sodium is about 6-times larger than the chloride one [69]. The strength of the thermoelectric field increases with the difference in Soret coefficients of the ions.

3.3 Experimental setup and methods

3.3.1 Microscale thermometry using fluorescence lifetime imaging

Measurements of the temperature gradients in the fluid induced through the absorption of near-infrared light by the Cr thin-films enabled quantification of the Soret coefficient for the both the polystyrene nano-spheres, and the ions in the solution. This required measuring the temperature distribution on the micro-scale.

Contact methods of microscale thermometry, such as the use of a micro-thermocouple [123], or a modified atomic force microscopy tip [124], can themselves act as a heat sink as they are usually made of higher thermal conductivity materials such a metals, instead of water. Non-contact methods rely on the physical properties of temperature tracers, such as the emission intensity of a dye, the refractive index change of the solution, or the emissivity of the material [125]. Rhodamine-B dye is a ubiquitous temperature (and viscosity) tracer in optical methods of microscale thermometry. Its sensitivity to temperature is a consequence of the flexibility of the diethylamino groups, which can rotate when the molecule is in its excited state, relative to the viscosity of its environment, and thus affect its quantum yield [126, 127]. This manifests as a reduction in the emission intensity and lifetime with increasing temperatures. Both quantities can be used to quantify temperature on the microscale. Intensity based measurements require the use of an additional, non temperature sensitive dye to normalise for laser fluctuations, and are therefore system specific [128]. Lifetime based measurements are more absolute but require fast electronics.

Herein, microscale thermometry was conducted using the fluorescent lifetime of Rhodamine-B, by using Time Correlated Single Photon Counting microscopy (TSCPC).

3.3.1.1 TCSPC fluorescence lifetime imaging

The characteristic lifetime decay of Rhodamine-B was determined by enumerating the photon arrival time from specific points of the sample using confocal microscopy architecture.

A 40 *MHz* pulsed Supercontinuum laser was used as a white light source, which was filtered by a 543 ± 11 *nm* spectral filter, to generate the excitation light needed for the Rhodamine-B molecules (542 *nm* peak). Steering mirrors (M1, M2, and M3) were used to couple the laser into the microscope's galvo-mirrors, scanning lens and imaging objective (Figure 3.9). The laser spot was scanned across the sample, and the emitted photons from the Rhodamine-B dye were collected by the imaging objective (Olympus 60x oil). The emitted light then passed through a beam-splitter (80:20), the confocal pinhole (300 μm), and was then spectrally selected using a 629 ± 28 *nm* bandpass filter. The laser pulses were time referenced by the PMT (Becker and Heckle) in order to discern the photon arrival times for a given segment of the sample. The excitation spot was scanned across the sample, and the emission of the Rhodamine-B dye collected, forming an image of the lifetimes, with each pixel containing its own intensity decay trace.

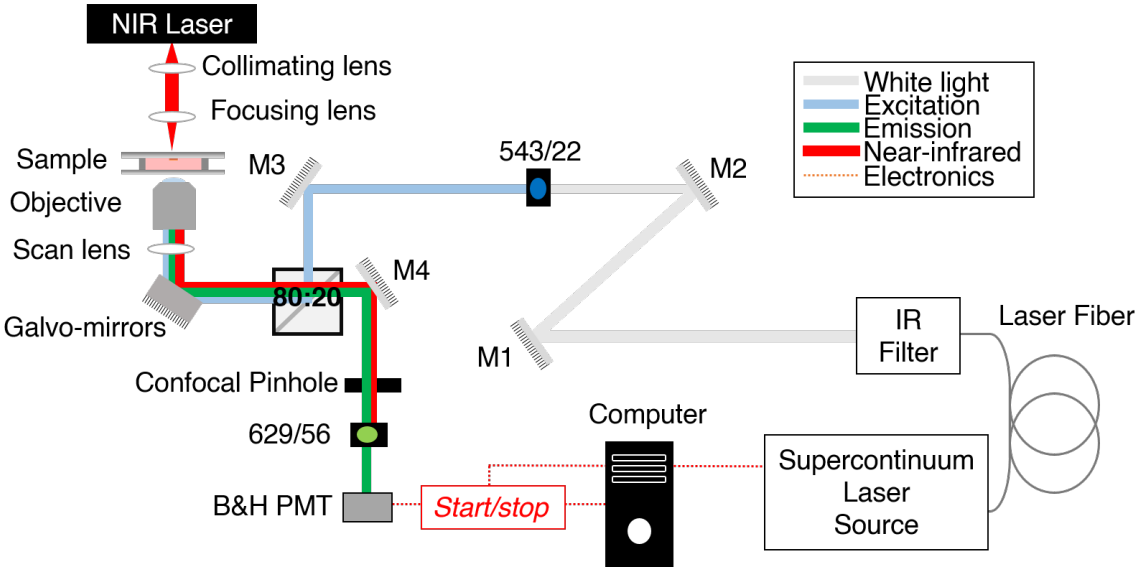

Fig. 3.9 A supercontinuum laser source was used to create a white light laser source. The infrared component of the generated light was filtered out, leaving just the visible spectrum for excitation of theRhodamine-B dye. A bandpass filter was used to select only 543 ± 22 *nm* range of the visible spectrum. This filtered light was then coupled into the microscope's focal plane, and was scanned across the sample by the x-y galvo-mirrors. The emitted fluorescence was collected by a fast photo-multiplier tube (PMT) synchronised with the emitted laser pulses. The near-infrared heating laser was also shown for completeness. The excitation and NIR light was filtered out by a 629 ± 56 *nm* bandpass spectral filter. Confocal TCSPC microscope built by the Laser Analytics group.

The TCSPC system has an associated response time, due to photon time of flight, and the electronics dead time, known as the instrument response function (IRF). The IRF was characterised by measuring the photon arrival times by reflecting them from a coverslip, set at the focal point of the imaging objective. All subsequent lifetimes were derived with respect to the IRF's peak position (Section 3.3.1.3).

A series of scans were performed for each sample in order to collect enough photon counts per pixel (ca. >1000 peak value), from which the lifetime was extracted. Nominally, a scanning duration of 3 minutes was used for each measurement (8 μs dwell time per pixel). For samples where the emission intensity was lower, the acquisition time was increased.

The near-infrared Cr heating laser was also shown in Figure 3.9 for completeness, and was discussed in greater detail in Section 3.3.2.1.

3.3.1.2 Temperature-lifetime calibration stage

The chosen method of microscale thermometry was the use of Rhodamine-B lifetime as temperature sensors. This required a calibration relation between the fluorescence lifetime values of Rhodamine-B at a range of temperatures. A heating stage was needed to heat up Rhodamine-B solution and to keep it at constant temperature, as well asa window that the solution could be imaged through. The thermal mass of a metallic block with a hole in its centre, acting as a sample chamber, was used to heat up and sustain the temperature of the Rhodamine-B solution. Cartridge heaters encased into the metallic block induced heating (Figure 3.10a). The temperature of the heating stage was maintained using a thermocouple (embedded in the metal) and a temperature controller (Figure 3.10b). A second thermocouple was used to monitor the temperature of the Rhodamine-B solution. There was approximately a 0.2 $^{\circ}C$ difference, between the two thermocouples (TC1 and TC2, Figure3.10a).

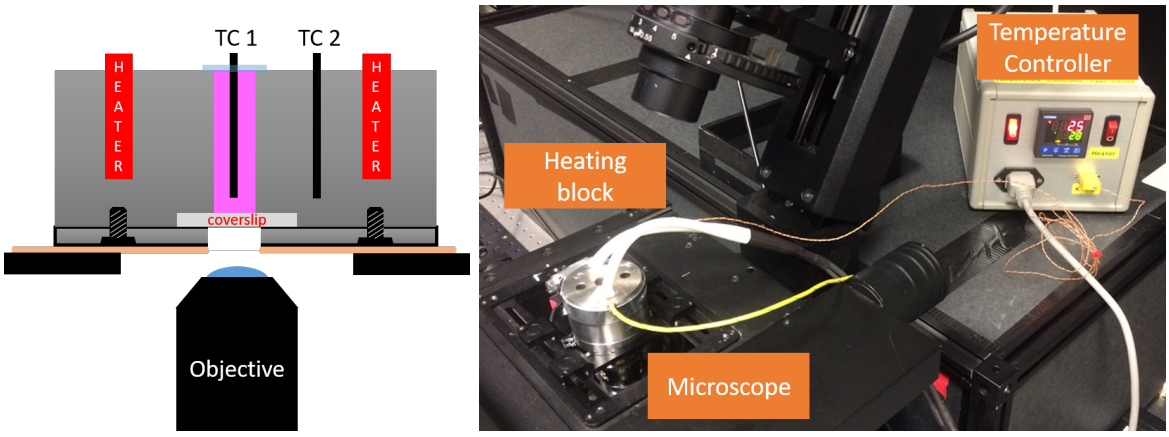

(a) (b)

Fig. 3.10 **(a)** Schematic of the heating stage built to calibrate the lifetime response of Rhodamine-B at different temperatures. Two cartridges heaters and a temperature controller used to keep the Rhodamine-B solution at a fixed temperature. Two thermocouples were used to monitor the temperature of the block and the solution. An imaging window was factored in the design to excite and collect the emitted fluorescence of the dye. The microscope was isolated from the heating block with an insulating material (orange band). **(b)** Showing the heating stage and temperature controller in operation on a microscope. Green wire was for earthing the device. Second thermocouple not shown in this diagram. Heat stage and electronics made by the working shop at chemical engineering. Design conceived by the author.

A bottom plate was screwed into the metallic block, which sealed the sample chamber using a coverslip and an O-ring, and provided an imaging window. A thin insulation material was used to shield the microscope stage from the heat of the temperature stage, retarding heat transfer between the them.

Approximately 2 ml of Rhodamine-B solution (20 μM), was pipetted into the sample chamber of the heating stage. The top of the sample reservoirs was sealed with parafilm to stop evaporation of the solution. The solution's thermocouple pierced through the parafilm, and was pushed down until it reached the coverslip. The tip of the thermocouple was imaged using the TSCPC microscope, from which the temperature dependent lifetime was derived. For each set temperature of the heating stage, a corresponding lifetime was recorded after equilibrating the temperature of the solution for two-minutes. The thermocouples used had an accuracy of $\pm$ 0.1 $^{\circ}C$. The electronics of the temperature controller and the heating stage was made by the Department of Chemical Engineering and Biotechnology.

3.3.1.3 TCSPC FLIM data analysis

The time-correlated data sets (*.sdt* file format used by Becker and Heckel) were analysed using Omero FLIMfit [34]. Once the non-spatially varying IRF and the measurements files were loaded into the software, a small region of interest from the intensity images was defined, from which preliminary single exponential fits were performed. This initial fitting to small subset of pixels ensured that pixel-wise fitting for the the entire dataset yielded small residuals. The *IRF Shift Estimator* function of FLIMfit was used to temporally synchronise the IRF peak with the measured data peak (Figure 3.11). This step defined the reference time point ($t = 0$), from which the decay lifetimes were determined.

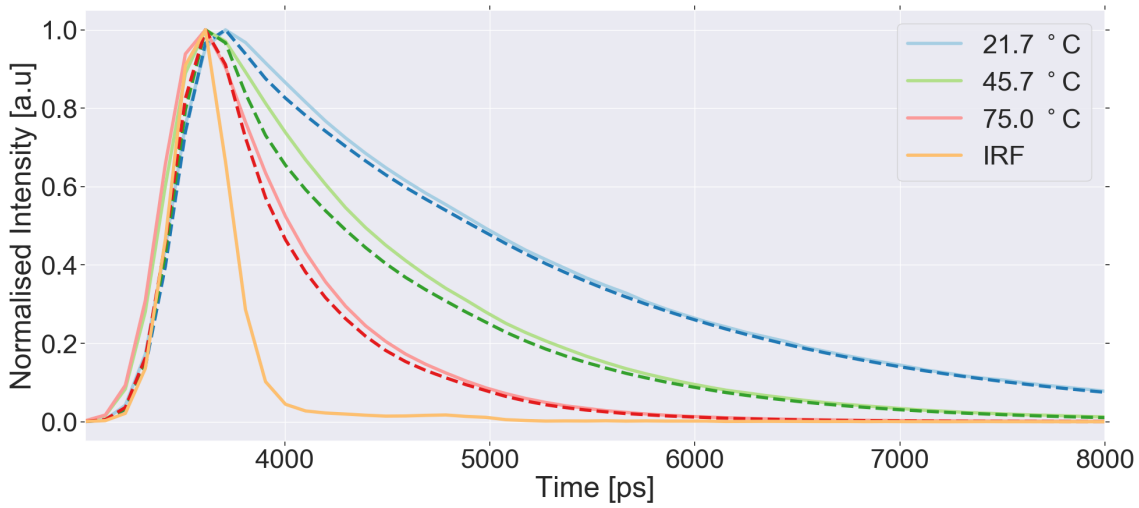

Fig. 3.11 Example preliminary fits (dashed lines) from the temperature calibration dataset (solid lines) for three different temperatures set on the heating stage. The IRF defined the time reference from which the characteristic decay time was determined. Data analysed and extracted using Omero FLIMfit [34].

The pixel-wise characteristic decay values obtained from single exponential fitting were then saved as *Tiff* images and analysed with *Python* scripts, where the lifetimes were converted into a temperature using the coefficients of the lifetime-temperature calibration curve fitting (Section 3.4.1.1).

3.3.2 Building a thermoelectric device

There were two steps followed to generate microscale temperature gradients and its subsequent electric field. Firstly, a near-infrared laser source was needed to induce

heating of Cr. Additionally, Cr thin film structures were needed to be patterned on glass and housed in a microfluidic chamber, where temperature gradients could be induced in the sample solution. Both parts needed to be mounted on conventional microscopes for imaging and characterisation of the thermo-electric fields.

3.3.2.1 A custom near-infrared laser device for Cr heating

A custom laser device was made to provide near-infrared laser light that was absorbed by the chromium thin film discs. The diode and its associated optics had to be compact and easily integratable with Olympus IX70 and IX71 inverted microscopes (microscopy frames for the TCSPC and fluorescence). This was achieved by building a device that fitted into the condenser lens holder of the microscope Figure 3.12. This was advantageous as the condenser's positioning screws and focusing reel were used to align the laser onto the chromium discs. All components of the device were mounted onto 30 *mm* cage plates, which were clamped onto the condenser holder. The whole device weighed less than the objective lens which ensured that the rack and pinion system of the focusing reel were not under excess load and therefore maintained a constant position.

A diode with two emitters was used to provide laser light; red (657 *nm*) for alignment proposes and a near-infrared (780 *nm*) for chromium heating. Only one emitter was used at any given time and powered by a variable current source which allowed for tunability in the emitted laser power (electronics designed by the Cavendish Electronic Suite). Each laser source was modulated using a MOSFET and an Arduino Uno. The lasers were always operated in continuously-on mode using the digital pins of the Arduino. The diode power source and control box were connected to the diode (mounted in the 30 *mm* cage system) via a dedicated cable which had an electrostatic discharge protection board. The laser diode casing was in direct contact with a cage mount which acted to passively temperature stabilise it.

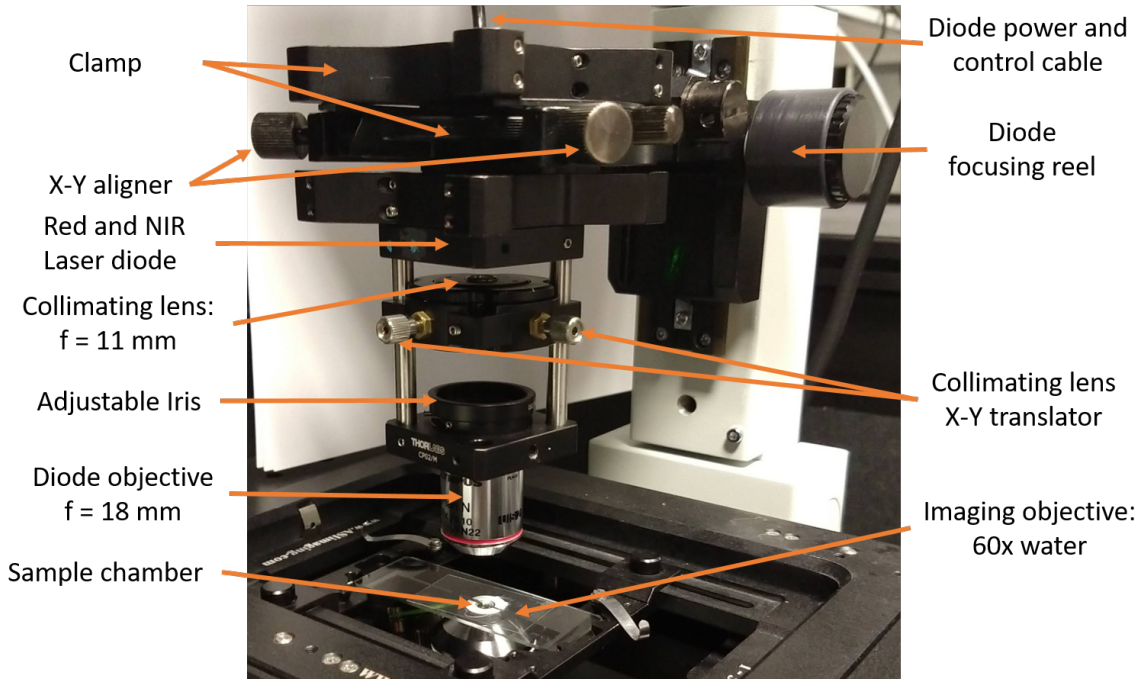

Fig. 3.12 Optical set-up of the near-infrared laser. The laser and its optics were designed to replace the condenser lens. A lens pair was used to image the laser diode on the back-facet of the Cr micro-disc, and thus induced a localised heating spot. The alignment of the laser was done using the adjustment screws of the condenser, and its focusing reel.

An image of the emitting diode was formed on the same focal plane as the imagining objective. A lens pair was used to collimate and focus down the laser light, with a magnification of 1.6x (ratio of focal length). The magnification was kept low to ensure a beam size smaller than the width of the chromium micro-discs and that all the laser light was absorbed. An aperture was used between the pair of lenses to cut out stray light from the emitting diode. The focusing diode objective was chosen to have a long enough focal length to provide clearance when loading and unloading the glass slide with the printed micro-discs, without moving the laser device. This meant that the system only needed to be aligned once.

When the focal point of the diode objective was coincident with the imaging objective, X-Y alignment thumb screws of the condenser were used to position the beam inside the field of view of the imaging camera. Once aligned, the position of the laser beam did not drift or go out of focus, even when samples were changed.

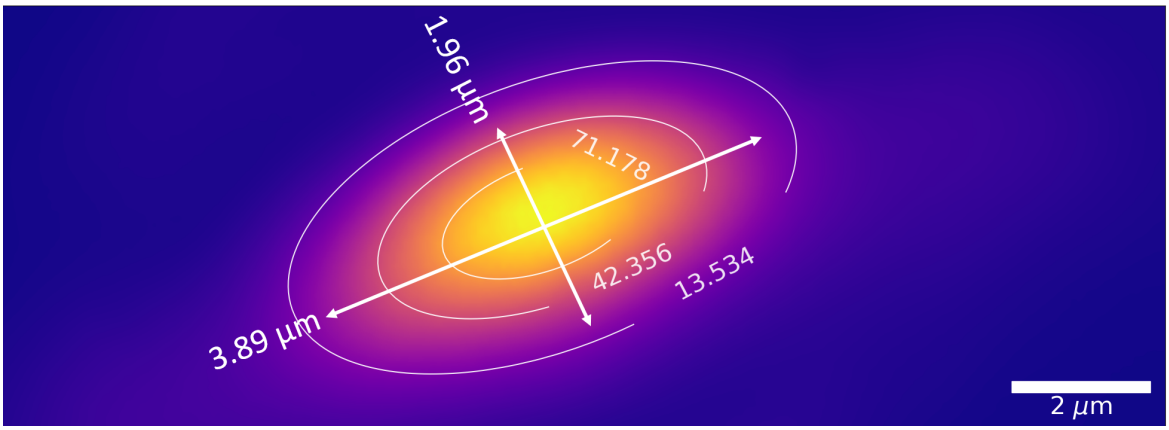

Fig. 3.13 Imaging the beam shape and determine the size at the focal point of the focusing lens. The background layer is the image taken with a camera (using the set up in Figure 3.16, and the contour lines are 2D-Gaussian fitting. Each level showed the percentage away from the peak. The beam spot size (w_0) was at 13.534% ($1/e^2$) from the peak value. The beam was almost double in one axis than the other, with a nominal size of 2.92 μm.

An important property of the near-infrared laser was its size (w_0) at the focal plane of the focusing lens. This value was needed to discern the relationship between heat generation of the Cr micro-discs and the intensity of the laser beam. The focal spot size was measured by imaging it with camera (using the set in Figure 3.16), and fitting the image to a 2D Gaussian profile (Equation in [100]). The shape was found to be elliptical, with its major axis being almost double in size than the minor axis (Figure 3.13). The mean size of the beam was determined to be 2.92 $\pm$ 0.51 μm ($w_0 = 1/e^2$ value from the peak), with the error originating from repeated measurements of matching the focal plane of the focusing objective and the imaging objective.

3.3.2.2 Fabricating a microfluidic heating chamber

The use of costly and time consuming conventional fabrication methods such as photolithography was bypassed by using Transmission Electron Microscopy (TEM) grids and a template mask. Grids with a circular array of 20 μm diameter holes (Agar Scientific) were chosen to pattern the thin film micro-discs on glass slides, by deposition of metals through the holes.

The glass slides were first cleaned using acetone and isopropyl alcohol, and nitrogen dried. The TEM grids were positioned on the glass slide using tissue paper, as the use of tweezers warped their shape. Two TEM grids were positioned at the centre of the

slide separated by approximately 2 *cm* along the larger dimension of the glass slide. Transparent tape was used to affix the grids onto the glass slide, ensuring that the central holes were not covered. The thin films were then deposited (100 *nm* Cr and 50 *nm* Au) over the entire glass slide (deposition done by Dean Kos, Nanophotonics Centre). Before peeling back the transparent tape and TEM grid, the layering of Au and Cr deposited through the holes were inspected with a *darkfield* microscope to examine coverage and surface roughness (Figure 3.14a). There are many scattering sites in each hole. Hence, the Au layer had surface roughness. However, this was unlikely to affect the heat generation of the thin film.

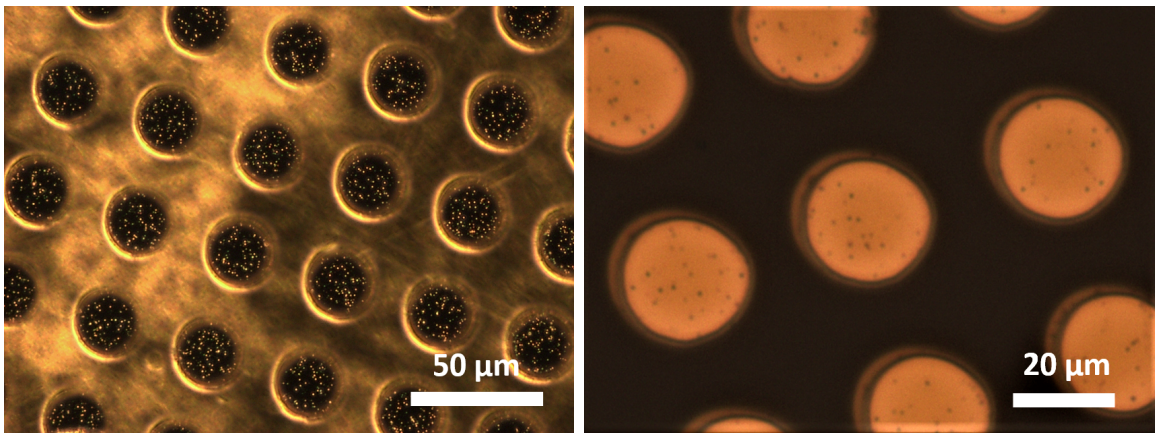

(a) (b)

Fig. 3.14 **(a)** Imaging the deposited Au surface through each hole of the TEM grid before peeling it off. The image is taken in darkfield to highlight the scattering and surface roughness of the deposition. **(b)** After peeling away the TEM grid, the resulting micro-discs are elliptical in shape, and have shadowing effects from the deposition angle. Au and Cr deposited by Dean Kos, Nanophotonics centre.

After peeling away the tape and TEM grid, the remaining structures were again inspected under a microscope (Figure 3.14b). The thin film structureswere elliptical in shape and had a 'shadow', arising from the deposition angle through the perforated TEM grid. This was evident from the fact that the angle of the shadows for each microstructure was the same. These artefacts were unlikely to affect the heating profile since the laser beam spot size was smaller than the structures.

With the thin film heating pads deposited on the glass slide, a microfluidic chamber was needed to contain the sample solution. A sticker, usually used for reinforcing

hole-punched paper, was used as a fluidic reservoir. The height of the sticker was measured to be 90 ± 5 μm using a digital vernier calliper. The sticker was positioned on the glass slide using tweezers such that micro-heating pads were at its centre (Figure 3.15).

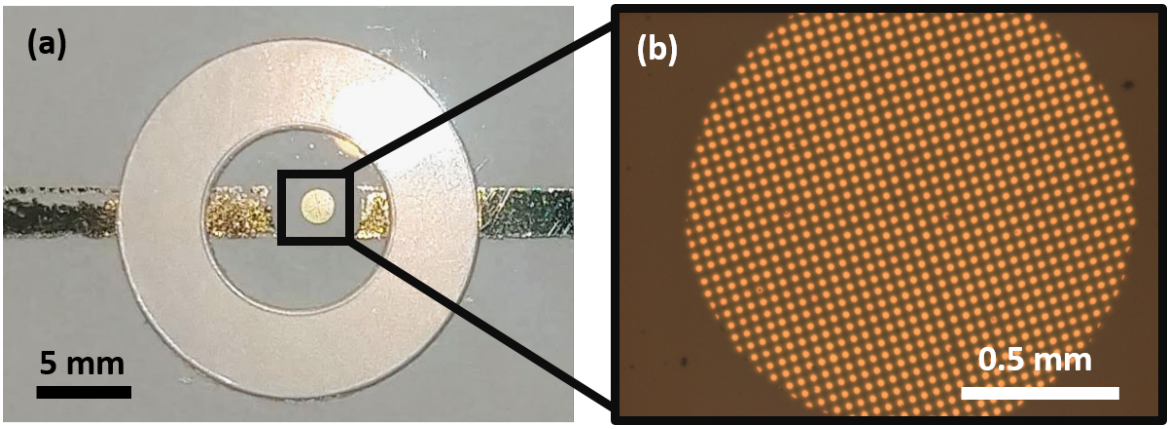

Fig. 3.15 **(a)** A fluidic reservoir created by a sticker which had a height of 90 μm. **(b)** The sticker was placed centrally over the deposited Au-Cr micro-discs. The chamber accommodated up to 5 μl of sample solution. A coverslip was then placed on top to seal the chamber and provide a flat imaging window. The coverslip could then be removed after imaging, and the chamber cleaned using the drip and drag technique used for cleaning optics.

This circumvented the need for conventional microfluidics using PDMS since flow of the sample solution was not required. Around 5 μl of sample solution was needed to fill the entire chamber. Then a coverslip was placed on top to seal the device temporarily. The sample was exchanged by removing the coverslip and dragging lens tissue on the microstructure to remove excess solution. Finally, the drip and drag method of cleaning optics with methanol and lens tissue was used to remove any debris attached on the surface of the microstructure or the glass slide.

3.3.3 Quantifying the thermoelectric field

To quantify the strength and distribution of the thermoelectric field, a carboxylate modified polystyrene spheres (26 nm diameter) were used as tracers particles. The nanoparticles were suspended in distilled water and 2 mM of sodium azide, which was used to stop the growth of bacteria in the solution. The separation of the sodium anion and the azide cations generated the thermoelectric field, which then affected the motion of the tracer particles. By quantifying the electrophoretic mobility (μ_e) and

velocity of the polystyrene nanoparticles in the solution, the thermoelectric field was determined ($E_T = v/\mu_e$).

The polystyrene tracer (made by Invitrogen FluoSpheres Lot: 1802239) beads were surface modified with carboxylate groups to inhibit aggregation of the beads through charge stabilisation [129]. The beads were fluorescently tagged with a red emitter embedded inside the sphere, which made them visible under a florescence microscope.

3.3.3.1 Imaging the motion of fluorescent nanoparticles

The motion of the charged nanoparticles in the presence of the thermoelectric field were captured using a florescence microscope (Figure 3.16a). A 561 nm laser was coupled into the microscope to excite the beads, and a notch filter (600 $\pm$ 37 nm) was used to filter out the excitation light and the near-infrared laser, and to only let though the emitted light from the beads (Figure 3.16b).

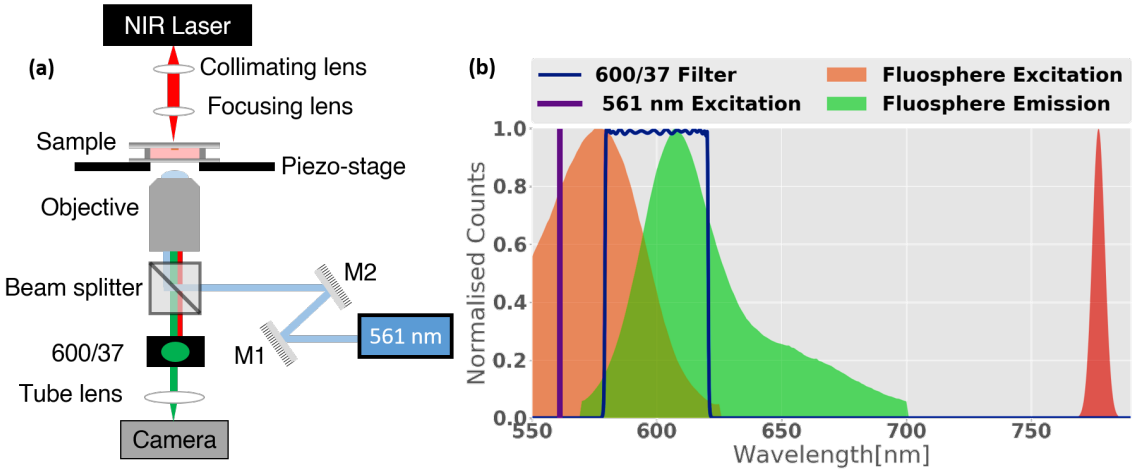

Fig. 3.16 **(a)** Fluorescence widefield microscope schematic which also included the thermoelectric device and the near-infrared laser used to induce heating of Cr. A 60x 1.3 NA water objective was used for imagining the Au-Cr and glass surface. The high numerical aperture meant that it had a shallow depth of focus. **(b)** Fluorescence emission and excitation spectra of the FluoSphere polystyrene beads. The 561 nm excitation laser and the 780 nm near-infrared laser were filtered out using a bandpass filter so that only the emission of the beads was imaged by the camera.

The near-infrared laser was mounted over the thermoelectric device, with its focal position matching the same plane as the imaging objective's (60x 1.3 NA water) focal plane. The sample rested on a piezo-stage (ASI imaging) which could move the sample

in all three-axes with increments of a few nanometres. The microscope also had an spatial light modulator (not shown in Figure 3.16a) to generate patterns for structure illumination microscopy, which enabled sub-diffraction imaging. However, this feature was not used due to slow refresh rate of the spatial light modulator with respect to the movement of the nanoparticle.

A Hamamatsu 16-bit camera, which was cooled to reduce noise (ca. $10°C$), was used to collect the light from the imaging plane of the objective. A series of 2000 frames were collected for each dataset, over a region of 512 by 512 pixels, with a frame rate of 43.47 frames per second. The pixel size was calibrated with a mm grid with 10 μm divisions, and corresponded to 83 nm per pixel. In all instances, a 1 mW (at the source) fluorescence excitation beam power was used. Higher laser powers quickly saturated the camera when the beads were trapped over the Au surface, which acted as a mirror for the emitted fluorescence. However, the large dynamic range of the camera meant that even dim particles were detected.

3.3.3.2 Video rate nanoparticle tracking

The Laplacian of Gaussian method (described in Section 2.3.6) was used to determine the particle locations frame by frame. A search range of 1-10 pixels (radius) in steps of 0.5 pixels was chosen to identify particle positions. The range was selected to limit the detection of out-of-focus particles and aggregated particles.

Once the locations were detected for each frame, the particle positions were linked into trajectories using the *link dataframe* function of *Trackpy*. Identified particles were connected if their successive displacement was less than 15 pixels. Higher displacements values yielded spurious linking of trajectories. However, the current value used did yield tracks which, by visual inspection, appeared to belong to a one trajectory but instead split into two or more tracks by linking function (Figure 3.17). Possible trajectories were identified by taking the standard deviation of each pixel across the entire 2000 frames. If a particle traversed across a pixel, its standard deviation increased. Hence, pixels with a higher standard deviation traced the motion of particles across the image.

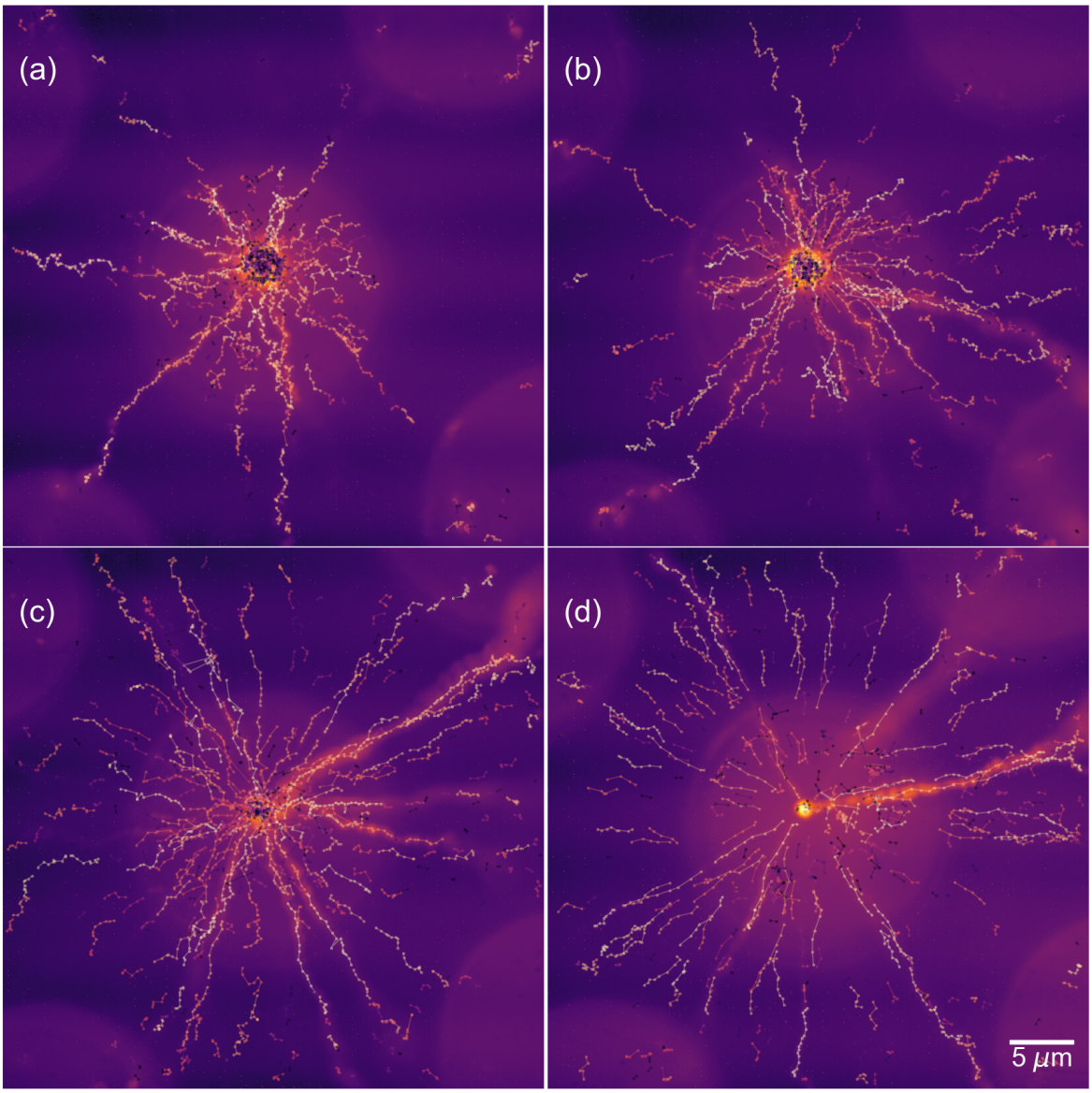

Fig. 3.17 Particle trajectories with increasing laser power. Each identified path has a different colour. **(a)** 1.2 $\mu W/\mu m^2$. **(b)** 1.7 $\mu W/\mu m^2$, **(c)** 2.7 $\mu W/\mu m^2$ **(d)** 8.4 $\mu W/\mu m^2$. Background image shows the standard deviation for each pixel across 2000 frames. Pixels with higher standard deviation show the streaked motion of the particles. Banding in images is a result of the spatial light modulator projecting a pattern for structured illumination microscopy. The background images are intensity normalised and presented using a logarithm scale for increased contract.

Particles were drawn into the centre of the Au-Cr micro-disc, where the heating source was located. More trajectories were identified over the Au surface. This occurred because particles were brought into focus by the presence of the thermoelectric field (refer to flow profile in Figure 3.8). Moreover, the emitted fluorescence from the

nano-spheres was reflected by the Au surface into the camera. Thus the nano-spheres have a higher intensity, which increases their propensity to be identified as a particle.

Lower near-infrared laser intensities (Figure 3.17a) resulted in the accumulation of more particles at the heating source than higher intensities (Figure 3.17b-d). At the highest intensity (8.4 $\mu W/\mu m^2$), particles were brought into the centre and then pushed out of focus, and only a single particle was trapped. Some of the particle tracks were also discontinuous over Au-Cr edge for this intensity.

For analysis of the particle velocities, the detected trajectories were converted into polar-coordinates, utilising the symmetry of the tracks with respect to the centre of the heating source (identified as the position of maximal intensity from the background images of Figure 3.17). This simplified the comparison of instantaneous velocity between each particle, as a function of its distance from the heating source.

3.3.3.3 Nanoparticle hydrodynamic and electrophoretic mobility measurements

Assessment of the thermoelectric trapping field required quantification of the electrophoretic mobility of the polystyrene particle. This meant subjecting the nanoparticle to a known electric field and measuring its velocity. In addition, the polystyrene nanoparticles were traversing a temperature field, hence the electrophoretic mobility was quantified as a function of temperature using a Malvern Zetasiser device. The viscous drag, or the ion exchange at the slipping plane of the nanoparticle, was expected to change with temperature.

A folded cell cuvette (Malvern) with electrodes either side of its U-shaped channel (Figure 3.18 inset) was used to apply a potential difference to the sample solution. This accelerated the nanoparticles' movement either towards the negative or positive terminal, depending on their charge. Doppler velocimetry of the scattered light from the nanoparticles was then used to quantify the electrophoretic mobility at a set temperature of the sample solution (Malvern Zetasizer [130]). Two metallic plates which attached to the front and back of the cuvette were used to heat up the sample solution, which was equilibrated for 2 minutes before the electrophoretic mobility was quantified. The electrophoretic mobility was determined from 20 - 65 $^{\circ}C$, in steps of 5 $^{\circ}C$ (temperature range limited by the deformation of the cuvette). For each

temperature, approximately 50 measurements runs were performed: the mean and standard deviation values were reported in Figure 3.18.

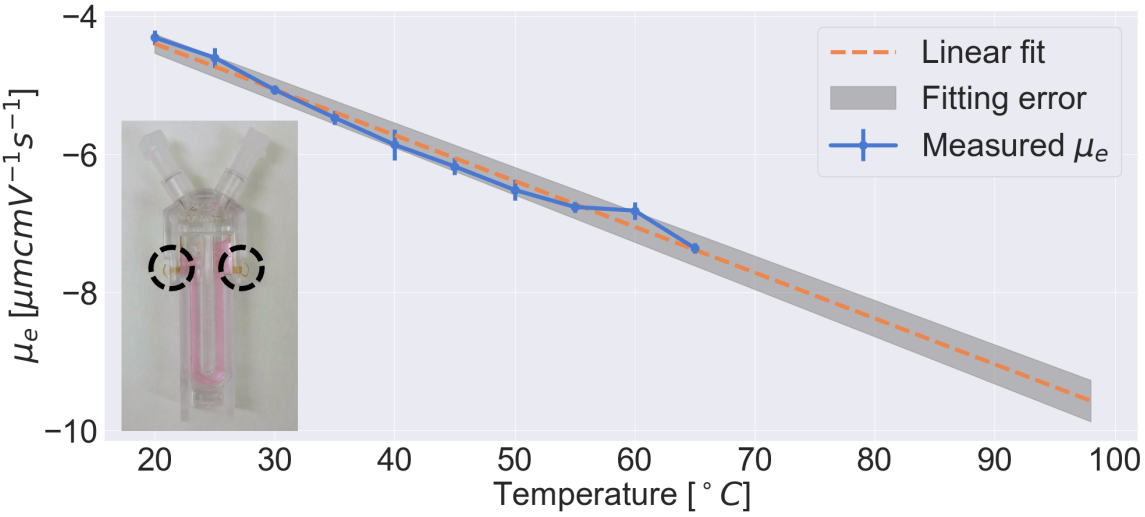

Fig. 3.18 The mean and standard deviation electrophoretic mobility (μ_e) for each temperature interval. Mobility increased (negatively) with increasing temperature. (Inset) Folded cell cuvette used for quantification of the electrophoretic mobility. Cuvette was loaded with 26 nm polystyrene Fluospheres with 80 μM sodium azide concentration. The electrodes either side of the U-shape sample chamber are shown in the dashed circles.

The electrophoretic mobility increased in absolute value with increasing temperature. It decreased linearly with a negative gradient as determined through linear regression fitting, with a slope and intercept values of -0.066 $\mu mcmV^{-1}s^{-1}K^{-1}$, -3.06 $\mu mcmV^{-1}s^{-1}$, respectively. The mobility was inversely proportional to viscosity and hydrodynamic radius, and both are dependent on temperature. Hence to discern which parameter was responsible for the increased electrophoretic mobility, the hydrodynamic radius was quantified for the same temperature range, in the same cuvette, using the Malvern Zetasizer (method outlined in Section 2.3.5). The hydrodynamic radius changed from a values of 18.23 nm to 19.55 nm, which is a difference of 1.32 nm. For the same temperature range, the viscosity changes from 1 $mPas$ to 0.43 $mPas$. Hence, the increase in the electrophoretic mobility was largely attributed to the reduction of the viscosity, for increasing temperatures.

3.4 Experimental results

3.4.1 Generating and measurement microscale temperature gradients

3.4.1.1 Rhodamine-B lifetime-temperature calibration

The heating stage was used to control and maintain the temperature of the Rhodamine-B solution in order to calibrate its temperature-lifetime dependence. The region near the thermocouple immersed into the solution was imaged and its corresponding lifetime, as a function of temperature, was discerned. For each set temperature, a distribution of lifetimes were obtained from the pixel-wise fitting (Figure 3.19). The variation was obtained from the lifetime fitting errors and the natural small temperature fluctuations of the solution itself.

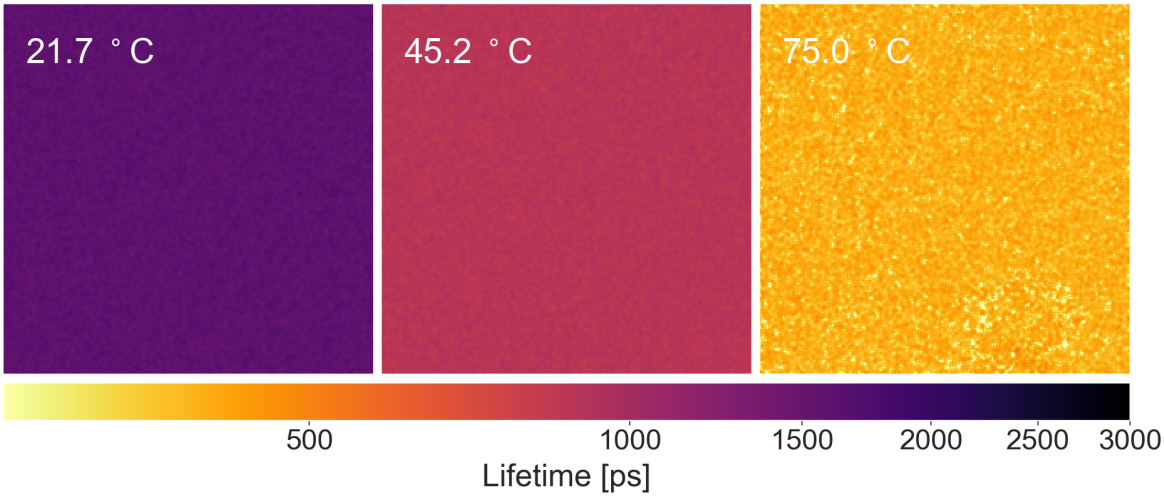

Fig. 3.19 The detected lifetimes for different set temperatures of the Rhodamine-B solution by the heating stage. Logarithmic colour scale to illustrate the fluctuations in the lifetime values.

The mean and standard deviation of the lifetime distributions for each temperature was determined. The lifetime decreased with increasing solution temperature for the tested temperature range of 21.7 $°C$ to 75 $°C$ (Figure 3.20). The obtained lifetimes varied approximately 3% from its mean value. The lifetime-temperature dependence of Rhodamine-B has been attributed to an Arrhenius-like relationship [131], whereby it can be described as a single exponential decay, such that:

$$\tau_{RhB} = A_{RhB} exp[T/T'] + c \tag{3.6}$$

where τ_{RhB}, A_{RhB} and T' were the Rhodamine-B lifetime, pre-exponential factor and characteristic temperature, respectively. The inverse of the lifetime, can be considered as a reaction rate, which increases with temperature. This can be thought of as an increase in the rotation of the molecular rotator, which more efficiently deactivates the excited state, due to a lower viscosity of the solution, mediated by the higher temperature [132]. The measured lifetimes with respect to temperature were fitted using Equation 3.6, and showed excellent agreement (Figure 3.20).

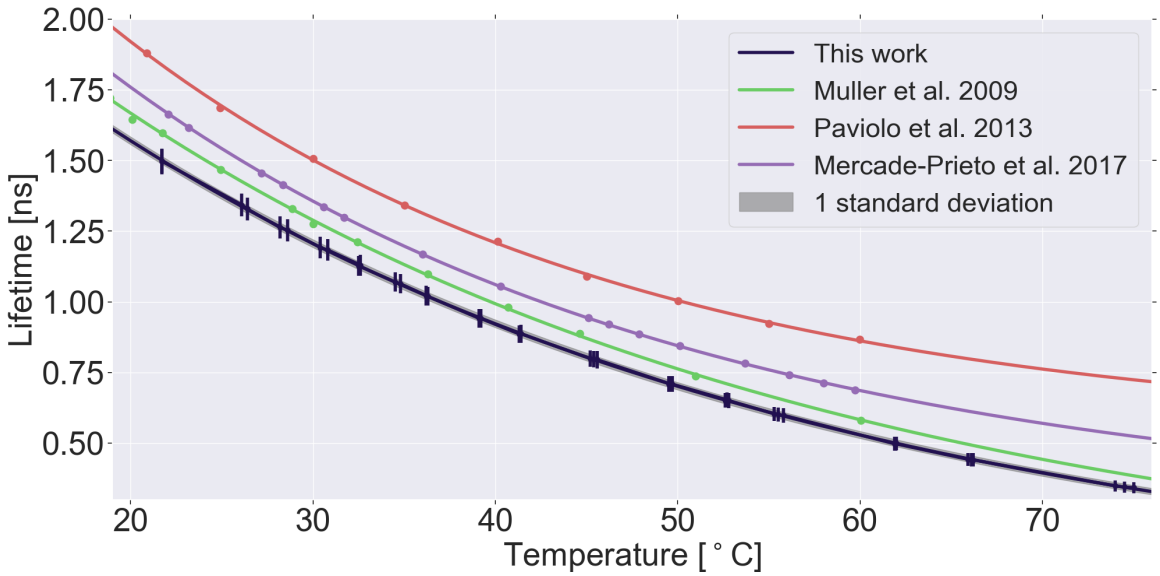

Fig. 3.20 Temperature-lifetime dependence of Rhodamine-B in Milli-Q water. The error bars show the spread in the temperature fluctuation (see Figure 3.19). The measured relation in this work, and other works are fitted to Equation 3.6 such that the coefficient can be used to back-calculate temperature from a lifetime value. The relation measured herein agreed well with the values reported by Muller *et al.* [35].

The fitting coefficients of the curve facilitated the back calculation of a temperature from a lifetime value. Upon comparison of Rhodamine-B temperature dependent lifetimes, the values reported herein were in agreement with Muller *et al.* [35], who report the combined results of Benninger *et al.* [133] and Kitamura *et al.* [132]. The reported lifetimes in this work were also similar to Paviolo *et al.* [134] and Mercade-Prieto *et al.* [131]. However, both works report higher lifetime values for the same given

temperature. The Rhodamine-B concentrations were similar between the mentioned studies and the values reported herein. Muller *et al.* show very similar lifetime values for single molecule Rhodamine-B and ensemble concentrations. Hence lifetimes were expected to be concentration independent.

3.4.1.2 Measuring temperature profiles induced by near-infrared absorption of Cr micro-discs

Once the lifetime-temperature relation of Rhodamine-B was defined, the heating induced by the Cr micro-discs due to varying near-infrared laser intensities, was quantified. A 3 μl solution of Rhodamine-B was pipetted into the heating micro-chamber to map the generated temperature profiles. From the measured lifetimes obtained as a function of laser intensity, the temperature was back-calculated for each pixel (by rearranging Equation 3.6). For consistency, the same array of micro-discs used for measuring the velocities of polystyrene nano-beads were used to measure the temperature profiles. The micro discs were cleaned from the presence of the polystyrene beads by sonication in acetone to dissolve the polystyrene. However, not all residue was removed in the cleaning process. Any remaining debris contributed to an altered Rhodamine-B lifetime due to surface interactions, which gave rise to temperature hotspots. This was parti-

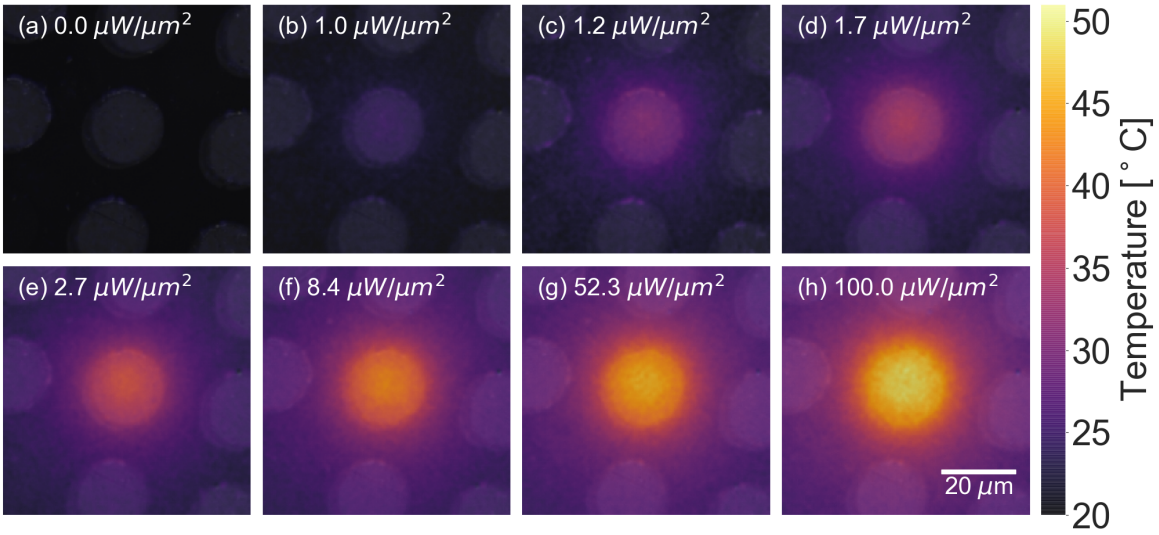

Fig. 3.21 Generated heating of the Cr micro-discs at varying laser intensities. The background mean temperature without the laser was measured to be 21.9 ± 0.5 °C. The focal plane was kept constant for all measured intensities. The same micro-disc was heated for consistency. Repeated measurements with other micro-discs at the same intensities conformed well, and only had a temperature difference of 0.5 °C.

-cularly the case for the edges of the micro-discs (Figure 3.21 a-h).

Initially, the ambient temperature of the solution and the micro-discs was quantified (Figure 3.21a). This step acted as a reference temperature, which took into account any potential quenching effects due to the presence of Au and glass surfaces and any small heating induced by Au absorption of the 561 nm laser used to excite Rhodamine-B (nominally 20 μW for the entire field of view (4 $nW/\mu m^2$)). The micro-discs were, on average, 1 $^{\circ}C$ higher than the surrounding glass. This was most likely due to the quenching of the Rhodamine-B in the presence of Au, which reduced the lifetime and gave rise to a corresponding, slightly higher, temperature [135]. The ensemble temperature, without the presence of heating (21.9 $\pm$ 0.5 $^{\circ}C$) matched the measured room temperature for the duration of the experiment (23.1 $\pm$ 1.3 $^{\circ}C$).

The near-infrared laser was aligned to be incident at the centre of the TCSPC's field of view. A micro-disc was then centrally position over the laser spot to absorb the light and generate heating. The laser intensity was varied from 1 - 100 $\mu W/\mu m^2$, and the corresponding temperature profile was measured from the lifetime of the Rhodamine-B (Figure 3.21 b-h). The temperature increased with increasing laser intensities. Despite the elliptical beam shape, which was twice the size in one-axis relative to the other (Figure 3.13), the generated heating was symmetrical. The temperature change from ambient (T_{amb}) and the heating distribution was determined by taking the mean of the central x- and y-axis, and approximating it as a Lorentzian function (f_L), such that:

$$f_L = \frac{T_p}{\pi}\left[\frac{\sigma_T}{(x-\mu_T)^2+\sigma_T^2} + T_{amb}\right] \tag{3.7}$$

where T_p was the peak temperature value, μ_T was the spatial position of the peak temperature, and σ_T was scale parameter (similar approximation made my Wolff *et al.* [136] and Reichl *et al.* [69]). The value of the scale parameter increased with the spatial extent of the heat distribution (Figure 3.22a). Herein, $2\sigma_T$ was used as the heat distribution length, as it corresponded to the FWHM value for the Lorentzian function (Figure 3.22b). Approximating the spatial distribution of the temperature profiles enabled inferences to be drawn regarding the epicentre of the nanoparticles trajectories and its corresponding temperature gradient of the thermoelectric force.

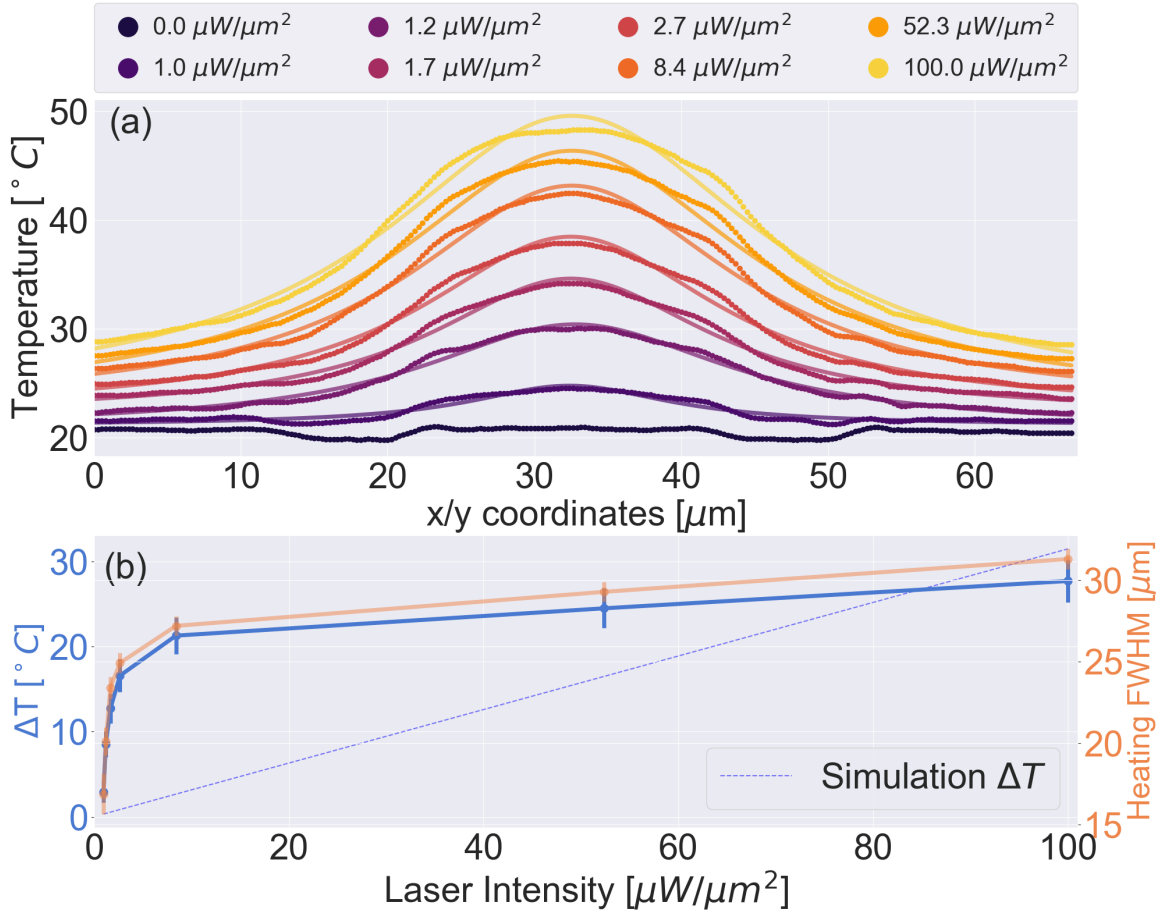

Fig. 3.22 **(a)** Central temperature profiles taken from Figure 3.21 and fitted to a Lorentzian to approximate the heating extent (FWHM) and change in temperature from T_{amb}. The baseline temperature also increased with higher intensities for the measurement window. For a bigger field of view, the temperature profile would tail-off to room temperature. **(b)** Blue curves show the temperature change as a function of laser intensity. ΔT nonlinearly increases with intensity, when is theoretically expected to be linear. The heating extent also increases with intensity, when is expected to be constant.

Heating profiles in the measured $\pm$ 33 μm window from heat source conformed well with Lorentzian fitting for intensities between 1 - 8.4 $\mu W/\mu m^2$ (Figure 3.22a). For higher intensities, the peak temperature rise was over estimated by the Lorentzian fitting, but its decay conformed well. In all instances, the fitting deviated at the Au-Cr layer's kinked temperature profile, which was a feature also observed in simulations (Figure 3.5).

The temperature change from ambient (Figure 3.22b) nonlinearly increased with laser intensity, which did not follow simulated linear behaviour (inset of Figure 3.5). Higher temperatures were achieved with lower intensities than expected. For instance, an intensity of 2.7 $\mu W/\mu m^2$ yielded a measured temperature rise of 39 $°C$, which should be achieved using an intensity of a 65 $\mu W/\mu m^2$ according to the simulated profiles (Figure 3.4). In addition, for intensities above 50 $\mu W/\mu m^2$, the temperature incrementally increased at a reduced rate with successive intensity increases. The ΔT curve of Figure 3.22b, suggests that the capacity of the Au-Cr layer to generate heating began to saturate above 10 $\mu W/\mu m^2$.

The spatial extent of the heating was approximately the same size as the Cr-Au micro-disc (Figure 3.22b) and similar to the simulated value of 20.8 μm. However, the FWHM increased with intensity when it should have remained constant. The increase was nonlinear, following the same shape as the temperature change (ΔT). This suggests that the material properties (e.g. k, C_p) vary with temperature more than in the simulations. For instance, the thin films may be experiencing significant thermal expansion, and thus causing temporary detachment from the glass surface.

3.4.1.3 Quantifying temperature gradients

The 3D temperature profile was measured by scanning the focal plane of the TCSPC away from the initial focal point (the surface of the glass slide). The focal position was

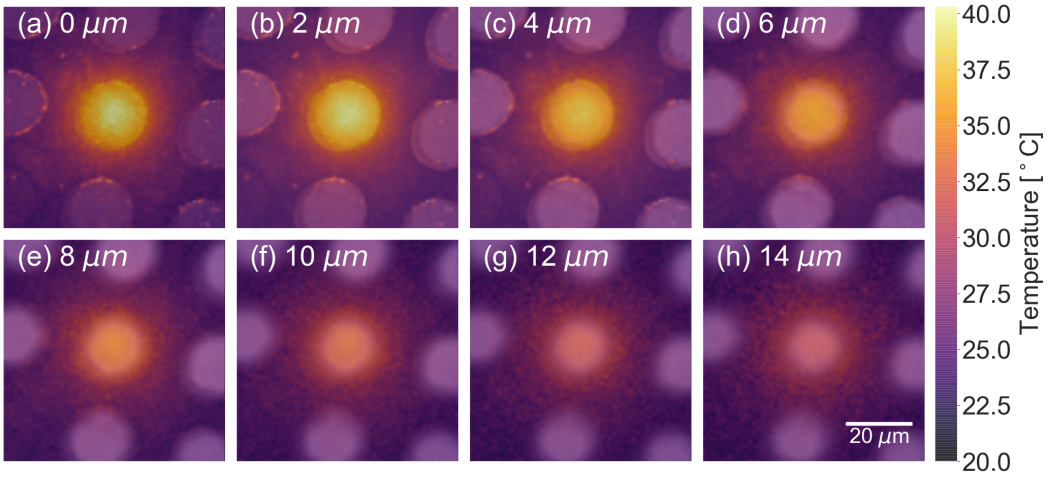

Fig. 3.23 Scanning the focal plane to obtain the corresponding temperature from the lifetime measurements with the laser intensity set to 2.65 μW. The further the focal plane was set away from the heating source, the lower the measured temperature.

shifted using the fine focusing reel of the microscope stage, which in turn moved the imaging objective down, rather than the sample stage. This meant that near-infrared laser intensity incident on the Cr layer was kept constant. Optical sectioning of 1-2 μm was achieved through the use of the 1.4 NA 60x oil objective. With the intensity kept constant (2.7 $\mu W/\mu m^2$), the temperature was determined in z-direction in 2 μm steps up to a distance of 14 μm from the surface of the glass slide (Figure 3.23).

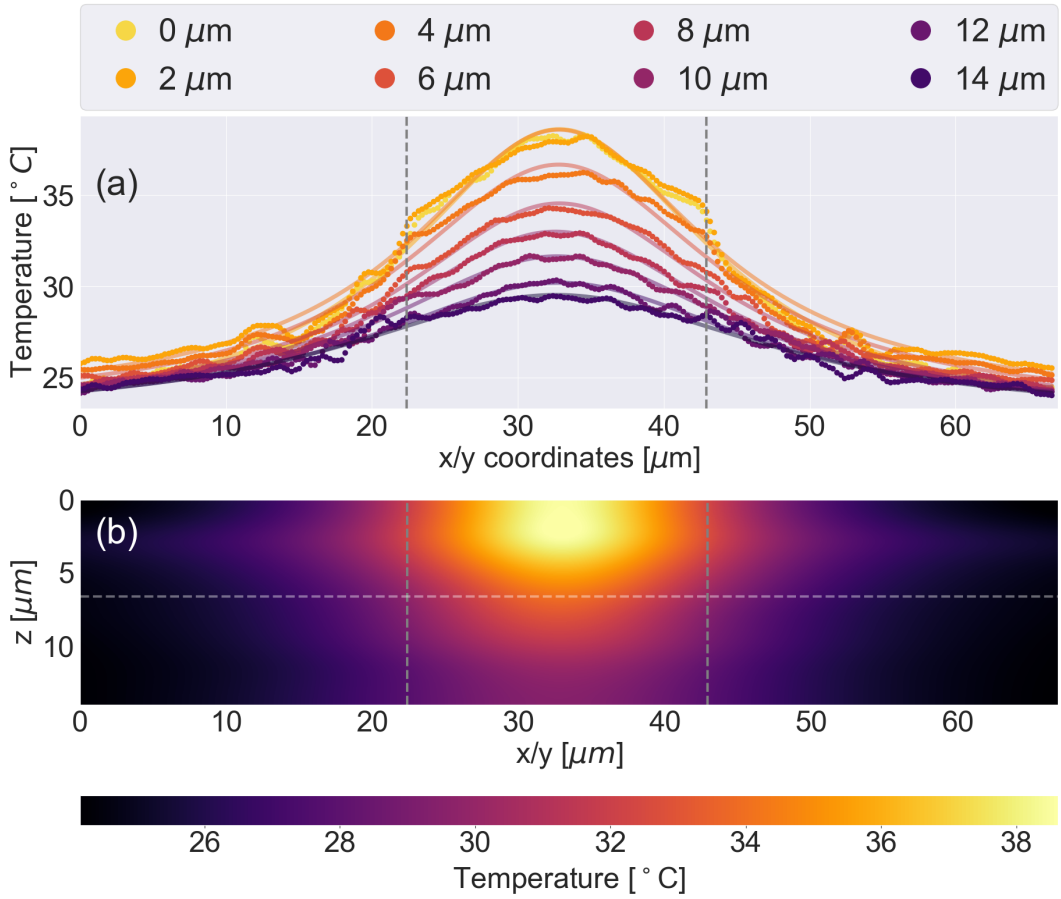

Fig. 3.24 **(a)** Temperature profiles for different focal planes away from the surface of the glass slide. The edge of the Cr-Ar layer appears as a shoulder in the temperature profile. The measured temperatures were fitted to a Lorentzian curve to determine the FWHM in both directions. **(b)** Projection of the fitted Lorentzian profiles. The temperature spread at z=2 μm has the greatest spread and may be due to the higher fluid flow at that plane. The vertical dashed lines denote the egdes of the Au-Cr micro-discs, whilst the horizontal white dash line marks the position of the FWHM in the z-direction.

From the initial focal plane to 2 μm above the surface, the peak temperature did not change. In all subsequent steps, the temperature reduced in peak value and became more spread out. A Lorentzian function (Equation 3.7) was fitted to the averaged central profiles in the x- and y-directions to quantify the heating extent and peak temperature for every focal plane measured (Figure 3.24a). The fitting once again conformed well to the measured radial temperature profiles.

At the 2 μm focal plane, the heating FWHM was larger than the 0 μm plane. This may have occurred due to the presence of higher fluid flow 2 μm above the surface which carried the heat away, whilst at the surface the flow velocity was zero. At these focal planes, the kink in the temperature profile corresponding to the edges of the Au-Cr layer was observed and matched the theoretical temperature profiles, which also exhibited the same feature (Figure 3.5).

Using the peak values obtained from the Lorentzian fitting, the FWHM of the temperature in the z-direction was numerically determined to be 6.6 μm, denoted by the white horizontal dash line of Figure 3.24b), which was an orthogonal projection of the fitted values. This value was smaller than the theoretical value of 9 μm. Approximating the profiles as a Lorentzian was useful as they smoothed out the temperature fluctuations, which would greatly be amplified when determining the gradients. Hence,

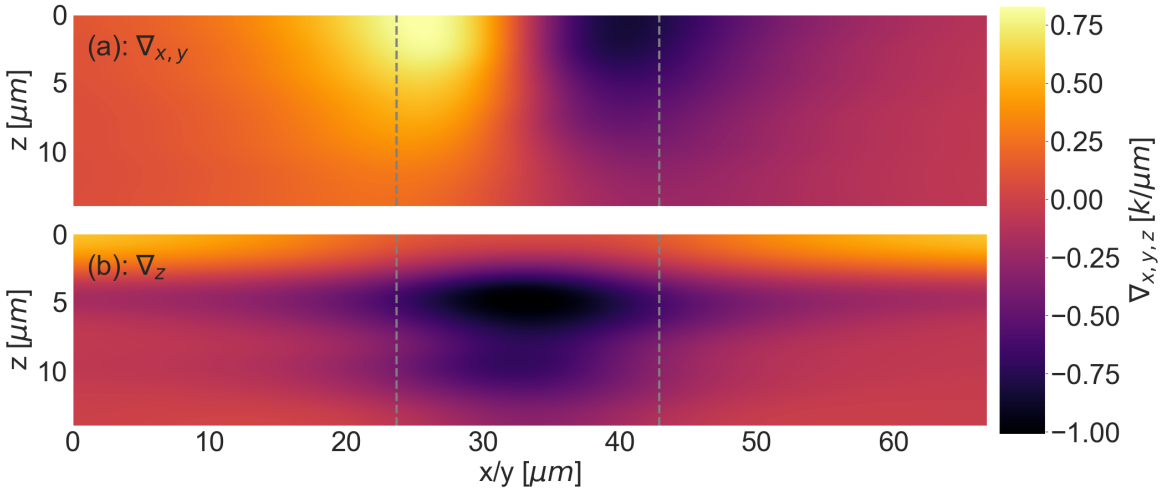

Fig. 3.25 Temperature gradients numerically calculated from Figure 3.5b. **(a)** Gradient is symmetrical about the heating centre. **(b)** Highest gradient occurs at around 4 μm above the surface of the Au.

the projection of the temperature from the fits (Figure 3.24b) was used to determine the temperature gradients in both directions (Figure 3.25).

The temperature gradients were approximately lower by 4x in the x-y-direction, and 3x in the z-direction, relative to theoretical values shown in Figure 3.7. The measured temperatures and its corresponding gradients were effectively an average of all the temperatures within the depth of focus of the imaging objective. Hence, the temperature profiles were smoothed out, which resulted in shallower measured gradients. Moreover, the Lorentzian estimate of the temperature profiles did take into account the kinked temperature aspect due to the edges of the Au-Cr layer. This particular feature had the highest gradient values in both directions, and was neglected in the values in Figure 3.25.

In the x/y-direction, the gradient was symmetrical around the central heating spot with the maximal value (0.83 $k/\mu m$) occurring at $\sim$7 μm from the heating centre (Figure 3.25a). In the z-direction, the highest gradient was approximately 4 μm above the surface of the glass slide with a value of 1.04 $k/\mu m$ (Figure 3.25b).

3.4.2 Nanoparticle swarming in a thermoelectric field

With the positions of the particles detected and linked into individual trajectories (Section 3.3.3.2), the instantaneous velocity was determined to quantify the strength of the thermoelectric field as a function of position with respect to the heating source, and at different temperatures (Figure 3.26).

When the laser intensity was set to 1.2 $\mu W/\mu m^2$, a temperature change of 8.5 $^\circ C$ was observed (Figure 3.21c. This gave rise to a thermoelectric field that affected the motion of the nanoparticles as shown in Figure 3.26a. The negatively charged particles were drawn in towards the heat source. Particle trajectories were mostly detected over the micro-disc, where they were brought into focus by the thermoelectric field. The net inward motion was affected by Brownian motion, resulting in meandering trajectories. Even though particles were trapped in the centre, they still had a small instantaneous velocity due to the movement of the cluster as a whole by Brownian motion.

Increasing the laser intensity to 1.7 $\mu W/\mu m^2$ ($\Delta T = 12.7^\circ C$) resulted in more particles being detected from outside the Au-Cr micro-disc, mediated by the greater heating extent than in the previous case (Figure 3.26b). Higher instantaneous velocities

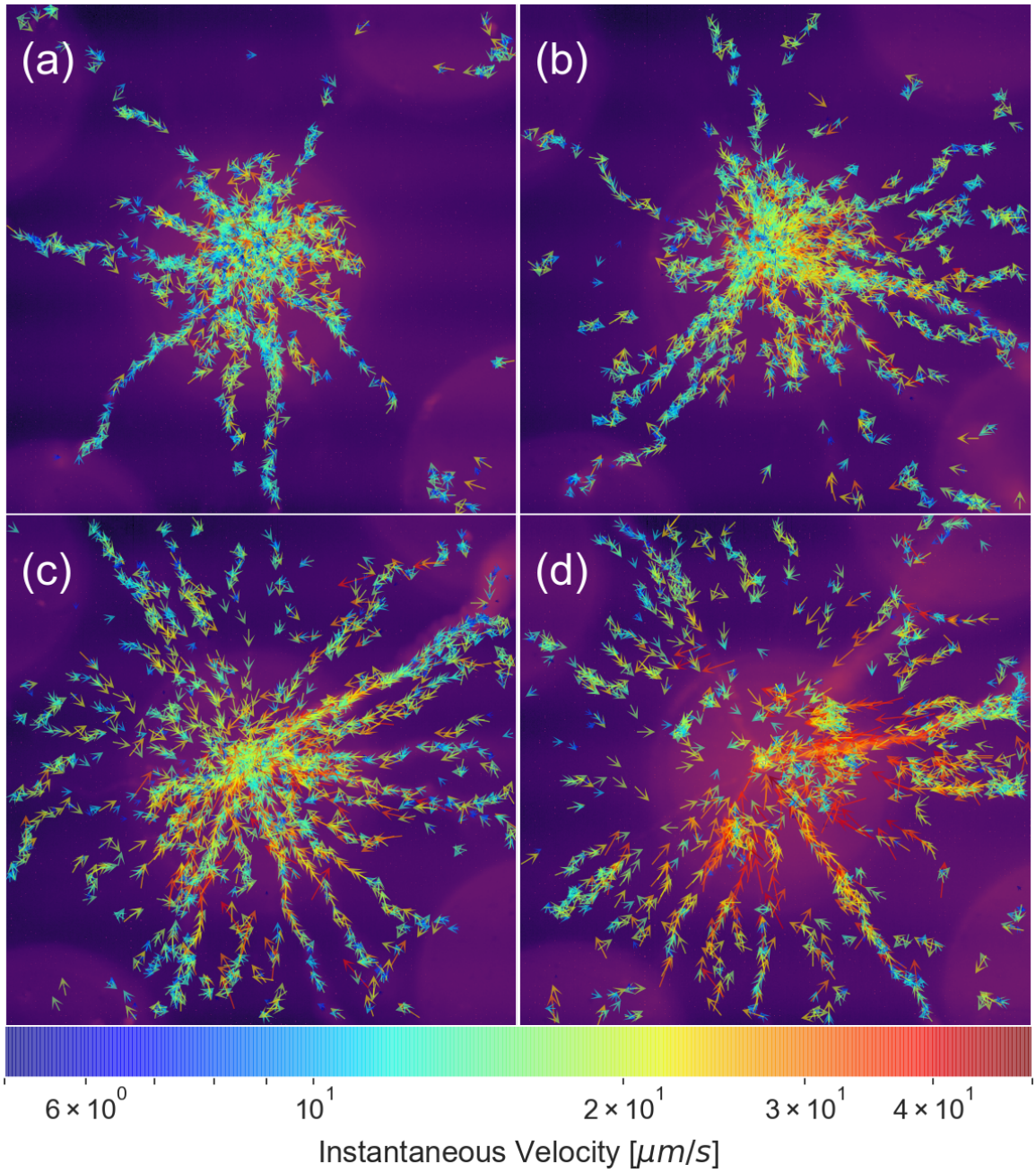

Fig. 3.26 Instantaneous velocities of individual particle trajectories. The colour and length of the arrows denote velocity. Particle are attracted to the centre (heating source) of the micro-disc, where they are then confined. Particles velocities increase as they approach the micro-disc. **(a)** 1.2 $\mu W/\mu m^2$ ($\Delta T = 8.5°C$). **(b)** 1.7 $\mu W/\mu m^2$ ($\Delta T = 12.5°C$). **(c)** 2.7 $\mu W/\mu m^2$ ($\Delta T = 16.6°C$). **(d)** 8.4 $\mu W/\mu m^2$ ($\Delta T = 21.3°C$). The ensemble velocity increases with increasing laser intensities and its corresponding temperature. Refer to Figure 3.21c-f for analogous temperature profiles.

were observed over the micro-disc. Even more particle trajectories from outside the micro-disc were detected with an intensity of 2.7 $\mu W/\mu m^2$ ($\Delta T = 16.6°C$). This was due to the increased temperature field penetrating further and attracting particles from outside the field of view of the image, in all directions (Figure 3.26c). The velocity of a particle increased as it approached the Au-Cr micro-disc, and then reduced at the centre where they were confined.

With a laser intensity 8.4 $\mu W/\mu m^2$ ($\Delta T = 21.3°C$), only a single very bright particle was trapped, which was brought into the centre with a high velocity (Figure 3.26d). Particles which were not trapped at the centre were pushed away from the Au-surface and out of focus. This occurred due to the higher negatively charged Au-surface mediated by the increased binding of the azide cations in the presence of the higher temperature.

The distribution of the radial velocities was quantified to discern how the thermo-electric field changed with laser intensity (Figure 3.27). A kernel density approach was

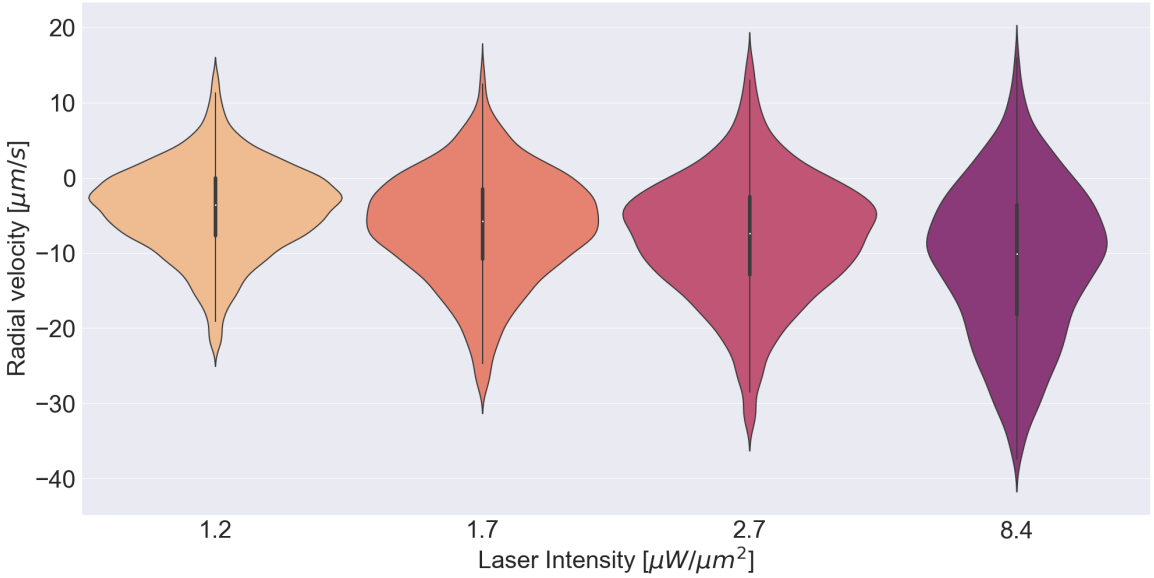

Fig. 3.27 Gaussian kernel density estimation of the instantaneous velocities from Figure 3.26 as a function of laser power. The distributions are symmetrically shown, and a greater width means more particles exhibiting that particular instantaneous velocity. Both the position of the maximum width and the spread of the velocities negatively increasing mean that particles are attracted inwards at a greater velocity with increased laser intensity. For each distribution, a box plot is also plotted on top with a median value represented by a white dot.

used to determine the spread of velocities rather than binning the dataset to form a histogram, which often can give a misleading representation of the distribution depending on the chosen bin size. Instead, each data point was represented by a Gaussian kernel, and the summation of all the kernels yielded a smooth histogram whilst still preserving any multimodality present in the datasets. The higher the density of kernels at a particular instantaneous velocity, the wider the distribution (plotted symmetrically for clarity). This allowed for comparisons to be made between the instantaneous velocity distributions as a function of each laser intensity dataset (Figure 3.27). All distributions were centred with a negative radial velocity, meaning that the majority of the particles were moving towards the radial origin. The position of maximum width shifted to higher negative radial velocities with increasing laser intensity. Moreover, the tail of the distribution negativelyincreased with intensity. Hence, there was a clear increase in the inward ensemble velocity of the particle with increased temperature.

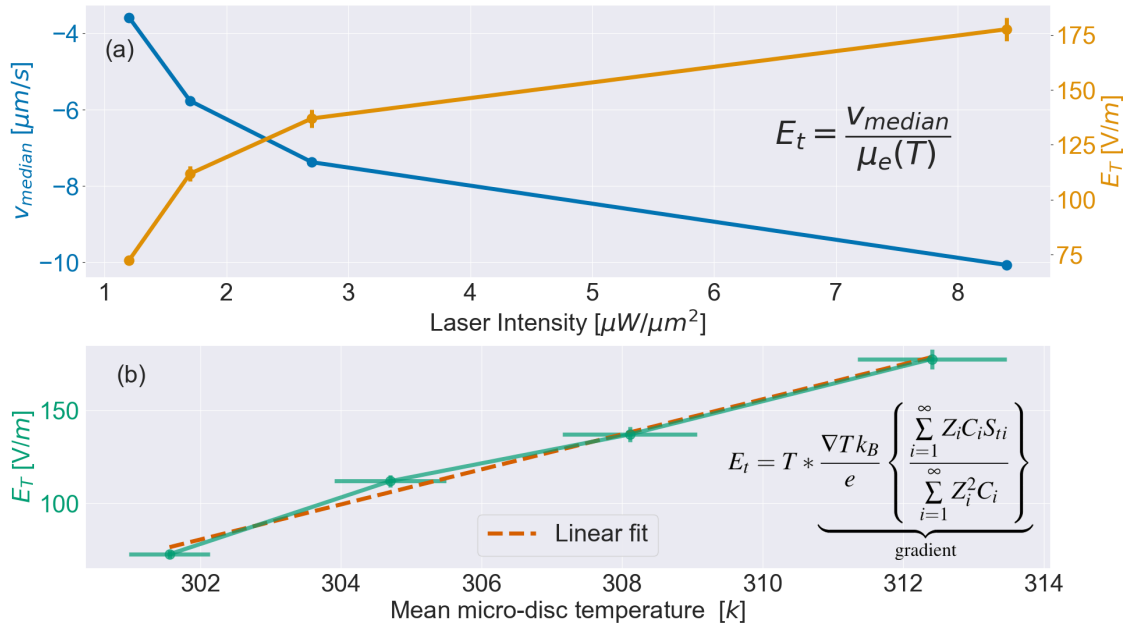

Fig. 3.28 **(a)** Median velocity (v_{median}) nonlinearly negatively increases with laser intensity (blue curve). Consequently, the thermoelectric field increases due to the increased heating. **(b)** The thermoelectric field (and therefore v_{median}) increases linearly with the mean temperature of the micro-disc, confirming the nonlinear nature of heating generated by the micro-discs with increasing laser power (Figure 3.22). The gradient of the linear fit is equal to the term shown with the under bracket. If the Soret coefficients of the solutes are know, the gradient can be used to determine concentration.

The median and interquartile range of the distribution were determined. They exhibited the same negative increase in velocity with laser intensity (box plot layered on top of the symmetric distribution in Figure 3.27). The median velocity (50^{th} percentile) increased nonlinearly with laser intensity (Figure 3.28a). Given the median velocities and the temperature dependence of the electrophoretic mobility ($\mu_e(T)$ from Figure 3.18) evaluated at the mean temperature over each micro-disc (Figure 3.21), the thermoelectric field (E_t) was quantified (Figure 3.28a).

The thermoelectric field also increased nonlinearly with laser intensity, as expected, from a value of 72.4 V/m (1.2 $\mu W/\mu m^2$, $\Delta T = 8.5°C$), to 177.6 V/m (8.4 $\mu W/\mu m^2$ $\Delta T = 21.3°C$). Upon comparison of the thermoelectric field with the mean temperature over the micro-disc, a linear relation was found. This conformed with Equation 3.1 (Figure 3.28b) and confirmed that the measured change in temperature with laser intensity (Figure 3.22) was indeed nonlinear.

The magnitude of the thermoelectric field generated by the separation of sodium azide ions was higher than that calculated for sodium chloride, even though the concentration of the latter was almost 2000x higher. This suggests that the Soret coefficient of the azide ion is several orders of magnitude higher than chloride.

3.4.2.1 Quantifying the Soret coefficient of azide ions

Up until now, the ensemble thermoelectric field has been quantified as a function of laser intensity and its consequential heating. There was also a spatial dependence of the thermoelectric field, as can be seen in Figure 3.26, originating from the radial temperature dependence and its ensuing gradient. This dependency was investigated by determining the mean velocity in radial bins of 1.5 μm for the 2.7 $\mu W/\mu m^2$ intensity-velocity dataset (Figure 3.29). For all evaluated bins the mean velocity was negative, minmised at approximately 7.5 μm from the origin. Upon comparing the temperature gradient for the same intensity at the same focal plane (calculated previously in Figure 3.25), the emerging radial dependence was similar to radially mean-binned velocities. Hence, the velocity field, and thus, the thermoelectric field, were largely determined from the gradient of the temperature field.

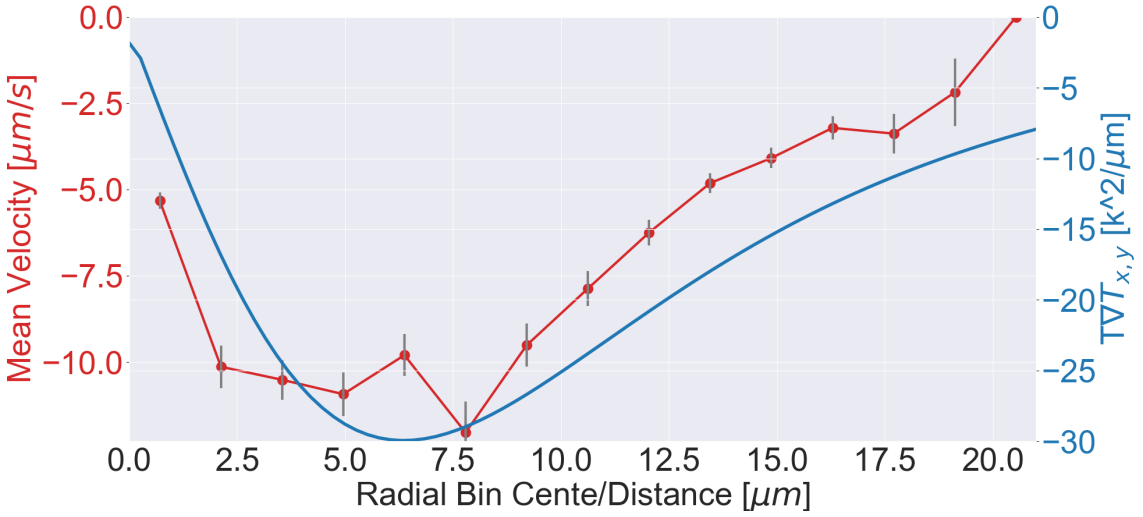

Fig. 3.29 The radial dependence of the velocity was determined by the temperature and its ensuing gradient. The mean radial velocity was determined using a bin size of 1.5 μm. The error in each bin was determined as the ratio of the mean over square root bin counts. The radial velocity was diminished 21 μm away from the heating centre, and increased to a maximum negative value of ca. 11 $\mu m/s$, 7.5 μm from the heating spot, where the temperature gradient was the highest.

Knowing the temperature distribution, its gradient, and the thermoelectric field generated, the Soret coefficient of the azide (S_{N_3}) was determined by rearranging Equation 3.1, such that:

$$S_{N_3} = \frac{\left\{\frac{v(r)}{\mu_e(T(r))} * (Z_{Na}^2 C_{Na} + Z_{N_3}^2 C_{N_3})\right\} - \left\{\frac{\nabla T(r) k_B T(r)}{e} * Z_{Na} C_{Na} S_{Na}\right\}}{\frac{\nabla T(r) k_B T(r)}{e} * Z_{N_3} C_{N_3}} \quad (3.8)$$

where the subscripts N_3 and Na were for the sodium and azide ions, respectively. The effects of hydronium and hydroxide ions were neglected due to their very low concentration (solution is pH 8). A concentration of $2.4x10^{-10}$ mol was used for both the sodium (C_{Na}) and azide (C_{N_3}), given the stock concentration of 80 μM, and the 3 μl volume of the fluidic chamber. The following values were used in conjunction with Equation 3.8 for the calculation of the Soret coefficient of the azide ions as a function of radial position: the radially dependent values for temperature (Figure 3.24a), the temperature gradient (Figure 3.29), the velocity (Figures 3.29), and the electrophoretic

mobility ($\mu_e(T(r))$, Figure 3.18). As the radial temperature profile is known, the values of the Soret coefficient at different temperatures were determined (Figure 3.30).

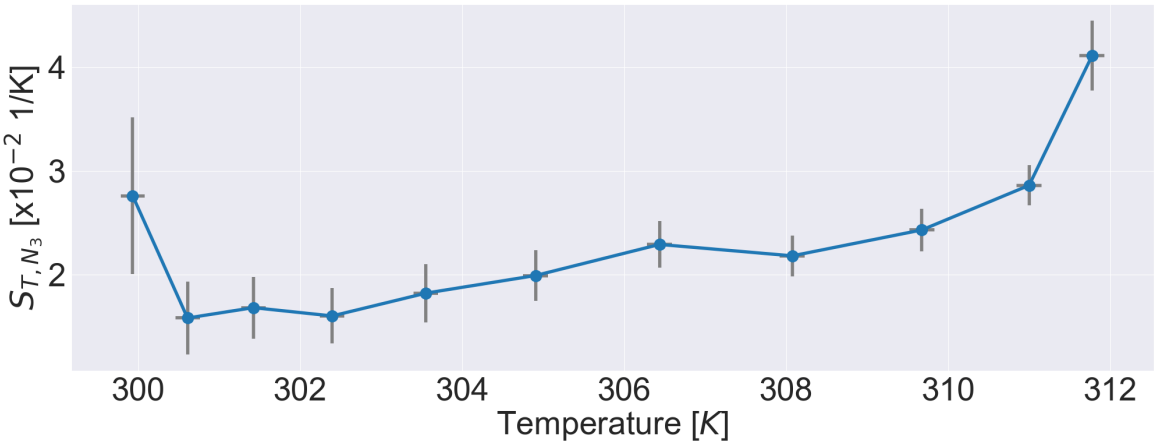

Fig. 3.30 The Soret coefficient with increasing temperature. The coefficient is approximately constant as a function of temperature, as expected. The errors are propagated forward, and it was assumed that the ion concentrations were to have an error of 5%.

The Soret coefficient for azide ions were temperature independent. Figure 3.30 shows that the first and the last values were different from those in between. The Soret coefficient at 300 K has a high error as there were few particles detected in the binned region corresponding to the edge of the image (Figure 3.26c). The Soret coefficient at 312 K was distorted by the presence of trapped particles at the centre, which affected the calculated value for E_T. By neglecting those points, the nominal Soret coefficient of azide ions was $2.15 \pm 0.41 \times 10^{-2} K^{-1}$. This value was approximately 30 times larger than the Soret coefficient of chloride ions. It is for this reason that the magnitude of the thermoelectric field for sodium azide was higher than sodium chloride, even though the concentration of sodium chloride ions was considerably higher.

The sign of the Soret coefficient for azide ions was positive, and thus they moved away from the heating source, much like the cationic CTAC micelles used by Zheng *et al.* [72]. Moreover, the magnitude of the Soret coefficient was also similar to the CTAC micelles.

3.4.2.2 Relocating the nanoparticle swarm

As a demonstration of the light controlled accumulation of the nanoparticles, the heating spot moved to a different position on the Cr micro-disc and the nanoparticles migrated to the new heating centre (Figure 3.31).

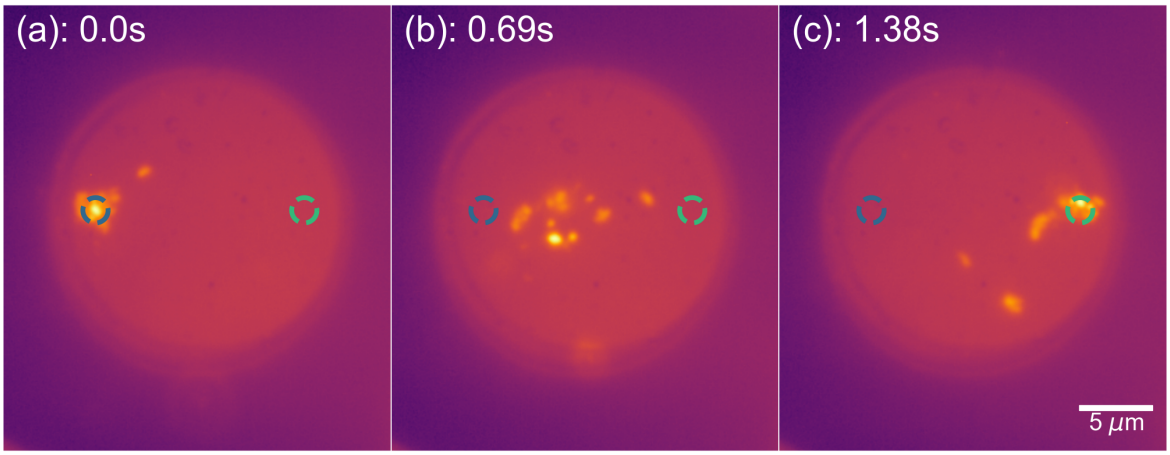

Fig. 3.31 The blue, and green target denote the initial and final location of the heating spot; radius of target approximately the same size as the near-infrared beam. **(a)** Nanoparticles pre-accumulating before the heating spot moved. (**b**): At 0.69 seconds after the heating region moved, the nanoparticles had already begin their journey to the new trapping centre. **c** All nanoparticles travelled to the new heated region, and more nanoparticles were attracted towards the cluster.

Initially, the heating spot was placed at the left edge of the micro-disc, and left there for a few seconds to accumulate nanoparticles (Figure 3.31 a blue target). Then, the piezo-stage was used to rapidly move the sample, such that the location of the heating region was moved to the right side of the Cr micro-disc (Figure 3.31a green target). Within less than a second after moving the heating spot, the particle had already traversed half the distance between the initial and final location of the heated area (Figure 3.31b). After approximately 1.5 seconds, all the particles had migrated over, and new particles were drawn in towards the swarm (Figure 3.31c).

3.5 Summary

Temperature gradients were created through the absorption of near-infrared laser light by chromium thin films deposited on a glass slide. This enabled complete control and flexibility of the location where heating was induced within a microfluidic chamber.

The steady state heating diffusion was simulated and the convective flow and thermoelectric field was modelled. The temperature induced convective flow of the fluid was found to be small in magnitude due to small Reynold's number of the system. Hence, fluidic effects were negligible and in the opposite direction of the observed nanoparticle movement. Despite the small difference between the Soret coefficient of sodium and chloride, the nanoparticle velocity simulated by taking into account the temperature gradients, was in the order of 10 $\mu m/s$ for a 20 degree temperature rise, which was substantial. The observed flow direction of the nanoparticles matched the simulated direction.

The heating profile was mapped out using the temperature dependent fluorescent lifetime of Rhodamine-B, which was obtained through time correlated single photon counting microscopy. The fluorescent lifetime response of Rhodamine-B was calibrated using a custom built heating stage, and the measured lifetime-temperature values. The latter matched closely to previously reported values. Heating was induced at various laser intensities incident on Cr micro-disc, at which the microscale temperature was obtained from the fluorescent lifetime of Rhodamine-B. The shape of the induced temperature profiles were similar to the simulated temperature profiles, and even had the kinked feature corresponding to the thermal conductivity difference between the edge of the Au-Cr and the glass. However, the simulated peak temperature profiles did not match the measured peak temperatures for a given laser intensity. Both the measured and simulated temperature gradients ($\sim 10^6 K/m$) in this work were lower than those estimated by Zheng *et al.* ($\sim 10^7 K/m$), despite similar geometries being used.

Fluorescently tagged 26 nm polystyrene beads which were modified with carboxylate to inhibit aggregation were used as tracer particles to map out the thermoelectric field. The modification meant that the nanoparticles were negatively charged with an electrophoretic mobility of approximately ca. -5 $\mu m cm V^{-1} s^{-1}$. Particle tracking was used to obtain the velocities of the nanoparticles migrating under the thermoelectric field at various induced temperatures. It was also found that the particles could be trapped near the Au surface, with bigger clusters forming at lower induced temperatures. This was the smallest reported nanoparticle size used in a thermoelectric trap or the thermophoretic trapping as a whole (i.e. quasi-static temperature gradients by Braun *et al.* [63]). With increasing temperatures, the particles migrated towards the hot spot

with greater velocities, due to the increase in the strength of the thermoelectric field. The ensemble strength of the thermoelectric field varied from 80 V/m ($\Delta T = 8.5°C$) to 180 V/m ($\Delta T = 21.3°C$). This value was similar to the estimates provided by Zheng's group (50 - 300 V/m) despite using a different cationic-, ionic-pairs for their thermoelectric field, and overestimating the induced temperature gradients in their system [72].

The Soret coefficient of azide ions was calculated in the present study to be 2.15 $\pm$ 0.41 $\times 10^{-2} K^{-1}$. Although the associated error was large, the was in line with the ca. 20% error commonly reported for Soret coefficients [65]. This value was similar in magnitude to the macro-cation micelles used by Zheng's group ($\sim \times 10^{-2} K^{-1}$) [72], as well as hydroxide ions (2.33 $\times 10^{-2} K^{-1}$) [69]. The ability to measure the Soret coefficient of ions further strengthens the sensitivity of using thermophoresis as a method of characterising sub-nanometer particles.

Chapter 4

Thermo-optic lensing of Au-nanoparticle suspensions

4.1 Introduction

In the presence of temperature gradients or intensity gradients, nanoparticle motion in solution is altered. They can either be confined by the presence of the gradient or be repelled away from it. In either case, nanoparticle redistribution leads to self induced local refractive index changes, which in turn, redistributes any light present within the region. These self lensing effects have particularly been reported when a beam is focused into a nanosuspension, and have been ascribed to optical forces or opto-thermal effects (Section 1.3). Of particular interest is the observed lensing effects for Au nanosuspensions due to the plasmonic nature of Au, which leads to enhanced absorption and scattering effects. As such, even for weakly focused beams, self induced focusing and defocusing effects have been reported (Figure 4.1) [26, 82, 27, 28].

Fardad *et al.* and Kelly *et al.* investigated non-linear lensing effects of a weakly focused beam into a cuvette containing 40 nm Au nanoparticles dispersed in an aqueous media. They found that at a low irradiance into the cuvette, the focused beam undergoes its inherent divergence as it propagates through the nanosuspension (Figure 4.1a). Increasing the laser power to 150 mW, they observe a self focusing, 'needle-like' beam, with a greater divergence than in the lower power case (Figure 4.1b). They attribute this behaviour to optical forces and migration of particles towards the high intensity region of the beam [26, 82]. Further increasing the laser power results in a significant increase in the beam's divergence relative to the low power, and the

beam penetrates far less into the solution (Figure 4.1c). Fardad *et al.* associate this behaviour to thermal effects overcoming optical effects, as the self focusing behaviour is compensated by the heating of the medium. Interestingly, Liberman *et al.* and Ortega *et al.* attribute the self-focusing behaviour purely to thermal effects, since the absorption cross-section dominates the scattering for Au nanoparticles below 60 nm in diameter [27, 28].

In this chapter, the experimental geometry of Fardad *et al.* (which is very similar to Kelly *et al.*) was recreated and their experimental observation verified in order to discern the exact mechanism behind their observed self-lensing effects. Their work was extended by quantifying the beam size and divergence at different powers, varying focal positions inside the nanosuspension, and nanoparticles suspended in fluids with different thermal diffusivity. In addition to extending the side cuvette self lensing work, the long optical path length cuvette (5 cm) was replaced by a short length cuvette (300 μm $L < Z_R$) and scanned along the focused beam to discern non-linear refraction coefficient (n_2) for 40 nm Au nanoparticles at various concentrations, powers and in media with different thermal conductivities. Moreover, n_2 was determined as a function of time to discern the associated temporal dynamics of the formation of self

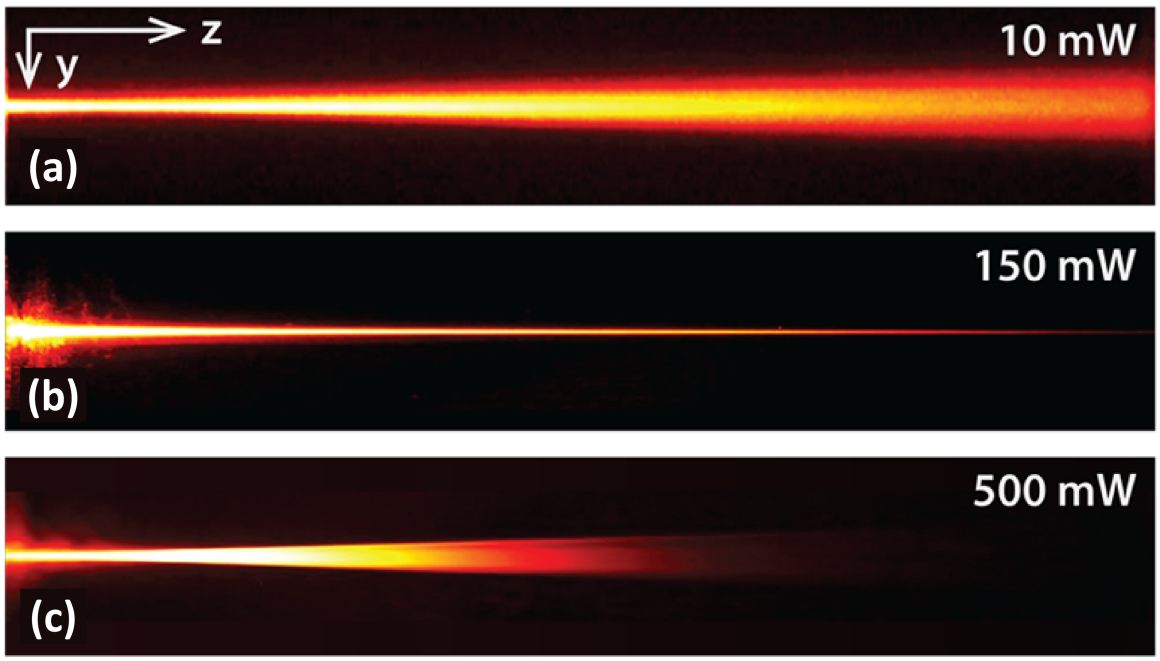

Fig. 4.1 The observed self-focusing and de-focusing of a focused beam into an Au nanosuspension at low- **(a)**,medium- **(b)**, and high-intensities **(c)**. From reference [26].

induced lensing effects. The heat generation and diffusion by nanoparticle absorption was simulated and compared to the time constants for n_2 as a means of confirming that the lensing effects were driven by thermal effects.

4.2 Optical, thermal and thermoelectric simulations for nanoparticle suspensions

A means of investigating the mechanism behind the observed lensing phenomenon reported by Fardad *et al.* [26], and Kelly *et al.* [82] was to consider the optical and thermal effects. Whilst the lensing behaviour has been ascribed to optical forces, the authors do not estimate or quantify the magnitude of the optical forces driving the lensing behaviour. The optical forces and temperature profile for Fardad *et al.*'s experimental geometry was modelled in this section.

The fundamental light-matter interactions occur between the nanoparticle and the laser light. The mechanism that unfolds from this interaction is consequentially responsible for the lensing effects. The extent of the nanoparticle's scattering and absorption govern the interplay with the optical and thermal forces. Plasmonic metals

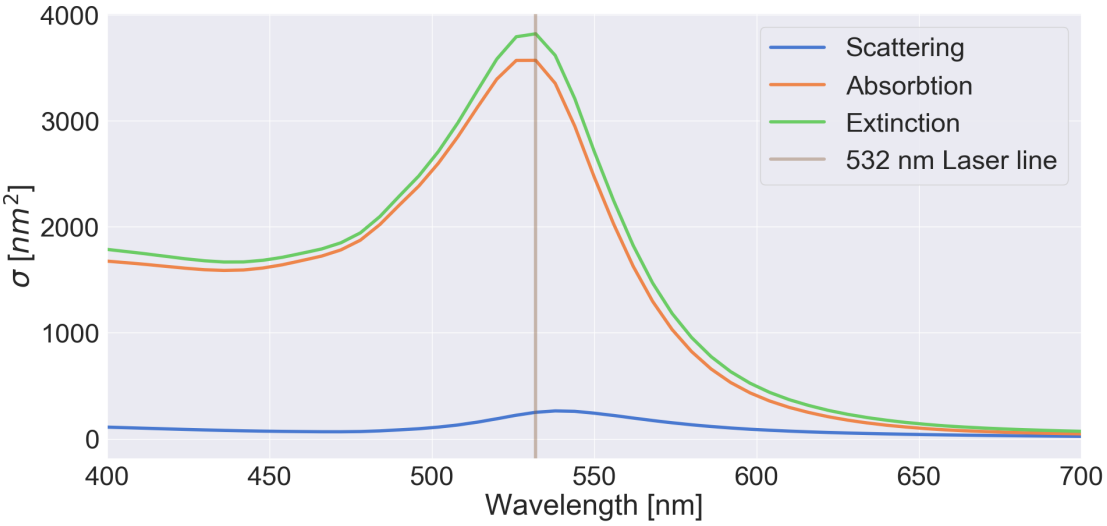

Fig. 4.2 The scattering, absorption and extinction cross-section for 40 *nm* Au-nanoparticles obtained from Mie theory. Absorption is the dominating mechanism of light matter interaction across the visible wavelength.

act to enhance the light matter interactions as discussed in Chapter 2. Hence, the absorption and scattering cross sections for 40 *nm* Au-nanoparticles (Figure 4.2) were obtained from the *NanoComposix Mie Theory Calculator* [36], and verified against the work of Fardad *et al.* [26].

The resonant peak for the Au-40 *nm* particles occurred at 532 *nm*, which coincided with the laser wavelength used by Fardad *et al.* The absorption cross section exceeded the scattering cross-section across the entire visible wavelength spectrum. Photons interacting with the particle were therefore significantly more likely to be resonantly absorbed by the nanoparticle, which acted to increase the nanoparticle's internal energy, effectively making them nano-heat sources. The generated heat was dissipated into the media, increasing its temperature. Although an increase in the thermal energy of the media acted to destabilise any trapping effects, optical forces may still have been significant enough for trapping, depending on the intensity gradients of the laser.

4.2.1 Refractive index gradients mediated by optical trapping

Fardad *et al.* attribute their observed behaviour to optical trapping forces, specifically to the Gradient force, with the nanoparticles having a positive polarisability. This would increase the nanoparticle concentration near the focal point, resulting in a higher refractive index, and thus, causing positive lensing effects that redistribute the light [26]. The propagating light will transition from a lower refractive region away from the focal point, to a higher index of refraction near the focal point, and hence refracting the light towards the normal. For this effect to be significant, several nanoparticles would have to participate in order to perturb the much larger Electric-field relative to the particle size.

To evaluate the contribution of the optical forces in forming self-focusing beams, the theoretical trapping forces were calculated using the formalism described in Chapter 2. Fardad *et al.* use a wavelength of 532 *nm* and a full-width-half maximum beam size of 15 μm, which corresponds to a beam-waist (w_0) of 12.7 μm. They report a 'needle-like beam' using a power of 150 mW for 40 *nm* Au-nanoparticle suspension. These parameters were used in the present study to simulate the theoretical optical trapping forces.

Firstly, the polarisability of 40 *nm* Au-nanoparticles used in the optical trapping force calculations were determined from their scattering- and absorption-cross-sections

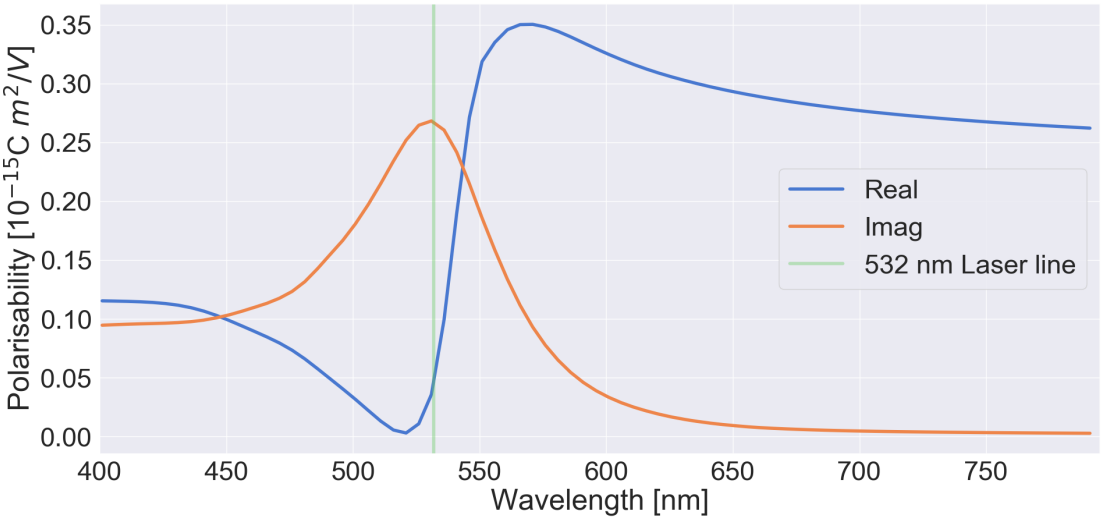

Fig. 4.3 The real and imaginary polarisability for Au-40 nm particles. The values were derived from the scattering and absorption cross-sections obtained from Mie theory [36, 26].

calculated from Mie theory (Figure 4.3 and verified against values reported by Fardad *et al.*).

At the laser line of 532 *nm*, the imaginary part of the polarisability was greater than the real part. This had a two-fold effect, increasing the temperature of the media due to the higher absorption, as well as increasing the magnitude of the scattering force relative to the gradient force (Equations 1.6,1.5. Both effects acted to reduce the probability of confining nanoparticles near the focal region.

In the simulations, the focal position of the beam was set to 1 *cm* inside the cuvette, similar to the experiential geometry used in Fardad *et al.*'s work (Figure 4.1). To ensure that intensity gradients were evaluated with sufficient spacial resolution, only two Rayleigh lengths on either side of the focal point were simulated, rather than the whole 5 *cm* cuvette. Furthermore, the attenuated intensity due to absorption and scattering over the considered optical path length, was taken into account such that:

$$\begin{aligned} I(z) &= I_0 e^{-\alpha_z z} \\ &= I_0 e^{\sigma_{ext}(f_v/V_{NP})z} \end{aligned} \tag{4.1}$$

where α_z, f_v, V_{NP}, and I_0 were the linear attenuation per unit length, filling fraction, nanoparticle volume and initial intensity, respectively. Fardad *et al.* report a filling fraction of 2 $\times 10^{-6}$, which corresponds to approximately 6×10^{10} particles per millilitre. From this, the optical gradient and scattering force were quantified for the experimental geometry reported by Fardad *et al.* (Figure 4.4).

The dominant optical force was the scattering force, which was several orders of magnitude higher than the gradient force, both in the lateral- and axial-direction. As a result, particles could not be optically near the focal point. At the focal position, the scattering force was 0.74 *fN*. Equating this to Stoke's drag force ($F_D = 6\pi\eta_w r_{np} v_{np}$), the particle's maximum velocity (v_{np}) due the scattering force was approximately 2 $\mu m/s$. This velocity was not significant enough to generate any concentration gradients mediated by the scattering force.

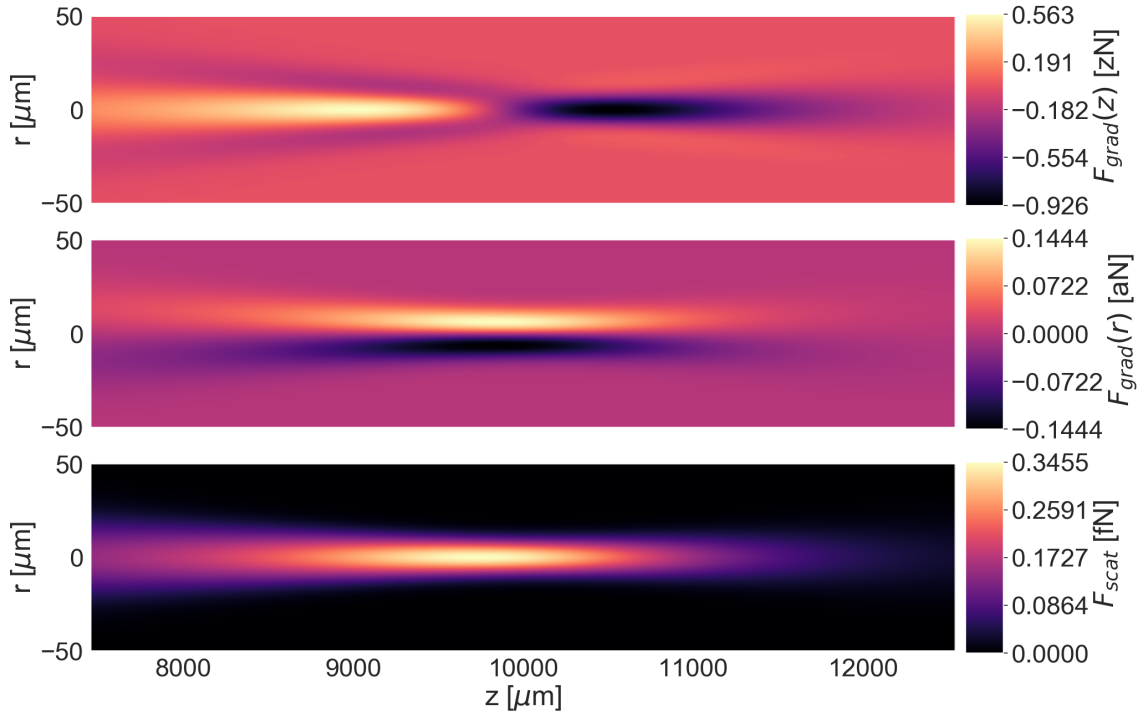

Fig. 4.4 Optical force calculations for confinement of 40 *nm* particles using a wavelength of 532 *nm*, a beam size of 12.7 μm, at a power of 150 *mW*. **Top**: Axial gradient force was in the zepto-Newton range. **Middle**: Radial gradient force was also very weak and in the order of atto-Newtons. **Bottom**: The scattering force was sub-femto-Newtons and was still insignificant to affect particle motion.

The maximum gradient forces in the axial- and radial directions were in the order of a few atto-Newtons and zepto-Newtons, respectively. These very weak forces arose due to the low intensity gradients originating from the large beam waist and the loss of intensity due to linear absorption of the light.

Concentration gradients mediated by optical forces could not be responsible for the lensing or 'self-focusing' behaviour reported by Fardad *et al.*

4.2.2 Thermally induced refractive index gradients

As the optical force was insufficient to mediate redistribution of nanoparticles, the thermal effects due to nanoparticle absorption and dissipation were considered. Comsol was used to simulate individual and ensemble nanoparticle heating (using Equation 3.2), as well as determining the associated heat dissipation time scales. As a consequence of the heat dissipation, the medium's temperature increased, which. given the negative thermo-optic coefficient of water [27], decreased the local refractive index, creating an effective lens with a radius of curvature dictated by the heating dissipation profile (Figure 4.5). Consequently, the beam size changed, which altered the amount of heating generated, feeding back into the refractive index of the medium until steady state was reached.

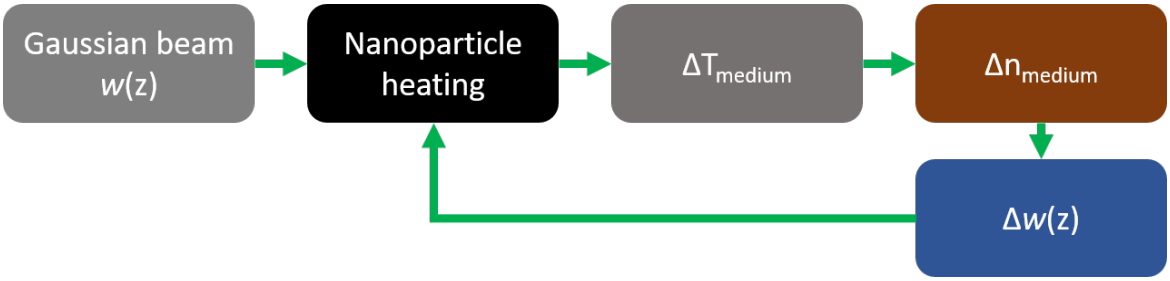

Fig. 4.5 The proposed mechanism behind the self induced lensing investigated herein. A Gaussian beam with initial size w_0 induced heating, changing the local index of refraction, causing lensing of the beam, which in turn changed the amount of heat generated. Once the lensing feedback reached steady state, the beam became stable.

4.2.2.1 Single nanoparticle heating

To determine how refractive index changes at the nanoscale drive thermal effects, the steady-state surface temperature, and heat dissipation profile of an individual 40 nm nanoparticle was simulated. The heating effects were evaluated for a single particle

placed at the central radial position of the beam focus.

The heat dissipation profile of the nanoparticle into the water medium was evaluated for a domain that was greater than ten-times the nanoparticle radius ($r_{np} = 20\ nm$). Initially, the nanoparticle and water medium temperatures were set to the ambient temperature of 20 $°C$ (T_{amb}). The boundary of the water domain, was also set to the ambient temperature to dissipate the heat away. This was equivalent to modelling the system as a single nanoparticle immersed in an infinite water bath. The heat generation source Q was evaluated such that:

$$Q = I(r,z)\frac{\sigma_{abs}(\lambda)}{V_{np}} \tag{4.2}$$

$$I(r,z) = \frac{2P}{\pi w(z)^2} e^{-\frac{2r^2}{w(z)^2}} \tag{4.3}$$

where $I(r,z)$ was the intensity profile of the laser, P was the laser power, and σ_{abs} was the wavelength-dependent absorption cross-section of the nanoparticle [137]. At the laser line of 532.8 nm, the absorption for 40 nm Au was resonant and the nanoparticle was maximally absorbing, with a cross-section of $3.57{\times}10^3\ nm^2$. The surface temperature and heating profile of a single nanoparticle were simulated using a laser power of 100 mW (Figure 4.6).

The surface temperature of the nanoparticle in the steady state reached 25.5 $°C$, which was 5.5 $°C$ above the initial ambient temperature. This meant that an increase of 0.55 $°C$ of the nanoparticle's surface temperature was expected per mW of laser power, since heat generation scaled linearly with laser power. There was a negligible temperature gradient across the nanoparticle. At the water-nanoparticle interface, the temperature was the same, after which it rapidly decayed to ambient at a distance of 10-times the nanoparticle's radius.

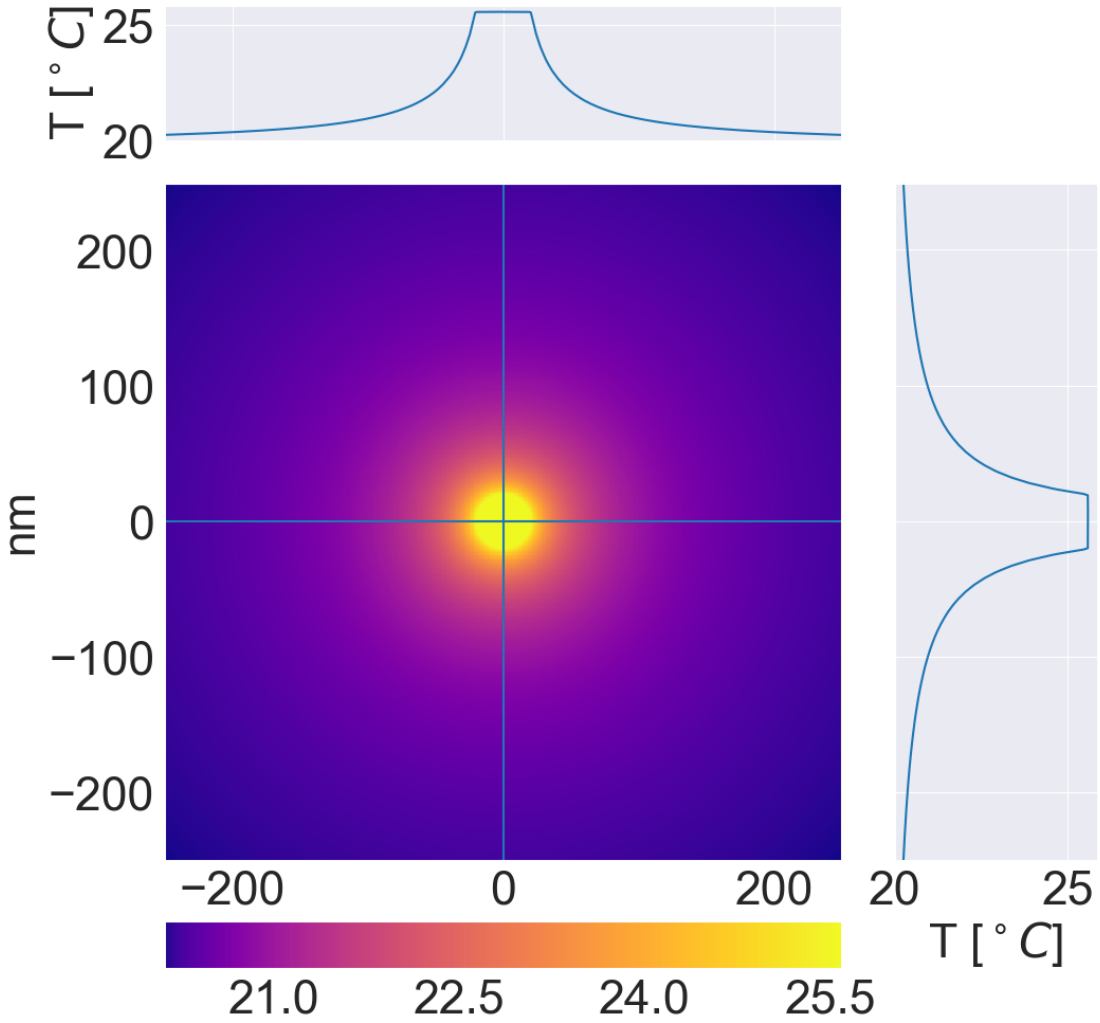

Fig. 4.6 Heating profile of single 40 *nm* particle in water due to the absorption of laser light. The top and right graphs show the heating profile. Around 200 *nm* away from the nanoparticle's centre, the temperature has decayed to ambient.

Each nanoparticle acted as a heating element, locally changing the temperature of the water media which they resided in. As there were approximately 1×10^{10} nanoparticles per millilitre of water, they collectively contributed to the increase in the temperature of the solution, and thus changed the relative permittivity of the medium. Consequently, this led to lensing effects of the initial beam.

4.2.2.2 Nanoparticle heating effects in a 5 cm cuvette

The steady-state 2D (axis-symmetric in cylindrical coordinates) heat diffusion equation (Equation 3.2) for a 5 *cm* quartz cuvette containing the nanoparticle solutions was

simulated. The boundaries of the cuvette were kept at T_{amb} (20 ° C) to dissipate the heat into the environment. The beam was simulated such that its focal position was 1 cm inside the cuvette. To ensure the a physical solution was calculated, the maximum mesh was set to focal spot size of the beam. The heat source (Q) was defined as:

$$Q = T_I e^{-a_z z} I(r, z) a_z \tag{4.4}$$

where T_I was the percentage of light transmitted through the Quartz cuvette interface with an optical path of 4 mm (cuvette thickness). Using the Fresnel reflection coefficients (Equation 2.8 of Chapter 2), it was found that 95% of the initial laser light was transmitted into the sample solution. The filling fraction of the Au solution used by Fardad *et al.* was far too high in concentration and meant that 90% of the light was absorbed in the first centimetre of the cuvette. Hence, to allow the laser beam to further transmit light into the cuvette and thus study how the beam profile affects the heating profile, a reduced (by a third) filling fraction of 7×10^{-7} was used. The reduction of concentration was representative of the experimental results discussed in later sections of this chapter. A laser power of 100 mW was used to determine the 2D heating profile generated by the Au-nano-suspension (Figure 4.7b).

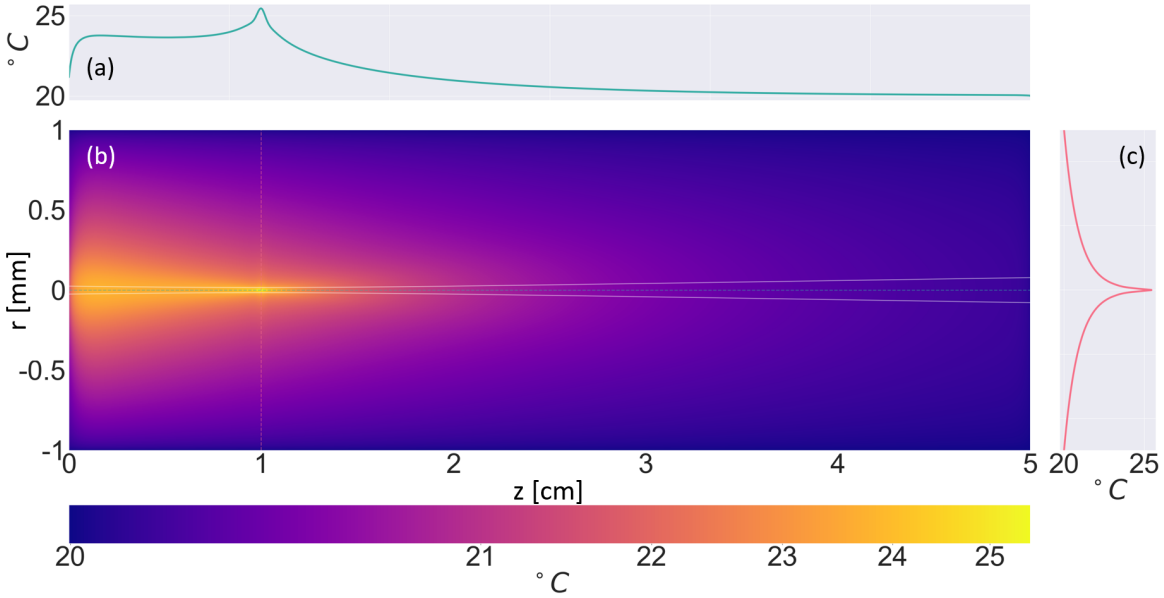

Fig. 4.7 **(a)** Axial temperature profile. **(b)** 2D temperature simulation due to Au-nanoparticle absorption of the laser beam. White lines show laser profile. **(c)** Radial temperature profile at the focal point.

The majority of the temperature rise occurred before the focal point, despite the lower concentration of nanoparticles used in the simulation (relative to Fardad *et al.*). The linear absorption was the dominant effect and resulted in a generally exponentially decaying axial temperature profile (Figure 4.7a). At the focal point, where the intensity was the highest, the biggest temperature change from ambient was observed (Figure 4.7a). The radial heating profile was Lorentzian-like and had a temperature change of approximately 5 $°C$ at the central position (Figure 4.7c). The heat dissipation extent in the radial direction was greater than the beam size (Figure 4.7b).

The heat diffusion simulations were re-evaluated for different focal positions along the cuvette to discern their effects on temperature profiles as the observed lensing effects have been reported to change as a function of the focal position [28] (Figure 4.8)

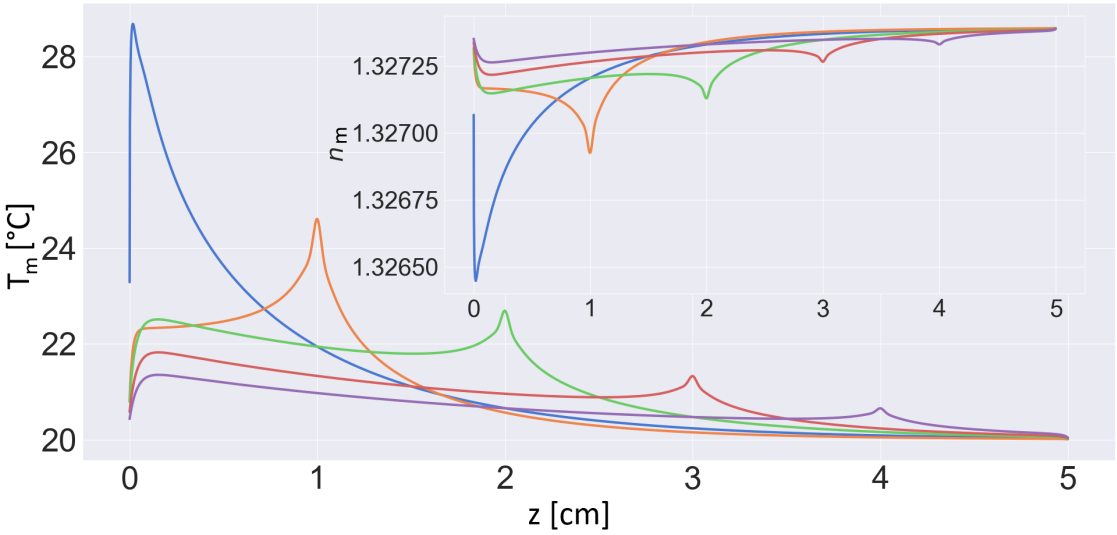

Fig. 4.8 Axial heating profiles of Au-40 nm suspension in a 5 cm cuvette at a power of 100 mW and a beam spot size of 8 μm. Adjusting the focal position of the beam resulted in different heating profiles and a change in the magnitude of heating induced. All profiles were predominantly exponentially decaying, arising from the linear absorption of the nanoparticles. **Inset**: Refractive index change determined from the dispersion relation of water at 532 nm.

The further the position of the focal point along the cuvette, the smaller the temperature change induced was, and the less dominating the exponential decay profile due to the linear absorption of the nanoparticles (Figure 4.8). For all focal positions, the quantified refractive index change was negative. This was obtained using the density

(atmospheric pressure), wavelength (532.8 nm), and temperature dependent dispersion relation of water [138] (Appendix 5). The further the focal point inside the cuvette, the greater the portion of the beam pre-focal point was altered.

The magnitude and heat dissipation profile could be altered by changing the nanoparticle medium. The thermal conductivity valus of alcohols, such as ethanol or methanol, are lower than water (0.162 $Wm^{-1}K^{-1}$, 0.2 $Wm^{-1}K^{-1}$ and 0.6 $Wm^{-1}K^{-1}$, respectively) [139]. Hence, alcohols dissipate the heat less, meaning that the temperature rise is higher than in the case of water. Moreover, the thermal diffusivity ($k/\rho C_p$) of the solutions play an important role in the thermal profiles they create. The thermal diffusivity of water relative to ethanol and methanol is 1.64 and 1.41 times lower, respectively [139]. The 2D heat diffusion was simulated with the Au-nanoparticles suspended in isopropyl alcohol with the focal position set to 1 cm inside the cuvette. In comparison to water, the temperature induced at the focal point was 1.44 times higher (Figure 4.9).

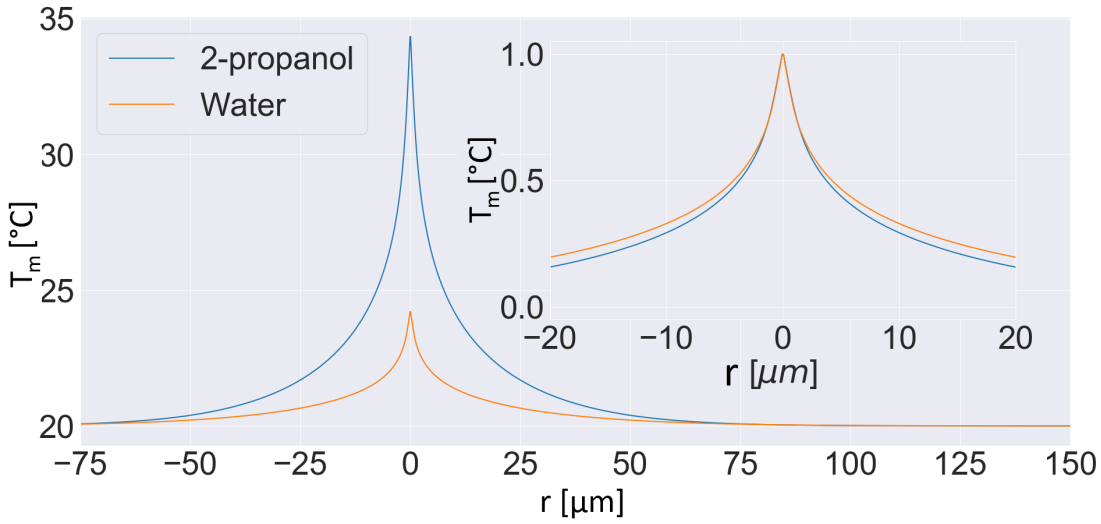

Fig. 4.9 Radial profiles of heating generated by 40 nm particles suspended in water, and 2-propanol alcohol, with an incident power of 100 mW. The radial profile was for the focal point placed 1 cm inside the cuvette, with a focal spot size of 8 μm. A larger temperature difference occurred in the alcohol solution due to its lower heat diffusivity coefficient. **Inset**: Normalised temperature for both media, illustrating the difference in heat diffusion between the two solutions.

The steady-state radial heating profile for isopropyl alcohol was broader than for water due to the higher induced temperature. However, upon normalising the temperatures for the different media, water was more dissipative, as expected (Figure 4.9 inset). Hence, re-suspension of the nanoparticles from a water media to alcohol based media, yielded greater heating effects and different refraction profiles (taking into account the thermo-optic coefficients).

4.2.2.3 Nanoparticle heating in a micro-cuvette

In the 5 cm cuvette, the temperature profile and its corresponding refractive index gradients depended on the heat diffusion of a large volume of medium relative to the volume of the beam. This essentially meant that the temperature profile at each position of the cuvette was affected by its temperature difference relative to the neighbouring position. The diffusion of heat in the large volume blurred the individual heating profiles generated for each segment of the intensity varying beam. By considering smaller light-matter interaction lengths of 300 μm rather than 5 cm, the heating effects at every segment of the beam's propagation were characterised independently. This allowed for direct comparisons between the measured refractive index changes using the z-scan method (Section 4.4.2.1) and the theoretical thermal lensing behaviour for each position of the beam in the axial direction.

Transient heat diffusion was simulated (using time dependent solution of Equation 3.2 in Comsol) for a cuvette with an optical path length of 300 μm. The sample

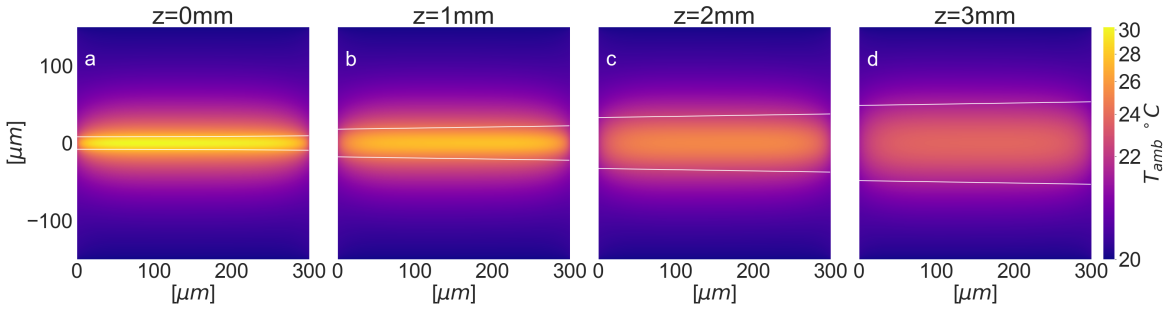

Fig. 4.10 Temperature profiles for a thin 300 μm optical path length cuvette at different positions of the laser beam. The white lines show the laser profile (w_0) at the given z-distance. A temperature rise of 10 $°C$ (P = 75 mW) occurred when the focal position was placed at the entrance of the cuvette (z=0 mm). The radial heating extent was greater than the size of the beam.

chamber of the cuvette was sandwiched between a coverslip (170 μm) and a glass slide (1 mm), both made of silica glass. The boundaries of the sample chamber and the silica glass were kept at T_m, and heat was allowed to diffuse between the water sample chamber and the silica glass, relative to their temperature difference and thermal properties. The heat source (Q) is the same as Equation 4.4, but T_I has value of 96% corresponding to transmitted light through silica coverslip interface. A laser power of 75 mW was used, corresponding to the maximum power used in the z-scan data (Section 4.4.2.1). The cuvette position was scanned along the z-direction and the heating profile determined for a total time of 10 ms (Figure 4.10). This time frame was the same as the acquisition time of the measured z-scan data. Due to the shorter cuvette length, a filling fraction of 2×10^{-6} was used, which corresponds to OD 1.

With the focal position at the entrance of the micro cuvette, a temperature rise of approximately 10 $°C$ was theoretically expected from a 75 mW beam being absorbed by 40 nm Au-nanoparticles (Figure 4.10a). The radial heating profile was larger than

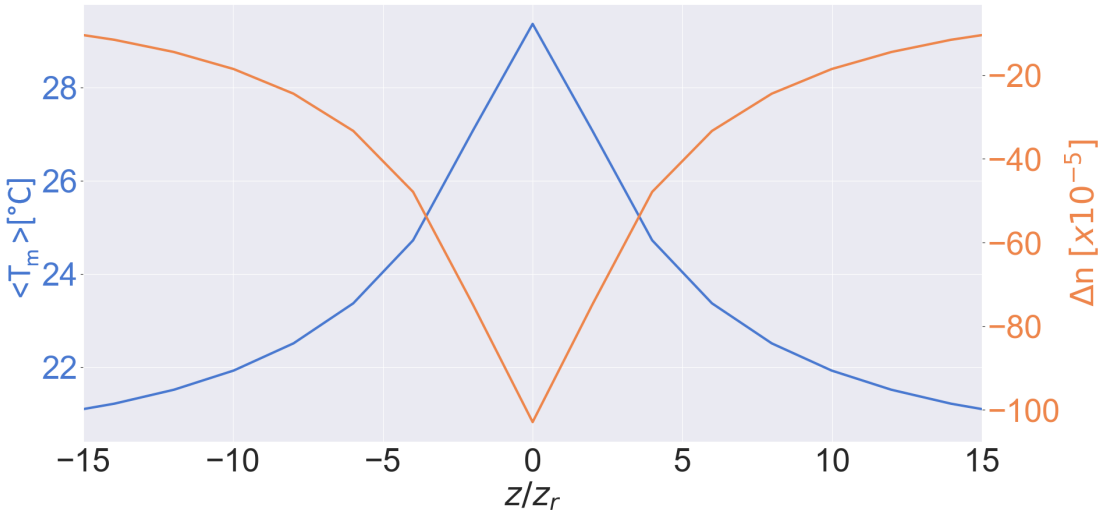

Fig. 4.11 Axial temperature profile evaluated by the mean temperature ($< T_m >$) of the central radial position (left axis and blue curve). The corresponding refractive index change due to temperature variations (right axis, orange curve) obtained from the dispersion relation of water. The profile was Lorentzian-like in shape. The power of the beam was 75 mW corresponding to the maximum power used in the z-scan measurements, and thus allowing for direct comparisons between simulated and measured Δn and n_2 values. Magnitude of Δn is comparable to the reported value of Ortega *et al.* for 5 nm Au nanoparticles (inset of Figure 1.27b).

the width of the beam at a time of 10 *ms*. The temperature generated reduced as the cuvette was scanned away from the focal point due to the lower intensity (Figure 4.10b-d). The axial heating profile due to the varying intensity of the laser beam was determined by quantifying the mean temperature ($< T_m >$, average of the central radial temperature) at the central radial position for every evaluated cuvette position (Figure 4.11).

The axial temperature profile was Lorentzian-like in shape. The axial coordinates were divided by the Rayleigh length (Z_r, 0.501 μm) of the beam, to allow for direct comparison between the refractive index change derived from the dispersion relation of water and the measured refractive index change (Section 4.4.2.1). Heating of the solution and a small change in refractive indices still occurred at distances ± 15 Rayleigh lengths away from the focal position. At the focal point, the refractive index change (Δn) was -103×10^{-5}, which corresponded to n_2 values of -1.38 ×10^{-12} m^2/W, for a

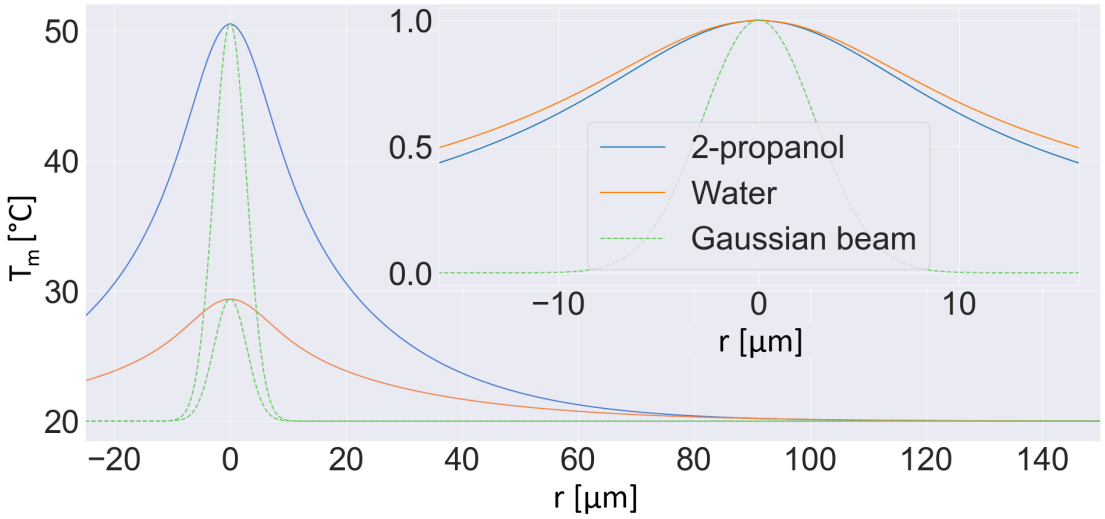

Fig. 4.12 Simulated temperature profiles of Au-nanoparticles suspended in different solutions in a 300 μm cuvette placed at the focus (w_0=8 μm, marked by the green dashed line). The temperature rise for isopropyl alcohol was much higher than water medium for the same power (75 mW). The beam size was much smaller than the heating profiles, which were no longer Gaussian in shape, but were more Lorentzian-like. **Inset**: Normalised temperature profiles for each solution, with the water having a more spread-out shape due its higher thermal diffusivity. The radius of curvature of the lens created by the isopropyl alcohol was smaller than water (at r=0) meaning that it was a stronger lens.

power of 75 mW and a beam size of 8 μm.

A means of investigating whether the lensing effects were indeed driven by thermal effects was to change the media of the nanoparticles suspension to a lower thermal diffusivity relative to water. In the 5 cm cuvette, the induced temperatures were 1.4 time greater for the same power, focal length and nanoparticle concentration when the particles were simulated in isopropyl alcohol media. In the same manner, the temperature profile of the nanoparticles suspended in isopropyl alcohol was simulated for the 300 μm cuvette placed at the focus with a laser power of 75 mW.

The average r-direction heating profile of nanoparticles in isopropyl alcohol media was broader and rose more steeply to its maximum values compared to water suspended nanoparticles. The peak temperature was also 1.7 times higher. In both media, the heat diffusion at a time of 10 ms was larger than the beam size (Figure 4.12 inset). The higher temperature rise and the steeper temperature gradients of isopropyl alcohol solution meant that it had a stronger lensing power. This was analogous to a lens with a smaller radius of curvature.

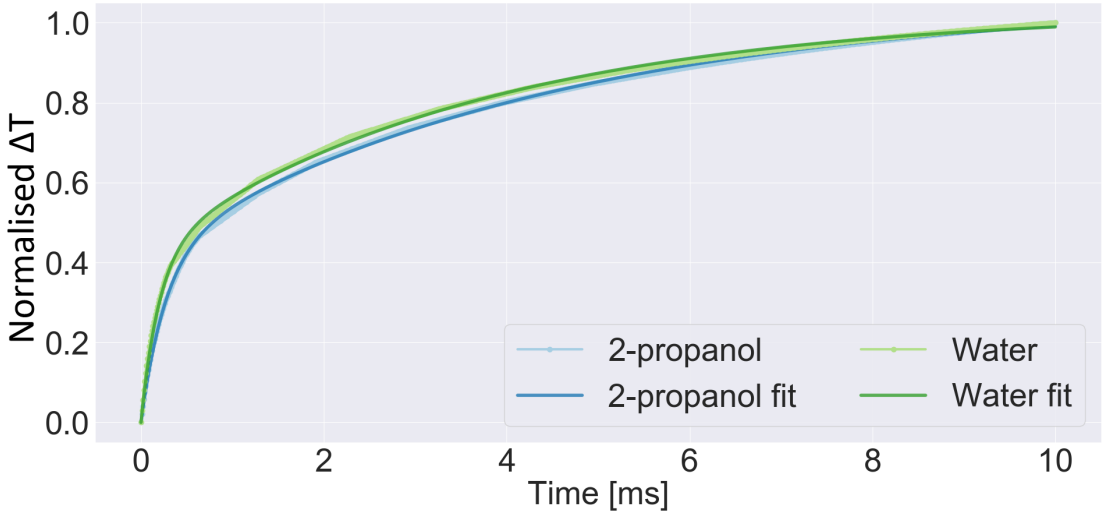

Fig. 4.13 Double exponential fitting to extract the associated time constants for the temperature increase of the central radial position with the cuvette placed at the focal point. Fitting values were reported in Table 4.1.

Comparison of time scales associated with the theoretical and measured evolution of the system could help elucidate the governing physical mechanism behind the observed lensing effects by Fardad *et al.*, and the work presented herein. The transient evolution of the temperature profiles in Figure 4.12 were quantified in steps of 10 μs up to 10 ms. For each time point, the mean temperature of the central radial position was evaluated and normalised relative to the temperature at 10 ms, for both water and isopropyl alcohol solutions (Figure 4.13).

The temperature rise from T_m appeared to rise exponentially for both media. In an analogous manner to other studies that quantified the temporal dynamics of temperature [140, 141], a two exponential rise function $f(t, \tau_1, \tau_2)$ was fitted to the theoretical temperature rise of Figure 4.13, such that

$$f(t, \tau_1, \tau_2) = a_1 \left(1 - exp\left[\frac{-t}{\tau_1}\right]\right) + a_2 \left(1 - exp\left[\frac{-t}{\tau_2}\right]\right) \tag{4.5}$$

where a_1, a_2, τ_1, and τ_2 were the relative weighting, and time constants, respectively [142]. The residuals of a single exponential fit also had an exponential behaviour, suggesting that a two exponential fit was more appropriate for representing the temporal dynamics of the temperature evolution.

Media	a1	τ_1 $[ms^{-1}]$	a2	τ_2 $[ms^{-1}]$
Water	0.42	0.19	0.61	3.67
Isopropyl Alcohol	0.42	0.27	0.63	4.42

Table 4.1 Time constant for the temperature rise at the central radial position of a micro-cuvette placed at the focal point of a laser with the 40 nm Au-nanoparticles suspended in different media. The heat diffusivity was slower for isopropyl alcohol relative to water, as expected.

The associated theoretical temperature rise in both media had a long (ms) and short (μs) time constants (Table 4.1). These time scales could correspond to the heat generation and dissipation of the Au-nanoparticles in their respective medium. In both cases, the longer time constant had a higher weighting. The isopropyl alcohol's short and long time constants were 1.4 and 1.2 times longer relative to water, respectively. This difference approximately corresponded to the lower thermal diffusivity of alcohols.

These theoretical time scales were compared against the measured transient z-scan results.

4.2.3 Thermophoretic effects

Lensing effects could also be caused by the thermophilic or thermophobic migration of the nanoparticles. There could be a local temperature gradient (across the nanoparticle with one side being slightly hotter) and global temperature gradients caused by the ensemble heating of the nanoparticles within the beam.

The nanoparticles used in this work were only suspended in Milli-Q water (according to the manufacturer's specification [143]), with an approximately neutral pH. Hence thermoelectric fields (generated by separation of ions in the presence of a temperature gradient) were likely very weak or not present.

Thermophoretic motion of nanoparticles could however be mediated by the entropic forces due to the hydration entropy of the Au-nanoparticles with the citrate molecules (used for charge stabilisation). If this was the dominating force, then the associated time scales for self induced lensing effects (measured by transient z-scan) were likely to be in the order of tens-of-seconds [20].

4.3 Thermal lensing methods and protocols

4.3.1 Optical setup for quantifying lensing behaviour

A DPSS laser was used to generate laser light with a wavelength of 532 nm. In General, DPSS laser generating a wavelength of 532 nm are achieved by using 808 nm and 1064 nm pump beams. A spectrometer was used to verify a single output of 532.8 nm, with no leakage of the pump beams present. The laser power was modulated using an Acousto-Optic Tunable Filter (AOTF), which effectively acted as a fast shutter, with a measured rise time of 2 μs. However, the AOTF (by AA Opto-electronic, France) can only modulate vertically polarised light so a half-wave plate was used to rotate the polarisation plane of the laser. The AOTF was modulated with a frequency of 121.6 MHz which gave the brightest first order output for the 532.8 nm laser. The output power of the laser was controlled by changing the amplitude of the AOTF's driving frequency. A power meter was used to characterise the laser output power from the

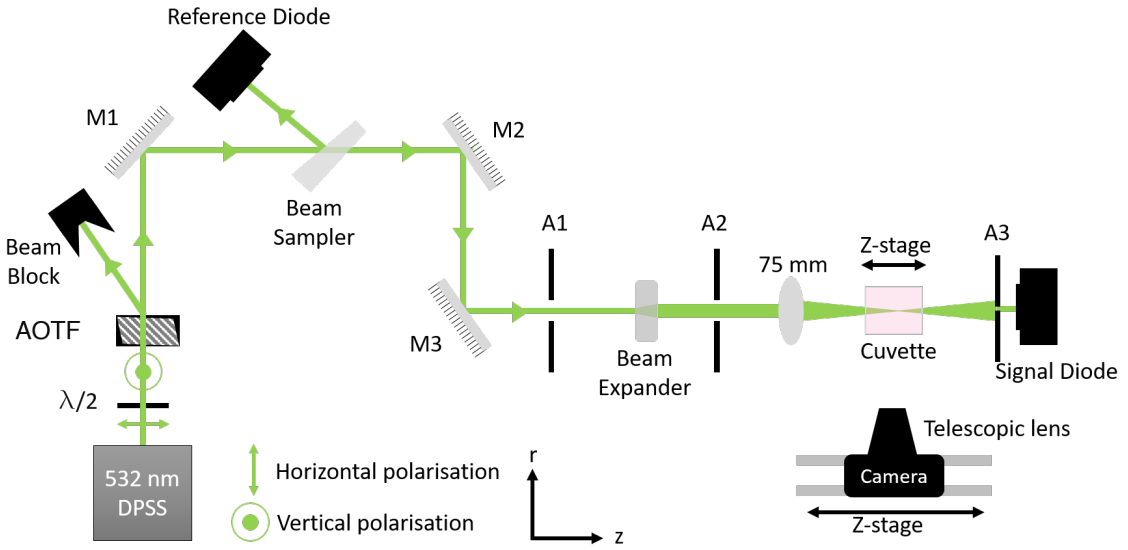

Fig. 4.14 The optical set-up used for both sides cuvette ($L = 5\ cm$) self lensing imaging and Z scan measurements ($L = 300\ \mu m$). An AOTF along the beam path acted as a fast shutter to allow transient measurements of the lensing effects for both types of measurements. For side cuvette imagining, a camera was placed perpendicularly to the cuvette, about 60 cm away, and was mounted on a manually translatable Z-stage to always keep the cuvette in the field of view. As the entire beam propagation through the cuvette was imaged, the imaging system had a low NA (not able to resolve actual beam size at the focus). For z-scan mode, the large cuvette was replaced by a smaller optical path length cuvette whilst keeping all the other optical components constant. The photons incident on the signal and reference photodiodes were then used to determined the amount of light transmitted through the aperture (A3) as a function of the cuvette's position in the z-direction (controlled by a motorised stage).

AOTF relative to the input voltage of the AOTF's driver module. A beam block was used to dump the zeroth order from the AOTF.

A series of mirrors (M1, M2, M3) was used to direct and align the beam onto a photodiode through an series of apertures (A1, A2, A3) used as reference points for beam alignment (Figure 2.15). An adjustable beam expander and a plano-convex lens with focal length of 75 mm were added to the beam path. A beam sampler was used to pick-off a 4% portion of the beam which was monitored by a reference photodiode. This accounted for power fluctuations of the beam and quantified the power presented at the focal point of the focusing lens. With the addition of each optical component, the beam alignment was checked through the referenced apertures.

A 5 *cm* Quartz or a custom-made 300 μm optical path length was placed onto a set of electronic actuation stages (r- and z-direction) for translating and positioning the sample solution at desired positions along the focused beam path. Custom-made cuvette holders were made that securely held the cuvette as well as minimise the tilt between the cuvette interface relative to the orthogonally propagating beam.

A CMOS-based camera and a telescopic lens (NA $\sim$ 0.05) with an adjustable magnification were used to image the lensing effects of the beam in the 5 *cm* cuvette. The camera body and lens were mounted on a movable stage to track the motion of the cuvette when the focal spot was scanned inside the cuvette's sample chamber. This ensured that the full length of the 5 *cm* cuvette remained in the full frame field of view of the camera.

For each z-scan measurement, the transmission ratio between the signal and reference photodiode was quantified by fully opening the iris of A3 without a sample in place. The aperture was then closed and a sample placed on the translation stage for measurement. The signals obtained from the photodiodes were then electronically acquired using a digital oscilloscope connected to a computer.

4.3.2 Z-scan data acquisition and processing

The translational stages, the signal acquisition and laser control through the digital oscilloscope (DO) were controlled by the computer using a *Python* script which governed the sequence of events. A list of laser powers and scanning locations were provided by the user which resulted in iteratively moving to the desired z-position, setting the laser power, and acquiring the data automatically.

The computer sent a command to the digital oscilloscope's arbitrary waveform generator to generate a 100 *Hz* Square-wave (Figure 4.15). Primarily, this acted as a trigger signal for data acquisition, but also set the desired laser power relative to its amplitude (0 - 1 *V*). However, the AOTF's control box required a trigger signal of 0 - 10 *V*, hence a 10x amplifier was used to access the full range of required input voltage, from which the amplitude of the AOTF's RF signal was set, which in turn controlled the laser power output by the AOTF. At the same time, two channels of the digital oscilloscopes began to acquire data from the signal and reference photodiode.

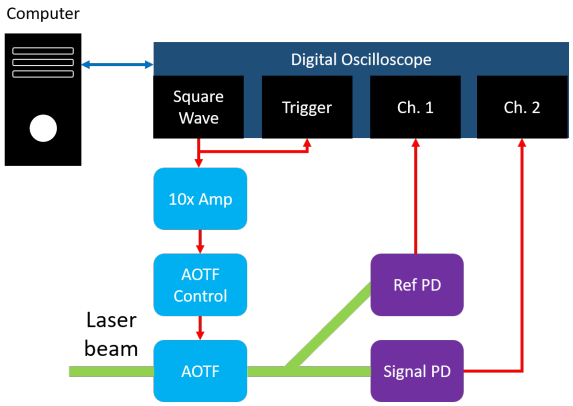

Fig. 4.15 Illustration of the signal path for z-scan data acquisition. Blue arrow was data relay via USB (between computer and digital oscilloscope). Red arrows were coaxial cables. A Square-wave was generated which triggers the acquisition process, and its amplitude determined the outputted laser power by the AOTF.

For each z-scan position, a total of 2.5×10^5 samples with a sampling interval of 40 ns were acquired from each photodiode, amounting to a 10 ms acquisition time. The samples were stored on the digital oscilloscope's buffer before being passed to the computer's memory. The laser power was then turned-off by the AOTF for a period of 1 s before the next measurement began. This ensured that the sample's temperature returned to ambient and thus avoided hysteresis between successive measurements. This process was repeated three-times for each z-scanned position, from which the mean and standard deviation values were calculated and stored on the computer's hard drive.

Once all the datasets were obtained for all the desired z-scan locations and laser powers, the data was processed in bulk using Python. Firstly, the signal and reference photodiode data were loaded onto the computer's memory for processing. The data were then binned in time bins of 0.4 μs, after which, the first 16 μs was discarded as it corresponded to the system's response. Time-binning the data reduced the high-frequency laser fluctuations present (short time scales) in both the signal and reference datasets. The transmission of the light for each position, at every time-point, was then quantified by dividing the time-binned signal data by the time-binned reference datasets, multiplied by the reciprocal of the open aperture transmission ratio. The baseline transmission was determined from the first time-bin, where non-linearity was not present. A scaling factor was then calculated to normalise the baseline transmission. All subsequent transmissions for every time-bin were normalised relative to the baseline

transmission by the scaling factor.

The change in the index of refraction from the transient z-scan data was quantified using the Sheik-Bahae formulation (Equation 1.12) by least-squared fitting to determine the on-axis phase shift at the focus ($\Delta\Phi(t)$, Equation 1.13). The errors obtained from time-binning the data were considered when applying the least squares fitting method. Moreover, the peak-to-valley change in transmission around the focal point was the critical parameter that quantified the change in refraction in the work by Sheik-Bahae *et al.*. Hence, the curve fitting process was modified to minimise the difference between the peak-to-valley values of the fit and the data. This was achieved by incrementally shifting the Z/Z_r values in steps of 0.001 Z/Z_r, until the difference between the peak-to-valley values of the fit and the data was minimised. This step centred the values of Z/Z_r at the focal point of the scanned region and effectively symmetrised the measured dataset about the y-axis. The fitting was conducted for each time-bin to determine the phase change as function of time, from which the change in index of refraction was evaluated.

4.3.3 Measuring beam propagation in a 5 *cm* cuvette

The same optical set-up as described in the previous section was used to investigate transient lensing behaviour in a 5 *cm* cuvette (Figure 4.14). The AOTF was used as a shutter to pulse the beam on and off at a 2 *Hz* frequency. A custom-made L-plate which held the cuvette securely was designed such that the beam intersected approximately 1 *cm* above the bottom of the cuvette. The holder also ensured that the cuvette did not move when the sample solution was exchanged. The translational stages were used to centre the beam through the cuvette. All alignment steps were done using a laser power of a few milliwatts.

Approximately 2 *ml* of solution were pipetted into the cuvette for each sample under investigation. Every time the sample solution was exchanged, the cuvette was washed out with Milli-Q water.

The telescopic lens was adjusted such that the cuvette's inner edges were just outside the camera's field of view. This ensured that the light matter interaction across the entire length of the sample was obtained. The frame rate of the camera was increased to 707 frames per second by only scanning a region of interest

that encompassed the beam. The gamma correction factor was set to 1 for linear intensity response from the pixels. For each experiment, the black level and exposure were manually set to avoid over exposed pixels and to maximise the intensity range.

The CMOS camera used for acquiring videos of the lensing effect had a limited dynamic range as it only had an 8-bit sensor. This meant that lower intensity regions of the beam (towards the end of the cuvette), had a low signal to noise ratio. To improve this, 20 on-off cycles of the laser beam in the cuvette were recorded in each video. Python was then used to merge the 20 on-off sequences into one, by averaging each pixel for each frame (time matched relative to the first 'on' frame of every sequence). This meant that each pixel for every frame had an associated deviation from its mean value, which ameliorated the quantification of the beam's size for low intensity regions.

4.3.4 Beam size and propagation measurements

Characterisation of the beam parameters, such as the spot size at the focus and Rayleigh length, were necessary as the value of n_2 was determined from them. More importantly, the Sheik-Bahae method of determining non-linear refraction required the optical path length of the sample cuvette to be shorter than the Rayleigh length of the beam [86].

The knife-edge method was used to measure the beam spot size at the focus and its corresponding Rayleigh length (in air). This technique involved scanning a flat edge, such as a razor blade, orthogonally with respect to the beam propagation direction [144]. By repeating the processes at various points around the focal point, the beam's size as it propagated was mapped out. Based on this, the Rayleigh length was determined. This method assumed that beam shape was not elliptical.

The signal photodiode, a razor blade and the translational stages were used to characterise the beam's propagation in air, as it focused down a 75 mm plano-convex lens. The blade was initially positioned at the focal position, which was determined approximately by eye and such that the edge was blocking all the laser light from being incident on the photodiode. It was then scanned in the r-direction by 100 μm, in steps of 5 μm, whilst the transmitted light was collected by the signal photodiode. A Sigmoid rise in the collected power was detected as the blade's edge was scanned

(Figure 4.16a). The normalised power for a given z-position ($f(r|z)$) was fitted to an Error-function (Equation 4.6) to quantify the beam size [145].

$$f(r|z) = \frac{1}{2} erf\left\{1 + \frac{(r - r_0)}{w(z)}\right\} \tag{4.6}$$

This process was repeated for $\pm$ 1 mm about the focal point and in the z-direction, such that the beam's size was measured at several points around the focus, from which the Rayleigh length and the focal position ((Figure 4.16b)) were obtained by fitting the data to Equation 2.2.

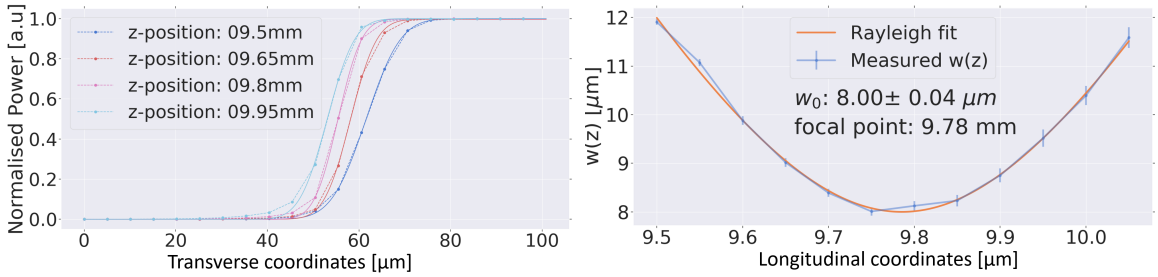

(a) (b)

Fig. 4.16 **(a)** The detected light by the signal photodiode as the razor blade was scanned across the beam for various z-positions. Equation 4.6 was fitted to the normalised data to obtain the beam size ($w(z)$). **(b)** The beam size around the focal point fitted to Equation 2.2 to determine both the beam waist at the focal spot and the Rayleigh length. The errors were determined from the Error Function fitting.

The beam waist at the focus and Rayleigh length were quantified to be 8.04 $\pm$ 0.04 μm, and 511 $\pm$ 16 μm. The focal point was identified to be 9.78 mm relative to the scanning coordinate of the z-direction translation stage. Determining the location of the focal point relative to the scanning coordinates of the z-scanning stage, allowed for higher sampling of the data near the focal region to better map the inflection points of the transmission curve.

4.3.4.1 Beam propagation characterisation

The beam parameters, such as size and divergence with varying laser powers, needed to be quantified to discern how the lensing effects form as a function of time. In addition, quantification of the beam parameters provided an opportunity to verify if

any non-diverging or self-focusing effects were present. The beam parameters were ascertained for every frame of the acquired video sets (power, focal position), by Gaussian fitting each column (vertical direction) such that:

$$f(r, r_0, w(z)) = Aexp\left[-\frac{2(r - r_0)}{w(z)}\right]^2 + c \tag{4.7}$$

where A, r_0, were the peak value and centre of the Gaussian, and c was the offset value (noise floor). The data for each column were normalised and the maximum value centred at zero (pixel value) before it was fitted to Equation 4.7). These pre-processing steps resulted in more reliable fitting. The error associated with each pixel value, obtained from averaging 20 laser pulse sequences per pixel and frame, were taken into account in the result of the least squares fitting (Figure 4.17). As a final measure to ensure reliable beam characterisation, fitting values were rejected if the associated error was bigger than three-standard deviations relative to the fitted values.

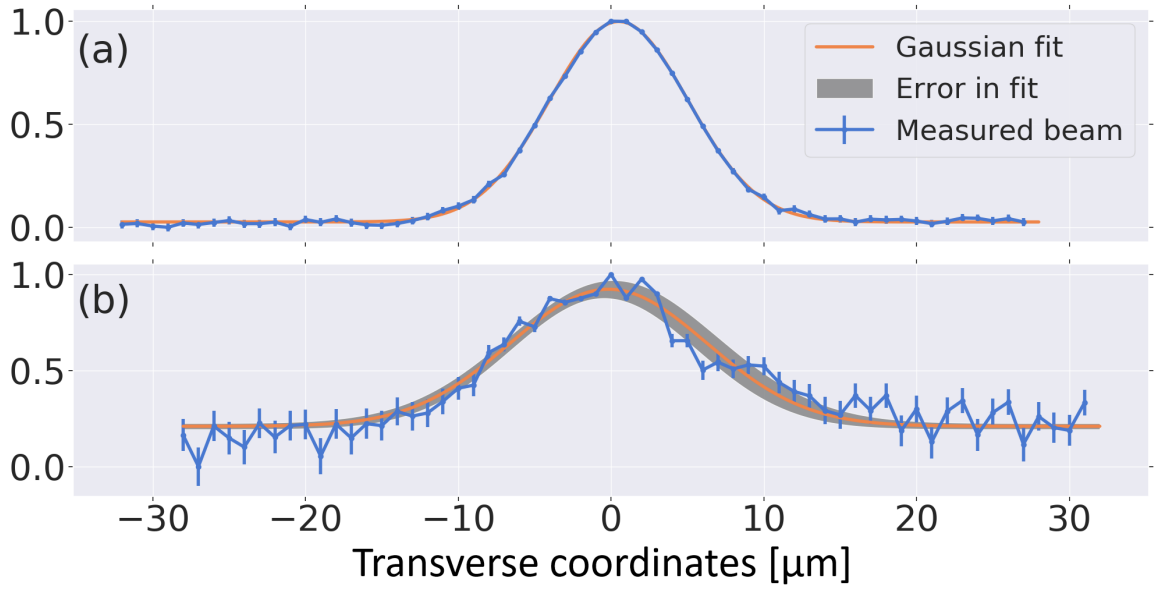

Fig. 4.17 Radial beam profile at the beginning (a) and end (b) of the cuvette. The Gaussian fitting (Equation 4.7) was a better fit with lower errors for the begining of the cuvette compared to the radial profile towards the end. This was because of the intensity reduction as the light propagated along the length of the cuvette. The radial profile did not change from a Gaussian for all investigated datasets. Only the width of the profile changed and was quantified.

The columns corresponding to the beginning of the cuvette had lower fitting errors due to the higher signal to noise ratio and smaller grey pixel value error (Figure 4.17a). In contrast, the columns towards the end of the image, related to the end of the cuvette had much higher deviation in the pixel value. The associated fits for this region were a good approximation of the beam shape and size (Figure 4.17b). Once all the fits were obtained for every video file, the values were converted from pixel coordinates to real space using a pixel calibration of 39 μm per pixel (1,272 pixels corresponding to 5 cm). The system was inherently diffraction limited (ideal diffraction $\lambda/2NA \approx 5.32$ μm, similar to w_0) due to the large field of view needed to probe the light matter interaction across the entire optical path length of the cuvette. Whilst an exact quantification of the beam size was limited due to point spread function of the optical set-up, the acquired beam size was approximately proportional to the transient evolution of the beam due the lensing effects.

The obtained beam size as it propagated in the cuvette was used to quantify the beam divergence, determined by the ratio of the beam size at the focal point divided by the Rayleigh length ($\theta = w_0/z_r$). The latter parameters were quantified by fitting the measured beam size to Equation 2.2. A negative change in the beam divergence as a function of time would suggest the beam was becoming self-focused.

4.3.5 Sample preparation and characterisation

The 40 nm Au-nanoparticles' concentration and quality were determined using spectroscopy in the visible region. Comparisons were made between the measured spectrum and theoretical extinction cross-sections to discern the size distribution of the nanoparticles. Deviations away from the theoretical curve would either be a result of a broader nanoparticle size-distribution or aggregation.

A cuvette with an optical path length of 1 cm containing a minimum sample solution of 1 ml was used to characterise the 40 nm Au-nanoparticles' spectrum, along with a white light source and a spectrometer. The same steps outlined in Section 2.3.5 were used to process the data collected from the spectrometer.

The nanoparticle concentrations from stock (OD 1) were both increased (by centrifuging) or decreased (by dilution) to obtained the desired optical density. The nanoparticle solution was centrifuged for 30 minutes at a speed of 3000 rpm, after

which, the supernatant was pipetted out. All nanoparticle suspensions were vortexed for 30 seconds and sonicated for 15 minutes before measurements. This step was critical for samples which had been centrifuged to ensure sufficient re-dispersion in the solution. A range of nanoparticle optical densities were tested for lensing effects for both water and isopropyl alcohol-water mixtures (Figure 4.18).

The measured spectrum for water at the various ODs conformed well to theoretical spectrum given the ± size distribution of the nanoparticles [143] (Figure 4.18a). However, as the OD increased, the measured spectrum broadened, indicating an increase in the size distribution. For isopropyl alcohol-water mixtures, the spectrum was similar to its theoretical counterpart in shape, but was broader for both shorter and longer wavelengths around the peak (Figure 4.18b).

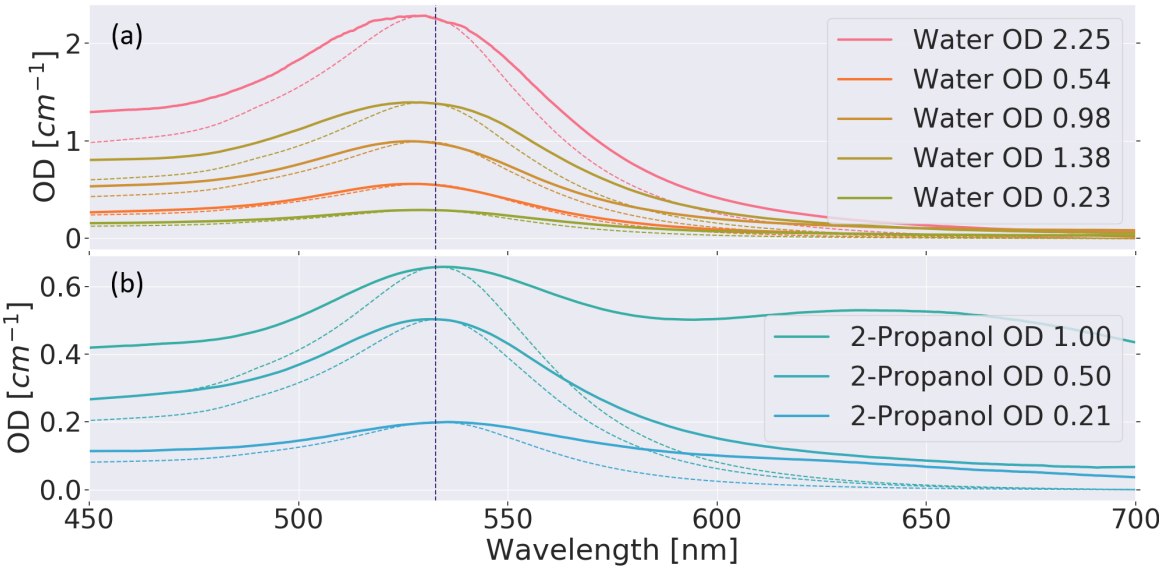

Fig. 4.18 **(a)** Visible spectrum of 40 *nm* Au nanoparticles at different concentrations suspended in Milli-Q water. The dashed lines were extinction cross-sections from Mie theory (obtain from [36]). Measured distributions were wider owing to their ±8 % size distributions. Peak positions matched between measured and theory, meaning they the sample solution was a good representation of 40 *nm* Au-nanoparticles. **(b)**: 40 *nm* Au-nanoparticles suspended in isopropyl alcohol-water mixtures at different concentrations. Dashed line as Mie theory for nanoparticles suspended in a refractive index of 1.37 (corresponding to the isopropyl alcohol, obtained from [36]). The OD 1 sample was not used for any measurements as the measured signal deviated significantly from theoretical values.

Attempts were made to re-suspend the Au-nanoparticles in a isopropyl alcohol environment with OD 1 at 532 *nm*. A 1 *ml* solution of nanoparticles in water were centrifuged, and 950 μl of supernatant was removed and replaced by 800 μl of isopropyl alcohol. Only OD 0.62 was achieved because particles had aggregated, evident from the presence of the secondary peak forming around 650 *nm* (Figure 4.18b). Consequently, this nanoparticle solution was not used in any measurements. The other isopropyl alcohol-water mixtures were stable and did not change in spectra over the course of a week.

The lower OD solutions (*ca.* OD 0.22) were used in the 5 *cm* cuvette measurements to allow the laser light to be transmitted along the entire length of the cuvette. The nanoparticle particle, acquired before and after the lensing effect measurements, did not change. Hence, the continuous heating and cooling of the nanoparticle solution as it interacted with the laser light, did not change the nanoparticle properties.

4.3.5.1 Sample preparation in micro-cuvettes

For z-scan measurements to be valid, the cuvette with an optical path length smaller than the beam's Rayleigh length was needed. This criteria ensured that the lensing effects were sampled in small enough segments along its propagation through the focal point. The cuvette had to have flat interfaces to not cause additional lensing, as well as being made of an optical grade material. In addition, the sample had to be contained and stored without degradation, evaporation, or leaking.

A double sided adhesive sticker (Bio-Rad Frame-Seal) was used to create a chamber between a coverslip and a glass slide. The coverslip and glass-slide provided a flat imaging interface, a rigid structure for handling the cuvette and a seal chamber so the solution did not evaporate. By using the sticker's inner dimensions (15 *mm* x 15 *mm*) and its volume capacity (65 μl), its thickness was calculated to be 300 $\pm 15 \mu m$.

Samples were embedded inside the cuvette's chamber by first cleaning the surfaces of the glass slide and coverslip using acetone, isopropyl alcohol and distilled water. They were then placed on top of lens tissue to avoid scratching and contamination. The first side of the adhesive film was pealed-off from the Frame-Seal sticker, after which it was positioned in the centre of the glass slide (adhesive side-down). The blue frame was then traced with the back of a tweezer to ensure proper contact of the adhesive

layer with the glass slide. Then, the top adhesive film was removed. In all instances, 35 μl of the sample was pipetted into the centre of the sticker (Figure 4.19a). The cleaned coverslip (24 mm x 24 mm) was then positioned a few millimetres above the adhesive layer and then dropped such that all parts of its interface came into contact with the adhesive layer at the same time. This was the best method of spreading the solution without it overflowing and consequently sealing the chamber (Figure 4.19a).

(a) (b)

Fig. 4.19 **(a)**: 40 nm Au nanoparticle solution (40 μl) pipetted at the centre of the Frame-Seal sticker which was adhered to the glass slide. **(b)**: Seal chamber using a coverslip placed the top adhesive surface. The seal cuvette with an optical path length of 300 μm was used for z-scan measurements.

The cuvette was then positioned onto a glass slide holder made by Thorlabs which held the slide in place securely using four rubber-tipped screws against a flat metallic plate. After each z-scan measurement, the seal cuvette along with its solution was preserved by storing it in a fridge.

4.4 Self induced lensing experimental results

In the first part of this section, the results of Fardad *et al.* were reproduced, quantified and extended by investigating transient lensing effects with varying the focal position inside the cuvette, at a variety of laser powers, and by changing the media of the nanoparticle suspension. In contrast to their finding, the lensing behaviour was driven by thermal effects. As further evidence of this, transient z-scan was performed on the nanosuspension to discern the refractive index change and the associated time scales at which the lensing effects develop.

4.4.1 Lensing behaviour in a 5 *cm* optical path length cuvette

All the measurements of the lensing behaviour were carried out with 40 nm nanoparticle suspensions with OD 0.3 per cm attenuation for both water and isopropyl. A lower

OD was used to permit light to penetrate the full extent of the cuvette and to be in the detection range of the camera.

Lensing behaviour was observed for approximately 0.5 s, with a sampling rate of 1.4 ms. The beam's initial size was referenced to the first frame of when the laser was present in the cuvette. The last frame, just before the beam was blocked, was regarded as the steady state beam shape. Comparisons were drawn between the two states to quantify changes in the beam's shape and size. From Gaussian fitting, it was determined that the radial beam profile did not change from a Gaussian, but rather underwent a change in size. This consequently affected the axial profile, which was investigated herein.

In all subsequent figures, the laser beam emerged from the left (beginning of the cuvette) and exited at the right (end of the cuvette). The initial focal position and the steady-state one were determined as the points where the beam waist was a minimum. The beam sizes measured were diffraction limited due to the large 5 cm field of view. The measured beam spot size at the focus using the knife-edge was 8 μm, whilst the smallest beam obtained from the camera images was approximately 40 μm.

4.4.1.1 Effects of focal position

The lensing effects of adjusting the focal position inside the 5 cm cuvette were investigated at a constant laser power of 98 mW. Heat diffusion simulations and its corresponding refractive index change at varying focal positions inside the cuvette, suggested that a bigger negative refractive index change was expected for focal positions near the cuvette's entrance. To corroborate this, beam profile measurements were taken with the focal position a few millimetres from the cuvette's entrance, up to the cuvette's mid point (Figure 4.20).

In all cases, except for when the focal spot was near the beginning of the cuvette, the size of the beam was smaller after the focal point relative to its initial size. As a result, the beam was less divergent. This is predominantly evident for regions towards the end of the cuvette, where the biggest difference in beam size occurred. In contrast, the portion of the beam before its respective focal point did not undergo much change in its apparent size.

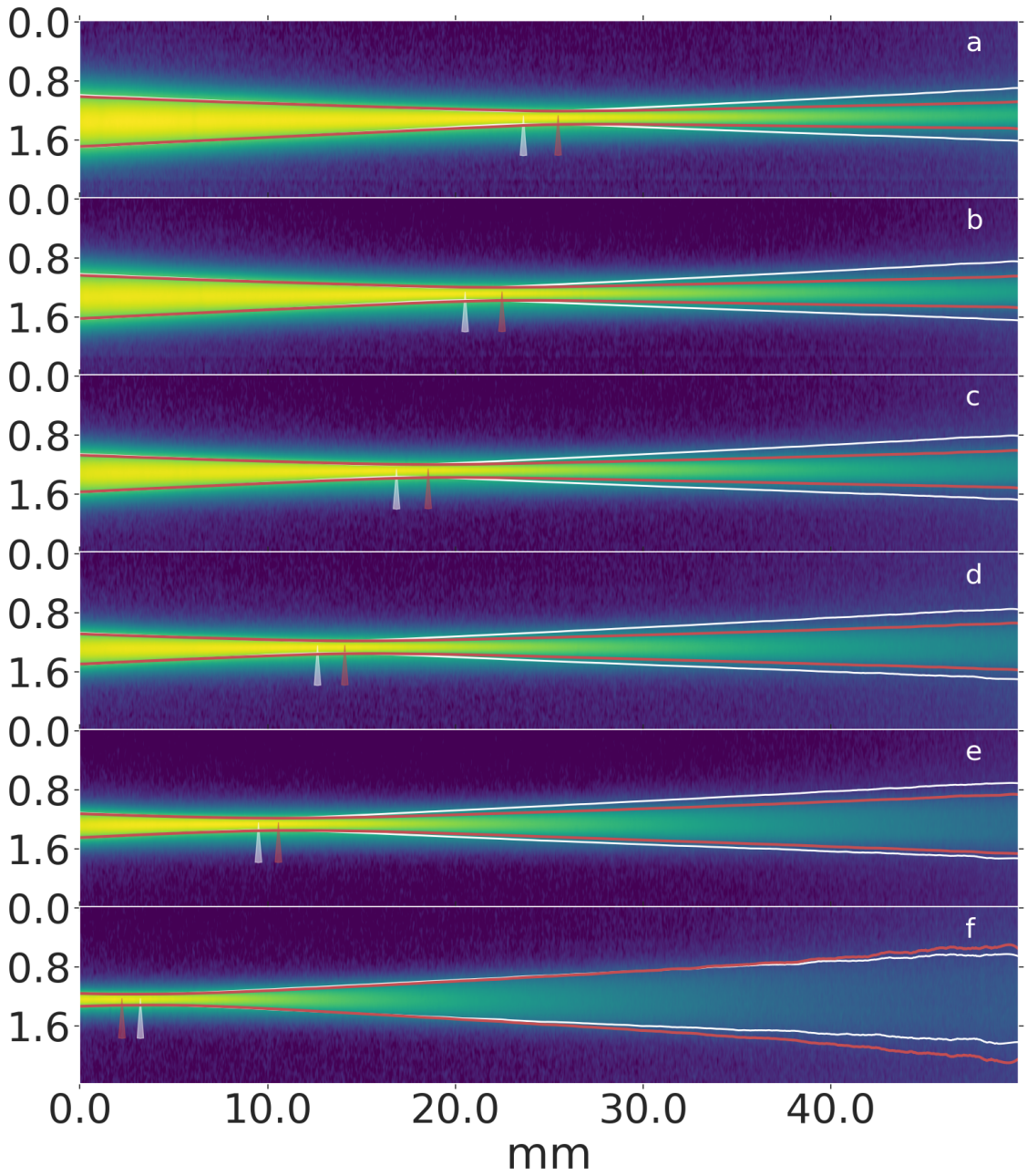

Fig. 4.20 Transient lensing behaviour with varying focal positions inside the cuvette. The initial (white) and steady-state (red) beam size ($w(z)$) were determined from Gaussian fitting in the radial direction. The arrows indicate the focal initial (white) and steady-state (red) focal positions. The beam was less diverging **(a-e)** for focal position >1 *cm*, and vice-versa **(f)**. The obtained $w(z)$ values from fitting have been smoothed using a Savitzky–Golay filter.

The simulated results of refractive change due to temperature (Fig 4.8) suggested that the greatest change of refractive index occurred near the focal region, which

correspondingly had the biggest lensing power. This was in agreement with measured results (Figure 4.20a-e), as most of the beam size deviation occurred at and after the focal point. This also manifested as a forward shift in the steady state focal point. This shift caused an increase in the beam's size at the focus, which consequently diverged at a smaller angle relative to its initial state.

The greater the portion of the beam before the focal point inside the cuvette, the less the beam was divergent at steady state, and the further the focal shiftwas in the forwards direction. Furthermore, the distance change of focal position increased with increasing of focal position inside cuvette (Figure 4.20a-e). This suggested that the first portion of the beam (before the focal point) increased the size of the focal spot, which in turn caused the beam to diverge less after the focal point. This also accounted for the greater beam divergence when the focal position was a few millimetres inside the cuvette. In this case, the focal shift was behind its initial position, which caused an apparent deduction of the focal spot and thus greater beam divergence thereafter.

4.4.1.2 Effects of laser power

Varying the focal position inside the cuvette did indeed affect the lensing behaviour, as both a converging and diverging beam were observed. The biggest changes in the beam's size and divergence were recorded when the focal point was near the mid-point of the cuvette (Figure 4.20a). For this reason, the focal position was kept at this point, and the laser power varied between 11.9 mW and 98.4 mW to discern if lensing effects were present across the power range (Figure 4.21).

Lensing effects were observed from the lowest power of 11.9 mW, right across the range until 98.4 mW. The beam became less diverging with increasing laser power, relative to the initial beam. In Figure 4.21, a change in the beam size occurred across the entire propagating length. The largest change occurred post-focal point with an increase of the beam waist at the focus which happened for all powers. To draw direct comparisons of the lensing behaviour, all steady state beam sizes were plotted in one graph for all powers relative to the initial beam size (Figure 4.22).

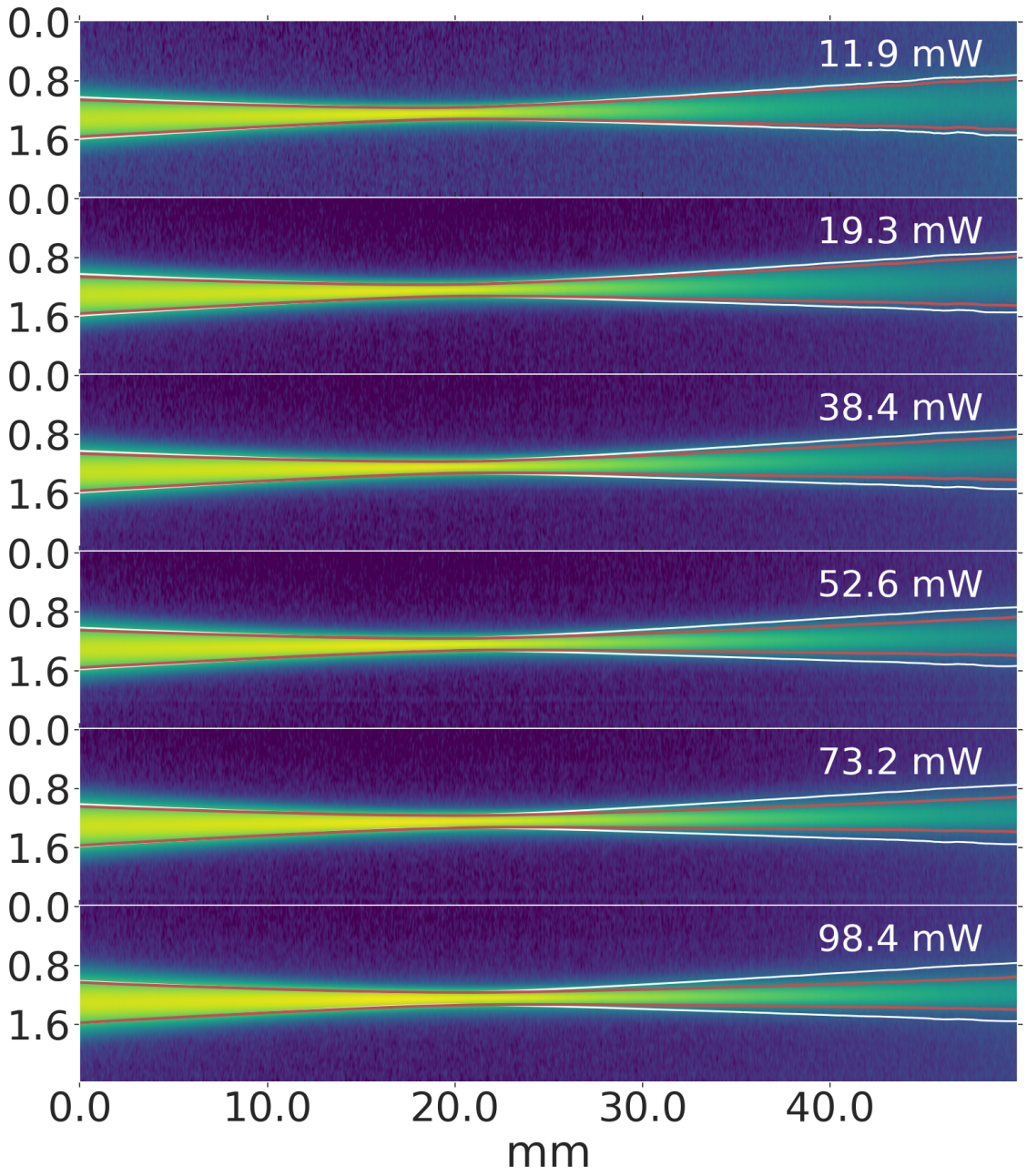

Fig. 4.21 Lensing effects at different beam powers for a fixed focal position. For all powers, the steady-state (red line) beam divergence was reduced compared to its initial state (white line). The divergence past the focal focal decreased with increasing laser power. y-axis scale is also in *mm*.

There was little deviation of the initial beam size. The dashed-line in Figure 4.22 was a mean of all the initial beam size for all the powers. As the light was focused down, the initial beam had the largest size and the steepest angle of approach, followed by

the 98.3 mW beam. The lowest power beam had the smallest size and the shallowest approach angle. There was a gradual increase in angle of approach to the focal point with increasing laser power, tending towards the initial angle of the beam. At the focus, the steady state beam size was slightly larger and the focal point had shifted forward, for all powers. After the focus, the beam divergence reduced with increasing laser power. However, the beam could be described as a soliton (self collimating beam as attributed to by Fardad *et al.* [26]) since the beam was still undergoing diffraction, even at the highest investigated power of 98.4 mW.

As a simple approximation, it can be assumed that a reduction of the beam angle before the focus, would lead to a larger focal spot, which consequently would result in a less diverging beam past the focal point. However, this cannot be attributed to the data of Figure 4.22. Instead, the divergence of the beam before the focal point increased with power, rather than decreased. Hence, the reduction of the beam divergence after the focal point occurred due to the lensing around the focal point (which could not be clearly resolved due to the optical set-up used in this work).

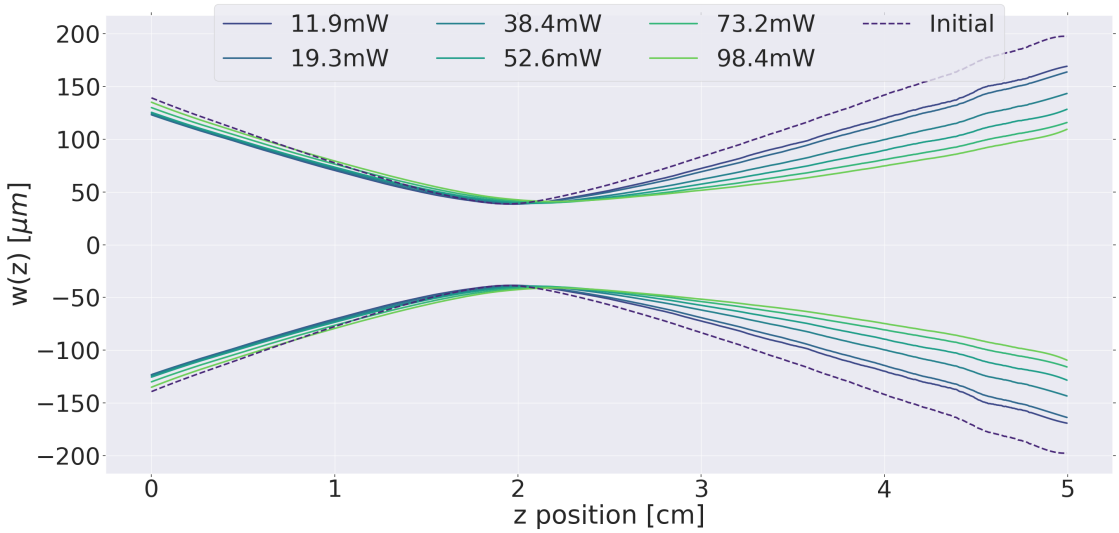

Fig. 4.22 Comparison of the initial and steady state beam shape for all powers. The dashed-line is the averaged initial shape across all powers.

4.4.1.3 Effects of Changing The Nanoparticle Medium

Changing the medium of the nanoparticles into an alcohol based solution resulted in a 1.4 times peak temperature rise of the central radial temperature (Figure 4.9), which acted to amplify the expected lensing effects. This was tested by diluting the stock OD 1 per cm 40 nm particles suspended in water, with isopropyl solution using a volume ratio of one to two, respectively. The lensing effects were quantified by Gaussian fitting the radial profiles for all frames of video sets corresponding to laser powers between 13.9 mW and 101 mW (Figure 4.23).

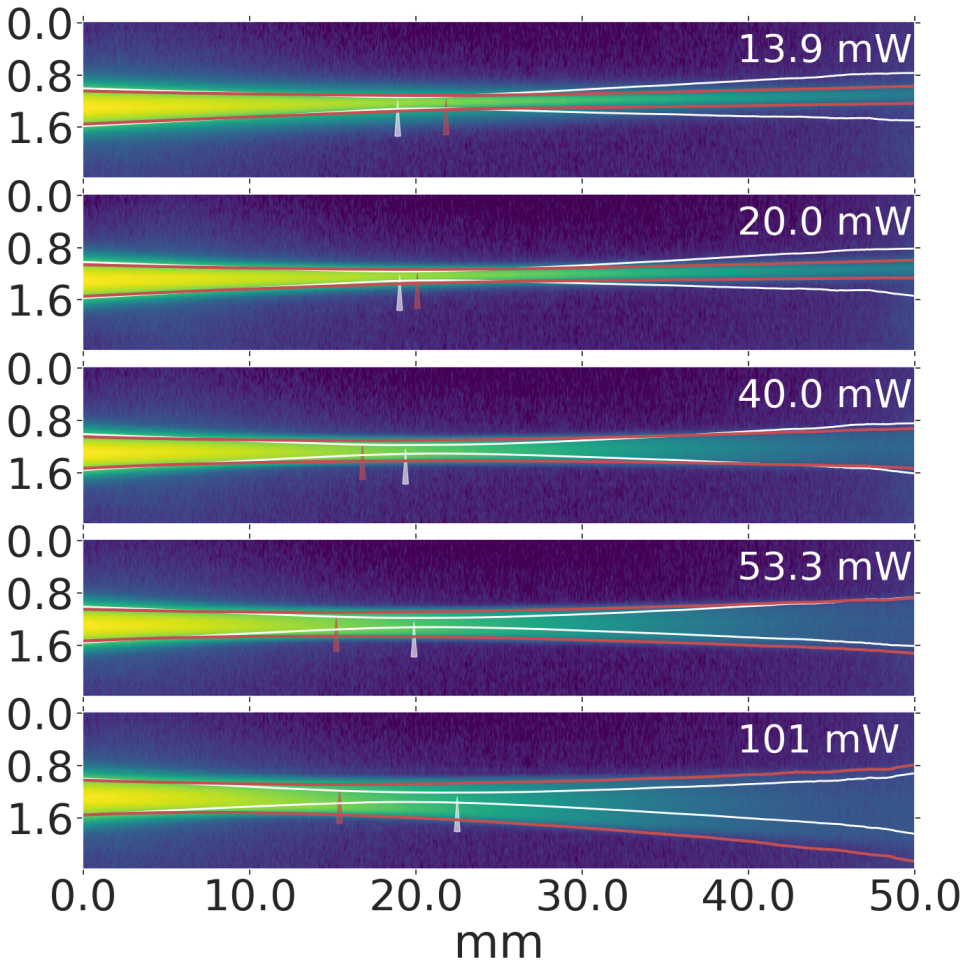

Fig. 4.23 Lensing effects of a water-isopropyl mixture (1:2 volume ratio). An inversion of the lensing behaviour transitioning from converging to diverging for powers higher than 20 mW. The initial and steady state beam shape are shown in red and white curves, respectively. For steady state beams with lower divergence (13.9 to 20 mW), the focal spot had shifted forward, and vice versa for higher diverging beams (40 to 101 mW).

At the lowest power of 13.9 mW, the beam size was significantly reduced after the focal point. For this power, the focal point had also shifted forward by almost 0.5 cm. Increasing the power slightly to 20 mW also resulted in a less diverging beam after the focal point, with a small forward shift of the focal point compared to the 13.9 mW case. At 40 mW, the beam size at the focal point was much larger, but remained approximately the same before and after the focus. The focal point had now shifted backward, opposite to the direction of the 13.9 mW and 20 mW beam. With increasing powers, the focal point was further back-shifted (up to 1 cm for 101 mW), and the beam size became larger and more diverging.

The initial beam shape for all the powers were approximately the same with a deviation of a few pixel across the entire propagation length. A mean of the initial beam shape, across the laser powers, was used to compared the evolution of the beam (Figure 4.24).

The initial beam state was symmetric about the focal point. Due the gradient in the index of refraction, the shape of the steady state beam was asymmetric around the focal point. In all cases, the beam sizes were larger at the focus point relative to the initial size. For powers below 21 mW, the beam was significantly less diverging after the focal point, staying approximately the same size after the focal point. For higher

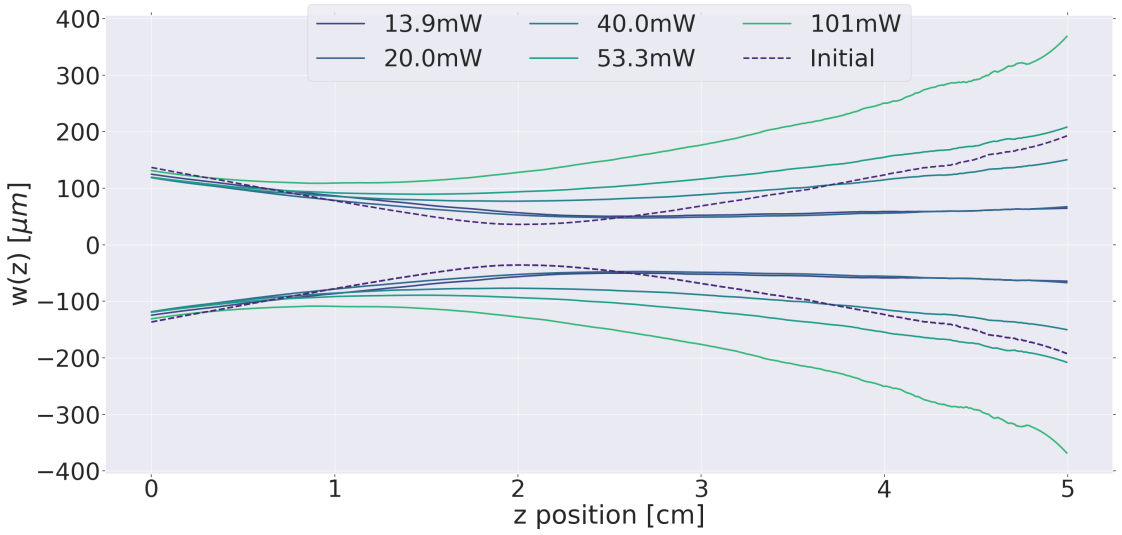

Fig. 4.24 Measured beam sizes at different powers propagating in water-isopropyl mixture (1:2 volume ratio from stock of 40 nm Au nanoparticles). Both self-focusing and de-focusing effects were observed whilst keeping the focal position fixed.

powers, the beam size was much larger after the focal position relative to the initial beam. An inversion in the lensing behaviour occurred, from converging after the focal point for powers below 21 mW, to diverging with higher powers.

4.4.1.4 Beam Divergence

The beam divergence was quantified to determine its relation with varying laser power, for both nanoparticle media. Due to the asymmetry about the focal spot for the steady state beam caused by the gradient index thermal lensing, the divergence was only quantified from the focal spot until the end of the cuvette. The initial beam shape was approximately the same for all powers and was therefore referenced to the beam-shape at 0 mW. The beam divergence (Θ) was calculated from the ratio of the Rayleigh length (Z_R) and the focal spot size (w_0) for each beam power and nanoparticle media

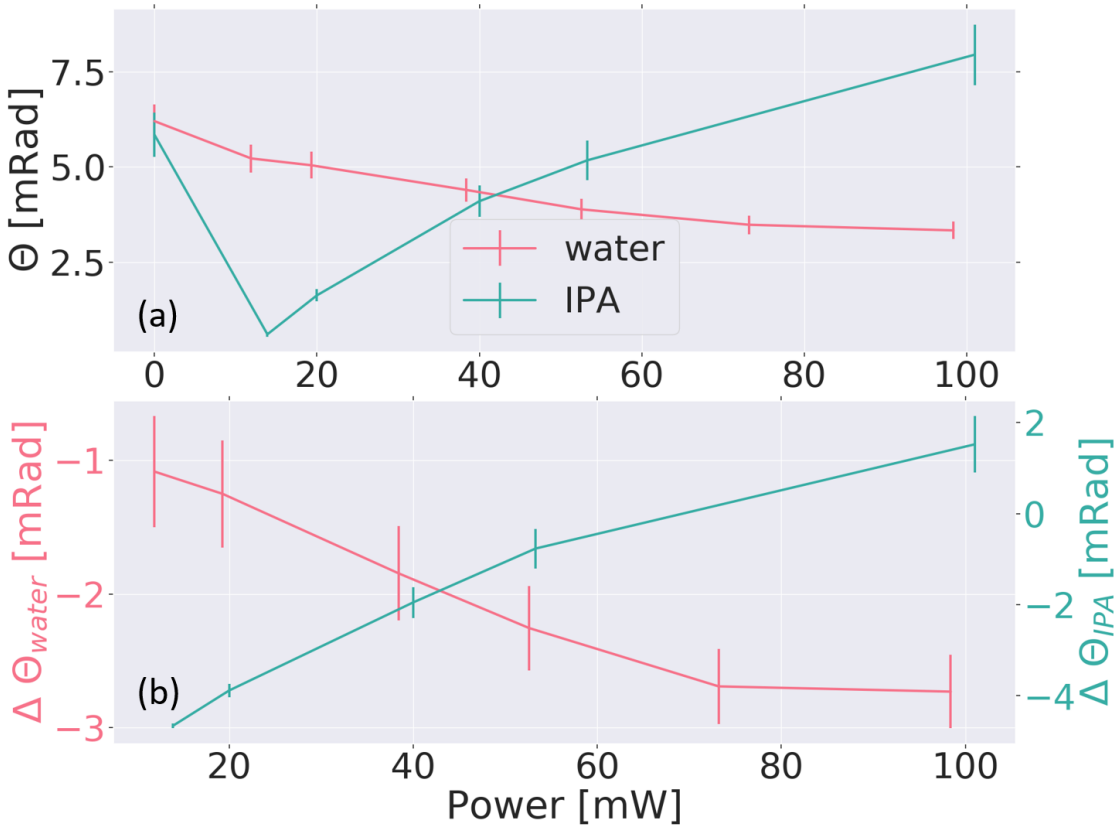

Fig. 4.25 **(a)**: The measured beam divergence obtained from least square fitting to Equation 2.2). **(b)**: The change in beam divergence relative to its initial state. For water, the divergence decreased with laser power. However for isopropyl-water mixture, the beam divergence increased or decreased depending on the laser power.

(Figure 4.25a). Least squares fitting (to Equation 2.2) was used to determine z_R and w_0 from the beam's size as it propagated in the z-direction.

The initial beam divergence for both nanoparticle media were approximately the same and within the obtained fitting error from one another. For water, the beam divergence continually reduced with increasing power, and appeared to plateau at a value of 3 $mRad$, approximately half of its starting value. The relative change of the divergence from its initial state, linearly reduced between 10 mW - 73 mW, after which the change plateaued (Figure 4.25b).

The beam divergence for isopropyl-water mixture was much lower for 10 mW - 20 mW than water media using powers of 100 mW (Figure 4.25a). Lower power reduced the beam divergence more than higher powers, which at a power of 50 mW, increased the divergence. Hence, using a isopropyl-water mixture medium for the nanoparticles facilitated tunable focusing and defocusing behaviour by varying the laser power.

4.4.2 Non-linear refraction from z-scan

Imaging the beam from the side to observe its thermal lensing behaviour yielded unexpected and interesting results. The refractive index change was negative with increasing temperature, which acted to increase the beam divergence. Hence, lensing effects in a 5 cm cuvette could be considered as an array of negative lenses. Despite this, a reduction of the beam divergence was observed with both nanoparticle media. This suggested that a set of negative lenses with various lensing power produce a less diverging beam. As a means of quantifying the individual lensing effects for small segments of beam, a thin cuvette with an optical path length of 300 μm was translated along the z-direction and along the beam propagation. The thin cuvette was scanned $\pm$ 7.5 mm around the focal point to quantify non-linear refraction (scanning range of a tenth of the focal length was sufficient).

The use of a camera to measure the lensing effects was spatio-temporally limited because of the frame rate (ms sampling) and the optical set-up (large field of view). Theoretically, the characteristic heat dissipation time constants were in the order of a few milliseconds (Table 4.1), which was the comparable to the sampling interval of the camera. This was ameliorated with the use of fast photodiodes, with data being acquired at a sampling rate of 40 ns (Figure 4.14). All datasets were acquired for a

duration of 10 ms, which was sufficiently long for the lensing effects to have reached a steady-state.

The linear absorption attenuation (a_z) needed to determine the effective cuvette length (L_{eff}) and the value for Δn was obtained from the OD of the sample. An interpolation function was used to determine OD at 532.8 nm from the measured spectra of Figure 4.18. The power, concentration, and media of the nanoparticles were varied to discern if any non-linearities were present for each parameter of interest.

Initially, both open and closed aperture z-scans were performed with water or isopropyl alcohol-water mixtures only, to evaluate the presence of nonlinear refraction and absorption from the media itself. For the tested power range of 15 - 75 mW, both open and closed transmission stayed constant across the entire z-scanned region. Furthermore, open aperture scans were performed with nanoparticle in both media at the highest power (75 mW), and no nonlinear absorption was observed. This was consistent with the observations made by Ortega *et al.* [32, 28]. Hence, only closed aperture z-scans were performed to quantify the nonlinear refraction of the nanoparticles.

4.4.2.1 Effects of laser power

The stock nanoparticle solution (OD 1 per cm) was used to determine the magnitude and sign of non-linear refraction between 15 - 75 mW, in steps of 10 mW. The cuvette was scanned in finer incremental steps around the focal point ($\pm$ 2.5 mm or $\pm$ 5 Z/Z_r) to map the inflection points at the peak and trough of the transmission curve. The cuvette was scanned $\pm$ 15 Z/Z_r, but only $\pm$ 10 Z/Z_r was shown for clarity (Figure 4.26). The transmission errors originated from the standard deviation of the time binning.

The transmission curve discernibly deviated from a value of 1 near the $\pm$ 7.5 Z/Z_r, and followed increases and decreases before and after the focal point, respectively, resulting in a negative value of n_2 [86]. Thiswas consistent with the previously reported n_2 values for Au-nanoparticles of different sizes and concentrations (Table 1.1). Accordingly, the refractive index change was negative and the thin cuvette functioned as a concave lens. A higher laser power induced a greater peak-to-valley transmission difference, corresponding to an increased negative lensing power from the nanosuspen-

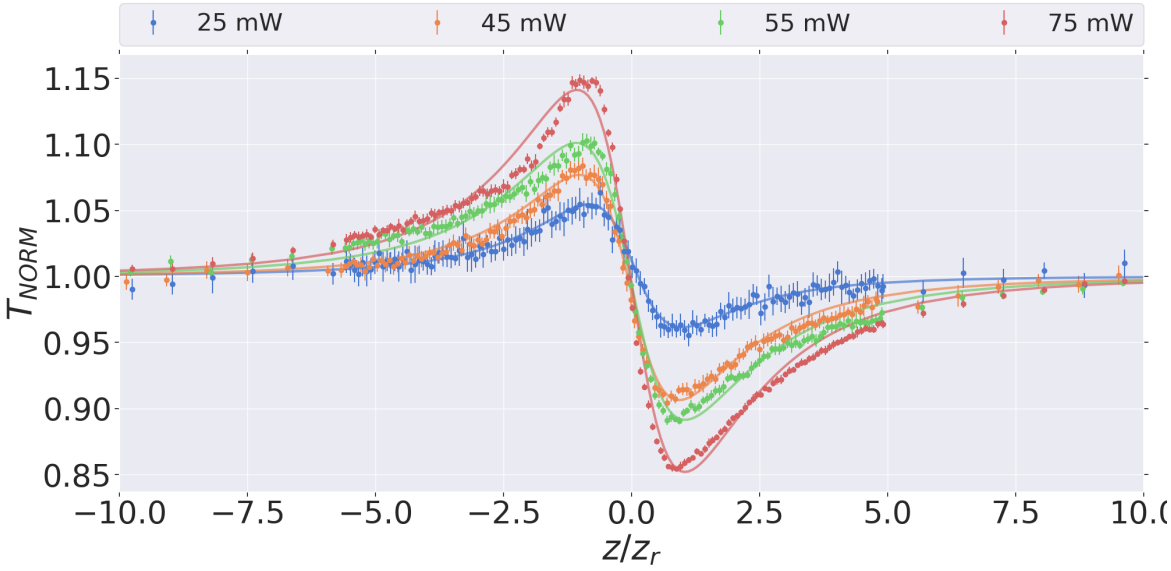

Fig. 4.26 Steady state z-scan transmission curves at various powers for OD 1 nanoparticle solution. The measured curves were fitted to Equation 1.12 to obtain the on-axis phase shift. The shape of the measured transmission curves were for a negative n_2 value, meaning that the refractive index change was also negative.

sion (Figure 4.26). The crest-trough transmission symmetry and separation distance did not change with laser power (therefore $\Delta\Phi \leq \pi$, criteria for Sheik-Bahae formalism met [86]). The associated phase change of the nonlinear refraction for each laser power was quantified through least-squares fitting of Equation 1.12 (solid curves in Figure 4.26).

The phase change ($\Delta\Phi$, Figure 4.27 inset) approximately linearly increased with laser power. At 75 mW, the phase changes was the highest, but was still below π, and therefore conformed with Sheik-Bahae *et al.*'s approach. However, the fitting deviated from the data at this power, especially near the peak transmission value (Figure 4.26). From the acquired phase change values, the intensity dependent refractive index (n_2) values were determined (Figure 4.27). The value of n_2 sharply increased between 15 mW and 25 mW, and then continued to increase but a reduced amount with increasing power. Compared to the theoretical value of n_2 at a power of 75 mW (1.38×10^{-12} m^2/W from Section 4.2.2.3), the measured value was 2.3 times lower. The difference arose from the approximations made by Sheik-Bahae *et al.* in omitting the full radial lensing contribution. The theoretical heat dissipation in the radial direction was greater

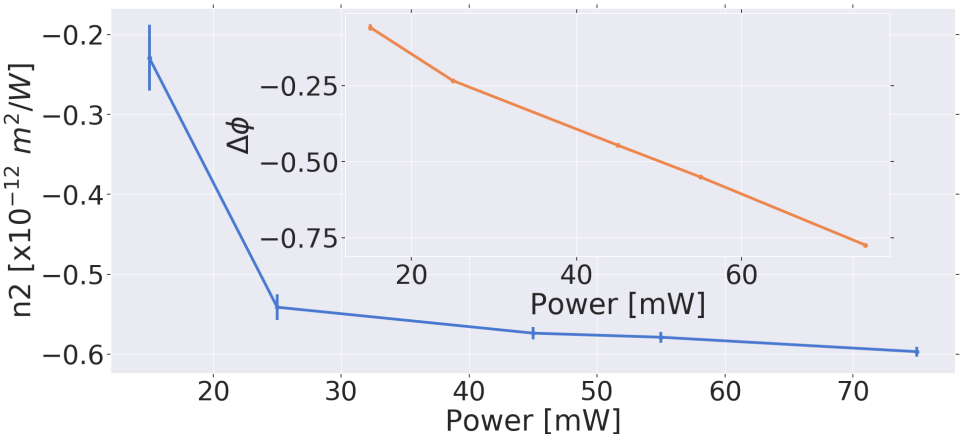

Fig. 4.27 Calculated n_2 and $\Delta\Phi$ values from closed aperture transmission curves of Figure 4.26. The phase change (in units of π) increase linearly with power (inset). n_2 values were same order of magnitude as reported values in literature for different sized nanoparticles (Table 1.1).

than the beam size, contributing to the greater lensing effects. The z-scan method of determining the non-linear refraction was a good indication of the lensing effects.

4.4.2.2 Effects of nanoparticle concentration

The same measurement set and data analysis as described in the previous section was performed, but the Au-nanoparticle concentration was varied to discern its non-linear

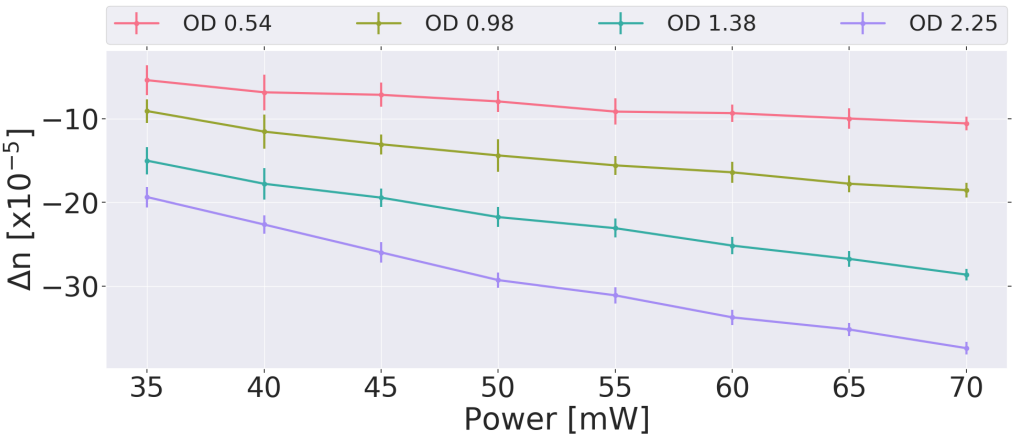

Fig. 4.28 The steady state refractive index change of various nanoparticle suspensions. Higher induced negative refractive index changes occurred with increased nanoparticle concentration and laser input power. Regardless of concentration, the input laser power scaled linearly with the observed refractive index change.

refraction dependence. Nanosuspension concentrations were changed from stock and characterised using optical spectroscopy (Section 4.3.5). For the lowest concentration (OD 0.54 per cm), a minimum power of 35 mW was needed to obtain statistically reliable (fitting error less than 3 times of mean value) quantification of $\Delta\Phi$ and its subsequent Δn value (Figure 4.28).

There was a linear increase in Δn values across all concentrations for the 35 - 70 mW tested power range. However, the slope of the refractive index change as a function of power was different for each concentration, becoming steeper for more concentrated nanosuspensions. In essence, a higher dynamic range of Δn values were facilitated by an increase in the nanoparticle concentration. The Δn values were normalised relative to their filling fraction (f_v) to quantify variability of the refractive index change, independent of nanoparticle concentration (Figure 4.29).

The slope of the refractive index change per unit filling fraction was approximately the same for all powers. This was a consequence of the constant heat transfer between each nanoparticle and the water media, and the fact that there were no non-linear absorption effects for the test power range. Hence a 'master-curve' was defined as the mean concentration independent refractive index change for each power (blue solid line in Figure 4.29). By linear regression fitting to this master-curve, the constant

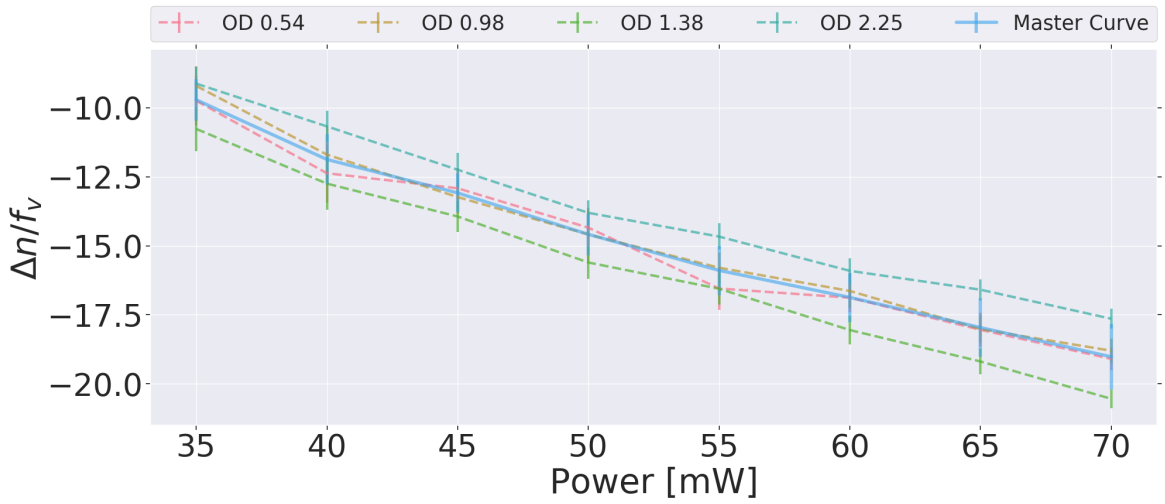

Fig. 4.29 Δn values of Figure 4.28, normalised by their respective filling fractions (fv). This yielded a concentration independent linear dependence of the refractive index change as a function of incident laser power.

of proportionality ($k_{\Delta n-P}$) between the concentration independent refractive index change and power was determined to be -0.28 mW^{-1}. Therefore, the value of refractive index change, for a given power, could be determined using Equation 4.8.

$$\Delta n = k_{\Delta n-P} * P * f_v \tag{4.8}$$

Equation 4.8 held for the test power range and was a good approximation for the expected refractive index changes. However, for higher laser powers, non-linear absorption may have dominated and affected the trend.

4.4.2.3 Effects of Isopropyl alcohol-water mixture as a medium

When the nanoparticles were suspended in an mixture of isopropyl alcohol and water, the observed lensing effects were much higher in the 5 cm cuvette. Interestingly, laser powers below 20 mW caused the beam to diverge less, whilst higher powers induced the beam to diverge more than its initial state (Figure 4.30). A one-to-one volume

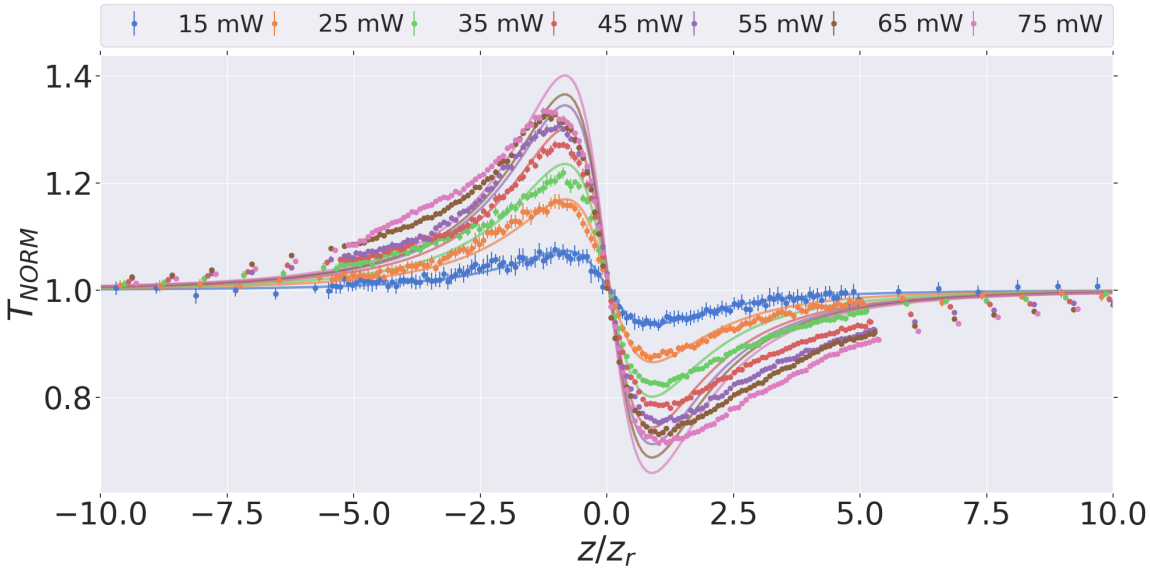

Fig. 4.30 Nonlinear refraction measurements for a 1:1 dilution ratio of isopropyl alcohol and water (containing the stock nanoparticle concentration). The normalised transmission through the aperture increased rapidly for low powers and then continued to increase but to a much lower extent. The fitted Sheik-Bahae formalism (Equation 1.12) fitted well for the powers up to 35 mW, after which, the fitted peak-to-trough values deviated significantly from the measured values, indicating that the Sheik-Bahae model was no longer representative.

ratio of stock nanoparticle solution was diluted with isopropyl alcohol (Section 2.3.5) to quantify its nonlinear refraction for the same power range as tested for water medium (Figure 4.30).

The normalised transmission curves increased before the focal point and decreased after for all powers. Hence, the lensing effects are always negative. The amplitude of the transmission increased with power, but not linearly. The successive peak-to-valley transmission differences decreased between consecutive powers (Figure 4.30). Increasing laser power beyond the tested range was unlikely to yield a greater maximum- or minimum-transmission extent. Furthermore, an asymmetry existed between crest-trough values across all powers.

For laser powers up 35 mW, transmission curve fits conformed to Sheik-Bahae formalism. For higher powers, the fitting over-estimated the peak-trough values. Additionally, the ascension and descension of the theoretical curves returned to a value of one at faster rate than the measured curves (Figure 4.30). This was further evident in the positions where the extrema values occurred. In essence, the measured curves appeared to be 'stretched out' in comparison to the fitted curves. This was because the

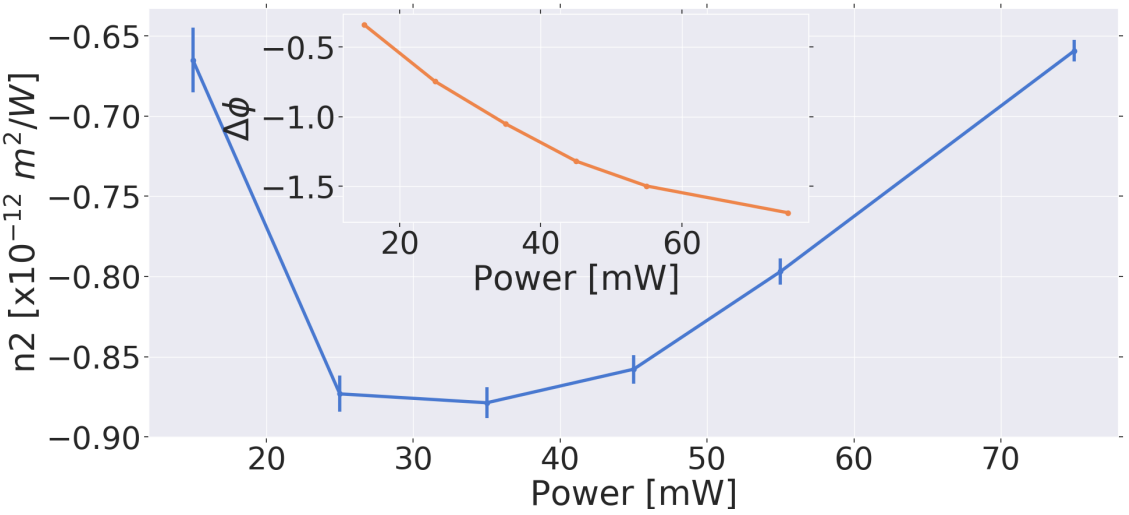

Fig. 4.31 The obtained $\Delta\Phi$ values from fitting to the measured Z scan transmission curves of Figure 4.30. $\Delta\Phi$ was no longer linearly increasing with power (which was the case for aqueous nanosuspensions). For powers above 30 mW, $\Delta\Phi \geq \pi$, hence Sheik-Bahae formalism was no longer upheld. Due to the poor fitting of the transmission curves, the n_2 values, as a function of power, increased and then decreased around a power of 35 mW.

Rayleigh length increased due to the lensing effects of the thin cuvette. Consequently, the beam radius increased, which was in direction violation of the first Sheik-Bahae criteria.

The phase change obtained from fitting increase with laser power is shown in Figure 4.31 inset. Above 35 mW, $\Delta\Phi > \pi$, which was outside the approximation range supported by Sheik-Bahae's formalism. This was another reason why the theoretical fits did not satisfy the measured transmission values above 35 mW.

The corresponding n_2 values obtained from the phase change increased and reached a maximum at a power of 35 mW, after which they decreased in value (Figure 4.31 inset). Despite the poor fitting for transmission curves above 35 mW, this trend would also be present with good fits since the difference in extrema transmission values reduces with laser power.

Non-linear absorption may be present in the measured transmission curves of Figure 4.30, indicated by the existence of asymmetry between crest-and-trough values. These non-linearities were not observed in open aperture scans as they were not within detection range of the system used herein.

4.4.2.4 Transients of nonlinear refraction

Up until now, only the steady-state refractive index change has been quantified. The time scales associated with evolution of the non-linearities, were an indicator of the driving mechanism for the lensing effects. Herein, the hypothesis was that the lensing effects were driven by the thermo-optic properties of the media and its associated heat absorption and diffusion, which occurred at *ca.* 0.2 ms and 4 ms nominally in both media (Table 4.1).

The transient evolution of the lensing effects were studied for water (stock diluted by a half), and isopropyl alcohol-water mixtures (1:1 ratio) at various powers using the z-scan technique. For all time points in the 10 ms window, the refractive index change was negative (Figure 4.32a,b).

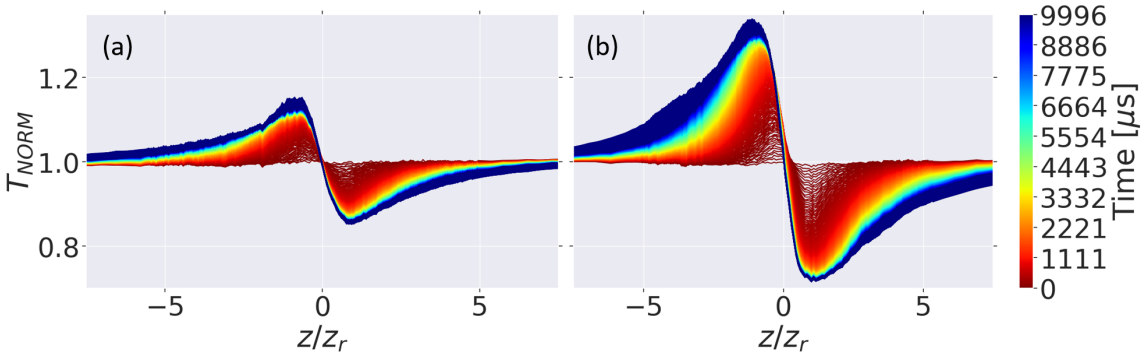

Fig. 4.32 For both water (a), and isopropyl alcohol-water mixtures (b) nanoparticle suspension, with an incident power of 75 mW the transmission through the aperture smoothly increased as a function of time. The dominating colour in both graph was red indicating the ensemble evolution of the lensing system was within 3 ms.

Upon a visual inspection of the Figures 4.32a,b, red was the most prominent colour, which indicated the the majorities of the refractive index change occurred within the first 3 ms. At each time point for both media, the measured transmission through the aperture was fitted to Equation 1.12 to obtain n_2 and its corresponding Δn value. Figure 4.33 shows how Δn changed with time for Au-nanoparticles suspended in water. It was evident from this Figure that the refractive index change plateaued at 10 ms.

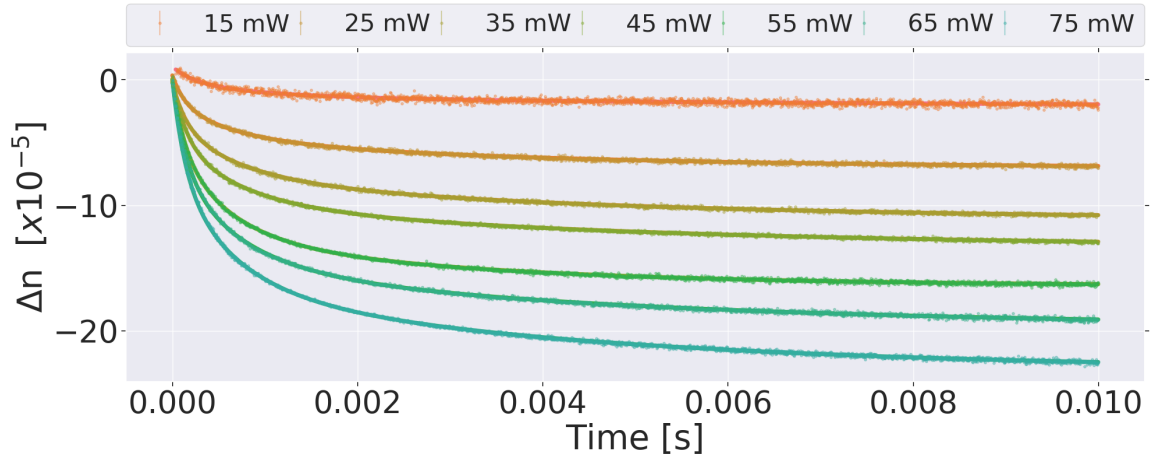

Fig. 4.33 Time dependence of Δn for nanoparticles in aqueous suspension, for various powers, fitted to a double exponential. Whilst the value of Δn increased for each power, the time constant was the same. For the test power range, the lensing behaviour had approximately reached steady state at 10 ms. The fitted time constants are reported in Table 4.2.

Media	τ_1 $[\mu s^{-1}]$	τ_2 $[\mu s^{-1}]$
Water	134 ± 14	4016 ± 525
Isopropyl alcohol-water (1:1)	158 ± 19	3483 ± 388

Table 4.2 Time constant obtained from double exponential fitting to the Δn curves of Figure 4.33.

The time constants associated with the temporal evolution of the refractive index change were extracted by fitting each curve of Figure 4.33 to a double exponential. The same process was conducted for isopropyl alcohol-water mixtures nanoparticles suspensions (fitting results reported in Table 4.2).

From the fact that the measured Δn time constants were in good agreement with the simulated temperature rise of the nanosuspension in a 300 μm optical path length cuvette, it was evident that the lensing behaviour was driven by thermo-optic effects. The nanoparticle was absorbing the light, and dissipating it as heat into the environment, which in turn reduced the medium's refractive index due to its negative thermo-optic coefficient. Moreover, the time constants were much less than a second indicating that the lensing effects could not be driven by thermophoretic migration of nanoparticles [65].

4.5 Summary

A focused beam into a solution of Au-nanoparticles (of sizes 5 - 50 nm) has been reported to induced self-focusing and de-focusing effects, with the proposed driving mechanism being associated to optical forces [26, 82] or thermal effects [28, 27]. The present work investigates the underlying mechanism of the self induced lensing by replicating and expanding the experimental findings of Fardad *et al.* and Kelly *et al.*. This chapter reports that self-focusing and -defocusing are due to the thermo-optic effect of the nanoparticle's medium.

The simulated optical forces using the experimental geometry of Fardad *et al.* (w_0 = 12.7 μm, P = 150 mW, λ = 532 nm) on 40 nm Au-nanoparticles are not strong enough to constitute redistribution of nanoparticle concentration to induced positive lensing (Figure 4.4). The beam size at the focus is large and therefore the gradient

in intensity is not strong enough to mediate nanoparticles confinement by the radial gradient force.

Nanoparticles below 60 nm in diameter have a higher absorption cross section than scattering, in the visible wavelength range [27]. Hence, the generation and dissipation by individual nanoparticles and nanoparticle solutions were simulated. A single 40 nm Au-nanoparticle placed at the focal point of a beam ($w_0 = 12.7\ \mu m$) generates a temperature rise $0.55°C$ per mW of laser power, which decays to ambient 200 nm away from the nanoparticle's surface (Figure 4.6). Hence, each individual nanoparticle acts as a nano-heater, absorbing the laser light and dissipating it as heat into the environment. The refractive index of water decreases with increasing temperature, and thus creates a negative lensing. For a beam focusing into a 5 cm cuvette, the axial and radial heating profiles creates a negative gradient index, with the lensing power being the strongest near the focus (Figure 4.8).

Self-induced lensing of a focused beam in a 5 cm cuvette is studied as a function of laser power, focal position along the cuvette, and with different mediums. The presence of lensing is confirmed by referencing the evolution of the beam shape with respect to the initial beam shape at *t=0* (first video frame). For self focusing behaviour, the focal position has to be placed in the cuvette, such that the radius of curvature before the focal point is compensated by the negative lensing of the medium, moving the focal point forward from its initial position, and generating a less diverging beam (Figure 4.20). When the focal point is positioned at the beginning of the cuvette, only a self-defocusing beam is observed. These findings are in agreement with the works of Ortega *et al.* [28], and agree well with the lensing profiles derived from heat diffusion simulations.

Both self-focusing and de-focusing are observed when the focal position is kept constant and the laser power varied, for both aqueous nanoparticle suspensions and isopropyl alcohol-water mixtures (Figures 4.21 - 4.24). Lensing effects are much stronger in isopropyl alcohol-water mixtures due its lower thermal diffusivity, with a significantly less diverging beam observed with just 14 mW and with a reverse (increasing) in the beam diverging occurring at 40 mW. The mechanism that causes beam divergence to occur with increase power is not clear at this current stage.

The transient heat diffusion for Au-nanosuspension in 300 μm placed at the focal point of a focused beam is simulated to determine the time scales for heat generation by the nanoparticle absorption, and dissipation into the environment. For a beam power of 75 mW a temperature increase of 9 $°C$ from ambient is generated by the presence of the nanoparticles, which correspond to a refractive index change of -1.03$\times 10^{-3}$ (Figure 4.11). For the same power, the measured refractive index change obtained for z-scan measurements is -(2.2$\pm$0.2)$\times 10^{-4}$. The measured value is lower as the heating profile in the radial direction is much larger than the beam envelope ($w(z)$, Figure 4.12). Due to this difference, the accumulated focusing power is greater than watch is accounted for by Sheik-Bahae formalism. As the measured values of n_2 (in this work) are the same order of magnitude and sign, as those reported in literature for Au-nanoparticles (Table 1.1). This suggests that the z-scan method is not a good approach for determining the absolute refractive index change mediated by thermal effects, but rather an indication of the refractive index change. An adjustment factor is required to upscale the measured refractive index change such that it takes into account the greater lensing induced by the heat dissipation profile of the medium.

Even though the z-scan method underestimates the absolute magnitude of the refractive index change for thermally induced nonlinear refraction, it is still sensitive to the temporal evolution of the self induced lensing. The time constants obtained from transient z-scan measurements for aqueous suspended nanoparticles correlate well with the simulated heat generation and dissipation by the nanoparticles (Table 4.2 compared to Table 4.1). This is further proof that the self induced lensing effect is mediated by opto-thermal effects, as proposed by Liberman *et al.* and Ortega *et al.* [28, 27]. Furthermore, the lensing effect reaching steady state within 10 ms rule out thermophoretic effects as the main lensing mechanism.

Chapter 5

Discussion and future work

From viruses drifting in the ocean to DNA molecules translocating in the cell nucleus, nanoparticles and biomolecules in fluidic environments are omnipresent in nature. As a means of studying them, researchers have used optical intensity- or thermal-gradients to manipulate and perturb their motion. Nanoparticles with known properties (such as size and charge) are often used to characterise how the presence of intensity- or thermal-gradients can be used to manipulate them. However, light and heat are inextricably intertwined and special considerations are needed in order to disentangle how each effect interacts with the nanoparticle and how its motion is affected within a fluidic environment.

In this work, two novel geometries for nanoparticle confinement are demonstrated using intensity- or thermal-gradients. These geometries are intended to manipulate misfolded proteins in future work. In addition, the thermo-optic mechanism for self-induced lensing of a focused beam into a nanoparticle solution is confirmed in a novel way by considering the transient evolution of the non-linear refraction obtained from Z-scan measurements.

In the first part of the present study, Au-nanoparticles are strongly confined in the axial direction and weakly trapped in the radial direction, by creating strong intensity gradients mediated by the interference of two counter-propagating beams. The heating effects are diminished by judiciously choosing a trapping wavelength that maximise nanoparticle scattering and consequently yield stronger optical gradient forces. A micro-mirror is created to back-reflect the incident light and cause self interference. This method of creating interference fringes does not suffer from phase drifting and

yields much stronger confinement factors in the axial direction, compared to two opposing fibres individually emitting light at twice the power (Table 2.2 compared to Table 2.3). For the two opposing fibres geometry, misalignment between the fibre cores reduces the extent to which the scattering force is cancelled by the counterpropagating beam and therefore reduces the trapping potentials. The mirror-fibre geometry is far less sensitive to misalignment (mirror diameter is much bigger than incident beam size), hence the depth of the potential wells is unaltered. Moreover, only one optical fibre with laser light coupled into it is required and thus complexity of the optical system is reduced.

Future plans to advance in this research direction include several avenues of investigating further the optical trapping results described. In the first instance, new data could be taken with finer power intervals for both the opposing fibre and mirror-fibre geometries to discern how the confinement factor γ scales with total incident power. This would also determine if there is an associated time interval for which nanoparticles remain confined. This is reminescent of the 150 mW case for the two opposing fibre geometry (Figure 2.36c), where nanoparticles are trapped for $\sim$0.7 s, followed by an increase of the MSD_x. As such, Kramers' theory for diffusion on a periodic potential [146, 147] could be used to bridge the simulated and experimentally measured results.

The nanoparticle trapping size limitation using the mirror-fibre interferometric geometry could be further investigated. For particles which cannot be trapped due to their size, the mirror-fibre separation distance should be reduced to increase the effective trapping potentials. The ability to trap nanoparticles with lower polarisability such as polystyrene, can also be explored. The heterogeneity of the effective trapping potentials in the axial direction could be used for nanoparticle chromatography. Nanoparticles with larger sizes have correspondingly larger scattering cross-sections, and therefore have a higher propensity of being trapped near the mirrored surface, where the scattering forces are weaker.

A second mirror and fibre can be placed orthogonally to the first mirror-fibre, creating a two-dimensional lattice of optical potentials wells. In this geometry, two-dimensional confinement of proteins such as BSA or α-synuclein can be investigated. If proteins can indeed be confined then the array of the trapping sites can be considered analogous to a well plate, but on the nanoscale (creating a 'photonic well-plate'). The

two-dimensional spatial confinement should increase the rate of aggregation mediated by increased collision rates between individual protein fragments. Surface coatings of the mirrored surfaces and the facet of the light emitting PM-fibres can be considered to inhibit biofouling, and thus increase the lifetime of the fibre-mirror microfluidic device.

The two-dimensional spatial confinement of shell isolated Au-nanoparticles (commonly used for SERS [148]) could be studied to establish if trapping of such nanoparticles in the presence of Rhodamine-6G yield higher Raman signal, collected by backscattered light into the PM-fibres.

In the second part of this work, the smallest reported nanoparticle size (26 nm polystyrene nanoparticles) swarming mediated by a thermoelectric field is described. The first thermoelectric field generated by the native chemical environment of the nanoparticles is reported herein. Notably, the fluorescence lifetime of Rhodamine-B is used in this work to three-dimensionally map the induced temperature profile. In this way, the Soret coefficient of azide ions is quantified for the first time. Trapping, releasing and positionally manipulating several nanoparticles is achieved by controlling the laser position and power.

A custom made near-infrared laser device (which replaced the condenser lens) with optics that images the diode onto the focal plane of the imaging objective is used to induce heating of Cr micro-discs. Time consuming and fickle lithography was circumvented by using TEM grids as templates for the micro-discs and a sticker to create an enclosed microfluidics chamber, making the thermophoretic device easily reproducible and accessible by other researchers.

The simulated and the measured values of temperature increase with the laser intensity are discrepant. Measured values non-linearly increase and plateau, whilst simulated temperatures linearly increase with laser intensity (Figure 3.22). Moreover, the measured temperature rise is much higher than simulated. A possible explanation for this is that both Cr and Au are plasmonic, and have enhanced absorption of the light. For high temperature rise ($> 20°C$), the thin film might be undergoing thermal expansion and temporarily detaching from the surface, and thus reducing its ability to generate more heating. As part of future experiments, the temperature-lifetime dependence of Rhodamine-B could be measured in conjunction with sodium azide

and pH at the same time. Moreover, the lifetime measured temperatures should be expressed in polar coordinates, taking advantage of the symmetry to reduce the noise in the measurements. As a consequence, the measured temperature gradients could be used in determining the Soret coefficient of azide ions, rather than the Lorentzian fitted equivalent.

Under the thermoelectric field, negatively charged nanoparticles are attracted more than 20 μm away from the heating source, and are confined to the hottest region. The greater the induced temperature gradients, the faster the velocity of the attracted nanoparticles is. However, fewer nanoparticles are trapped at the centre for higher induced temperatures (Figure 3.17). A reason for this may be that the vertically repulsive electric field increases due to temperature mediated absorption of azide ions on the Au surface, creating an imbalance of the opposing thermoelectric field generated by the temperature gradient in the z-direction. Hence, particles of larger size or higher surface charge density remain trapped. This can be used as an advantage to separate nanoparticles with different charges by subjecting them to an array of decreasing thermal gradients, under fluid flow. Highly charged particles will get confined to the first and strongest thermal gradient, whilst nanoparticles that are not trapped get carried along by the fluid flow to the next thermoelectric trap with a lower thermal gradient where they have a higher propensity to be trapped.

Fluorescent depletion methods of obtaining the Soret coefficient of nanoparticles and biomolecules which are experimentally less demanding, suffer from photobleaching and other environmentally dependent intensity changes, which are not entirely accounted for. Nanoparticles traversing in a temperature field will undergo intensity changes. Even commonly used fluorescent molecules, such as Alexa Fluor, have been proven to have a strong intensity dependence with temperature [149]. Particle tracking and analysis of each nanoparticle in polar coordinates as conducted herein, offers a more comprehensive and precise way of obtaining the Soret coefficient ($S_T = D_T(r)D(r)$) relative to the Fluorescent depletion method. The tangential displacement of the nanoparticle traversing a temperature field can be used to define the diffusion coefficient $D(r)$ at various temperatures (taking into account the measured radial dependence of the temperature profile $T(r)$)). The thermo-diffusion coefficient can be calculated from the nanoparticle's radial velocity at each position ($D_T(r) = v(r)/\nabla T(r)$)). Hence, for a single induced temperature profile, the Soret coefficient of a nanoparticle or

biomolecule can be obtained for a variety of temperatures, without being affected by environmentally-induced fluorescence intensity changes.

Light from a focused beam interacting with nanoparticles in suspension has been shown to induce self-focusing and defocusing effects. Whilst the exact mechanism for the self-induced lensing is not universally agreed on in literature, the last part of this work provides extensive evidence both experimentally and from simulated data of lensing being fundamentally driven by the thermo-optic effect. This is achieved by studying Au-nanosuspensions that have a low scatter-to-absorption cross section ratios.

This self-focusing and defocusing behaviour mediated by nanoparticle absorption can be used to create tunable liquid lenses by varying the laser intensity, allowing millisecond actuation of the beam size at the far field. Additionally, it can be used to protect photosensitive optical elements from photodamage as using high laser intensities in a nanosuspension leads to significant defocusing of the beam. The critical power at which the beam undergoes defocusing can be tuned by engineering the thermal diffusivity (and its consequential thermo-optic coefficient) of the medium, as described in this work by using isopropyl alcohol-water mixtures.

The observed self-defocusing of the beam at high intensity needs further investigation as a concise mechanism for collapse has not been reported for continuous-wave self-induced lensing. The beam collapse may arise from the non-linear absorption effects becoming significant. Hence measurements need to be conducted at higher laser powers in both media to scrutinise the transient non-linear absorption effects. Additionally, wave propagating through the negative gradient index lens (calculated from the heating profile using the dispersion relation of water) should be simulated and compared to the observed lensing effects. These simulations may offer insights into why an inversion in the lensing behaviour occurs.

Thermophoretic migration of nanoparticles might also contribute to observed defocusing. As defocusing is observed at higher intensity, the induced gradients near the focus can become significant enough to cause thermophobic migration of nanoparticles. This causes a significant decrease of the refractive index at the focus, and thus greatly diverges the beam. Hence, the thermophoretic behaviour of the 40 nm Au-nanoparticles

should be investigated using the thermophoretic device.

This work shows that using Sheik-Bahae formalism to quantify the absolute refractive index changes mediated by thermal effects is not suitable. This is a consequence of the larger lensing profiles dictated by the radial heat diffusion, which is always larger than the beam size. This breaks the assumption of the Sheik-Bahae's formalism that the sizes of the lens and the beam are approximately constant [86]. A way of demonstrating the difference between the expected and measured transmission through an aperture placed at the far field would be to simulate the lensing induced by the presence of the thin cuvette at various positions along the focused beam. Whilst the Z-scan technique does not yield the absolute magnitude of Δn, it is useful for quantifying the temporal dynamics of the self-induced lensing.

In this thesis, new methods are introduced for manipulating, studying, and controlling nanoparticles in suspension using light, heat, and careful engineering of the fluidic environment. The experimental geometries are kept simple, minimising fabrication requirements, and using readily available commercial parts to increase the adoptability of the created optical systems.

References

[1] A. Ashkin, "Acceleration and trapping of particles by radiation pressure," *Physical review letters*, vol. 24, no. 4, p. 156, 1970.

[2] A. Ashkin, J. M. Dziedzic, J. E. Bjorkholm, and S. Chu, "Observation of a single-beam gradient force optical trap for dielectric particles," *Optics Letters*, vol. 11, no. 5, p. 288, May 1986. [Online]. Available: https://doi.org/10.1364/ol.11.000288

[3] P. M. Hansen, V. K. Bhatia, N. Harrit, and L. Oddershede, "Expanding the optical trapping range of gold nanoparticles," *Nano letters*, vol. 5, no. 10, pp. 1937–1942, 2005.

[4] O. Brzobohatỳ, M. Šiler, J. Trojek, L. Chvátal, V. Karásek, A. Paták, Z. Pokorná, F. Mika, and P. Zemánek, "Three-dimensional optical trapping of a plasmonic nanoparticle using low numerical aperture optical tweezers," *Scientific reports*, vol. 5, p. 8106, 2015.

[5] C. R. Head, E. Kammann, M. Zanella, L. Manna, and P. G. Lagoudakis, "Spinning nanorods–active optical manipulation of semiconductor nanorods using polarised light," *Nanoscale*, vol. 4, no. 12, pp. 3693–3697, 2012.

[6] P. M. Bendix and L. B. Oddershede, "Expanding the optical trapping range of lipid vesicles to the nanoscale," *Nano letters*, vol. 11, no. 12, pp. 5431–5437, 2011.

[7] M.-y. Wu, D.-x. Ling, L. Ling, W. Li, and Y.-q. Li, "Stable optical trapping and sensitive characterization of nanostructures using standing-wave raman tweezers," *Scientific reports*, vol. 7, p. 42930, 2017.

[8] V. Demergis and E.-L. Florin, "High precision and continuous optical transport using a standing wave optical line trap," *Optics express*, vol. 19, no. 21, pp. 20 833–20 848, 2011.

[9] T. Čižmár, M. Šiler, M. Šerỳ, P. Zemánek, V. Garcés-Chávez, and K. Dholakia, "Optical sorting and detection of submicrometer objects in a motional standing wave," *Physical Review B*, vol. 74, no. 3, p. 035105, 2006.

[10] Y.-C. Li, H.-B. Xin, H.-X. Lei, L.-L. Liu, Y.-Z. Li, Y. Zhang, and B.-J. Li, "Manipulation and detection of single nanoparticles and biomolecules by a photonic nanojet," *Light: Science & Applications*, vol. 5, no. 12, p. e16176, 2016.

[11] J.-B. Decombe, F. J. Valdivia-Valero, G. Dantelle, G. Leménager, T. Gacoin, G. C. Des Francs, S. Huant, and J. Fick, "Luminescent nanoparticle trapping with far-field optical fiber-tip tweezers," *Nanoscale*, vol. 8, no. 9, pp. 5334–5342, 2016.

[12] B. Fazio, C. D'Andrea, A. Foti, E. Messina, A. Irrera, M. G. Donato, V. Villari, N. Micali, O. M. Maragò, and P. G. Gucciardi, "Sers detection of biomolecules at physiological ph via aggregation of gold nanorods mediated by optical forces and plasmonic heating," *Scientific reports*, vol. 6, p. 26952, 2016.

[13] M. Dienerowitz, M. Mazilu, P. J. Reece, T. F. Krauss, and K. Dholakia, "Optical vortex trap for resonant confinement of metal nanoparticles," *Optics Express*, vol. 16, no. 7, p. 4991, Mar. 2008. [Online]. Available: https://doi.org/10.1364/oe.16.004991

[14] S. Nedev, A. S. Urban, A. A. Lutich, and J. Feldmann, "Optical force stamping lithography," *Nano letters*, vol. 11, no. 11, pp. 5066–5070, 2011.

[15] X. Peng, L. Lin, E. H. Hill, P. Kunal, S. M. Humphrey, and Y. Zheng, "Optothermophoretic manipulation of colloidal particles in nonionic liquids," *The Journal of Physical Chemistry C*, vol. 122, no. 42, pp. 24 226–24 234, 2018.

[16] S. A. Seidel, P. M. Dijkman, W. A. Lea, G. van den Bogaart, M. Jerabek-Willemsen, A. Lazic, J. S. Joseph, P. Srinivasan, P. Baaske, A. Simeonov *et al.*, "Microscale thermophoresis quantifies biomolecular interactions under previously challenging conditions," *Methods*, vol. 59, no. 3, pp. 301–315, 2013.

[17] M. Jerabek-Willemsen, T. André, R. Wanner, H. M. Roth, S. Duhr, P. Baaske, and D. Breitsprecher, "Microscale thermophoresis: Interaction analysis and beyond," *Journal of Molecular Structure*, vol. 1077, pp. 101–113, 2014.

[18] M. Wolff, J. J. Mittag, T. W. Herling, E. De Genst, C. M. Dobson, T. P. Knowles, D. Braun, and A. K. Buell, "Quantitative thermophoretic study of disease-related protein aggregates," *Scientific reports*, vol. 6, p. 22829, 2016.

[19] S. Duhr and D. Braun, "Optothermal Molecule Trapping by Opposing Fluid Flow with Thermophoretic Drift," *Physical Review Letters*, vol. 97, no. 3, p. 038103, Jul. 2006. [Online]. Available: https://link.aps.org/doi/10.1103/PhysRevLett.97.038103

[20] M. Braun, A. P. Bregulla, K. Gunther, M. Mertig, and F. Cichos, "Single molecules trapped by dynamic inhomogeneous temperature fields," *Nano letters*, vol. 15, no. 8, pp. 5499–5505, 2015.

[21] M. Fränzl, T. Thalheim, J. Adler, D. Huster, J. Posseckardt, M. Mertig, and F. Cichos, "Thermophoretic trap for single amyloid fibril and protein aggregation studies," *Nature Methods*, p. 1, 2019.

[22] L. Lin, M. Wang, X. Peng, E. N. Lissek, Z. Mao, L. Scarabelli, E. Adkins, S. Coskun, H. E. Unalan, B. A. Korgel, L. M. Liz-Marzán, E.-L. Florin, and Y. Zheng, "Opto-thermoelectric nanotweezers," *Nature*

Photonics, vol. 12, no. 4, pp. 195–201, Apr. 2018. [Online]. Available: http://www.nature.com/articles/s41566-018-0134-3

[23] A. Kotnala and Y. Zheng, "Opto-thermophoretic fiber tweezers," *Nanophotonics*, vol. 8, no. 3, pp. 475–485, 2019.

[24] L. Lin, X. Peng, M. Wang, L. Scarabelli, Z. Mao, L. M. Liz-Marzan, M. F. Becker, and Y. Zheng, "Light-directed reversible assembly of plasmonic nanoparticles using plasmon-enhanced thermophoresis," *ACS nano*, vol. 10, no. 10, pp. 9659–9668, 2016.

[25] W. Man, S. Fardad, Z. Zhang, J. Prakash, M. Lau, P. Zhang, M. Heinrich, D. N. Christodoulides, and Z. Chen, "Optical nonlinearities and enhanced light transmission in soft-matter systems with tunable polarizabilities," *Physical review letters*, vol. 111, no. 21, p. 218302, 2013.

[26] S. Fardad, A. Salandrino, M. Heinrich, P. Zhang, Z. Chen, and D. N. Christodoulides, "Plasmonic resonant solitons in metallic nanosuspensions," *Nano letters*, vol. 14, no. 5, pp. 2498–2504, 2014.

[27] V. Liberman, P. D. Robinson, G. P. Geurtsen, S. M. Tysk, and M. W. Geis, "Highly efficient all-optical beam modulation utilizing thermo-optic effects," *Optics express*, vol. 26, no. 8, pp. 9502–9514, 2018.

[28] A. Balbuena Ortega, E. Brambila, V. López Gayou, R. Delgado Macuil, A. Orduña Diaz, A. Zamilpa Alvarez, A. Arzola, and K. Volke-Sepúlveda, "Light control through a nonlinear lensing effect in a colloid of biosynthesized gold nanoparticles," *Journal of Modern Optics*, vol. 66, no. 5, pp. 502–511, 2019.

[29] E. Ule, "Measurement of the nonlinear refractive index by z-scan technique," 2015.

[30] T. Jia, T. He, P. Li, Y. Mo, and Y. Cui, "A study of the thermal-induced nonlinearity of au and ag colloids prepared by the chemical reaction method," *Optics & Laser Technology*, vol. 40, no. 7, pp. 936–940, 2008.

[31] V. Lenart, R. Turchiello, G. Goya, and S. Gómez, "Enhanced thermal lens effect in gold nanoparticle-doped lyotropic liquid crystal by nanoparticle clustering probed by z-scan technique," *Brazilian Journal of Physics*, vol. 45, no. 2, pp. 213–218, 2015.

[32] A. Balbuena Ortega, M. Arroyo Carrasco, M. Méndez Otero, V. Gayou, R. Delgado Macuil, H. Martínez Gutiérrez, and M. Iturbe Castillo, "Nonlocal nonlinear refractive index of gold nanoparticles synthesized by ascorbic acid reduction: comparison of fitting models," *Journal of modern optics*, vol. 61, no. sup1, pp. S68–S73, 2014.

[33] P. K. Jain, K. S. Lee, I. H. El-Sayed, and M. A. El-Sayed, "Calculated absorption and scattering properties of gold nanoparticles of different size, shape, and composition: applications in biological imaging and biomedicine," *The journal of physical chemistry B*, vol. 110, no. 14, pp. 7238–7248, 2006.

[34] S. C. Warren, A. Margineanu, D. Alibhai, D. J. Kelly, C. Talbot, Y. Alexandrov, I. Munro, M. Katan, C. Dunsby, and P. M. French, "Rapid global fitting of large fluorescence lifetime imaging microscopy datasets," *PLoS One*, vol. 8, no. 8, p. e70687, 2013.

[35] C. B. Müller, K. Weiß, A. Loman, J. Enderlein, and W. Richtering, "Remote temperature measurements in femto-liter volumes using dual-focus-fluorescence correlation spectroscopy," *Lab on a Chip*, vol. 9, no. 9, pp. 1248–1253, 2009.

[36] nanoComposix, "Mie theory calculator." [Online]. Available: https://nanocomposix.com/pages/tools

[37] A. Ashkin and J. Dziedzic, "Optical trapping and manipulation of viruses and bacteria," *Science*, vol. 235, no. 4795, pp. 1517–1520, Mar. 1987. [Online]. Available: https://doi.org/10.1126/science.3547653

[38] K. Svoboda, C. F. Schmidt, B. J. Schnapp, and B. S. M. Block, "Direct observation of kinesin stepping by optical trapping interferometry," *Nature Publishing Group*, vol. 365, no. October, pp. 721–727, 1993.

[39] M. D. Wang, H. Yin, R. Landick, J. Gelles, and S. M. Block, "Stretching DNA with Optical Tweezers," *Biophysical Journal*, vol. 72, no. March, pp. 1335–1346, 1997.

[40] C. Selhuber-Unkel, P. Yde, K. Berg-Sørensen, and L. B. Oddershede, "Variety in intracellular diffusion during the cell cycle," *Physical Biology*, vol. 6, no. 2, p. 025015, Jul. 2009. [Online]. Available: https://doi.org/10.1088/1478-3975/6/2/025015

[41] J. Guck, R. Ananthakrishnan, H. Mahmood, T. J. Moon, C. C. Cunningham, and J. Käs, "The optical stretcher: a novel laser tool to micromanipulate cells," *Biophysical journal*, vol. 81, no. 2, pp. 767–784, 2001.

[42] L. P. Ghislain and W. W. Webb, "Scanning-force microscope based on an optical trap," *Optics Letters*, vol. 18, no. 19, pp. 1678–1680, 1993.

[43] A. Terray, "Microfluidic control using colloidal devices," *Science*, vol. 296, no. 5574, pp. 1841–1844, Jun. 2002. [Online]. Available: https://doi.org/10.1126/science.1072133

[44] F. Wang, W. J. Toe, W. M. Lee, D. McGloin, Q. Gao, H. H. Tan, C. Jagadish, and P. J. Reece, "Resolving stable axial trapping points of nanowires in an optical tweezers using photoluminescence mapping," *Nano Letters*, vol. 13, no. 3, pp. 1185–1191, 2013.

[45] T. Rodgers, S. Shoji, Z. Sekkat, and S. Kawata, "Selective aggregation of single-walled carbon nanotubes using the large optical field gradient of a focused laser beam," *Physical Review Letters*, vol. 101, no. 12, Sep. 2008. [Online]. Available: https://doi.org/10.1103/physrevlett.101.127402

[46] R. B. Liebert and D. C. Prieve, "Force exerted by a laser beam on a microscopic sphere in water: designing for maximum axial force," *Industrial & engineering chemistry research*, vol. 34, no. 10, pp. 3542–3550, 1995.

[47] W. S. Pegau, D. Gray, and J. R. V. Zaneveld, "Absorption and attenuation of visible and near-infrared light in water: dependence on temperature and salinity," *Applied Optics*, vol. 36, no. 24, p. 6035, Aug. 1997. [Online]. Available: https://doi.org/10.1364/ao.36.006035

[48] K. C. Neuman and S. M. Block, "Optical trapping," *Review of Scientific Instruments*, vol. 75, no. 9, pp. 2787–2809, Sep. 2004. [Online]. Available: https://doi.org/10.1063/1.1785844

[49] S. E. S. Spesyvtseva and K. Dholakia, "Trapping in a material world," *ACS Photonics*, vol. 3, no. 5, pp. 719–736, May 2016. [Online]. Available: https://doi.org/10.1021/acsphotonics.6b00023

[50] A. Lehmuskero, P. Johansson, H. Rubinsztein-Dunlop, L. Tong, and M. Käll, "Laser trapping of colloidal metal nanoparticles," *ACS Nano*, vol. 9, no. 4, pp. 3453–3469, Apr. 2015. [Online]. Available: https://doi.org/10.1021/acsnano.5b00286

[51] C. Bradac, "Nanoscale optical trapping: A review," *Advanced Optical Materials*, vol. 6, no. 12, p. 1800005, Apr. 2018. [Online]. Available: https://doi.org/10.1002/adom.201800005

[52] S. E. S. Spesyvtseva and K. Dholakia, "Trapping in a material world," *Acs Photonics*, vol. 3, no. 5, pp. 719–736, 2016.

[53] A. Kyrsting, P. M. Bendix, and L. B. Oddershede, "Mapping 3d focal intensity exposes the stable trapping positions of single nanoparticles," *Nano letters*, vol. 13, no. 1, pp. 31–35, 2012.

[54] K. Svoboda and S. M. Block, "Optical trapping of metallic rayleigh particles," *Optics letters*, vol. 19, no. 13, pp. 930–932, 1994.

[55] O. Brzobohatỳ, M. Šiler, J. Trojek, L. Chvátal, V. Karásek, and P. Zemánek, "Non-spherical gold nanoparticles trapped in optical tweezers: shape matters," *Optics express*, vol. 23, no. 7, pp. 8179–8189, 2015.

[56] P. M. Bendix, L. Jauffred, K. Norregaard, and L. B. Oddershede, "Optical trapping of nanoparticles and quantum dots," *IEEE journal of selected topics in quantum electronics*, vol. 20, no. 3, pp. 15–26, 2013.

[57] Y. Shi, S. Xiong, L. K. Chin, J. Zhang, W. Ser, J. Wu, T. Chen, Z. Yang, Y. Hao, B. Liedberg *et al.*, "Nanometer-precision linear sorting with synchronized optofluidic dual barriers," *Science advances*, vol. 4, no. 1, p. eaao0773, 2018.

[58] Y. Shi, L. K. Chin, J. Wu, T. Chen, L. Ai-Qun, and H. Zhao, "Manipulation of nanoparticles using quadrangular microlens," in *CLEO: QELS_Fundamental Science*. Optical Society of America, 2015, pp. JW2A–83.

[59] T. Shoji and Y. Tsuboi, "Plasmonic optical tweezers toward molecular manipulation: tailoring plasmonic nanostructure, light source, and resonant trapping," *The journal of physical chemistry letters*, vol. 5, no. 17, pp. 2957–2967, 2014.

[60] W. Cui, L. Mu, X. Duan, W. Pang, and M. Reed, "Trapping of sub-100 nm nanoparticles using gigahertz acoustofluidic tweezers for biosensing applications," *Nanoscale*, 2019.

[61] M. A. Gerspach, N. Mojarad, D. Sharma, T. Pfohl, and Y. Ekinci, "Soft electrostatic trapping in nanofluidics," *Microsystems & nanoengineering*, vol. 3, p. 17051, 2017.

[62] A. P. Fields and A. E. Cohen, "Electrokinetic trapping at the one nanometer limit," *Proceedings of the National Academy of Sciences*, vol. 108, no. 22, pp. 8937–8942, 2011.

[63] D. Braun and A. Libchaber, "Trapping of dna by thermophoretic depletion and convection," *Physical review letters*, vol. 89, no. 18, p. 188103, 2002.

[64] M. Asmari, R. Ratih, H. A. Alhazmi, and S. El Deeb, "Thermophoresis for characterizing biomolecular interaction," *Methods*, vol. 146, pp. 107–119, 2018.

[65] S. Duhr and D. Braun, "Why molecules move along a temperature gradient," *Proceedings of the National Academy of Sciences*, vol. 103, no. 52, pp. 19 678–19 682, 2006.

[66] S. J. Marrink, M. Berkowitz, and H. J. Berendsen, "Molecular dynamics simulation of a membrane/water interface: the ordering of water and its relation to the hydration force," *Langmuir*, vol. 9, no. 11, pp. 3122–3131, 1993.

[67] L. Lin, X. Peng, Z. Mao, X. Wei, C. Xie, and Y. Zheng, "Interfacial-entropy-driven thermophoretic tweezers," *Lab on a Chip*, vol. 17, no. 18, pp. 3061–3070, 2017.

[68] S. Di Lecce, T. Albrecht, and F. Bresme, "The role of ion–water interactions in determining the soret coefficient of licl aqueous solutions," *Physical Chemistry Chemical Physics*, vol. 19, no. 14, pp. 9575–9583, 2017.

[69] M. Reichl, M. Herzog, A. Götz, and D. Braun, "Why charged molecules move across a temperature gradient: The role of electric fields," *Physical review letters*, vol. 112, no. 19, p. 198101, 2014.

[70] M. Reichl, M. Herzog, F. Greiss, M. Wolff, and D. Braun, "Understanding the similarity in thermophoresis between single-and double-stranded dna or rna," *Physical Review E*, vol. 91, no. 6, p. 062709, 2015.

[71] A. Majee and A. Würger, "Thermocharge of a hot spot in an electrolyte solution," *Soft Matter*, vol. 9, no. 7, pp. 2145–2153, 2013.

[72] L. Lin, J. Zhang, X. Peng, Z. Wu, A. C. Coughlan, Z. Mao, M. A. Bevan, and Y. Zheng, "Opto-thermophoretic assembly of colloidal matter," *Science advances*, vol. 3, no. 9, p. e1700458, 2017.

[73] D. Vigolo, S. Buzzaccaro, and R. Piazza, "Thermophoresis and thermoelectricity in surfactant solutions," *Langmuir*, vol. 26, no. 11, pp. 7792–7801, 2010.

[74] A. L. Sehnem, A. M. F. Neto, D. Niether, and S. Wiegand, "Diffusiophoresis as ruling effect: Influence of organic salts on thermodiffusion of iron oxide nanoparticles," *Physical Review E*, vol. 98, no. 6, p. 062615, 2018.

[75] L. M. Keil, F. M. Möller, M. Kieß, P. W. Kudella, and C. B. Mast, "Proton gradients and ph oscillations emerge from heat flow at the microscale," *Nature communications*, vol. 8, no. 1, p. 1897, 2017.

[76] M. Jerabek-Willemsen, C. J. Wienken, D. Braun, P. Baaske, and S. Duhr, "Molecular interaction studies using microscale thermophoresis," *Assay and drug development technologies*, vol. 9, no. 4, pp. 342–353, 2011.

[77] M. Braun and F. Cichos, "Optically controlled thermophoretic trapping of single nano-objects," *ACS nano*, vol. 7, no. 12, pp. 11 200–11 208, 2013.

[78] X. Peng, J. Li, L. Lin, Y. Liu, and Y. Zheng, "Opto-thermophoretic manipulation and construction of colloidal superstructures in photocurable hydrogels," *ACS applied nano materials*, vol. 1, no. 8, pp. 3998–4004, 2018.

[79] Y. Liu, L. Lin, B. Bangalore Rajeeva, J. W. Jarrett, X. Li, X. Peng, P. Kollipara, K. Yao, D. Akinwande, A. K. Dunn *et al.*, "Nanoradiator-mediated deterministic opto-thermoelectric manipulation," *ACS nano*, vol. 12, no. 10, pp. 10 383–10 392, 2018.

[80] M. Y. Salazar-Romero, Y. A. Ayala, E. Brambila, L. A. Lopez-Peña, L. Sciberras, A. A. Minzoni, R. A. Terborg, J. P. Torres, and K. Volke-Sepúlveda, "Steering and switching of soliton-like beams via interaction in a nanocolloid with positive polarizability," *Optics letters*, vol. 42, no. 13, pp. 2487–2490, 2017.

[81] V. I. Ivanov, G. D. Ivanova, and V. K. Khe, "Light induced lens response in nanosuspension," in *Asia-Pacific Conference on Fundamental Problems of Opto- and Microelectronics*, vol. 10176. International Society for Optics and Photonics, 2016, p. 1017607.

[82] T. S. Kelly, Y.-X. Ren, A. Samadi, A. Bezryadina, D. Christodoulides, and Z. Chen, "Guiding and nonlinear coupling of light in plasmonic nanosuspensions," *Optics letters*, vol. 41, no. 16, pp. 3817–3820, 2016.

[83] E. W. Van Stryland and M. Sheik-Bahae, "Z-scan technique for nonlinear materials characterization," in *Materials Characterization and Optical Probe Techniques: A Critical Review*, vol. 10291. International Society for Optics and Photonics, 1997, p. 102910Q.

[84] M. Sheik-Bahae and M. P. Hasselbeck, "Third-order optical nonlinearities," vol. IV, 2000.

[85] R. Del Coso and J. Solis, "Relation between nonlinear refractive index and third-order susceptibility in absorbing media," *JOSA B*, vol. 21, no. 3, pp. 640–644, 2004.

[86] M. Sheik-Bahae, A. A. Said, T.-H. Wei, D. J. Hagan, and E. W. Van Stryland, "Sensitive measurement of optical nonlinearities using a single beam," *IEEE journal of quantum electronics*, vol. 26, no. 4, pp. 760–769, 1990.

[87] P. B. Johnson and R. W. Christy, "Optical constants of the noble metals," *Physical Review B*, vol. 6, no. 12, pp. 4370–4379, Dec. 1972. [Online]. Available: https://doi.org/10.1103/physrevb.6.4370

[88] G. M. Hale and M. R. Querry, "Optical constants of water in the 200-nm to 200-μm wavelength region," *Applied Optics*, vol. 12, no. 3, p. 555, Mar. 1973. [Online]. Available: https://doi.org/10.1364/ao.12.000555

[89] P. Zemánek, A. Jonáš, L. Šrámek, and M. Liška, "Optical trapping of rayleigh particles using a gaussian standing wave," *Optics Communications*, vol. 151, no. 4-6, pp. 273–285, Jun. 1998. [Online]. Available: https://doi.org/10.1016/s0030-4018(98)00093-5

[90] H. Kogelnik, "On the propagation of gaussian beams of light through lenslike media including those with a loss or gain variation," *Applied Optics*, vol. 4, no. 12, p. 1562, Dec. 1965. [Online]. Available: https://doi.org/10.1364/ao.4.001562

[91] T. Kolb, J. Kraxner, K. Skodzek, M. Haug, D. Crawford, K. K. Maaß, K. E. Aifantis, and G. Whyte, "Optomechanical measurement of the role of lamins in whole cell deformability," *Journal of biophotonics*, vol. 10, no. 12, pp. 1657–1664, 2017.

[92] W. Demtröder, "Electrodynamics and Optics," ser. Undergraduate Lecture Notes in Physics. Cham: Springer International Publishing, 2019, pp. 219–223. [Online]. Available: http://link.springer.com/10.1007/978-3-030-02291-4

[93] J. Xu and S. L. Craig, "Influence of the extent of hybridization on the hydrodynamic radius of dna-functionalized gold nanoparticles," *Langmuir*, vol. 23, no. 4, pp. 2015–2020, 2007.

[94] T. Zheng, S. Bott, and Q. Huo, "Techniques for accurate sizing of gold nanoparticles using dynamic light scattering with particular application to chemical and biological sensing based on aggregate formation," *ACS applied materials & interfaces*, vol. 8, no. 33, pp. 21 585–21 594, 2016.

[95] N. Chenouard, I. Smal, F. de Chaumont, M. Maška, I. F. Sbalzarini, Y. Gong, J. Cardinale, C. Carthel, S. Coraluppi, M. Winter, A. R. Cohen, W. J. Godinez, K. Rohr, Y. Kalaidzidis, L. Liang, J. Duncan, H. Shen, Y. Xu, K. E. G. Magnusson, J. Jaldén, H. M. Blau, P. Paul-Gilloteaux, P. Roudot, C. Kervrann, F. Waharte, J.-Y. Tinevez, S. L. Shorte, J. Willemse, K. Celler, G. P. van Wezel, H.-W. Dan, Y.-S. Tsai, C. O. de Solórzano, J.-C. Olivo-Marin, and E. Meijering, "Objective comparison of particle tracking methods," *Nature Methods*, vol. 11, no. 3, pp. 281–289, Jan. 2014. [Online]. Available: https://doi.org/10.1038/nmeth.2808

[96] J. C. Crocker and D. G. Grier, "Methods of Digital Video Microscopy for Colloidal Studies," *Journal of Colloid and Interface Science*, vol. 179, no. 1, pp. 298–310, Apr. 1996. [Online]. Available: https://linkinghub.elsevier.com/retrieve/pii/S0021979796902179

[97] T. Lindeberg, "Feature Detection with Automatic Scale Selection," *International Journal of Computer Vision*, vol. 30, no. 2, pp. 79–116, 1998. [Online]. Available: http://link.springer.com/10.1023/A:1008045108935

[98] "Trackpy: Trackpy V0.4.1," Apr. 2018. [Online]. Available: https://zenodo.org/record/1226458

[99] T. Lindeberg, "Scale selection properties of generalized scale-space interest point detectors," *Journal of Mathematical Imaging and vision*, vol. 46, no. 2, pp. 177–210, 2013.

[100] H. Kong, H. C. Akakin, and S. E. Sarma, "A generalized laplacian of gaussian filter for blob detection and its applications," *IEEE transactions on cybernetics*, vol. 43, no. 6, pp. 1719–1733, 2013.

[101] R. Metzler, J.-H. Jeon, A. G. Cherstvy, and E. Barkai, "Anomalous diffusion models and their properties: non-stationarity, non-ergodicity, and ageing at the centenary of single particle tracking," *Phys. Chem. Chem. Phys.*, vol. 16, no. 44, pp. 24 128–24 164, 2014. [Online]. Available: http://xlink.rsc.org/?DOI=C4CP03465A

[102] R. Metzler and J. Klafter, "The random walk's guide to anomalous diffusion: a fractional dynamics approach," *Physics Reports*, vol. 339, no. 1, pp. 1–77, Dec. 2000. [Online]. Available: https://linkinghub.elsevier.com/retrieve/pii/S0370157300000703

[103] H. Park, D.-J. Lim, J. B. Vines, J.-H. Yoon, and N.-E. Ryu, "Gold nanoparticles for photothermal cancer therapy," *Frontiers in chemistry*, vol. 7, p. 167, 2019.

[104] C. J. Wienken, P. Baaske, U. Rothbauer, D. Braun, and S. Duhr, "Protein-binding assays in biological liquids using microscale thermophoresis," *Nature communications*, vol. 1, p. 100, 2010.

[105] J. Chen, H. Cong, F.-C. Loo, Z. Kang, M. Tang, H. Zhang, S.-Y. Wu, S.-K. Kong, and H.-P. Ho, "Thermal gradient induced tweezers for the manipulation of particles and cells," *Scientific Reports*, vol. 6, no. 1, p. 35814, Dec. 2016. [Online]. Available: http://www.nature.com/articles/srep35814

[106] J. F. Torres, A. Komiya, D. Henry, and S. Maruyama, "Measurement of Soret and Fickian diffusion coefficients by orthogonal phase-shifting interferometry and its application to protein aqueous solutions," *The Journal of Chemical Physics*, vol. 139, no. 7, p. 074203, Aug. 2013. [Online]. Available: http://aip.scitation.org/doi/10.1063/1.4817682

[107] E. L. Talbot, J. Kotar, L. Parolini, L. Di Michele, and P. Cicuta, "Thermophoretic migration of vesicles depends on mean temperature and head group chemistry," *Nature Communications*, vol. 8, no. 1, p. 15351, Aug. 2017. [Online]. Available: http://www.nature.com/articles/ncomms15351

[108] H.-R. Jiang, H. Wada, N. Yoshinaga, and M. Sano, "Manipulation of Colloids by a Nonequilibrium Depletion Force in a Temperature Gradient," *Physical Review Letters*, vol. 102, no. 20, p. 208301, May 2009. [Online]. Available: https://link.aps.org/doi/10.1103/PhysRevLett.102.208301

[109] C. Zhao, J. Fu, A. Oztekin, and X. Cheng, "Measuring the Soret coefficient of nanoparticles in a dilute suspension," *Journal of Nanoparticle Research*, vol. 16, no. 10, p. 2625, Oct. 2014. [Online]. Available: http://link.springer.com/10.1007/s11051-014-2625-6

[110] J. Gargiulo, T. Brick, I. L. Violi, F. C. Herrera, T. Shibanuma, P. Albella, F. G. Requejo, E. Cortés, S. A. Maier, and F. D. Stefani, "Understanding and Reducing Photothermal Forces for the Fabrication of Au Nanoparticle Dimers by Optical Printing," *Nano Letters*, vol. 17, no. 9, pp. 5747–5755, Sep. 2017. [Online]. Available: https://pubs.acs.org/doi/10.1021/acs.nanolett.7b02713

[111] L.-H. Yu and Y.-F. Chen, "Concentration-Dependent Thermophoretic Accumulation for the Detection of DNA Using DNA-Functionalized Nanoparticles," *Analytical Chemistry*, vol. 87, no. 5, pp. 2845–2851, Mar. 2015. [Online]. Available: https://pubs.acs.org/doi/10.1021/ac504296e

[112] "Optical Glass Data Sheet," May 2019, publisher: Schott. [Online]. Available: https://www.schott.com/d/advanced_optics/ac85c64c-60a0-4113-a9df-23ee1be20428/1.14/schott-optical-glass-collection-datasheets-english-may-2019.pdf

[113] P. Johnson and R. Christy, "Optical constants of transition metals: Ti, V, Cr, Mn, Fe, Co, Ni, and Pd," *Physical Review B*, vol. 9, no. 12, pp. 5056–5070, Jun. 1974. [Online]. Available: https://link.aps.org/doi/10.1103/PhysRevB.9.5056

[114] Comsol, "Theory for the Single-Phase Flow Interfaces," in *CFD Module User's Guide*. Comsol, 2018, pp. 130–132. [Online]. Available: https://doc.comsol.com/5.4/doc/com.comsol.help.cfd/CFDModuleUsersGuide.pdf

[115] C. Hong, S. Yang, and J. C. Ndukaife, "Optofluidic control using plasmonic tin bowtie nanoantenna," *Optical Materials Express*, vol. 9, no. 3, pp. 953–964, 2019.

[116] J. Garcia-Guirado, R. A. Rica, J. Ortega, J. Medina, V. Sanz, E. Ruiz-Reina, and R. Quidant, "Overcoming diffusion-limited biosensing by electrothermoplasmonics," *ACS Photonics*, vol. 5, no. 9, pp. 3673–3679, 2018.

[117] E. T. Topal, "A flow induced vertical thermoelectric generator and its simulation using comsol multiphysics," in *COMSOL Conference, Boston, MA, October*, 2011, pp. 13–15.

[118] S. R. Turns, "Thermodynamics: concepts and applications." New York: Cambridge University Press, 2006, pp. 441–442, oCLC: ocm62341549.

[119] A. G. Whittington, "Heat and Mass Transfer in Glassy and Molten Silicates," in *Measurements, Mechanisms, and Models of Heat Transport*. Elsevier, 2019, pp. 327–357. [Online]. Available: https://linkinghub.elsevier.com/retrieve/pii/B9780128099810000103

[120] B. J. Roxworthy, A. M. Bhuiya, S. P. Vanka, and K. C. Toussaint Jr, "Understanding and controlling plasmon-induced convection," *Nature communications*, vol. 5, p. 3173, 2014.

[121] B. Wang and X. Cheng, "Enhancement of binding kinetics on affinity substrates by laser point heating induced transport," *Analyst*, vol. 141, no. 5, pp. 1807–1813, 2016.

[122] H. Li, S.-r. Sun, J. Q. Yap, J.-h. Chen, and Q. Qian, "0.9% saline is neither normal nor physiological," *Journal of Zhejiang University-SCIENCE B*, vol. 17, no. 3, pp. 181–187, 2016.

[123] H. Guo, M. H. Wang, J. X. Liu, Z. H. Nie, F. Ye, and C. F. Ma, "Temperature distribution on anodic surface of membrane electrode assembly in proton exchange membrane fuel cell with interdigitated flow bed," *Journal of Power Sources*, vol. 273, pp. 775–783, Jan. 2015. [Online]. Available: https://linkinghub.elsevier.com/retrieve/pii/S037877531401578X

[124] K. Kim, J. Chung, G. Hwang, O. Kwon, and J. S. Lee, "Quantitative Measurement with Scanning Thermal Microscope by Preventing the Distortion Due to the Heat Transfer through the Air," *ACS Nano*, vol. 5, no. 11, pp. 8700–8709, Nov. 2011. [Online]. Available: https://pubs.acs.org/doi/10.1021/nn2026325

[125] M. M. Kim, A. Giry, M. Mastiani, G. O. Rodrigues, A. Reis, and P. Mandin, "Microscale thermometry: A review," *Microelectronic Engineering*, vol. 148, pp. 129–142, Dec. 2015. [Online]. Available: https://linkinghub.elsevier.com/retrieve/pii/S0167931715300873

[126] K. G. Casey and E. L. Quitevis, "Effect of solvent polarity on nonradiative processes in xanthene dyes: Rhodamine B in normal alcohols," *The Journal of Physical Chemistry*, vol. 92, no. 23, pp. 6590–6594, Nov. 1988. [Online]. Available: https://pubs.acs.org/doi/abs/10.1021/j100334a023

[127] M. Vogel, W. Rettig, R. Sens, and K. H. Drexhage, "Structural relaxation of rhodamine dyes with different N-substitution patterns: A study of fluorescence decay times and quantum yields," *Chemical Physics Letters*, vol. 147, no. 5, pp. 452–460, Jun. 1988. [Online]. Available: https://linkinghub.elsevier.com/retrieve/pii/0009261488850073

[128] M. Kim and M. Yoda, "Dual-tracer fluorescence thermometry measurements in a heated channel," *Experiments in Fluids*, vol. 49, no. 1, pp. 257–266, Jul. 2010. [Online]. Available: http://link.springer.com/10.1007/s00348-010-0853-9

[129] Invitrogen, "Working With FluoSpheres Fluorescent Microspheres," publisher: Thermofisher. [Online]. Available: https://assets.thermofisher.com/TFS-Assets/LSG/manuals/mp05001.pdf

[130] "Measuring Zeta Potential - Laser Doppler Electrophoresis Explained," 2018, publisher: Malvern Panalytical Limited. [Online]. Available: https://www.malvernpanalytical.com/en/learn/knowledge-center/technical-notes/TN150611LDEexplained

[131] R. Mercadé-Prieto, L. Rodriguez-Rivera, and X. D. Chen, "Fluorescence lifetime of rhodamine b in aqueous solutions of polysaccharides and proteins as a function of viscosity and temperature," *Photochemical & Photobiological Sciences*, vol. 16, no. 11, pp. 1727–1734, 2017.

[132] N. Kitamura, Y. Hosoda, C. Iwasaki, K. Ueno, and H.-B. Kim, "Thermal phase transition of an aqueous poly (n-isopropylacrylamide) solution in a polymer microchannel-microheater chip," *Langmuir*, vol. 19, no. 20, pp. 8484–8489, 2003.

[133] R. K. Benninger, Y. Koç, O. Hofmann, J. Requejo-Isidro, M. A. Neil, P. M. French, and A. J. deMello, "Quantitative 3d mapping of fluidic temperatures within microchannel networks using fluorescence lifetime imaging," *Analytical chemistry*, vol. 78, no. 7, pp. 2272–2278, 2006.

[134] C. Paviolo, A. Clayton, S. McArthur, and P. Stoddart, "Temperature measurement in the microscopic regime: a comparison between fluorescence lifetime-and intensity-based methods," *Journal of microscopy*, vol. 250, no. 3, pp. 179–188, 2013.

[135] K. Aslan, Z. Leonenko, J. R. Lakowicz, and C. D. Geddes, "Annealed silver-island films for applications in metal-enhanced fluorescence: interpretation in terms of radiating plasmons," *Journal of fluorescence*, vol. 15, no. 5, p. 643, 2005.

[136] M. Wolff, D. Braun, and M. A. Nash, "Detection of thermoresponsive polymer phase transition in dilute low-volume format by microscale thermophoretic depletion," *Analytical chemistry*, vol. 86, no. 14, pp. 6797–6803, 2014.

[137] Y. Seol, A. E. Carpenter, and T. T. Perkins, "Gold nanoparticles: enhanced optical trapping and sensitivity coupled with significant heating," *Optics Letters*, vol. 31, no. 16, p. 2429, Aug. 2006. [Online]. Available: https://www.osapublishing.org/abstract.cfm?URI=ol-31-16-2429

[138] I. Thormählen, J. Straub, and U. Grigull, "Refractive Index of Water and Its Dependence on Wavelength, Temperature, and Density," *Journal of Physical and Chemical Reference Data*, vol. 14, no. 4, pp. 933–945, Oct. 1985. [Online]. Available: http://aip.scitation.org/doi/10.1063/1.555743

[139] J. Wang and M. Fiebig, "Measurement of the thermal diffusivity of aqueous solutions of alcohols by a laser-induced thermal grating technique," *International Journal of Thermophysics*, vol. 16, no. 6, pp. 1353–1361, Nov. 1995. [Online]. Available: http://link.springer.com/10.1007/BF02083545

[140] X. Z. Yan, Q. S. Wu, X. Wang, and X. Y. Sun, "Semi-cool temperature compensation algorithm based on the double exponential model in the ultrasonic positioning system," *IEEE Transactions on Instrumentation and Measurement*, 2019.

[141] G. Arias-Gil, F. W. Ohl, K. Takagaki, and M. T. Lippert, "Measurement, modeling, and prediction of temperature rise due to optogenetic brain stimulation," *Neurophotonics*, vol. 3, no. 4, p. 045007, 2016.

[142] M. L. Crespillo, J. T. Graham, Y. Zhang, and W. J. Weber, "Temperature measurements during high flux ion beam irradiations," *Review of Scientific Instruments*, vol. 87, no. 2, p. 024902, Feb. 2016. [Online]. Available: http://aip.scitation.org/doi/10.1063/1.4941720

[143] *EM Grade Data Sheet Gold colloid – 40nm*, BBI Solutions, 2019, batch #023761.

[144] J. M. Khosrofian and B. A. Garetz, "Measurement of a Gaussian laser beam diameter through the direct inversion of knife-edge data," *Applied Optics*, vol. 22, no. 21, p. 3406, Nov. 1983. [Online]. Available: https://www.osapublishing.org/abstract.cfm?URI=ao-22-21-3406

[145] M. A. de Araújo, R. Silva, E. de Lima, D. P. Pereira, and P. C. de Oliveira, "Measurement of Gaussian laser beam radius using the knife-edge technique: improvement on data analysis," *Applied Optics*, vol. 48, no. 2, p. 393, Jan. 2009. [Online]. Available: https://www.osapublishing.org/abstract.cfm?URI=ao-48-2-393

[146] R. Ferrando, R. Spadacini, and G. Tommei, "Kramers problem in periodic potentials: Jump rate and jump lengths," *Physical Review E*, vol. 48, no. 4, p. 2437, 1993.

[147] R. Ferrando, R. Spadacini, G. Tommei, and G. Caratti, "Time scales and diffusion mechanisms in the kramers equation with periodic potentials (i)," *Physica A: Statistical Mechanics and its Applications*, vol. 195, no. 3-4, pp. 506–532, 1993.

[148] J.-F. Li, Y.-J. Zhang, S.-Y. Ding, R. Panneerselvam, and Z.-Q. Tian, "Core–shell nanoparticle-enhanced raman spectroscopy," *Chemical reviews*, vol. 117, no. 7, pp. 5002–5069, 2017.

[149] Q. Jiang, B. Rogez, J.-B. Claude, G. Baffou, and J. Wenger, "Temperature measurement in plasmonic nanoapertures used for optical trapping," *ACS Photonics*, 2019.

A

Microfluidic fabrication protocol

The template for the microfluidic chips were creating using lithography of SU-8 (2050 series) using a direct laser writer (LPKF). Once a design was drawn into the software controlling the LPKF machine, the procedure for creating channel heights of 125 μm (same size as fibre diameter) is as follows:

1. Clean silicone wave with distilled water, acetone and then isopropyl alcohol. Air dry with gun
2. Place on spin coater and apply vacuum
3. Add SU-8 (2-3 ml)
4. Spin coat for 10 seconds with 500 rpm and acceleration of 100 rpm/s
5. Spin coat 1000 rpm for 30 seconds and acceleration of 300 rpm/s
6. Soft bake at 65°C for 5 minutes (reduced thermal shock), and then 35 minutes at 95°C
7. Calibrate the LPKF laser before loading sample (auto procedure)
8. Load into LPKF tray (upside down) making sure the tray is on a flat even surface
   (a) Set exposure to 500 mJ/cm^2
   (b) Initiate device levelling by clicking three points to define a plane
   (c) Set autofocus (for the laser and camera) and click on the first defined coordinate to find it using the back reflected light from the wafer
   (d) Crudely Level device using manual control of the piezo-levelling stage and let auto levelling run twice

(e) Send to laser, preview the run and then press start to begin laser writing

9. Post exposure bake: 5 minutes $65°C$ followed by 5 minutes $95°C$
10. Develop in PGMEA for 6 mins
11. Rinse with isopropyl, acetone to stop development
12. Hard bake again if needed
13. Place wave on a petri-dish and cover

Once a mould was created, the following steps were taken to imprint it on PDMS:

1. Mix PDMS and curing agent (10:1 by weight) to fill half a petri-dish (*ca.* 15 *ml*). Mix well
2. Pour PDMS solutions over the SU-8 mould
3. Put into a desiccator to remove trapped air bubbles in the PDMS
4. Once all bubbles removed, place it on a flat surface, either in a cell incubator or a hot plot (at $65°C$) until PDMS has hardened
5. Use scalpel to peal away PDMS from petri-dish, taking care not to damage silicone wafer and SU8 structures
6. Trim off excess PDMS

B

Dispersion Relation of Water

The dispersion relation for a given wavelength (λ), temperature (T) and pressure (p) was calculated using [138]:

$$\begin{aligned} n(\lambda,T,p) &= \sqrt{(a1/(\lambda^2-\lambda_a^2))+a2+(a3*l^2)+(a4*\lambda^4)+(a5*\lambda^6)} \\ &+ ((b1+(b2*\lambda^2)+(b3*\lambda^4))*(T-T_b))+((b4+(b5*\lambda^2) \\ &+ (b6*\lambda^4))*(T-T_b)^2)+((b7+(b8*\lambda^2)+(b9*\lambda^4))*(T-T_b)^3) \\ &+ ((c1+(c2*\lambda^2)+(c3+(c4*\lambda^2))*T)*(p-p_b)) \\ &+ ((c5+(c6*\lambda^2))*(p-p_b)^2) \end{aligned} \tag{.1}$$

which has the following coefficients:

T_b = 19.993 (reference temperature, in $°C$, valid between -10$°C \leq T < 100\ °C$)
p_b=1.01325 (reference pressure in *bar*, valid between 1 *bar* $\leq$ p $\leq$ 1200 *bar*)
λ_a^2 = 0.018085 (reference wavelength in μm, valid between 0.182 $\mu m \leq \lambda \leq$ 2.770μm)

a1 = 5.743534e-13, a2 = 1.769238, a3 = -2.797222e-2, a4 = 8.715348e-3, a5 = -1.413942e-3

b1 = -8.454823e-5, b2 = -2.787742e-5, b3 = 2.608176e-6, b4 = -2.050671e-6, b5 = 1.019989e-6, b6 = -2.611919e-6, b7 = 8.194989e-9, b8 = -8.107707e-9, b9 = 4.877274e-8

c1 = 8.419632e-6, c2 = 1.941681e-5, c3 = -7.762524e-8, c4 = 4.371257e-8, c5 = 7.089664e-9, c6 = -2.240384e-8